Studies on the Properties of Graphene and Sucrose Palmitate Reinforced Poly(lactic acid) Nanocomposite Films

A Thesis submitted in partial fulfillment of the requirements for the degree of

DOCTOR OF PHILOSOPHY

by

V. Ravi babu
Roll No.: 10610715

Department of Chemical Engineering
Indian Institute of Technology Guwahati
Guwahati - 781039, India

JANUARY 2015

Dedicated To

My Parents

&

The Almighty

Department of Chemical Engineering
Indian Institute of Technology Guwahati
Guwahati - 781039, India

CERTIFICATE

This is to certify that the thesis entitled **"*Studies on the Properties of Graphene and Sucrose Palmitate Reinforced Poly(lactic acid) Nanocomposite Films*"** being submitted by ***V. Ravi babu*** for the award of PhD degree has been carried out under our guidance and supervision. The work documented in this thesis has not been submitted to any other University or Institute for the award of any degree or diploma.

(Dr. Vimal Katiyar)
Associate Professor
Department of Chemical Engineering
Indian Institute of Technology Guwahati
Guwahati - 781039, India.

(Dr. G. Pugazhenthi)
Professor
Department of Chemical Engineering
Indian Institute of Technology Guwahati
Guwahati - 781039, India.

Department of Chemical Engineering
Indian Institute of Technology Guwahati
Guwahati - 781039, India

CERTIFICATE

This is to certify that the thesis entitled **"*Studies on the Properties of Graphene and Sucrose Palmitate Reinforced Poly(lactic acid) Nanocomposite Films*"** being submitted by ***V. Ravi babu*** for the award of PhD degree has been carried out under our guidance and supervision. The work documented in this thesis has not been submitted to any other University or Institute for the award of any degree or diploma.

(Dr. Vimal Katiyar)
Associate Professor
Department of Chemical Engineering
Indian Institute of Technology Guwahati
Guwahati - 781039, India.

(Dr. G. Pugazhenthi)
Associate Professor
Department of Chemical Engineering
Indian Institute of Technology Guwahati
Guwahati - 781039, India.

ACKNOWLEDGEMENTS

I would like to express my sincere thanks to my thesis advisors, Dr. Vimal Katiyar and Dr. G. Pugazhenthi for providing me guidance, support and encouragement throughout my doctoral work. I am always indebted to them for providing me an opportunity to work under their guidance. Through their actions, they have shown me how research should be carried out and trained me to develop my technical, communication and writing skills. I sincerely appreciate their flexibility and friendly nature. It has been a great privilege working under their guidance and learn from their research expertise.

I sincerely express my heartfelt thanks to my doctoral committee members Prof. Ramgopal Uppaluri, Dr. Amit Kumar, Department of Chemical Engineering and Dr. Mohammad Quershi, Department of Chemistry. Their suggestions and advices during my review seminars have helped me to improve the quality of my research work. I extend my sincere thanks to all other faculty members of my department for their advices and help during my doctoral work. I am thankful to Prof. P.K. Iyer, Department of Chemistry for kindly allowing me to utilize the polarized optical microscopy facility available in his research lab.

I am also thankful to all the technical staffs Mr. Harsha, Mr. Kaustav, Ms. Ritumoni, Mr. Lukumoni, Mr. Prasun, Mr. Debojit … and non-technical staffs Mr. Kalyan, Mr. Bhagya Bora … of my department for their kind co-operation and help during my entire doctoral work. I am extremely grateful to the technical staffs of my department for teaching me how to use several characterization instruments described in this work on my own, which has helped me to complete my work on time. I am thankful to the Central Instruments Facility of IIT Guwahati for allowing me to carry out Scanning Electron Microscopy and Field-Emission Scanning Electron Microscopy analysis on my own for my research work. I am extremely grateful to the “Centre of Excellence for Sustainable Polymers (CoE-SUSPOL)”, IIT Guwahati for providing me with experimental and characterization facilities to carry out my research work.

I am thankful to all my co-research fellows Arvind, Neelima, Akilesh, Prodyut, Rahul, Sai Phani, Phani Kumar, Anup, Surendra, Umesh, Atanu, Melaku, Shasanka, Bhasney, Narendran, Gourhari, Ananya, Debashis, Medha, Monika, Samir, Dr. Dhruba, Dr. Rashmi, ….. and entire “CoE-SUSPOL team” for their help in several forms during my doctoral work. I would always cherish the wonderful moments I have shared with my entire team members. I take this opportunity to express my heartfelt thanks to all my school, under-graduate and post-graduate friends and well-wishers for extending their support and help in my life.

I am blessed to have wonderful family, which include my parents, in-laws and my wife. Words cannot define the limits of appreciation for our relationship. Without the sacrifices and hard work of my parents, it is never possible for me to reach this stage in my life. Above all, I owe it all to the Almighty for being all in all and enabling me to the completion of my doctoral work.

V. Ravi babu

ABSTRACT

Environmental and sustainability issues concerning petroleum-based feedstocks have begun a growing emphasis on the opportunity for novel category of eco-friendly materials. The domination of biodegradable plastics for packaging sector is expanding as a result of the depletion of resources of petroleum-based plastics and the increasing environmental problems associated with plastic wastes. In this perspective, the possible replacement of conventional plastics with biodegradable and renewable polymers has been explored during the past decade. Poly(lactic acid) (PLA) is one of such potential representative biodegradable polymers, which has rapidly become the most industrialized bio sourced synthetic polyester. However, the drawbacks associated with PLA such as poor ductility, slow crystallization rate and barrier effects for gaseous substances (water vapour, oxygen (O_2), and carbon dioxide (CO_2) limit its versatility as food packaging material. An effort has been undertaken in the current doctoral work to address these limitations by the fabrication of poly(lactic acid) based nanocomposites.

In the current work, the effect of two different nanofillers, “graphene” (GR) and “sucrose palmitate” (SP) on the structural, morphological, optical, thermal, mechanical and barrier properties of PLA is investigated. Thermal exfoliation of expandable graphite (EG) is carried out at different temperatures ranging from 200-1000 °C. Based on the carbon yield (%), the optimum temperature for thermal exfoliation of EG is determined to be 750 °C. X-ray diffraction (XRD) results disclose the effect of sonication time on the dispersion ability of GR in the PLA matrix. A high resolution transmission electron microscopy (TEM) image of GR pictoriated after sonication process demonstrates a monolayer structure of GR. Thermo-gravimetric analysis reveals that the decomposition temperature for the PLA composite with 0.5 wt% GR content is increased about 31 °C over neat PLA, when 10% weight loss is taken as a point of comparison. Differential scanning calorimetry (DSC) analysis authenticates that GR acts as a nucleating agent and enhances the melting point of PLA composites over neat

PLA. The enhancement of elongation at break (51%) is obtained for PLA-GR nanocomposites as compared to neat PLA. The permeation of oxygen is reduced by 22% after incorporating 0.1 wt% GR in the PLA matrix. This is attributed to the tortuous path effect generated by the exfoliated GR nanosheets. The ordered orientation of the SP in the PLA matrix is visualized by TEM analysis, and this in turn verifies the uniform dispersion of SP filler into PLA matrix. DSC and XRD results validate that the incorporated biofiller acts as a nucleating agent and partially contributes towards the crystallinity of PLA-SP nanocomposites. The enhancement of elongation at break up to 56% is achieved for 5 wt% loading of SP in the PLA matrix. The best positive influence for the oxygen barrier is confirmed for the PLA-SP nanocomposite film, where the reduction in oxygen permeability of 69% is achieved in comparison with pure PLA.

Further, thermal degradation kinetic studies for PLA, PLA-GR and PLA-SP nanocomposites are carried out using thermogravimetric analysis (TGA) under the dynamic heating regime of 10, 20 and 30 °C/min. Various models such as Coats-Redfern, Flynn-Wall-Ozawa and Kissinger methods, are employed to understand the thermal degradation kinetics of PLA, PLA-GR and PLA-SP nanocomposites. It is observed that the addition of GR in the PLA matrix shows enhancement in the activation energy, which is indicative of improvement in the thermal stability of PLA. In case of PLA-SP nanocomposites, decreasing trend in the activation energy is observed with respect to loading. In addition to this, investigation on the non-isothermal cold crystallization kinetics of PLA, PLA-GR and PLA-SP nanocomposites is also performed using differential scanning calorimetry (DSC) under the dynamic heating conditions of 2.5, 5, 7.5 and 10 °C/min. Avrami and Tobin models used in the study elucidate the effect of SP and GR on the cold crystallization kinetic process of PLA. The Avrami and Tobin coefficients obtained for both PLA-GR and PLA-SP nanocomposites suggest the faster rate of crystallization process in comparison with neat PLA. The nucleation as well as the growth of spherulites in case of PLA, PLA-GR and PLA-SP nanocomposites are further observed using polarized optical microscopy (POM). After incorporation of GR and SP in the

PLA matrix, an increase in the overall crystallization rate for PLA is reflected by the decline in the nucleation induction period and subsequent enhancement in the number of primary nucleation sites. The influence of GR and SP on the hydrolytic degradation behavior of PLA is examined at different temperatures (35 and 55 °C) and pH (acidic, neutral and basic) conditions. The results clearly demonstrate that the elevated temperature and basic pH conditions highly favor the hydrolytic degradation process, irrespective of PLA, PLA-GR and PLA-SP nanocomposites. Improvement in the crystallinity and opacity of the samples is observed with respect to the duration of degradation, indicating the leaching of amorphous domains from PLA matrix. It is also found that the presence of SP exhibits greater influence on the hydrolytic degradation behavior of PLA. The rate of degradation is also found to be faster in case of PLA-SP nanocomposites, as compared to PLA and PLA-GR.

CONTENTS

LIST OF FIGURES

LIST OF TABLES

NOMENCLATURE

Abbreviations

ACO	Acetyl choline
ASTM	American society for testing and materials
BP	Benzoyl peroxide
BET	Brunauer Emmett Teller
BHT	Butylated hydroxy toluene
CNC	Cellulose nanocrystals
CNT	Carbon nanotube
CRP	Crystallization rate parameter
CTE	Co-efficient of thermal expansion
DOPO	(9,10-dihydro-9-oxa-10-phospha-phenanthrene-10-oxide)
DSC	Differential scanning calorimetry
EG	Expandable graphite
EXG	Exfoliated graphite
FC	Flax cellulose nanofibres
FDA	Food and drug administration
FE-SEM	Field emission scanning electron microscopy
FTIR	Fourier transform infrared spectroscopy
FWO	Flynn-Wall-Ozawa
GR	Graphene
GMA	Glycidyl methacrylate
HDPE	High density polyethylene
HDT	Heat deflection temperature
HDTA	Hexa decyl trimethyl ammonium bromide
JNF	Jute nanofibrils

LDH	Layered double hydroxide
MA	Maleic anhydride
MC	Microcrystalline cellulose
MCNC	Modified cellulose nanocrystals
MMT	Montmorillonite
MWCNT	Multi-walled carbon nanotube
NPCC	Nano sized precipitated calcium carbonate
OMLS	Organically modified layered silicates
OP	Oxygen permeability
PBS	Poly(butylene succinate)
PBSL	Poly(butylene succinate co-L-lactide)
PEG	Polyethylene glycol
PEO	Polyethylene oxide
PGLA	Poly(D,L-lactide-co-glycolide)
PLA	Poly(lactic acid)
PLF	Pineapple leaf fibres
POM	Polarized optical microscopy
PS	Polystyrene
PU	Polyurethane
PVA	Polyvinyl acetate
PVC	Polyvinyl chloride
RH	Relative humidity
SAED	Selected area diffraction
SCNC	Surfactant modified cellulose nanocrystals
SEC	Size exclusion chromatography
SEM	Scanning electron microscopy
SP	Sucrose palmitate
SWCNT	Single-walled carbon nanotube

TEM	Transmission electron microscopy
TGA	Thermogravimetric analyser
UCNC	Unmodified cellulose nanocrystals
U.S	United states
VASE	Variable angle spectroscopic ellipsometry
XRD	X-ray diffractometer
2D	Two dimensional
3D	Three dimensional

Notations

A	Pre-exponential factor (kJ/mol)
E_a	Activation energy (kJ/mol)
k	Avrami kinetic constant
K_T	Tobin rate constant
n	Avrami exponent
n_T	Tobin exponent
R	Universal gas constant (J/mol/K)
R^2	Regression co-efficient
t	Crystallization time (min)
$t_{1/2}$	Half crystallization time (min)
T_0	Onset cold crystallization temperature (°C)
T_c	Cold crystallization temperature (°C)
T_g	Glass transition temperature (°C)
T_m	Melting temperature (°C)
T_∞	Final cold crystallization temperature (°C)
$X(t)$	Relative degree of crystallinity
ΔH_c	Enthalpy of fusion at cold crystallization temperature (J/g)

ΔH_m	Enthalpy of fusion at melting temperature (J/g)

Greek letters

λ	Cu-Kα radiation wavelength (nm)
β	Heating rate (°C/min)
θ	diffraction angle (deg.)

CHAPTER 1

INTRODUCTION

The chapter provides a brief outline on the environmental issues spurred by conventional plastics derived from fossil-fuel origin. The importance of biopolymers as potential alternatives for replacement of petrochemical derived polymers is highlighted. The merits and de-merits of biopolymer based packaging materials are discussed. The technological concept used for mitigation of limitations associated with biopolymers to achieve targeted properties is discussed. Subsequently, the history of various additives used as reinforcements in the PLA matrix reported so far in the literature is elaborated. Thereafter, the chapter presents the objectives of the doctoral thesis followed by organization of the thesis.

1.1. Introduction

Plastics play a very important role in the modern society due to its potential usage in several applications such as automobiles, construction, electronics, biomedical, and packaging (**Zhang et al., 2012)**. This is because of certain attributes of plastics such as inexpensive, easy processability, light weight and non-corrosive nature (**Ali et al., 2011; Simoneit et al., 2005)**. In particular, packaging remains as the prime application in which huge volume of plastics are being consumed world-wide (Figure 1.1). The reason behind this is owing to its ease of handling, storage efficiency, attractiveness, light weight, inexpensive and prolonged product display. It also possibly protects food from spoilage by microbial contamination, physical damage or bio-chemical reactions during storage (**Dallyn et al., 1988; Siracusa et al., 2008**). At present, majority of plastics used for packaging application are derived from petrochemical sources. The primary polymers which are derived from fossil-fuel origin and currently being used in packaging sector include polyethylene terephthalate (PET), polypropylene (PP), polyvinyl chloride (PVC), high density polyethylene (HDPE), low density polyethylene (LDPE) and polystyrene (PS) (**Sorrentino et al., 2007**).

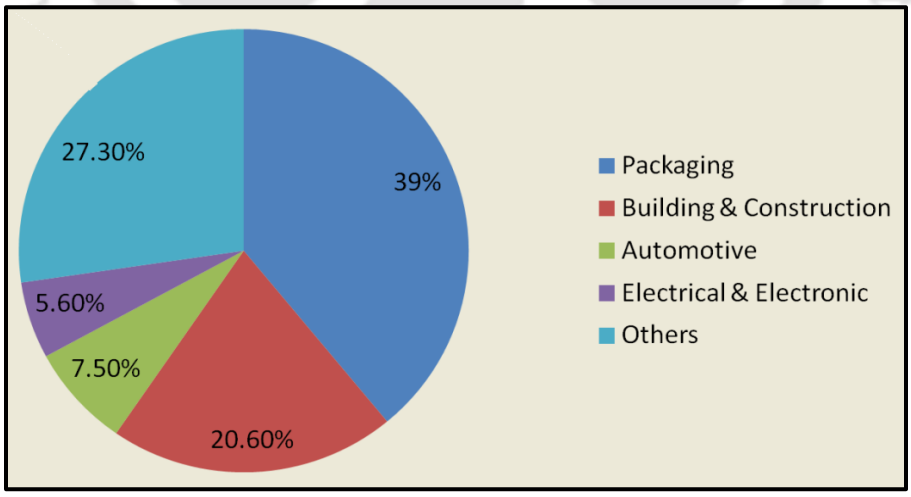

Figure 1.1. Percentage consumption of plastics for different applications

The plastics mentioned above are used in the packaging sector because of their distinctive characteristics. For example, PET possesses very good tensile strength and is transparent even after subjected to processing, which makes it suitable for packaging application (**Amano et al., 2004**). However, PET can melt easily, which in turn limits its application for storage of hot fluids. Similar to PET, PP also exhibits high mechanical properties and finds potential application in the production of firm containers. As PVC can be stretched easily and extruded into sheets, it is generally used for wrapping purpose in the packaging sector. Both HDPE and LDPE can be manufactured using cheaper raw materials. Due to good strength, HDPE finds application in the production of clouded containers where optical transparency is not required. In the case of LDPE, it exhibits excellent stretch characteristics and therefore, holds the potential to be used as bags for storage (**Patel et al., 2008**). PS is generally used for manufacturing of Styrofoam containers, which needs to be essentially firm and also highly resistant to heat. The thermal, mechanical and barrier properties of different conventional polymers discussed above are presented in Table 1.1.

Table 1.1. Properties of different conventional polymers

Properties	PET	PP	PVC	HDPE	LDPE	PS
Thermal Conductivity (W/mK)	0.14	0.11	0.14-0.20	0.47	0.32	0.12
Tensile strength (MPa)	47 - 71	30 - 40	39 - 50	21 - 30	7 - 30	34 - 50
Yield Strength (MPa)	59	30 - 36	39 - 43	25 - 32	8 - 14	-
Percent Elongation (%)	31 - 301	99 - 599	39 - 79	9 -1199	99 - 649	1.1 - 2.3
Elastic Modulus (GPa)	2.6 - 4	1 - 1.4	2.3 - 4	1.1	0.16 - 0.27	2.1 - 3.1
Oxygen Transmission Rate (CC-MIL/100 SQ IN. - 24 HR)	13	134	16	184	299	329

Despite the plastics derived from fossil fuel origin has brought considerable benefits to the society, it is important to accept that our ecosystem is being continuously disturbed due to the disposal issues associated with these non-degradable polymers. In order to free our environment from plastic wastes, two approaches are thought off, which includes (i) Dumping of plastic waste materials at landfill sites, (ii) Utilization of waste plastics through incineration and recycling process. However, burial of waste plastic materials cannot be practiced in reality due to the unavailability of satisfactory landfill sites. The drawback associated with the latter case is that incineration process leads to the production of huge quantity of carbon dioxide and other toxic gases, which in turn contributes to pollution and global warming problem. Recycling seems to be an appropriate option to address the issues associated with the conventional polymers. However, recycling is an energy intensive process, which includes several pre-treatment steps, before it's reprocessing into end product and also lacks in terms of quality when compared to the fresh manufactured product. Moreover, the accessibility of petrochemical resources is finite. Therefore, the development of eco-friendly plastic materials from renewable energy resources has become an essential task for mankind at this stage (**Ray et al., 2005**). The manufacturing process of renewable plastics does not comprise the utilization of toxic compounds. Also, the renewable plastics possess the advantage of superior biodegradation property in comparison with conventional polymers and hence, they could be readily compostable to natural degradation products. Owing to these reasons, research and development units in academia as well as industries are more attracted towards the development of environmentally benign plastics for packaging, which are biodegradable in nature and non-toxic to the environment (**Alexandre et al., 2000; Yang et al., 2007; Siracusa et al., 2008**).

1.2. Biopolymers

Biopolymers are basically polymeric constituents in which, at least one single step in the degradation process should be induced by microbial action. As a consequence of microbial

metabolism, biodegradation results in the production of fragmented products, which are noxious to the environment (**Siracusa et al., 2008**). However, it becomes essentially important to understand the fact that the biodegradation process can be ensured under certain conditions in terms of pH as well as temperature conditions, availability of oxygen and level of moisture content or humidity, prior to microbial action.

1.2.1. Classification of biopolymers

In general, biopolymers are classified into four categories based on their origin as presented in Figure 1.2.

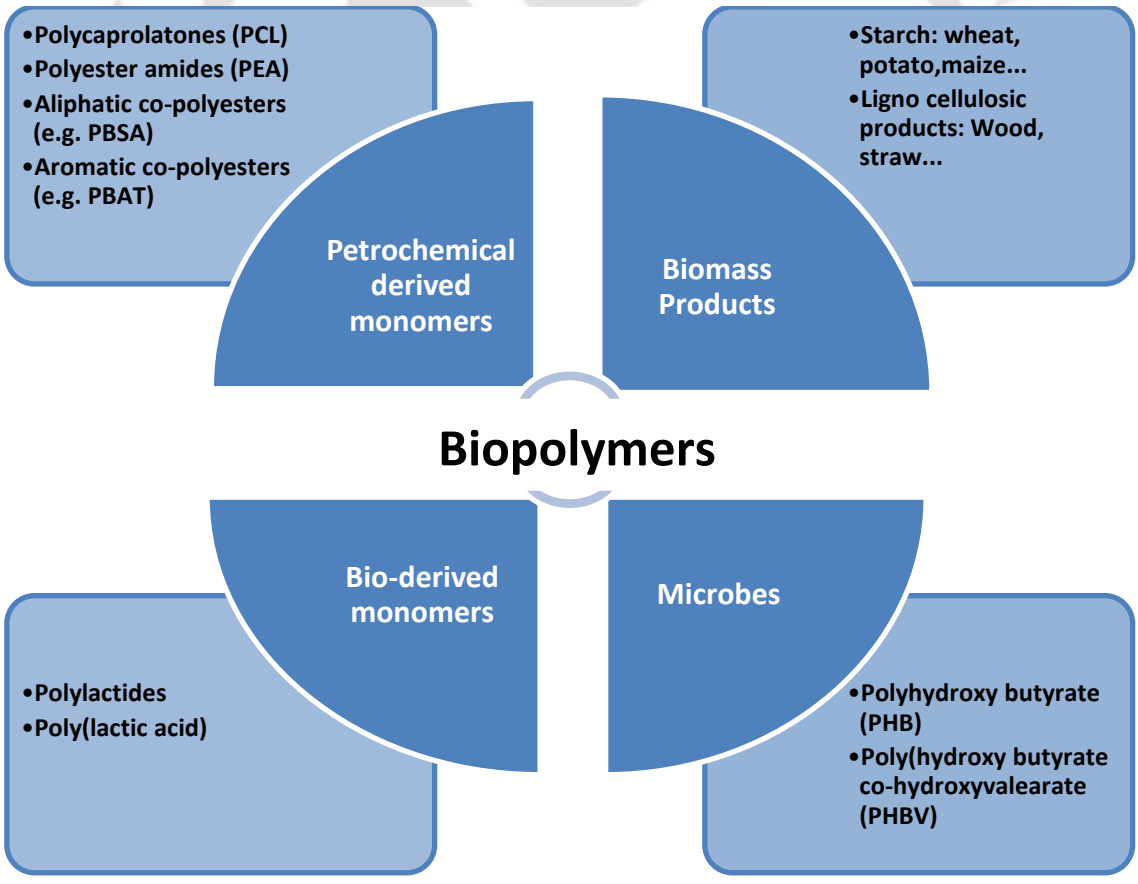

Figure 1.2. Classification of biopolymers

These include

a) Polymers that can be obtained from agro-based resources.
b) Polymers that can be obtained through microbial fermentation process.
c) Polymers that can be synthesized by conventional method using bio-derived monomers.
d) Polymers that can be synthesized by conventional method using monomers derived from petrochemical resources.

The blooming of innovative technologies for massive production with cheaper processing cost facilitates poly(lactic acid) (PLA) to occupy a vital position in the mart of sustainable polymers (**Armentano et al., 2013**). PLA is currently explored as a sustainable alternative to petrochemical derived polymers of fossil fuel origin and hence, it possesses significant potential for application in the field of commodity areas like, packaging. PLA is linear, aliphatic, thermoplastic polyester that can be produced from either L-lactic acid or D-lactic acid monomers for useful applications. These monomers are obtained through fermentation of corn starch, sugarcane juice or other agricultural resources. PLA is commercially available in variety of grades and has been approved by the U.S. Food and Drug Administration (FDA). The manufacture of PLA provides several benefits as compared to other biopolymers as follows.

a) The precursor for PLA, i.e., lactic acid can be produced by subjecting the agro-based resources to fermentation process.
b) Carbon dioxide fixation can be possible via cultivation of agro-based resources such as corn for production of PLA.
c) Considerable improvement in terms of agricultural economy is possible.
d) Substantial savings in terms of energy is probable.
e) PLA can be recycled again to its precursor lactic acid via hydrolysis process.

In addition to this, PLA displays various assets when compared to conventional polymers used for packaging application. Those advantages include

a) **Biocompatibility:** PLA has the ability to degrade into its monomeric constituent i.e. lactic acid, in the human body through scission process. Furthermore, PLA exhibits the characteristics of undergoing hydrolytic cleavage under in-vivo conditions without the aid of enzymes for catalyzing the same (**Anderson et al., 1997**). However, the rate of degradation depends on the size as well as shape of PLA and temperature conditions of the hydrolysis reaction. It has been reported that the extent of degradation of PLA into lactic acid continues at least up to two years (**Garlotta, 2001**).

b) **Degradation in natural ecological conditions:** PLA exhibits the potential to undergo degradation in natural environmental conditions, which includes soil as well as compost (**Rudeekit et al 2008**). Under such circumstances, the degradation of PLA is known to proceed via two stages; (i) hydrolytic and (ii) enzymatic degradation process. In the hydrolysis process, water firstly diffuses into the PLA that results in the cleavage of ester groups by random chain scission process. This in turn, leads to the subsequent decrement in the molecular weight of PLA followed by production of oligomer moieties together with lactic acid. Once the molecular weight of PLA is reduced up to 10-20 kg mol^{-1}, microbial flora present in the soil can start up assimilating the same and transform to CO_2, humus and water. Therefore, hydrolytic cleavage forms the basis for degradation of PLA followed by enzymatic cleavage process, which is due to microbial action.

c) **Transmission of visible light:** PLA demonstrates good optical transparency by transmitting the visible light in the 540-560 nm wavelength regime. The percentage transmission of visible light for PLA has been demonstrated to be typically higher in comparison with the commercial polymers such as PS and PET (**Auras et al., 2004**).

d) **Processability:** PLA holds the flexibility to be processed using several processing techniques such as extrusion, injection moulding and thermoforming.

Although PLA possess the prospective to compete with the conventional plastics, it is important to spell out the drawbacks, which limits its usage in the packaging application (**Armentano et al., 2013**) as follows

a) PLA is highly brittle in nature which restricts its applications such as flexible films.
b) PLA exhibits poor thermal resistance.
c) PLA has slow crystallization rate.
d) PLA suffers from poor gas barrier properties in comparison with conventional polymers.

Over the past few years, the incorporation of nano-fillers in PLA matrix to produce nanocomposite materials has been explored as an innovative and effective alternative for enhancing the mechanical performance, thermal stability and barrier properties of PLA. Polymer nanocomposites refer to the multiphase systems, wherein, the nanoparticles with at least one dimension in the nanoscale regime are dispersed in the polymer matrix. The term "nanocomposites" was first coined by Toyota Central Research Laboratory near the beginning of 1990s. Thereafter, extensive research activities have been carried out world-wide on the topic entitled "polymer nanocomposites" due to the fact that substantial improvement in the properties are possible with incorporation of nanofillers even with exceptionally small loadings. At the nanoscale, such particles have significantly large surface area and exhibit the possibility to interfere with polymer chain mobility, thereby manipulating the matrix properties. Polymer nanocomposites can be prepared via three different routes, as described below:

a) **Solution method:** This method involves the dissolution of polymers in an appropriate solvent, after which, the nanofillers are usually added in the solvent-polymer mixture. After subsequent period of processing, the solvent is removed via evaporation (**Rahim et al., 2009; Jamshidian et al., 2012; Gong et al., 2014)**.
b) **Melt-mixing method:** This technique involves the melt-integration of polymers with the nano reinforcements directly. This relates to the process under which the mixture of

polymer and nanofiller is annealed slightly above the softening or melting point of the polymer (**Najafi et al., 2012; Tawakkal et al., 2014).**

c) **In situ polymerization method:** In this process, first, the nano materials are allowed to be well dispersed in the monomer solution, which in turn, is subsequently polymerized in the existence of nano fillers (**Song et al., 2007**).

The expected improvements in the properties are deemed to be directly dependent on the dispersion of the nanoparticles in the polymer matrix that manipulates physical or chemical interaction between the matrix and the reinforcing phases. The optimization of dispersion and interactions of nanoparticles in polymer matrices through mechanical and chemical approaches has been investigated by several researchers for the development of high quality nanocomposites (**Krikorian et al., 2003; Ray et al., 2002; Winey et al., 2006; Yoon et al., 2010; Baghaei et al., 2013; Yu et al., 2014; Tsai et al., 2013**). Numerous studies involving a variety of fillers in the development of PLA based nanocomposites have endeavored (**Urbanczyk et al., 2009; Jiang et al., 2007; Paive et al., 2005; Xie et al., 2007; Kumar et al., 2010; Ramzy et al., 2014; Wu et al., 2013**). More recently, clay (**Chang et al., 2003; Jiang et al., 2007; Najafi et al., 2012; Khatua et al., 2014; Jos et al., 2014**), carbonaceous (**Tasis et al., 2006; Park et al., 2013; Raja et al., 2013; Chen et al., 2013; Lee et al., 2014**), silica (**Yuzay et al., 2010; Wu et al., 2013; Tsai et al., 2013,**) and green fillers (**Bax et al., 2008; Liu et al., 2010; Song et al., 2013; Oza et al., 2014; Siengehin et al., 2014,**) are increasingly used as load-bearing constituents in developing PLA composites. A detailed literature survey on the properties of PLA nanocomposites reinforced with the above discussed fillers is as follows:

1.3. Literature review on PLA composites

1.3.1. PLA-clay nanocomposites

Layered silicates have received significant attention as nano reinforcements in the polymer matrix, due to its potential in improving the thermal, mechanical, barrier properties of the polymer. The extent to which the layered silicates dispersed in the polymer matrix plays a key role in improvement of the fore-mentioned properties. The level of dispersion of layered silicates usually depends on the (i) interaction between the polymer and layered silicate and (ii) preparation method through which the nanocomposite is synthesized. Therefore, based on the variation in the interaction between the polymer and the layered silicate, three different structures of polymer nanocomposites are possible as shown in Figure. 1.3.

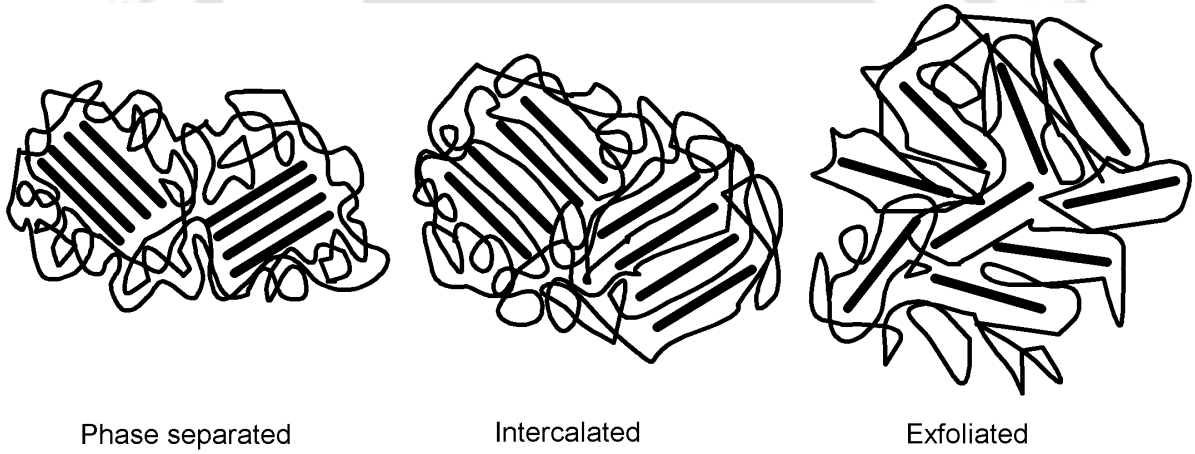

Figure 1.3. Different structures of polymer nanocomposites

a) **Phase separated structure:** If the interaction between the layered silicate and the polymer is quite low, intercalation of the polymer between the silicate layers will not be achieved. The microcomposite, thus resulted under such circumstances is referred to as phase separated composites. The properties of such phase separated composites are

rather hardly ever enhanced or may exhibit downturn after the reinforcement (**Mittal et al., 2009; Raquez et al., 2013**).

b) **Intercalated structure:** If the intercalation of polymer segments between the inter layers of silicate occurs to a partial extent, then the resultant structure is referred to as intercalated nanocomposite. The formation of intercalated structure is usually accompanied by the enhancement in the interlayer distance (**Mittal et al., 2009; Raquez et al., 2013**).

c) **Exfoliated structure:** When the layered silicates are dispersed in the polymer matrix as individual segments, the resultant structure is referred to as delaminated or exfoliated nanocomposite. Achieving exfoliated structures can lead to a profound enhancement in the thermal, mechanical and barrier properties of the polymer. Under practical processes, it is merely rather difficult to achieve completely exfoliated structures (**Mittal et al., 2009; Raquez et al., 2013**).

Several studies endeavored the replacement of inorganic cations in the interlayers of layered silicate by organic cations with alkyl chains that can further enhance the affinity between the layered silicate and the polymer (**Krikorian et al., 2003; Mittal et al., 2009; Raquez et al., 2013**). This is because of the presence of organic cations together with alkyl chain can help in increasing the distance between the silicate interlayers, thereby, allowing for a superior dissemination of polymeric chains inside the galleries.

In this regard, an attempt has been made to fabricate PLA/organoclay (Cloisite 30B, 25A, 15A) nanocomposites via solution casting approach (**Krikorian et al., 2003**). It was mentioned that all the nanocomposite systems retained their optical clarity due to the nanoscale dispersion of exfoliated clay particles in the PLA matrix. The crystallinity of PLA-organoclay nanocomposites was perceived to exhibit inverse order with respect to loading irrespective of the type of clay incorporated in the PLA matrix. Transmission electron microscopy (TEM) and X-ray diffraction

studies (XRD) indicated that Cloisite 30B demonstrated the best improvements in terms of mechanical properties. The incorporation of 15 wt% of Cloisite 30B showed around 61% increment in the storage modulus as compared to neat PLA. It was also declared that the improvement in the mechanical properties was possible due to the firm affinity between carbonyl moieties of PLA and diol groups available in the organoclay.

In a separate contribution, the same research group investigated the effect of trimethyl octadecyl ammonium cation modified montmorillonite (MMT) clay on the mechanical, barrier and biodegradation properties of PLA (**Ray et al., 2003**). After the addition of reinforcement in the PLA matrix, the storage modulus enhanced by ~66% in comparison with neat PLA. A maximum improvement in the flexural modulus of ~21% was achieved with 4 wt% loading of organic clay. Further increment in the loading led to the development of brittleness in the nanocomposite system. The relative permeability coefficient obtained for PLA-clay nanocomposite system (0.885) was comparatively lower than PLA, which indicated the good barrier effect provided by the reinforcement. The organically modified clay also showed considerable advancement in the biodegradation properties of PLA. It was discussed that the extent of decrement in the molecular weight and the residual weight was same for both PLA and PLA-clay nanocomposite. By the completion of first month of the biodegradation study, a sharp weight loss for the nanocomposite system was experienced. The compost was completely degraded within two months from the time period at which the biodegradation study was initiated.

Different weight loadings of organically modified MMT clay were reinforced in the PLA matrix through melt extrusion technique and the effect of MMT on the mechanical properties was investigated by **Ray et al.,** (**2002**). TEM analysis revealed the intercalation of silicate layers with PLA and random distribution of MMT clay in the PLA matrix. It was observed that the storage

modulus showed increasing trend with respect to MMT loading (3-7 wt%). The increment in the storage modulus of nanocomposites was reported to be ~ 33-140% higher than that of the neat PLA.

In situ polymerization of D, L-lactide in the interlayers of organically modified clay (Cloisite 30B) was carried out using supercritical CO_2 as the medium of polymerization (**Urbanczyk et al., 2009**). A good degree of exfoliation of Cloisite 30B in the PLA matrix was evidenced by the TEM analysis. Flexural as well as impact tests were carried out to investigate the effect of clay on the mechanical properties of PLA. An improvement in the stiffness and impact resistance up to some extent was possible after the reinforcement. The presence of Cloisite 30B in the PLA matrix enhanced the flexural modulus by ~17% as compared to neat PLA. In addition to this, the reinforcement led to the improvement in the toughness by ~15% when compared with unfilled PLA matrix.

Two different organo clays such as MMT and fluorinated mica modified with hexadecylamine (C_{16}-MMT and C_{16}-mica), were synthesized (**Chang et al., 2003**). Thereafter, the respective clays were dispersed in the PLA matrix via solution casting approach and the effect of various loadings of clays on the thermal and mechanical properties of PLA was investigated. When 2% weight loss is taken as a point of comparison, it was found that the thermal degradation temperature of the composites (with 8 wt% loading) shifted to lower temperature at a maximum of ~49 °C for C_{16}-MMT and ~16 °C for C_{16}-mica. The improvement in the tensile strength of ~32% and ~57% was obtained for C_{16}-MMT and C_{16}-mica reinforced PLA nanocomposites for clay loading of 4 wt%, respectively. With further increase in the loadings, both the nanocomposites exhibited decreasing trend in the tensile properties, due to the agglomeration of clay nanoparticles resulted by the improper dispersion. In case of modulus, PLA/C_{16}-mica nanocomposites showed three fold improvements as compared to neat PLA. The possible

reason for this was due to the good orientation of the filler in the PLA matrix as well as high aspect ratio of the layered mica.

The effect of chain length of organic modifiers (*n*-octyl tri-*n*-butyl phosphonium bromide (C_8), *n*-dodecyl tri-*n*-butyl phosphonium bromide (C_{12}), *n*-hexadecyl tri-*n*-butyl phosphonium bromide (C_{16}) and methyl triphenyl phosphonium bromide (C_{Ph})) on the properties of PLA composites was investigated with different clays such as smectite, MMT and mica (**Maiti et al., 2002**). XRD analysis revealed that the *d* spacing increased with increasing the chain length of the organic modifier (d = 1.69, 1.78 and 1.87 for C_8, C_{12} and C_{16}, respectively). In case of fixed organo modifier, the d spacing showed increasing trend with an increase in the lateral dimension of the reinforcement. In case of C_{Ph}, it was observed that no intercalation of PLA occurred due to the immiscible nature of the modifier in the PLA matrix. The PLA/C_{16}-smectite nanocomposite system showed a maximum improvement in the mechanical properties in terms of storage modulus in comparison with other nanocomposite formulations. The storage modulus showed increasing trend with respect to clay loadings and a maximum extent of improvement ~65% was noticed for 4 wt% loadings of PLA/C_{16}-smectite nanocomposite over neat PLA. The same nanocomposite system also performed well in terms of barrier effects with reduction in the oxygen transmittance rate of ~40% as compared to neat PLA. The better performance of PLA/C_{16}-smectite nanocomposites in terms of mechanical and barrier properties was due to good dispersion of clay in the PLA matrix as well as high aspect ratio.

Nano sized precipitated calcium carbonate (NPCC) and organically modified MMT were used as reinforcements in the PLA matrix and the nanocomposites were prepared via melt-extrusion technique (**Jiang et al., 2007**). The addition of NPCC in the PLA matrix shifted the cold crystallization temperature (T_{cc}) to lower side indicating the strong nucleation effect of the filler. The organically modified MMT clay also showed stronger nucleation effect in comparison with

NPCC by shifting the T_{cc} to even lower temperature range with a greater enthalpy of crystallization. The elongation-at-break showed improvements with respect to increase in NPCC loadings and a maximum enhancement of ~13% was obtained for 7 wt% loading as compared to neat PLA. The PLA/organically modified MMT (2.5 wt%) displayed an increment in the elongation-at-break around ~15.9% over neat PLA. In case of tensile properties, PLA/organically modified MMT nanocomposites exhibited enhancement in the tensile properties up to 5 wt% loading, whereas, in case of PLA/NPCC system demonstrated decreasing trend with respect to loading. The reason for downturn experienced in PLA/NPCC nanocomposites was due to the poor interfacial adhesion between the filler and the matrix.

Organically modified rectorite was incorporated in the PLA matrix through melt-extrusion process (**Li et al., 2009**). Both XRD and TEM analyses confirmed the presence of partially intercalated and exfoliated nanocomposite structures after the reinforcement of the filler in the PLA matrix. Polarized optical microscopy (POM) observations together with the differential scanning calorimetry (DSC) analysis elucidated the change in the spherulite morphology and improvement in the crystallization rate for PLA/organically modified rectorite nanocomposite. The reinforcement also led to the improvement in elongation-at-break by ~210% as compared to neat PLA. However, the reinforcement guided to decrement in the tensile strength of ~19% in comparison with neat PLA, which was explained to be due to the cavitation effect between PLA and the clay, as a result of poor interaction.

The effect of two different organically modified MMT clays (Cloisite 25A and Cloisite 30B) on the hydrolytic degradation behavior of PLA was investigated (**Paul et al., 2005**). The melt-intercalated samples were placed in a phosphate buffer for five months. The decrement in the molecular weight of the samples was confirmed by the size exclusion chromatography (SEC) with respect to hydrolysis time. The improvement in the crystallization properties for both

nanocomposites was evidenced by the DSC analysis. Both the nanocomposite samples exhibited loss in the thermal stability and the same was found to be proportional to decreasing molecular weight of PLA with respect to the hydrolysis time. It was also reported that the hydrophilic nature of the clay layers played a significant role in the hydrolytic degradation process of PLA, which led to enhancement in the rate of degradation.

In a separate study, the effect of PLA crystallinity on the hydrolytic degradation process was investigated (**Zhou et al., 2008**). Both the amorphous and semi-crystalline polymer samples (pure and organically modified with MMT (5 wt %)) were subjected to hydrolytic degradation process in the temperature regime of 50-60 °C. The increased permeation effect led to increment in the degradation rate constants for both the amorphous PLA and its nanocomposites as compared to semi-crystalline PLA and its composite system. The rate of degradation was faster at the elevated temperature conditions irrespective of crystallinity effects of PLA and their nanocomposites. It was concluded that the site at which the degradation gets initiated is interface between the matrix and the reinforcement leading considerable variations in the morphology of the samples subjected to hydrolytic degradation process.

The influence of chain extender (Joncryl-ADR 4368F) on the PLA/organically modified clay (Cloisite 30B) based nanocomposites was studied by **Najafi et al.** (**2012**). It was inferred that the presence of Joncryl chain extender could improvise the degree of dispersion of the filler in the PLA matrix. The higher degree of dispersion of the modified clay with the chain extender also led to improvement in the barrier effects as compared to that of the unmodified one. The PLA nanocomposite synthesized with modified clay showed ~37% reduction in the oxygen permeability, whereas, the unmodified nanocomposite sample displayed only ~28% reduction as compared to neat PLA. However, it was also discussed that both the PLA nanocomposites

(unmodified and modified with chain extender) could exhibit only ~8% improvement in the tensile strength as compared to neat PLA.

Potato starch was gelatinized in the presence of sodium montmorillonite (NaMMT) and then incorporated in the PLA matrix through melt mixing method (**Khatua at al., 2014**). The morphological study performed using SEM and TEM indicated that delaminated structure of NaMMT was obtained in the potato starch matrix. The PLA/starch/NaMMT nanocomposite showed ~75% and 64% improvement in the tensile strength and elongation-at-break, respectively, as compared to neat PLA, indicating the existence of better compatibility between the PLA and starch. The considerable reduction in the water absorption (~12%) was also reported for the nanocomposite system.

The optical properties of PLA nanocomposites synthesized by solution casting method using various content (3-7 wt %) of organically modified MMT (Cloisite 30B) was investigated by **Cele et al.** (**2014**). The variable angle spectroscopic ellipsometry (VASE) studies indicated the positive correlation between the refractive index and thickness of the nanocomposite films. PLA/Cloisite 30B nanocomposites showed increment in the absorption of light in the visible regime of the electromagnetic spectrum, which revealed the improvement in the reflectivity for the nanocomposite films.

PLA, wood flour and Cloisite 20A were processed through melt extrusion technique for the fabrication of PLA/Cloisite 20A/wood flour nanocomposites (**Meng et al., 2010**). Along with the intercalated structure of Cloisite 20A with PLA, the morphological analysis also revealed that the presence of wood flour could lead to improvement in the spacing between the galleries present in the intercalated Cloisite 20A. At a clay loading of 5 wt%, the nanocomposites exhibited ~47% and ~36% improvement in the tensile as well as flexural moduli, respectively, in comparison

with neat PLA. The presence of Cloisite 20A delayed the thermal degradation process by improving the degradation temperature around ~10 °C for PLA/Cloisite 20A/wood flour nanocomposites when compared to PLA/wood flour composite system.

Sodium MMT (Cloisite Na^+) was organically modified with hexadecyl trimethyl ammonium bromide (HDTA) and Acteylcholine (ACO) chloride, respectively, and reinforced in the PLA matrix through melt compounding method (**Jos et al., 2014**). The incorporation of HDTA-MMT and ACO-MMT in the PLA matrix enhanced the barrier properties. The PLA/HDTA-MMT nanocomposite demonstrated ~37% reduction in terms of water vapour transmission rate in comparison with neat PLA, whereas, in case of PLA/ACO-MMT nanocomposite reduced the transmission by only ~22%. In case of oxygen permeability, both the nanocomposites exhibited ~40% reduction as compared to neat PLA. The transparency of both the nanocomposites was influenced by the presence of clay in the PLA matrix and the same was observed to decrease with respect to filler loadings.

Nanomer 1.24TL clay was modified with an alkylamide type organic modifier and incorporated in the PLA matrix to achieve exfoliated PLA/Nanomer hybrids via melt compounding method (**Hung et al., 2013**). Exfoliated as well as partial intercalated nanocomposite structures were visualized by TEM analysis. The presence of organoclay in the PLA matrix highly influenced the nucleation as well as the rate of crystal growth by promoting the crystallization process. It was inferred that the alkylamide modified Nanomer acted as a nucleating agent by enhancing the crystallinity of the PLA/nanocomposite by ~75% when compared to neat PLA. During the melt crystallization process, it was observed that the PLA/organoclay exhibited ~7-17 times faster rate of crystallization ability than the neat PLA.

A study on the influence of Cloisite 30B on the gas barrier properties of PLA/poly(butylene succinate) (PBS) blend was carried out by **Bhatia et al.** (**2012**). The PLA and PBS composition in the blend were fixed to be 80 and 20 wt%, respectively and then the contents of the clay was varied (1-10 wt %). TEM analysis revealed the intercalated and exfoliated structure of clay in the PLA/PBS matrix, when the clay content was fixed to be 1 wt%, whereas, clustered structures of clay nanoparticles were visualized for higher loadings. The PLA/PBS/5 wt% Cloisite 30B nanocomposite exhibited ~26% reduction in the oxygen permeability as compared to neat PLA, due to the tortuous path effect of the clay layers.

Investigation on the influence of NB2 nanoclay on the nonisothermal cold crystallization behavior of PLA was carried out using DSC analysis (**Wu et al., 2007**). The DSC results revealed that the degree of crystallinity decreased with increasing clay loadings at lower heating rates (<5 °C/min). In case of higher heating rate i.e., 10 °C/min, the presence of clay considerably increased the degree of crystallinity. Avrami, Ozawa and Kissinger methods were used to analyze the crystallization kinetics data obtained by DSC analysis. It was concluded that the clay plays as nucleating agent promoting the crystallization process to certain level at lower loadings, whereas, the reinforcement impedes the rate of crystallization at higher loadings.

1.3.2. PLA-carboneceous nanocomposites

The two main classes of carboneceous nanofillers include carbon nanotubes (CNTs) and graphene (GR), which are considered as the most promising reinforcements for the synthesis of PLA nanocomposites. CNTs are regarded as one dimensional nanostructure and can be obtained when graphene sheet is rolled in tubular shape. CNTs possess huge potential to be used as nanofiller due to its superiority in terms of thermal, mechanical and electronic properties. CNTs exhibit Young's modulus value of ~ 1 TPa and the tensile strength properties are reported to be fifty times higher than that of stainless steel (63 GPa). In addition to this,

CNTs also demonstrate excellent thermal conductivity of ~3000 W/mK (**Yang et al., 2002**). Apart from this, CNTs are also stable to chemical and environmental conditions, which make them attractive as nano reinforcements in the PLA matrix. With respect to PLA-CNT composites, much of the work is not devoted especially for packaging applications. However, the following section discusses the available information on PLA-CNT nanocomposites.

It is highly difficult to disperse CNTs homogeneously in the PLA matrix to obtain satisfying improvements in the properties. Direct blending of CNTs in the PLA matrix led to agglomeration and resulted in a heterogeneous composite system, which in turn, affected the mechanical properties of PLA deleteriously (**Winey et al., 2006**). Therefore, functionalization of CNTs before mixing in the polymer matrices have received considerable interest, so that, it was deemed that the load can be transferred more effectively from the polymer matrix to the filler (**Paiva et. al., 2005; Tasis et al., 2006; Yang et al., 2007; Xie et al., 2007**). In view of this, an effort has been undertaken to synthesize PLA/multi-walled (MW) CNT nanocomposites and predicted their structural property relationship (**Yoon et al., 2010**). First, MWCNTs were acid functionalized followed by the ring-opening polymerization reaction of L-lactide monomer to obtain different chain lengths of PLA and added in the commercialized PLA matrix. The morphological analysis revealed that the degree of dispersion was much better with respect to increment in the chain length of PLA. It was found that the PLA/MWCNT nanocomposite (where the molecular weight of PLA grafted onto MWCNT was 530 g/mol) exhibited a highest improvement in the tensile modulus (2275 MPa), which is close to the theoretical value of ~2911 MPa, indicating the excellent interfacial adhesion achieved between the reinforcement and the PLA matrix.

Various weight loadings of MWCNT (0-10 wt %) were added in the polymer blend (50/50 wt %) made of PLA/maleic anhydride-grafted polypropylene (PP) via melt-mixing process (**Lee et al., 2014**). The morphological analysis carried out using SEM disclosed the well dispersed state of PLA in the polymer blend and also confirmed the homogeneous dispersion of MWCNTs in the

PP domains. The DSC analysis demonstrated the nucleating ability of MWCNTs, which was confirmed by the improvement in the melt-crystallization temperature of the nanocomposite films. It was observed that the addition of MWCNTs in the blend exhibited the enhanced thermal stability of the nanocomposites. The nanocomposite with 5 wt% MWCNT demonstrated ~18% enhancement in the thermal degradation temperature as compared to neat PLA/PP blend.

The effect of DOPO (9, 10-dihydro-9-oxa-10-phosphaphenanthrene-10-oxide) functionalized MWCNT on the thermal properties of PLA nanocomposite was investigated by **Yu et al.,** (**2014**). The morphology of MWCNTs was characterized by the presence of hollow core encompassing open ends on both the sides. In addition to this, the TEM image pictoriated for non-functionalized MWCNTs showed a smooth surface with no evidence of additional phase. In case of DOPO grafted MWCNTs, a thin layer covering the surface of the nanomaterial was visualized, indicating the successful grafting of DOPO onto the surface of MWCNTs. In terms of thermal stability, DOPO-MWCNTs showed considerable increase in the thermal loss in the temperature regime of 300-450 °C, owing to the decomposition of the functionalizing agent, whereas, non-functionalized MWCNTs were stable for more than 600 °C. However, the nanocomposites (PLA/DOPO-MWCNTs) were characterized by the presence of higher weight residue of char at 700 °C, as compared to PLA/MWCNT nanocomposite sample. This suggested that the functionalizing agent imparts thermal stability for PLA to certain extent.

The influence of CNT on the mechanical and crystallization properties of PLA was investigated for the PLA/CNT nanocomposites synthesized via melt extrusion process (**Park et al., 2013**). The crystallization kinetic data obtained for the PLA/CNT nanocomposites under isothermal conditions by DSC analysis was analyzed by Avrami model. It was inferred that the presence of CNTs in the PLA matrix influenced the crystallization rate for the nanocomposites more efficiently by heterogeneous nucleation mechanism. Polarized optical microscopy (POM) studies revealed that the CNTs acted as the nucleating agent by enhancing the number of

primary nucleation sites and therefore, the size of the spherulites decreased significantly. The thermal degradation temperature for the nanocomposites was enhanced by the presence of CNT up to a maximum of 2 °C, as compared to neat PLA. The improvement in the degradation temperature was possibly due to the barrier effect as well as good thermal stability of the CNTs. However, mechanical properties such as, tensile strength and elongation-at-break (%), decreased with an increase in the CNT content due to the brittleness developed in the nanocomposite samples.

The UV irradiated MWCNTs were incorporated in the thermoplastic polymer blend containing polyurethane (PU) and PLA via melt extrusion process (**Raja et al., 2013**). It was observed that the modified MWCNT nanocomposites demonstrated a considerable enhancement in the mechanical properties of the polymer blend as compared to unmodified MWCNT incorporated nanocomposite. The PLA/PU/MWCNTs displayed better storage modulus properties as compared to neat PLA/PU blend due to better interfacial attachment between the filler and the matrix, thereby, enforced restriction for the movement of polymeric segments. After incorporation of modified MWCNTs in the polymer blend, the resulted nanocomposites exhibited even higher improvement in terms of storage modulus i.e., 42% than that of PLA/PU/MWCNTs. This indicated the enhancement in the stiffening property owing to the homogeneous distribution in the matrix after surface modification.

In a separate contribution, PLA and MWCNTs were grafted with chloropropyl triethoxy silane and vinyl trimethoxy silane respectively, and were cross-linked together (**Kuan et al., 2007**). XRD results revealed the transformation of crystalline nature of PLA into semi-crystalline form after the cross-linking reaction. DSC analysis confirmed the reduction in the T_{cc} during the cold crystallization process with respect to increase in the reaction time. A significant improvement in the heat deflection temperature (HDT) was also noticed for the cross-linked nanocomposites. After covalently linking the PLA and the MWCNTs, it was observed that the HDT significantly

improvised up to 106 °C from 62 °C. The nanocomposites showed an improvement of ~13% in terms of tensile strength as compared to neat PLA. With respect to loadings of MWCNTs and higher reaction period, the tensile properties were not enhanced significantly. In comparison with neat PLA the cross-linked PLA/MWCNTs also demonstrated ~11 °C improvement in thermal stability.

CNTs were acid treated and incorporated in the PLA matrix via melt-blending technique in order to fabricate PLA/CNT nanocomposites (**Chen et al., 2013**). The morphological analysis revealed the uniform dispersion of CNTs in the PLA matrix and the degree of hydrophilicity for the nanocomposite samples was observed to increase with increasing CNT loadings. The DSC analysis confirmed that the improvement in the crystallinity of the samples was solely determined by the annealing temperature used during the synthesis process. Besides, it was also inferred that CNTs acted as nucleating agents by decreasing the T_{cc} for the nanocomposite samples during the cold crystallization process. The presence of CNTs also showed promising results in terms of hydrolytic degradation behavior and the extent to which the hydrolytic degradation occurred was shown to be associated with the loadings of CNT in the PLA matrix. It was inferred that higher the content of CNTs, greater was the extent of hydrolytic degradation process due to the development of highly crystalline structure of PLA.

PLA/poly(butylene succinate-co-L-lactate) (PBSL)/CNT nanocomposites were prepared by melt-mixing technique and subsequently subjected to compression molding (**Chou et al., 2011**). The flexural strength of the nanocomposites increased up to a maximum of ~6.25% for CNT loading of 0.5 wt%. It was discussed that the enhancement in the flexural properties obtained for the nanocomposites was due to the high aspect ratio of the reinforcement, which helped in improvising the surface area for contact between the filler and the matrix. At further high loadings of CNTs, the flexural strength was observed to decrease because, the relatively higher surface energies held by the nano reinforcement resulted in agglomeration. The water

absorption uptake for all the nanocomposite samples was found to increase with increasing soaking time, which was attributed to the hydrolytic degradation behavior of PLA.

In situ polymerization technique was followed for preparation of PLA/acid functionalized MWCNT based nanocomposites (**Li et al., 2013**). SEM analysis revealed that the functionalized MWCNTs were uniformly distributed in the PLA matrix, whereas, the unmodified MWCNTs were characterized by the uneven dispersion due to the lack of affinity between the reinforcement and the PLA matrix. XRD analysis revealed the presence of highly intense diffraction patterns for acid functionalized MWCNTs as compared to neat MWCNTs. However, the diffraction position remained the same irrespective of whether the CNTs are functionalized or not. The presence of carboxyl functionalized MWCNTs in the PLA matrix displayed a weight loss of ~98%, whereas, the neat PLA presented a mass loss of ~99% after pyrolysis process.

The influence of covalently and non-covalently functionalized single walled (SW) CNTs on the hydrolytic degradation behavior of poly(D,L-lactide-co-glycolide) (PGLA) based nanocomposites was examined by **Armentano et al.** (**2008**). DSC analysis confirmed that the presence of SWCNTs in the PLGA matrix led to considerable decrement in the glass transition temperature (T_g), which was attributed to the plasticization phenomenon of water entering inside the PGLA matrix upon its acquaintance to hydrolytic medium. The T_g values were found to decrease continuously with respect to hydrolytic degradation time for the PGLA/covalently functionalized SWCNTs, whereas, the same was observed to decrease for neat PGLA and PGLA/non covalently functionalized nanocomposites. This was attributed to the cross-linking phenomenon that existed between the PGLA and the reinforcement after the partial chain scission induced by the hydrolysis process.

1.3.3. PLA-bio filler composites

PLA/cordenka rayon fibres and flax fibres were reinforced in the PLA matrix via injection moulding technique and the effect of reinforced fibres on the mechanical properties of PLA was investigated (**Bax et al., 2008**). PLA/cordenka rayon fibres exhibited ~6.5% improvement in the tensile strength as compared to PLA/flax fibres, due to good interfacial interaction between cordenka rayon fibres and the PLA matrix. In a separate contribution, flax mat and modified flax mat fibres were incorporated in the PLA matrix by hot pressing technique (**Siengehin et al., 2014**). The PLA/flax composite demonstrated ~13.5% higher tensile strength as compared to neat PLA, whereas, the modified flax did not improve the tensile strength considerably. In terms of elongation-at-break (%), the PLA/modified flax composite exhibited 32% enhancement as compared to neat PLA, indicating that modification of flax fibre favoured the improvement in ductility.

Cellulose nanofibres were synthesized from flax yams via acid hydrolysis and different weight loadings (2.5 and 5.0 wt %) of flax cellulose nanofibres (FC) were reinforced in the PLA matrix by solution casting approach (**Liu et al., 2010**). The reinforcement of FC in the PLA matrix showed good improvement in terms of tensile strength and tensile modulus with respect to loadings. In comparison with neat PLA, PLA/5 wt% FC nanocomposite showed ~59% and 47% improvement in the tensile strength and tensile modulus, respectively. In addition to this, the presence of FC acted as a nucleating agent and improved the crystallization of PLA.

The influence of amphiphilic additives such as mandelic acid and dicumyl peroxide on the biodegradation properties of PLA/woven fibre reinforced composites was investigated by **Kumar et al.** (**2010**). It was noticed that the presence of mandelic acid exhibited 25% reduction in the weight after two months and accelerated the biodegradation process. When dicumyl peroxide was used as an additive, the weight loss accounted for only 5-10% by the end of three months, which was relatively slower as compared to other additive. Therefore, the outcome of this study

indicated that amphiphilic additives can be selected based on the application, in which the nanocomposite finds its end use.

The influence of hemp fibres on the thermal and mechanical properties of PLA composites processed by compression-moulding technique was investigated (**Baghaei et al., 2013**). With respect to increase in the weight loadings of the hemp fibres, a significant improvement in the tensile and flexural strength was noticed. A maximum enhancement of tensile and flexural strength by ~50% and ~67%, respectively, was achieved for 45 wt% loadings of the hemp fibre, as compared to neat PLA. In a separate contribution, it was reported that the PLA/hemp composites showed greater water uptake as compared to neat PLA (**Baghaei et al., 2014**). The crystallinity of PLA was also enhanced, owing to the presence of hemp that encouraged the heterogeneous nucleation during the crystallization process.

The benefit of utilizing maleic anhydride (MA) as a compatabilizer in the fabrication of PLA/ramie fiber composites was demonstrated by **Yu et al.** (**2014**). The existence of better interfacial adhesion between the PLA and the fibre was verified by SEM. The tensile strength of PLA/ramie fibre exhibited an improvement of ~23%, whereas, PLA/MA/ramie fibre showed even further enhancement of ~30%, as compared to neat PLA.

Chemical modification of hemp fibre with acetic anhydride, alkali and silane compound was carried out and the influence of the same on the thermal properties of PLA was investigated (**Oza et al., 2014**). Thermal degradation kinetic study was done using Flynn-Wall-Ozawa method. It was reported that hemp fibre treated with acetic anhydride exhibited 10-13% greater activation energy as compared to silane and alkali treated hemp fibres incorporated PLA composites. The high bond energy that existed between the acetic anhydride treated hemp fibre and PLA led to improvement in the thermal stability for the composites.

PLA/hemp fibre composite was fabricated via twin-screw extrusion technique and the effect of different loadings (10-40 wt %) of the hemp fibre on the mechanical properties of the composites was examined (**Song et al., 2013**). At 40 wt% loading of hemp fibre, a maximum enhancement in the mechanical properties of PLA was noticed. The presence of hemp fibre in the PLA matrix accounted for ~40% and ~90% improvement in the tensile strength and tensile modulus, respectively. In addition to this, flexural strength as well as flexural modulus were improved by ~60% and ~89%, respectively, as compared to neat PLA.

The influence of different alignments of various dosages (0-100 kGy) of electron beam treated jute fibres (random and two-directional alignment) on the thermal properties of PLA was investigated and the nanocomposites were prepared by compression molding process (**Ji et al., 2012**).The maximum improvement in the coefficient of thermal expansion (CTE) was experienced at 100 kGy irrespective of the filler alignments. In contrast, the highest improvement in terms of heat deflection temperature (HDT), thermal stability as well as storage modulus were obtained for both the alignments irradiated with an electron beam dosage of 10 kGy. However, it was found that significant difference in terms of the above discussed properties was not observed with respect to alignment.

PLA based composite films were fabricated via solution casting approach by incorporation of jute nanofibrils (JNF) and microcrystalline cellulose (MC), respectively (**Baheti et al., 2013**). In comparison with neat PLA, the nanocomposite demonstrated a maximum enhancement of tensile strength and modulus of ~206% and 167%, respectively. The presence of improved cellulose content and surface active sites in the jute nanofibrils after chemical treatment led to the significant improvement in terms of mechanical properties of PLA.

A new type of nanomaterial (sisal) was incorporated in the PLA matrix and the effect of the filler in terms of thermal, water absorption and mechanical properties of PLA was investigated

(**Ramzy et al., 2014**). It was observed that the water absorption reduced by ~50% after incorporation of the nanofiller in comparison with neat PLA. A significant improvement in the tensile strength was experienced in the presence of nanofiller and the enhancement was found to be ~50% higher than that of the neat PLA. The thermal degradation temperature was improved by ~20 °C after the reinforcement of sisal fibre in the PLA matrix. In a separate contribution, the effect of benzoyl peroxide (BP) treated sisal fibres on the mechanical properties of PLA composites fabricated by injection molding process was studied (**Asaithambi et al., 2013**). Morphological analysis carried out by SEM elucidated the better interfacial adhesion between the treated filler and the matrix. The tensile and flexural moduli were also enhanced after the reinforcement of sisal in the PLA matrix.

PLA was reinforced with abaca fibres (untreated and treated with acetic anhydride) and the biodegradability characteristics of resultant composites were investigated (**Naozumi et al., 2004**). It was found that a significant reduction in the weight was not exhibited by both the PLA and PLA/treated abaca fibre composites even after two months. However, PLA/untreated abaca fibre composite system showed ~10% weight loss for the same biodegradation period.

The effect of coir fibre on the thermal, mechanical and biodegradation characteristics of PLA was investigated (**Dong et al., 2014**). The tensile as well as flexural strength of the composites was found to be lower as compared to neat PLA due to voids and weak bonding between the filler and the PLA matrix. With respect to weight loadings, the properties were even affected further because of agglomeration of fibre. In particular, the thermal stability of PLA was reduced considerably after the reinforcement. The presence of coir in the PLA matrix acted as a nucleating agent, which was confirmed from the reduction in T_{CC} during the cold crystallization process. Soil burial tests indicated that the addition of coir in the PLA matrix influenced the biodegradation characteristics.

Investigation on the biodegradation properties of PLA, starch and PLA/starch/coir composites was performed by **Iovino et al.** (**2008**). It was found that neat starch showed greater extent of biodegradation characteristics in comparison with neat PLA and PLA/starch/coir composites. The high susceptibility of the starch towards biodegradation was due to the preferential attack of the same by microbes. From the evolution percentage of carbon dioxide, it was confirmed that the role of fibres in the biodegradation process was secondary. However, optical microscopy analysis allowed visualizing the growth of microbes such as bacteria and fungi on the samples subjected to biodegradation process. DSC analysis revealed the reduction in the melting temperature with respect to incubation period for all the three specimens indicating the polymer degradation.

Jang et al. (**2011**) investigated the influence of plasma treated coconut fibre on the mechanical properties of PLA. The results indicated that the plasma treatment turned to be highly influencing in terms of tensile strength of PLA in comparison with untreated coconut fibre, due to better adhesion between the PLA and the reinforcement. In case of elongation-at-break (%), the PLA matrix reinforced with plasma treated coconut fibre exhibited ~20% improvement as compared to neat PLA.

In the work of **Surin et al.** (**2015**), the tensile strength as well as water absorption properties of PLA/starch/coir and PLA/MA/starch/coir biocomposites were studied. It was observed that the maximum improvement in the tensile properties was achieved at ~20 and ~30 wt% loadings of coir in case of PLA/starch and PLA/MA/starch blends, respectively. Water absorption tests revealed that swelling ratio was found to be less for MA grafted PLA/starch/coir composites as compared to PLA/starch composites.

The influence of various loadings of untreated and alkali treated coir fibres (10 to 50 wt %) on the thermal and mechanical properties of PLA were investigated (**Nam et al., 2012**). It was

found that PLA composites reinforced with alkali treated coir fibres exhibited ~73% improvement in the interfacial shear strength as compared to untreated fibres. The best improvement in terms of tensile strength was also achieved for the alkali treated composites with 20 wt% coir loading. However, thermal stability of both the composites (PLA reinforced with alkali treated and untreated coir fibres) was comparatively lower than that of neat PLA.

Pineapple leaf fibre (PLF) was modified with triethoxy vinyl silane and incorporated in the PLA matrix. The effect of thermal as well as mechanical properties of PLA/silane modified PLF biocomposites was examined (**Shih et al., 2013**). The morphological study revealed that better compatability existed between the filler and the matrix after silane functionalization, which in turn showed positive effect in terms of reduction in the water absorption properties as compared to neat PLA. The tensile and flexural strength of the biocomposites were found to be improved by ~65% and ~66%, respectively, as compared to neat PLA. In addition to this, the biocomposites exhibited an improvement of ~75% in terms of heat deflection temperature in comparison with neat PLA.

The effect of alkali, silane and combination of both treatments on the pineapple fibre modification and its subsequent influence on the properties of PLA was investigated (**Huda et al., 2014**). The pineapple fibres used after both treatments showed a maximum improvement of ~9 °C in thermal degradation temperature over untreated, alkali treated and silane treated fibres. PLA composites reinforced with alkali and silane treated fibre demonstrated 80% improvement in the impact strength as compared to PLA/untreated pineapple composites due to enhanced adhesion between the matrix and the fibres.

Pineapple leaf fibre was modified with silane coupling agent (3-glycidyloxypropyl trimethoxysilane) before reinforcement in the PLA matrix and the influence of same on the mechanical as well as crystallization properties of PLA was studied (**Shih et al., 2014**). The PLA

composites incorporated with treated pineapple fibres showed improvement in terms of loss modulus by ~6% as compared to neat PLA. The enhancement was due to the rigidness and toughness developed in the PLA after the reinforcement. POM studies revealed that the reinforcement acted as a nucleating agent by increasing the number of nucleation sites. In a separate contribution, PLA/pineapple leaf fibre biocomposite was fabricated via twin-screw extrusion and the effect of various loadings (10-50 wt %) of pineapple leaf fibre on the mechanical properties of PLA was investigated (**Kaewpirom et al., 2013**). It was found that the tensile strength and elongation-at-break (%) of PLA composites (at 40 wt% loadings) were improved by ~47 % and ~110%, respectively, as compared to neat PLA.

Cellulose fibres were extracted from bamboo and then subsequently treated with alkali, silane coupling agent and maleic anhydride (MA) before the reinforcement in the PLA matrix (**Lu et al., 2014**). The influence of various treatments discussed above on the mechanical characteristics of PLA was investigated. The study described that the alkali treatment highly influenced the tensile strength and Young's modulus characteristics of the composites and the improvement was reported to be ~28% and ~34%, respectively as compared to PLA composites containing untreated fibres. Silane treatment was found to influence the impact roughness and elongation-at-break (%) to the maximum extent and the improvement was reported to be ~115% and ~62%, respectively, in comparison with PLA/untreated fibres composites.

Olive pit powder (OPP) was used as reinforcement for the synthesis of PLA based biocomposites and mechanical properties of the composites were investigated (**Koutsomitopoulou et al., 2013**). The results indicated that the mechanical properties decreased with increasing weight loadings of the filler, due to agglomeration as well as improper distribution of OPP in the PLA matrix.

Chitosan and starch were blended with the PLA matrix and the antimicrobial and mechanical properties of PLA/chitosan/starch blends were examined (**Bie et al., 2013**). The results clearly demonstrated that chitosan acted as the antimicrobial agent among the other two components in the blend. The presence of starch in the blend favoured the diffusion of chitosan from the surface of the films and exhibited its antimicrobial action when contacted with the meat, which contained moisture. The addition of starch and chitosan in the blend led to the reduction in the tensile strength of PLA and improved the ductility of the films.

The effect of different particle size (715 and 180 µm) and weight loadings (5 and 10 wt %) of chitosan on the antimicrobial as well as thermal property of PLA was investigated (**Bonilla et al., 2013**). It was observed that the addition of chitosan in the PLA matrix neither affected nor promoted the thermal stability of the PLA films. However, it affected the tensile strength as well as elongation-at-break (%), as the PLA/chitosan composite films became more fragile than PLA after the reinforcement, irrespective of the particle size. With respect to loadings, similar behaviour in the mechanical properties was observed, due to lack of compatibility between the chitosan and the PLA matrix. The microbial count was significantly reduced in the presence of chitosan because of the positive charges in the chitosan participated in interacting with the negative charges encompassed in the macromolecule content of the microbial cell wall leading to collapse in the nutrient exchange process.

A comparative investigation on the influence of two different fillers such as chitosan and keratin on the thermal and mechanical properties of PLA was examined by **Tanase et al.,** (**2014**). The DSC analysis revealed that the addition of chitosan in the PLA matrix led to reduction in the percentage crystallinity for PLA composites, whereas, the presence of keratin showed improvement in the crystallinity of the samples. However, no significant improvement in terms of tensile strength was shown by both the composites, indicating poor compatibility as well as interfacial adhesion between the filler and the matrix.

In a separate study, chitosan and epoxidized natural rubber were blended with PLA via solution casting approach and the composites were subjected to morphological and mechanical characterizations (**Zakaria et al., 2013**). SEM analysis revealed smooth surface as well as homogeneous distribution of chitosan in the blend up to 15 wt% loadings and thereafter, segregation in the phase as well poor compatibility was visualized. In addition to this, the tensile strength of the composites was improved by ~33%, where only chitosan was reinforced in the PLA matrix. In case of PLA/chitosan/epoxidized natural rubber blend, it was observed that the tensile strength was drastically affected.

PLA/cellulose nanocrystals (CNC) based nanocomposites were fabricated and the effect of functionalization of CNC with glycidyl methacrylate (GMA) and pre-dispersion of CNC in poly (vinyl acetate) (PVA) before incorporation in the PLA matrix was investigated (**Pracella et al., 2014**). The agglomeration of non-functionalized CNC in the PLA matrix at higher loadings was observed by SEM analysis and uniform distribution of functionalized as well as pre-dispersed CNC in the PLA matrix was evidenced.

PLA nanocomposites incorporated with unmodified cellulose nanocrystal (UCNC) and cellulose nanocrystal modified with surfactant (MCNC) were fabricated by solvent casting method (**Fortunati et al., 2012**).The morphological analysis carried out by TEM revealed the agglomeration of unmodified cellulose crystals in the PLA matrix due to hydrogen bonding with each other. The MCNCs were found to be uniformly distributed in the PLA matrix indicating that modification of CNC with surfactant influenced the dispersion ability of the nanocrystals. The PLA/MCNC nanocomposite system exhibited better oxygen and water vapour barrier effects as compared to the unmodified CNC reinforced nanocomposite sample. It was observed that maximum reduction in the oxygen transmission rate of ~48% and water vapour permeability of ~15% was exhibited, when 5 wt% MCNCs were incorporated in the PLA matrix.

Acid hydrolysis was used to derive cellulose nanocrystals (CNC) from microcrystalline cellulose and the effect of pristine CNC as well as surfactant modified CNC on the thermal and crystallization properties of PLA/poly(hydroxyl butyrate) (PHB) was investigated (**Arrieta et al., 2014**). It was observed that the presence of surfactant modified CNC enhanced the thermal stability of the PLA/PHB blend and the maximum improvement in the thermal degradation temperature of ~10 °C was obtained for the PLA/PHB/SCNC nanocomposite system. DSC analysis revealed that the reinforcement acted as a nucleating agent by improving the crystallinity of the blend.

Cellulose nanocrystals were functionalized with polyethylene oxide (PEO) before incorporation in the PLA matrix and investigation on the mechanical properties of PLA/CNC/PEO nanocomposite was performed (**Arias et al., 2014**). Morphological analysis authenticated the agglomeration of CNCs in the PLA matrix and also considerable reduction in the agglomeration of CNCs was visualized with respect to PEO concentration. However, the tensile strength was enhanced only ~9% for the PLA/CNC/PEO nanocomposite as compared to neat PLA. The elongation-at-break (%) of PLA was drastically affected after the incorporation of PEO functionalized CNC.

PLA nanocomposites based on cellulose nanocrystals (CNC), surfactant modified cellulose nanocrystals (SCNC) and SCNC/silver nanoparticles (Ag) were fabricated (**Fortunati et al., 2012**). The morphological analysis verified that the uniform distribution of cellulose nanocrystals was facilitated by the surfactant modification. The tensile modulus enhanced tremendously and the increment was found to be ~115% for PLA/SCNC nanocomposite as compared to neat PLA. In addition to this, SCNCs promoted the nonisothermal crystallization of PLA by acting as a nucleating agent. The presence of Ag nanoparticles together with SCNC influenced the antimicrobial properties, which is an essential feature for packaging application.

1.3.4. PLA-silica nanocomposites

Silica nanoparticles were also used as the reinforcement in the PLA matrix and the effect of the same on the thermal and mechanical properties of PLA was investigated (**Wu et al., 2013**). For PLA/silica nanocomposites, the maximum improvement in the elongation-at-break (%) and Young's modulus was observed at silica loading below 1.5 wt%. The addition of silica nanoparticles in the PLA matrix improved the HDT significantly by 25 °C, which is due to the high thermal stability of silica. The spherulite size was also decreased after the reinforcement, which is indicative of nucleating ability of the silica nanoparticle. The incorporation of silica in the PLA matrix delayed the thermal degradation process of the composites by enhancing the thermal stability of the samples by ~20 °C. In a separate contribution, sol-gel process was employed to fabricate PLA/SiO_2/Al_2O_3 nanocomposites (**Tsai et al., 2013**). The uniform distribution of the reinforcement was confirmed through morphological analysis. Positive influence in terms of thermal expansion coefficient was reflected by the filler and the improvement was around 225 fold greater in comparison with neat PLA. However, the thermal stability of PLA decreased with increasing Al_2O_3. The effect of zeolite 4A and chabazite zeolite on the thermal properties of PLA was investigated (**Yuzay et al., 2010**). Both the zeolites enhanced the nucleation sites and improved the crystallinity of the PLA composites, whereas, the glass transition and melting temperatures remained unaffected by the addition of zeolites in the PLA matrix. The activation energy was found to exhibit downturn for both the zeolite incorporated PLA composites as compared to PLA, demonstrating decreased thermal stability of PLA after the reinforcement.

1.4. Outcome of literature review

The detailed literature survey discussed above reveals the continuing efforts focused on improving the thermal, mechanical and barrier properties of PLA. In this regard, the present

doctoral work focuses on the fabrication of PLA based nanocomposites by incorporation of two different nanofillers (graphene (GR) and sucrose palmitate (SP)) in the PLA matrix and understanding the influence of the reinforcement on the thermal, mechanical and barrier properties of PLA. Graphene is selected as reinforcement in the PLA matrix due to the following advantages possessed by the filler; (i) when nanoscale graphene sheets are well dispersed in the PLA matrix, it is expected that the tremendous aspect ratio of this filler could contribute to PLA chain confinement effects leading to improvement in strength, (ii) the nanoscale filler being layered structures can provide a zigzag torturous diffusion path leading to enhancement in barrier performance for gas transmission. Especially for food packaging applications, it is important to understand both mechanical and barrier properties of filler materials as well as their compatibility with food during storage. Hence, exploration of non-toxic substances approved for food contact needs to be essentially prospected as fillers. In this regard, U.S food and drug administration (FDA) approved food additive, sucrose palmitate is chosen as one of non-toxic fillers for the fabrication of PLA nanocomposites. Besides, being readily biodegradable and non-toxic in nature, the novel filler (sucrose palmitate) also offers many advantages such as antimicrobial, mechanical and barrier properties, which make them potential for the storage of food. Therefore, the objectives of the doctoral work are framed as follows:

1.5. Objectives

- Synthesis and characterization of graphene and sucrose palmitate reinforced PLA nanocomposites.
- Crystallization studies of graphene and sucrose palmitate incorporated nanocomposites.
- Thermal degradation kinetic studies of PLA-graphene and PLA-sucrose palmitate nanocomposites.
- Influence of graphene and sucrose palmitate on the hydrolytic degradation behavior of PLA.

1.6. Organization of doctoral thesis

The doctoral thesis is organized in seven chapters as follows:

Chapter 1: Introduction

Chapter 2: Synthesis and Characterization of Graphene Reinforced PLA Nanocomposites

Chapter 3: Synthesis and Characterization of Sucrose Palmitate Reinforced PLA-Nanocomposites

Chapter 4: Crystallization Studies of Sucrose Palmitate and Graphene Reinforced Nanocomposites

Chapter 5: Thermal Degradation Kinetic Studies of Sucrose Palmitate and Graphene Nanocomposites

Chapter 6: Influence of Sucrose Palmitate and Graphene on the Hydrolytic Degradation Behavior of PLA

Chapter 7: Conclusions and Future Directions

CHAPTER 2

Synthesis and Characterization of Graphene Reinforced PLA Nanocomposites

In this chapter, the influence of temperature on the exfoliation of expandable graphite (EG) and its structural properties were investigated in detail. The EG exfoliated at 750 °C was subjected to sonication and further used as reinforcement material in the poly(lactic acid) (PLA) matrix to investigate the influence of "graphene" (GR) on the structural, morphological, thermal, optical, mechanical and oxygen barrier properties of PLA composites. X-ray diffraction results disclose the effect of sonication time on the dispersion ability of GR in the PLA matrix. A high resolution transmission electron microscopy image of GR pictoriated after sonication demonstrated a monolayer structure of GR. Thermo-gravimetric analysis reveals that the T_{onset} value for the PLA composite with 0.5 wt% GR content is increased by 31 °C over neat PLA, when 10% weight loss is taken as a point of comparison. Differential scanning calorimetry analysis confirms that GR acts as a nucleating agent that enhances the melting point of PLA composites over neat PLA. A maximum enhancement of tensile strength (17%) and elongation at break (51%) is obtained for PLA composite with 0.1 wt% loading of graphene as compared to neat PLA. This part of work has been published in ***RSC Advances****, 2015, 5, 28410-28423.*

2.1. Introduction

PLA composites reinforced with carbonaceous nanofillers, like CNTs are evidenced to reveal a noteworthy balance of properties in terms of mechanical, thermal and barrier effects (**Hussain et al., 2006**). However, the high cost factor associated with CNTs limit their widespread applications in industrial corners and hence, additional proxies need to be prospected. Recently, a new category of cost-effective nanodimensional (2D) material called as graphene, a hexagonally arranged sp^2-carbon, chemically alike to CNTs and structurally akin to silicate layers, has recognition as potential reinforcement material for the polymer matrices (**Bao et al., 2009)**. Graphite, if exfoliated into graphene and homogeneously dispersed, the target properties can be improved at comparatively lower loading than conventional carbon reinforcements. However, so far, the exfoliation of graphite to graphene and its reinforcement into polymeric materials has not been completely fruitful. Owing to the existence of strong Van der Waals interactions (2 eV/nm^2) between the interlayer spacing, it is indeed tough to attain a completely alienated state of graphene (**Stankovich et al., 2006; Cao et al., 2010**). Several research works have been endeavored describing the exfoliation and optimization of the dispersion of graphite sheets via the process of intercalation of alkali metals between the carbon layers (**Viculis et al., 2005)** or by subjecting the same to strong acidic treatment (**Carr et al., 1970; Chen et al., 2003; Pan et al., 2000**). The interlayer spacing has also been expanded via heat treatment or microwave irradiation and subsequently trailed by mechanical crushing (**Kalaitzidou et al., 2007**). The process of expansion led to considerable enhancement in the surface area of graphite, as a consequence of which, advancement in the inherent properties of the polymeric matrix are evidenced (**Cao et al., 2010; Cao et al., 2010; Niyogi et al., 2010**). **Murariu et al.** (**2010**) investigated the addition of expandable graphite (EG) on the properties of PLA composites which was prepared by the melt compounding method. In their study, complete

exfoliation of EG into graphene sheets was not achieved, as a result, the tensile strength of the PLA composites exhibited downturn with an increase in the EG (%wt) loading. To the best of our knowledge, study on optimization of exfoliation temperature for GR synthesis and highlighting the performance of PLA/GR composites have not been reported before. In this chapter, EG is subjected to exfoliation at different temperatures ranging from 200-1000 °C and the optimum temperature for exfoliation is identified based on carbon yield (%) and bulk density (kg/cm^3) of the resultant exfoliated graphite (EXG). Then, sonication technique is adopted to completely exfoliate the EXG into graphene sheets (GR). Thereafter, PLA-GR composites with various content of GR are synthesized via solution casting method and resultant films are characterized in detail to emphasize their performance.

2.2. Experimental

2.2.1. Materials

Expandable graphite (EG, 99.9%) was obtained from Asbury Carbons (USA). Poly(lactic acid) (grade 2003D) obtained from Nature work® was used as the bio-polymer matrix. Chloroform obtained from Merck (India) Ltd., was used as the solvent for synthesizing poly(lactic acid)-graphene (PLA-GR) composites.

2.2.2. Exfoliation of expandable graphite (EG)

Accurately, 0.05g of EG was weighed and placed in a silica crucible. Thermal exfoliation of expandable graphite was carried out at different temperature ranging from 200 to 1000 °C. The crucible containing expanded graphite was inserted in a muffle furnace (which was already set at a desired temperature) for 2 min in order to obtain exfoliated graphite samples (EXG 200-1000 °C). After thermal treatment, an expansion volume was measured using a measuring cylinder. The actual reason for exfoliation is the increase in volume, and the resultant pressure, caused by the rapid heating of the intercalated compound. The following relations were used to calculate bulk density (kg/cm^3) and carbon yield (%).

Bulk density (kg/cm^3)= $\frac{mass\ of\ the\ exfoliated\ graphite}{volume\ of\ the\ exfoliated\ graphite}$ (2.1)

Carbon yield (%) = $\frac{mass\ of\ the\ exfoliated\ graphite}{mass\ of\ the\ expandable\ graphite}$ (2.2)

2.2.3. Synthesis of PLA-GR composites

PLA-GR composites were fabricated by a simple solution-casting method as follows: First, PLA (~0.95 g) was dissolved in 30 mL of chloroform with continuous stirring for 2 h in order to completely dissolve the PLA (Solution A). Graphene (0.1, 0.3, 0.5 wt % with respect to PLA) was dispersed in chloroform (20 mL) separately by bath sonication for 30 min (Solution B). Subsequently, the solution containing dispersed GR (Solution B) was transferred into PLA-chloroform mixture (Solution A) and further subjected to bath sonication for 15 min and 30 min (Solution C). The corresponding photographs of solution A, B and C are portrayed in Figure 2.1.

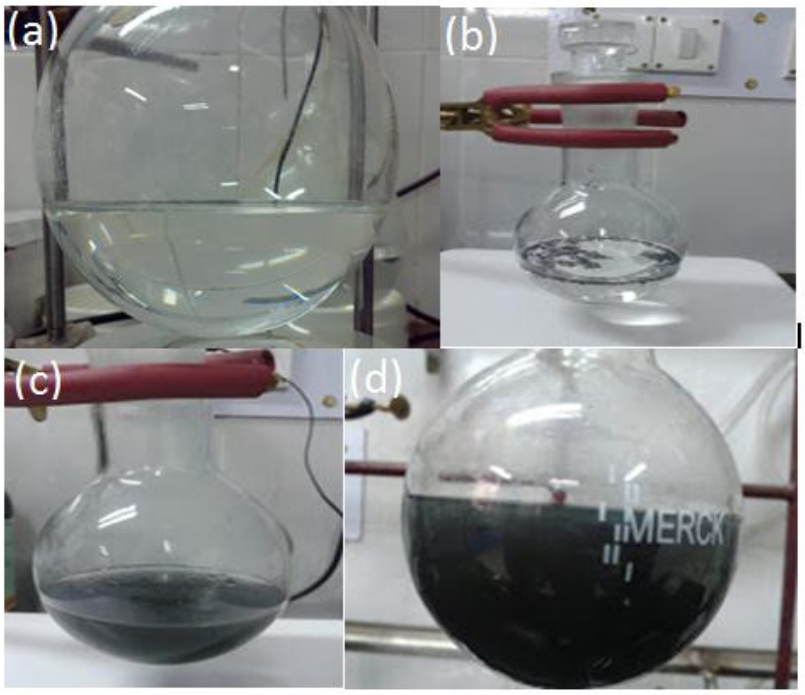

Figure 2.1. (a) PLA (Solution A), (b) EXG 750 in chloroform before sonication, (c) EXG in chloroform after sonication (Solution B) and (d) PLA-GR composite

(Solution C)

Finally, the PLA-GR solution was casted on Teflon petriplates and further, dried under ambient conditions for 24 h. The dried composite films were peeled off carefully from the petriplates. The resulting films were finally dried in a vacuum oven at 40 °C for 12 h. The obtained films were stored in airtight bags at room temperature for further characterization. The thickness of the fabricated films was measured using a film thickness meter (indi 6156, India). Twenty measurements were taken on each film and the average thickness of the films was found in the range of 60 ± 5 μm. Thereafter, all the samples were designated as neat PLA, PLA-GR-0.1, PLA-GR-0.3, and PLA-GR-0.5 for 0, 0.1, 0.3 and 0.5 (wt%) graphene loading, respectively.

2.3. Characterization

2.3.1. X-ray diffraction analysis (XRD)

XRD analysis of neat PLA and composite films were carried out under air atmosphere at room temperature on a Bruker A8 advance instrument using Cu-Kα (λ= 0.15406 nm) radiation operating at 40 kV and 40 mA. The diffraction data were recorded in the 2θ range of 1 - 50° with a scanning rate of 0.05° s^{-1} and 0.5 s step size.

2.3.2. Fourier transform infrared spectroscopy (FTIR)

FTIR spectra for neat PLA and composite films were recorded between 4,000 and 450 cm^{-1} region using spectroscopic quality KBr powder with a Shimadzu IR affinity-1 model spectrometer.

2.3.3. BET surface area analysis

Nitrogen physisorption measurements were conducted on a Beckman Coulter surface area analyzer (COULTER SA 3100 model). The samples were degassed at 105 °C for 4 h prior to N_2 adsorption-desorption measurements. The specific surface area was calculated by BET

(Brunauer, Emmett, and Teller) model. The total pore volume was estimated at a relative pressure of 0.99, assuming that full surface saturation has been achieved with nitrogen.

2.3.4. Morphological analyses

The morphology and the selected area diffraction (SAED) pattern of graphene were visualized using transmission electron microscopy (TEM) (JEOLJEM 2100) operated at 200 kV. By direct casting of graphene solution over the carbon-coated copper TEM grid, images of the same were obtained. The morphology of PLA-GR composites was pictoriated using field-emission scanning electron microscopy (FE-SEM) (Zeiss Sigma model) operated at 2 kV. The dispersion of GR in PLA composites was investigated by Leica DM 2500P polarizing optical microscope fitted with a QICAM FAST1394 camera.

2.3.5. Thermogravimetric analysis (TGA)

Thermogravimetric analysis was performed on a Mettler Toledo thermo gravimetric analyzer (TGA/SDTA 851® model). Samples (10.5± 0.3 mg) were placed in a 900 µl crucible. Neat PLA and PLA-GR composites were heated from 25 to 700 °C in a 60 mL/min flow of N_2 at a heating rate of 10 °C/min.

2.3.6. Differential scanning calorimetry (DSC)

Thermal properties and crystallization behavior of PLA and PLA-GR composites were studied using a differential scanning calorimetry (Mettler Toledo-1 series). Samples (10±0.5 mg) were hermetically sealed in aluminum pans and heated from 25 to 180 °C at a heating rate of 5 °C/min in the N_2 atmosphere (N_2 flow rate of 50 mL/min). All the samples were first heated from 25 to 180 °C and held at this temperature for 5 min to eliminate the effect of thermal and processing history. Glass transition temperature (T_g), cold crystallization temperature (T_c), enthalpy change at T_c (ΔH_c), melting temperature (T_m) and enthalpy of fusion at T_m (ΔH_m) for neat PLA and composite samples were determined from the DSC thermograph during the

second heating cycle. The percentage crystallinity (% X_c) of PLA was calculated according to the following relation.

$$\%X_c = \frac{\left(\Delta H_m - \Delta H_c\right)}{\left(\Delta H_{mp}\right)} \times 100\% \quad (2.3)$$

Where, ΔH_m is enthalpy of fusion at melting temperature (T_m), ΔH_c is the enthalpy of fusion at cold crystallization temperature (T_c). ΔH_{mp} is the heat of fusion of a perfect PLA crystal (93.6 J/g) (**Garlotta et al., 2001**).

2.3.7. UV-Visible spectrophotometry

Transparency measurement for composite films was carried out using UV-Visible spectrophotometer (Make: Perkin Elmer, Model: Lambda 35). The wavelength range was varied between 200-600 nm with a scan rate of 50 nm/min and a spectral bandwidth of 2 nm.

2.3.8. Mechanical testing

The tensile properties such as tensile strength and elongation-at-break were measured under ambient temperature (25 °C) with a 50 kN load cell on a tensile tester (Make: Kalpak instruments, Model: KIC-2-050-C, India). The cross-head speed was fixed as 5 mm/min. Average specimen parameters were: thickness of 0.06 mm, width of 10 mm and length of 50 mm. Three specimens of each sample were subjected for testing and the average values were reported. The ASTM standard D 882-12 was followed for the preparation of the dumb-bell shaped samples used in this test.

2.4. Results and discussion

2.4.1. Effect of temperature on exfoliation

The influence of temperature on exfoliation of EG in terms of volume exfoliated, weight after exfoliation, bulk density and carbon yield are presented in the Table 2.1. It is clearly seen from the Table 2.1 that the volume of expandable graphite (EG) increases with increasing

temperature up to 750 °C. This is due to the maximum swelling of intercalates taking place at 750 °C that increases the interlayer distance between graphene sheets resulting in high volume of expansion. After 750 °C, the expansion volume, bulk density and carbon yield (%) decreases. This indiactes that the imparted heat is enough for evaporation of intercalates as CO_2 and SO_2 and sample expansion (**Chen et al., 2003**). It is also important to mention that the carbon yield (%) value drops down after 750 °C. Eventhough, the least bulk density value might correspond to a maximum increase in exfoliation rate; two other factors (the volume of exfoliation and carbon yield) should be taken into consideration for optimization of temperature. In the present study, it is considered that 750 °C is the optimum condition for thermal exfoliation based on the information obtained from exfoliation volume, carbon yield, and bulk density. However, no significant change in weight is noticed after exfoliation at the temperature ranging between 200 and 750 °C. Table 2.1 clearly reveals that 80% of carbon yield is obtained at an exfoliation temperature of 750 °C. A further upsurge in exfoliation temperature decreases the carbon yield (%) to below 70%, which is an indication of defects in the C-C bond of graphitic structure (**Zhang et al., 2013**). When expandabale graphite is subjected to thermal shock, high temperature causes the expansion agent to gasify and produces enormous pressure to push adjacent graphite layers apart. In addition to this, when intercalates escape from the interlayers, it will be converted into gaseous products such as CO_2 by reacting with carbon. These gaseous products while escaping creates pores in the graphitic structure due loss of carbon and this in turn helps in increasing the surface area after exfoliation.

Table 2.1. Effect of temperature on exfoliation of EG

Sample name	Volume exfoliated (mL)	Weight after exfoliation (g)	Bulk density (mg/cm^3)	Carbon yield (%)
EXG 200	0.1	0.05	500	100
EXG 300	3	0.046	15.33	92
EXG 400	4.5	0.043	9.56	86
EXG 500	9	0.041	4.55	82
EXG 600	12.5	0.041	3.28	82
EXG 700	15	0.041	2.73	82
EXG 750	15.5	0.040	2.58	80
EXG 800	14	0.034	2.43	68
EXG 900	12	0.023	1.92	46
EXG 1000	4	0.007	1.75	14

*EXG 200 represents the EG exfoliated at 200 °C.

2.4.2. Characterization of expandable graphite (EG), exfoliated graphite (EXG) and graphene (GR)

2.4.2.1. XRD analysis

The XRD patterns of EG and EXG samples are depicted in Figure 2.2. EG exhibits a sharp diffraction peak (0 0 2) at 26.52° indicating that EG is a sort of gas intercalated compounds (GIC) containing certain intercalated graphite structure. The basal peak position remains same for EG in comparison with natural graphite reported in the literature (**Chen et al., 2003; Murariu et al., 2010; Xiang et al., 2011; Yasmin et al., 2006**). This signifies that the carbon crystal layer, which is the elementary constituent, does not undergo any change after intercalation. When all the EXG samples are subjected to XRD analysis, no significant deviation in the peak position (26.52°) is observed. Nevertheless, the peak intensity (26.52°) gradually decreases when compared to EG with an increase in the exfoliation temperature. This represents that

lower the peak intensity, higher will be the degree of exfoliation subject to the same sample loading and packing density (**Yasmin et al., 2006**).

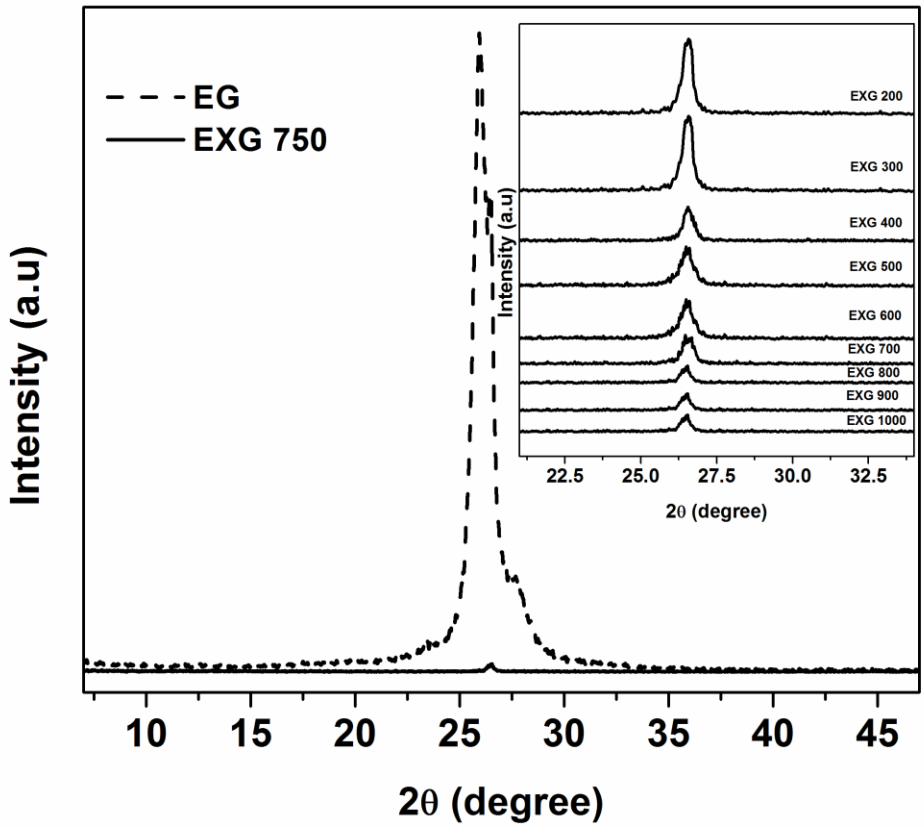

Figure 2.2. XRD patterns of expandable graphite (EG) and exfoliated graphite (EXG)

2.4.2.2. Surface area analysis

Nitrogen (N_2) adsorption-desorption isotherms are shown in Figure 2.3. In the isotherm pattern observed for the EG sample, the convexity suggests that adsorption of N_2 takes place by cooperative mechanism. It means that adsorbate-adsorbent interaction is less importance than adsorbate-adsorbate interaction in nonporous materials like EG. Because of weak interaction between N_2 and EG, the isotherm curve is flat in the initial P/P_0 regions. Nevertheless, once adsorption of the N_2 molecule begins, N_2-N_2 interaction tends to aggrandize the adsorption of

more N_2 molecules thus translating the isotherm to be convex with respect to the relative pressure values in the abscissa. With respect to increase in exfoliation temperature, type III isotherm gradually changes to type II pattern, which is the characteristic feature of EXG (**Singh et al., 1985**). Type II isotherm pattern observed for EXG samples is indicative of enhanced interaction between N_2 and EXG. This is confirmed by the presence of knee portion in the initial P/P_0 region for all the EXG samples. It is apparent from the inset graph (Figure. 2.3), that an increase in intercept (c) value or knee region for EXG samples with respect to exfoliation temperature occurs up to 900 °C. In general, greater the surface area, maximum will be the exfoliation (**Xiang et al., 2011**).

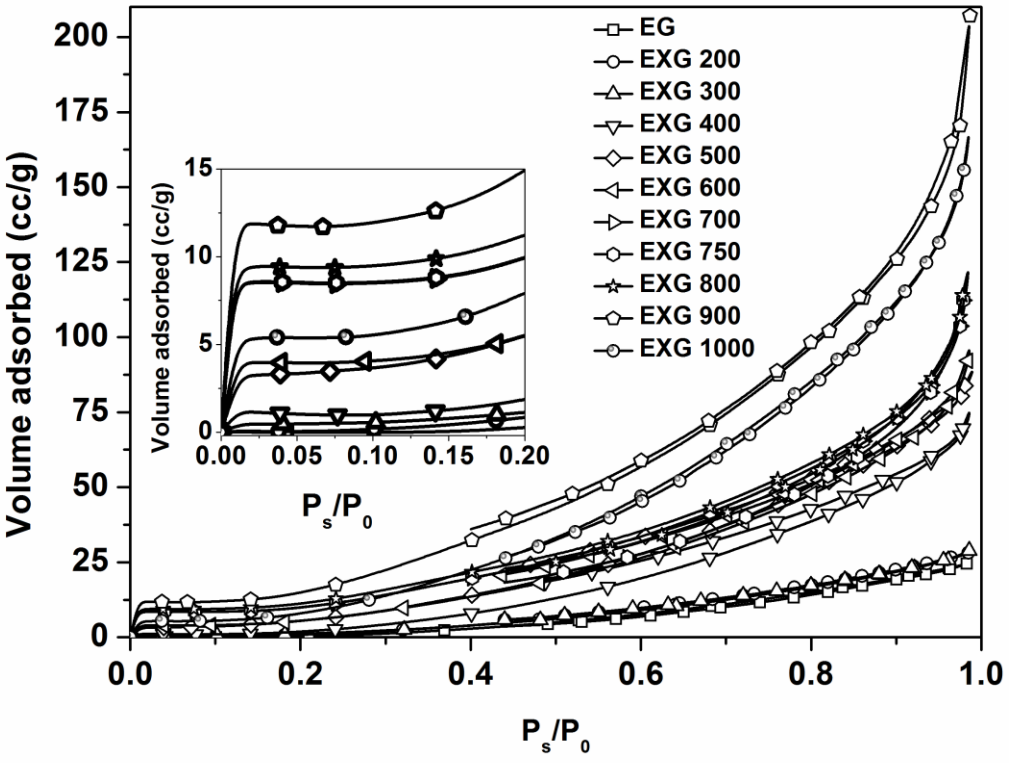

Figure 2.3. N_2 adsorption-desorption isotherms for expandable graphite (EG) and exfoliated graphite (EXG)

BET surface area and the pore volume of the EXG samples are presented in the Table 2.2. Surface area and the pore volume increase with an increase in the exfoliation temperature. This behavior reveals that pores are created in the graphite surface due to the removal of intercalates that escape from the graphitic interlayers during exfoliation (**Stankovich et al., 2007; Afanasov et al., 2010; Fukushima et al., 2010**). The maximum surface area (51.32 m^2/g) and pore volume (0.29 cc/g) are obtained for EXG 900 sample that signifies the maximum degree of exfoliation. However, the surface area, intercept (c) and volume of N_2 adsorbed are reduced for the EXG-1000 sample. This is because of restacking of graphene layers due to the complete removal of intercalates after exfoliation at 1000 °C. Although, a maximum surface area is obtained for EXG 900, carbon yield (%) is drastically reduced to 46%. It is reported that carbon yield (%) below 70% leads to defect in the C-C bond of graphitic structure (**Zhang et al., 2013**). Considering this fact, 750 °C is chosen as the optimum exfoliation temperature and hence, EXG-750 is utilized as a source for the synthesis of GR and PLA-GR composites.

Table 2.2. Surface area characteristics for EG and EXG obtained at different temperatures

Sample name	S_{BET} (m^2/g)	Pore volume (cc/g)
EG	0	0.0429
EXG 200	0	0.0429
EXG 300	5.881	0.0434
EXG 400	19.413	0.1285
EXG 500	19.732	0.1299
EXG 600	20.198	0.1375
EXG 700	33.459	0.1755
EXG 750	36.325	0.1762
EXG 800	38.411	0.1769
EXG 900	51.321	0.2912

2.4.2.3. Morphological analyses

The morphological images of EG and EXG samples are depicted in Figure 2.4. EG is partially oxidized form of graphite containing intercalated compounds between graphene layers as shown in Figure 2.4(a). EG can undergo exfoliation when subjected to sudden thermal shock at a desired temperature. In case of Figure 2.4(b), it can be observed that exfoliation of EG is just initiated due to the insufficient exfoliation temperature (200 °C). Figures 2.4 (c) and (d) show selected FE-SEM micrographs of the EXG 750 sample at different magnifications. These images elucidate that EG is exfoliated several hundred times along with the c-axis. This results in a massive enhancement in volume of EG. Origin of this process lies in the vaporization of the intercalate indicating that gaseous products cause the explosive expansion of the EG (**Michel., et al., 2007**). After expansion, graphite becomes porous structure material with improved surface area comprising of many sheets of nanometer thickness.

The morphology and SAED patterns of GR are visualized by TEM as depicted in Figure 2.4 (e, f). The TEM image (Figure 2.4(e)) pictoriated after sonication demonstrates a monolayer structure. This suggests that, the graphene sheet obtained after sonication process is indeed a monolayer GR. Figure. 2.4(f) depicts the selected area electron diffraction (SAED) pattern of graphene, which is recorded by selecting a specified area from the graphene sheet slung overhead to a micrometer-sized hole on a 200 mesh copper grid. This clearly displays the crystalline structure of GR. The inner six member ring corresponds to the (1 1 0 0) plane, whereas six intense dots are ascribed to the [0 0 0 1] diffractions (**Michel et al., 2007; Cui et al., 2011**). The diffraction pattern images confirm that the resulted graphene retains the hexagonal symmetry of carbon framework.

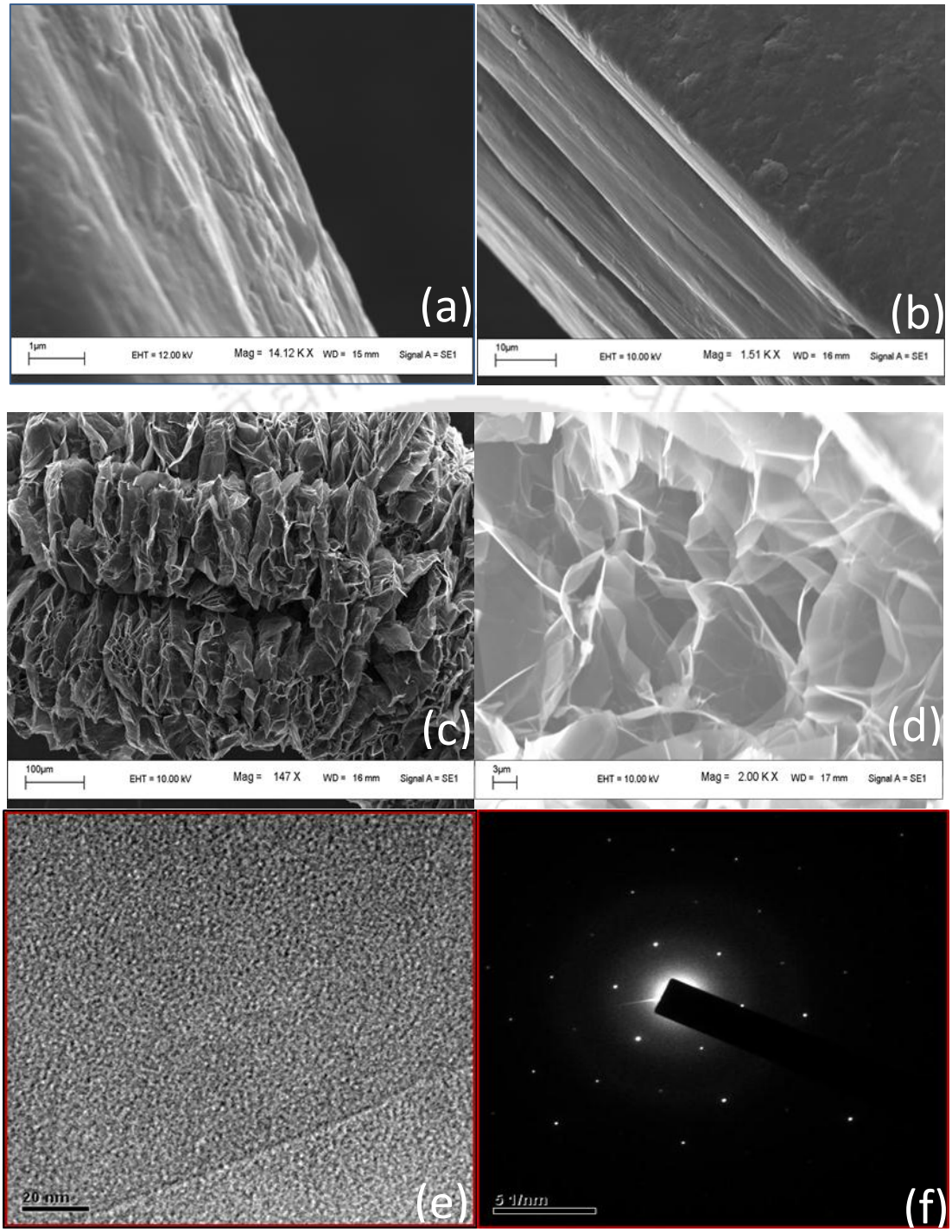

Figure 2.4. FE-SEM images of (a) expandable graphite, (b) EXG 200, (c) EXG 750 (low magnification), (d) EXG 750 (high magnification), (e) TEM image of GR and (f) SAED pattern of GR

2.4.3. Characterization of PLA-GR composites

2.4.3.1. XRD analysis

XRD analysis of neat PLA and its composites is carried out to determine the crystallographic properties of the PLA composites. The diffractograms recorded for PLA composite samples prepared with 15 and 30 min sonication are illustrated in Figure 2.5(a) and 2.5(b), respectively. A scattered intense distribution with a broad peak observed at $2\theta \approx 16.7°$ corresponds to the reflections of (1 1 0) and (2 0 0) planes of orthorhombic α-crystalline phase of PLA (**Krikorian et al., 2003**). In all the composites, the peak position ($2\theta = 16.7°$) corresponding to the crystal structure of PLA is not altered. Hence it is clear that lattice parameters are not altered with the incorporation of GR. However, it is clearly seen from Figure 2.5(a) that for PLA composites, a sharp peak appears at 26.5° corresponding to the (0 0 2) graphitic carbon structure (**Chen et al., 2003; Murariu et al., 2010; Yasmin et al., 2006**). This ratifies the existence of pure graphite in the form of stacked GR sheets, suggesting that 15 min sonication applied during the synthesis of PLA-GR solution is not sufficient to completely exfoliate the graphene layers. Also some of the graphene sheets may persist in the aggregate conformation. To overcome this issue, 30 min sonication was applied during the synthesis of PLA-GR composites and the XRD profiles of the composites are depicted in the Figure 2.5(b). It is clear from Figure 2.5(b) that for PLA composites, no peak is appeared at $2\theta = 26.5°$ corresponding to graphite. These results elucidate that the graphite has been successfully exfoliated into single- or few-layers of stacking platelets and also completely dispersed in the PLA matrix. In the work reported by **Narimissa et al.** (**2012)** and **Murariu et al.** (**2010**) on PLA-nano graphite platelet (NGP) and PLA-expanded graphite composites, respectively prepared via melt-compounding process, the XRD results confirmed the presence of the graphitic peak at 2θ value of 26.5° for all the composite systems. This suggests the fact that the melt-compounding used in their study could not completely exfoliate or isolate the graphene layers and several platelets existed in the amassed form, which in turn affected the mechanical properties. In reality, as the graphene nanosheets in EG are

always interlinked with each other, “complete exfoliation” has no sense as in the case like organically modified layered silicates (OMLS) (**Murariu et al., 2010**). However, a conclusion can be drawn from the current study that the sonication used for separating the interlinked nanosheets of EXG has the effect on the exfoliation as well as the dispersion quality of graphene sheets in the PLA matrix. Based on the XRD analysis, now it is known that 30 min sonication (during the preparation of PLA-GR solution) disperses GR well in the PLA matrix and hence further analyzes are carried out for the samples prepared with 30 min sonication.

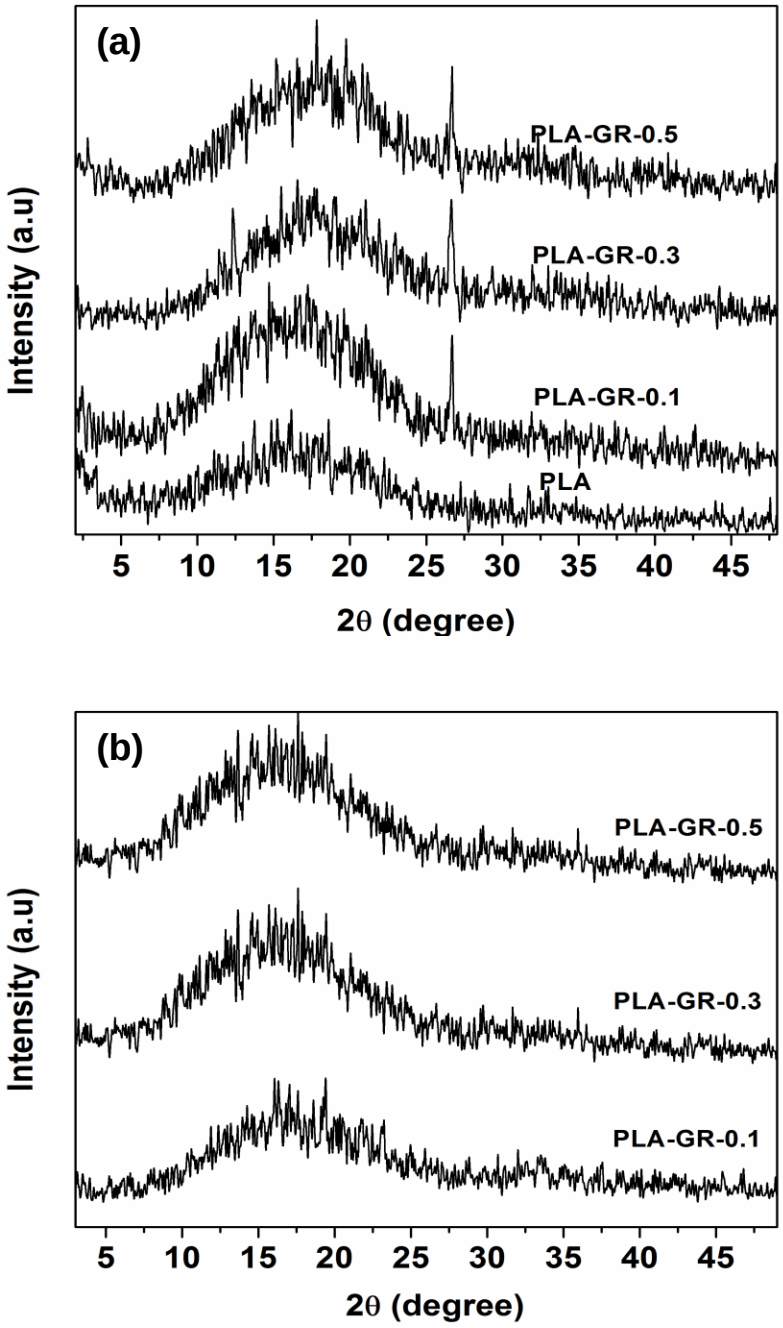

Figure 2.5. XRD patterns of neat PLA and PLA-GR composites prepared with (a) 15 min sonication and (b) 30 min sonication time

2.4.3.2. FTIR analysis

Figure 2.6 portrays the FTIR spectra of PLA and PLA-GR composites. The asymmetric and symmetric mode of C-H stretching in PLA is ascribed by the presence of peaks at 3000 and 2937 cm^{-1}, respectively (**Pamula et al., 2001**). A strong absorption peak is observed at ~1750 cm^{-1}, which is attributed to the carbonyl group present in the ester linkage of PLA matrix. The existence of the CH_3 band in the PLA is characterized by the presence of a peak at 1456 cm^{-1}. The appearance of a peak at 1386 cm^{-1} is assigned to the C-H deformation. The peak present around 1083 cm^{-1} is due to the C-O asymmetric group in the ester group (**Mai et al., 2012**). The stretching frequency observed at 956 and 922 cm^{-1} are mainly attributed to the rocking mode of CH_3 (**Pamula et al., 2001; Mai et al., 2012**). The peak corresponding to the C-C skeleton vibration of the carbon ring in the graphene generally appears at 1400-1500 cm^{-1} (**Han et al., 2013**). However, in the PLA-GR composites, the characteristic peak corresponding to the carbon ring in graphene is masked by PLA due to the relatively lower content of GR in the PLA matrix.

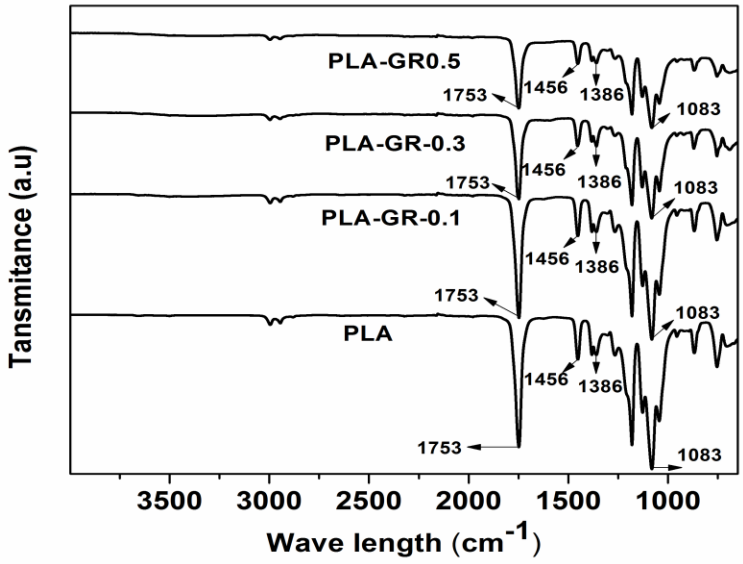

Figure 2.6. FTIR spectra of neat PLA and PLA-GR composites

2.4.3.3. Morphological analyses

The dispersion of graphene sheets in the polymer matrix and their interfacial bonding are vital features that influence the enhancement of physical and mechanical properties of the composite materials. In order to evidence the dispersion of GR in the PLA matrix, FE-SEM and TEM analysis are performed using PLA-GR composite films and the images are shown in Figure. 2.7.

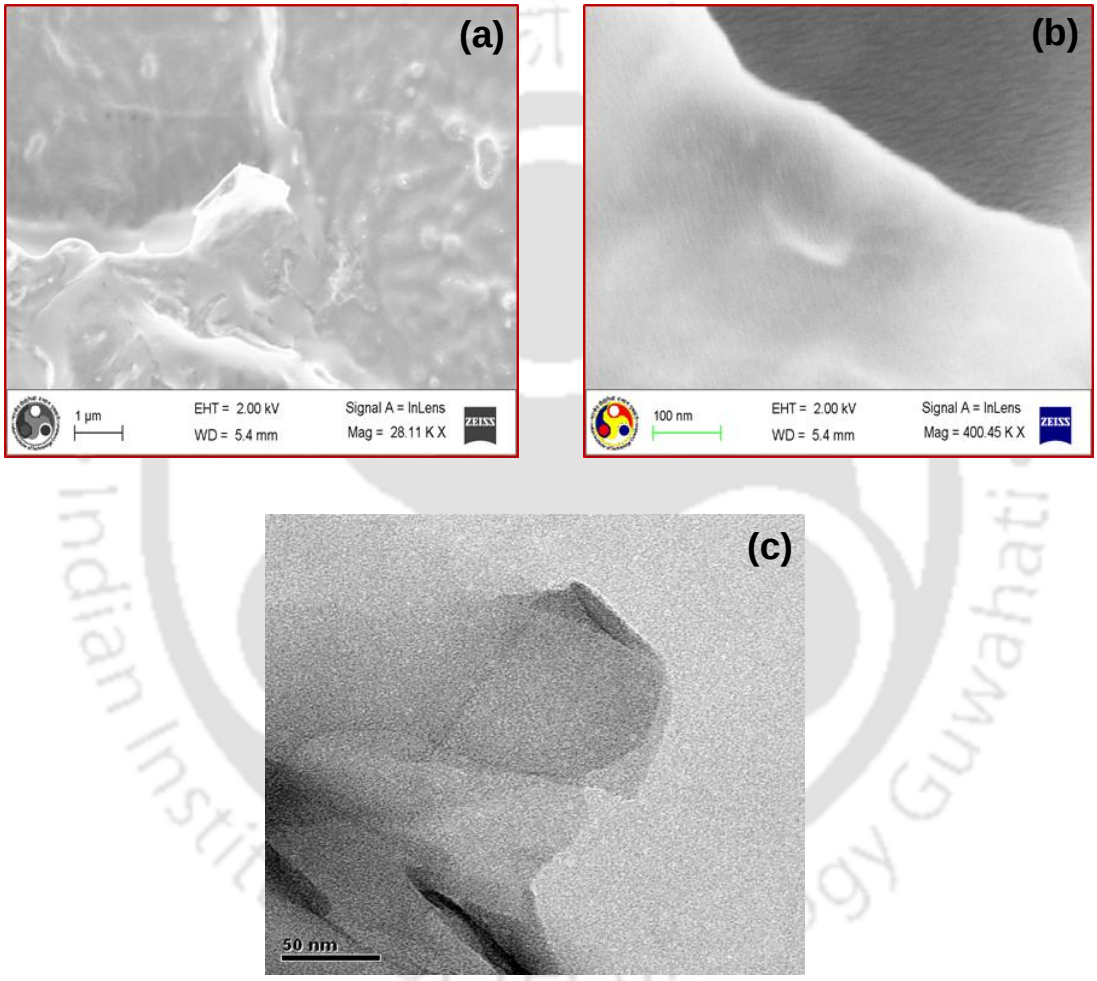

Figure 2.7. FE-SEM images of (a) PLA-GR composite (low magnification), (b) PLA-GR composites (high magnification) and (c) TEM image of PLA-GR-0.1

It is clear from Figure 2.7 that GR sheets are arbitrarily dispersed in the PLA matrix. These results are in good agreement with the XRD patterns of PLA-GR composites (See Figure. 2.5), where the peak corresponding to the graphite layer structure at 26.5° is not observed even at higher loadings of GR. These results suggest that the dispersion of GR in PLA matrix is near to a single sheet level. Aggregation of EG in the PLA matrix was reported by **Murariu et al.** (**2010**). This is in contrast to the present study, where GR sheets are not restacked in the PLA matrix, which might be due to the effectiveness of the sonication process used for the synthesis of PLA-GR composite.

The morphology of the PLA and PLA-GR composites is also investigated using the polarized optical microscopy to know the dispersion of GR in the PLA matrix. Figure 2.8 shows the optical reflection micrographs of PLA composites with the various GR contents. The black portion is the GR sheets and the background is the polymer matrix. It is seen that, at the microscopic level, the GR sheets display a homogeneous distribution in the form of nanosheet clusters throughout the PLA matrix. As the content of the GR increases, the black portion of the micrograph also increases.

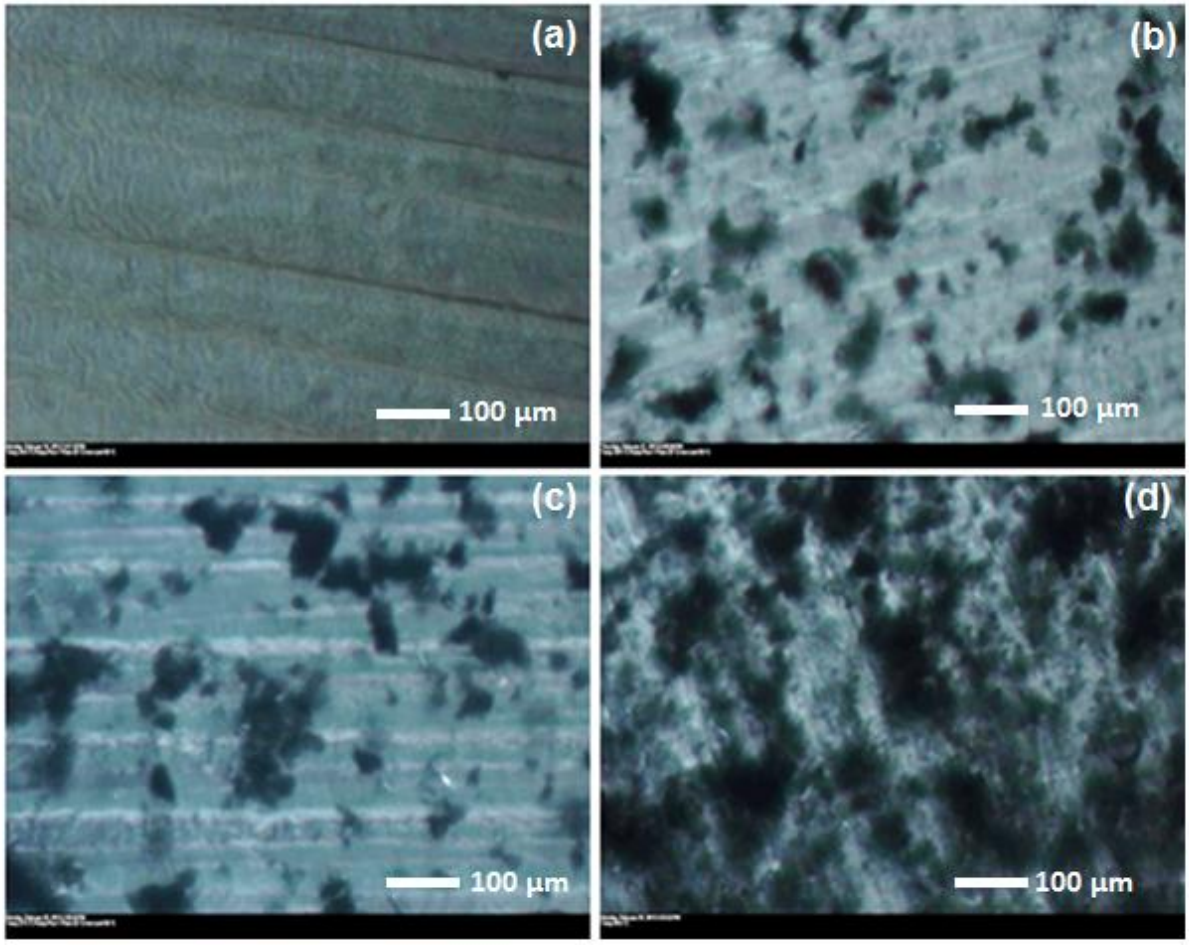

Figure 2.8. Optical microscopy images of (a) PLA, (b) PLA-GR-0.1, (c) PLA-GR-0.3 and (d) PLA-GR-0.5

2.4.3.4. Thermo gravimetric analysis

In order to cognize the influence of GR content on the thermal stability of PLA matrix, TGA analysis is carried out for PLA and PLA–GR composites. Figure 2.9 depicts the temperature-dependent (TGA) and derivative weight loss profiles (DTG) for PLA and PLA-GR composites performed under the nitrogen atmosphere at a heating rate of 10 °C/min. In Figure 2.9(a), the first region of weight loss up to ~100 °C corresponds to removal of adsorbed moisture. The second stage of the thermal degradation process of PLA begins at temperature above 300 °C,

which is principally attributed to intra-molecular trans-esterification (backbitting reaction) (**Han et al., 2004; Fan et al., 2004; Taubner et al., 2001; Wang et al., 2005; Wang et al., 2008; Yu et al., 2003**). When 10% weight loss is taken as a point of comparison, T_{onset} is found to be 268, 278, 283 and 299 °C for PLA, PLA-GR-0.1, PLA-GR-0.3 and PLA-GR-0.5, respectively (see Table 2.3). The obtained results clearly specify that PLA-GR composites exhibit around 10-31 °C improvement in thermal stability over neat PLA. The decomposition temperature at 50% weight loss for neat PLA and PLA-GR composites (0.1, 0.3, and 0.5 wt%) is 333, 334, 334, and 337 °C, respectively (see Table 2.3).

The temperature which corresponds to the maximum rate of weight loss ($T_{max.}$) is regarded as another significant thermal property for the polymer composite system. The T_{max} is defined as the peak value that is obtained from the first derivative curve of TGA thermograph. The first derivative curves for PLA, and PLA-GR composites are depicted in Figure 2.9(b). All the PLA-GR composites and neat PLA show a single peak signifying that the main degradation of these materials proceeded in only one step. It can be noticed that there is an improvement in the T_{max} value (347 °C) for PLA-GR-0.5 sample in comparison with PLA (345 °C) (see Table 2.3). The enhancement in thermal stability is ascribed to the “tortuous path” effect of GR layers, which deferments the diffusion pathway of the degradation by-products and hinders the diffusion of volatile decomposition products (**Cao et al., 2010; Wang et al., 2012**). The delay in the thermal degradation of PLA matrix is also due to the shielding effect presented by flake like nano-filler (**Yu et al., 2003**). Due to the high surface area of graphene, its noteworthy effects on the composite properties can be seen at lesser loading (wt%) of GR.

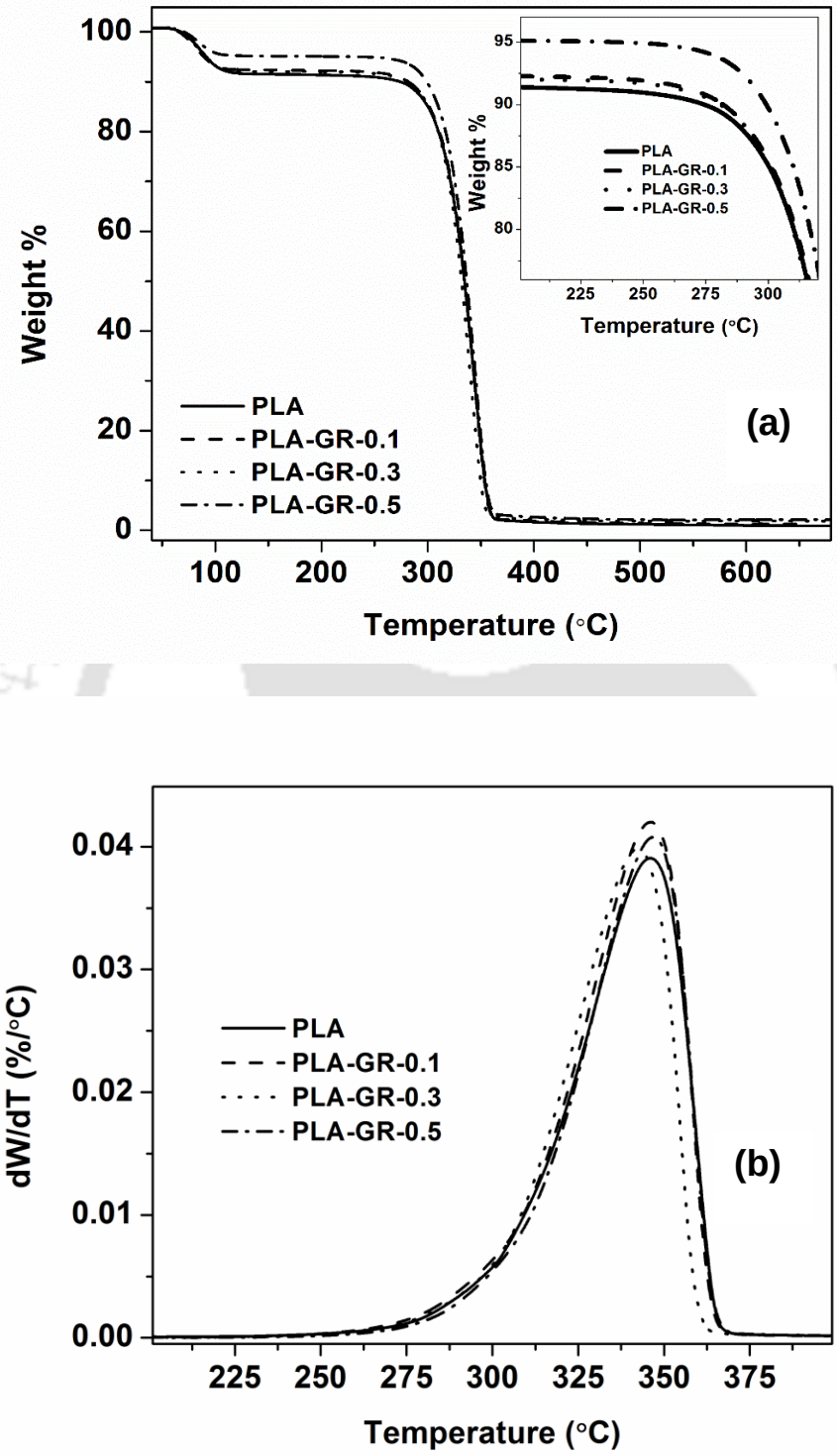

Figure 2.9. (a) TGA and (b) DTG curves of neat PLA and PLA-GR composites

Table 2.3. TGA and DTG results for PLA and PLA-GR composites

S:No	Sample name	$T_{10\%}$ (°C)	$T_{50\%}$ (°C)	T_{max} (°C)
1	PLA	268	333	345
2	PLA-GR-0.1	278	334	346
3	PLA-GR-0.3	283	334	346
4	PLA-GR-0.5	299	337	347

2.4.3.5. DSC analysis

Non-isothermal cold and melt crystallization behavior of PLA and PLA-GR composites were investigated using DSC analysis. DSC second heating thermographs of neat PLA and PLA composites are shown in Figure 2.10. The positive effect of reinforced nanofiller on the crystalline properties of PLA can be observed from the Table 2.4. The unimodal endothermic peak (Figure. 2.10) can be seen in the melting region of PLA (T_m=149 °C), which reveals the *α*-crystalline form of PLA (**Peng et al., 2011; Saiwai et al., 2003; Hoogsteen et al., 1990**). This unimodal endotherm peak indicates the absence of heterogeneous distribution of crystals and uniform crystal thickness developed after reinforcement of GR due to the melting of stable crystals of PLA formed (**Yu et al., 2003; Peng et al., 2011; Saiwai et al., 2003; Hoogsteen et al., 1990**). The addition of GR in the PLA matrix increases the T_m value by 4-5 °C due to the fact that the reinforced nanofiller reduces the critical nucleus size required for the formation of a thick and stable crystal in PLA. Besides, the shift in T_m indicates that the addition of the GR does not lower the molecular weight of PLA. The current result signifies that the GR acts as a better nucleating agent by enhancing T_m.

In the present study, T_g for PLA composites does not change significantly in comparison with neat PLA. This indicates that the reinforcement of GR does not induce the formation of short chain PLA molecules (**Wang et al., 2005; Hoogsteen et al., 1990**). It is noticed that, all the composite samples display greater level of crystallinity (see Table 2.4). The neat PLA presents

a crystallinity of 6.5%, whereas an addition of GR up to 0.3 wt% in the PLA matrix exhibits enhanced crystallinity of 11.83% (Table 2.4). When the GR loading increases above 0.3 wt%, the level of crystallinity decreases slightly. This is probably due to aggregation and poorer dispersion of GR in the matrix. The improved PLA crystallinity with the addition of GR is significant due to the possibility of existence of the greater number of delaminated GR platelets, which can facilitate the PLA crystallization process.

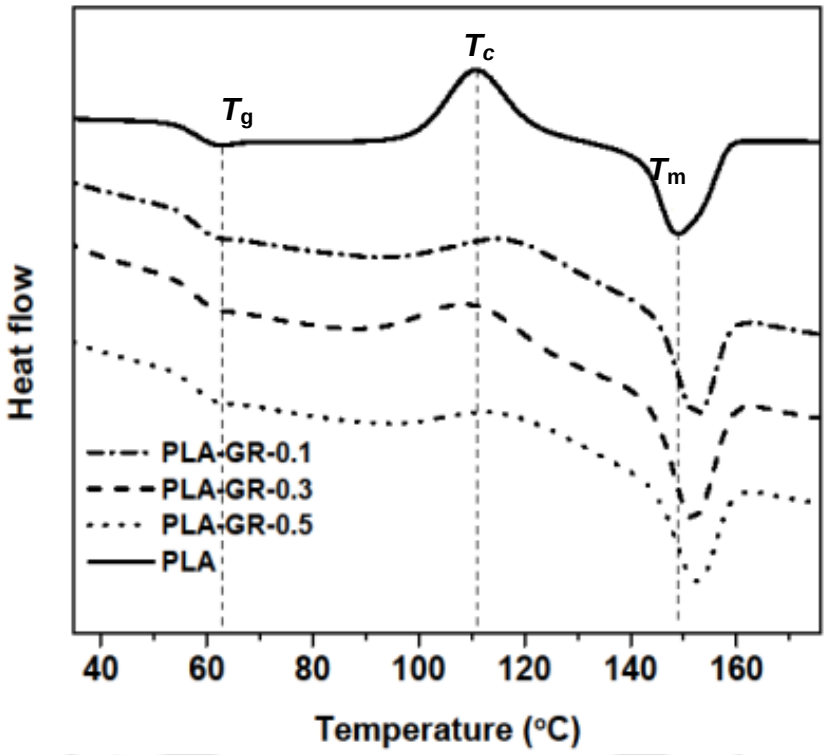

Figure 2.10. DSC second heating thermographs for PLA and PLA-GR composites at a heating rate of 5 °C/min

Table 2.4. DSC results for PLA and PLA-GR composites

Sample name	T_g (°C)	T_{cc} (°C)	T_m (°C)	T_{mc} (°C)	ΔH_{cc} (J/g)	ΔH_m (J/g)	X_c (%)
PLA	62	110	148	-	13.7	19.80	6.5
PLA-GR-0.1	63	114	152	100	6.63	15.04	8.98
PLA-GR-0.3	64	113	152.8	101	7.80	18.84	11.83
PLA-GR-0.5	64	110	152.6	101	4.84	14.17	10.01

T_g = Glass transition temperature, T_{cc} = Cold crystallization temperature, T_m = Melting temperature, T_{mc} Melt crystallization temperature, ΔH_{cc} = Enthalpy of cold crystallization, ΔH_m = Enthalpy of melting, X_c = crystallinity (%).

2.4.3.6. Transparency

The transmission of both visible light and ultraviolet radiation (200-700 nm) is considered as important parameters in designing the packaging materials for specific applications. The photochemical degradation of plastics occurs when exposed to high energy radiation called as UV-B (315-280 nm). Deterioration of food products that are sensitive to visible light takes place in the wavelength region of 400-700 nm (**Chen et al., 2008; Auras et al., 2004**). Conventional plastics like polyethylene terephthalate (PET), occupy a principal position in the packaging sectors, because the above mentioned wavelength range cannot transmit through this polymeric material (**Auras et al., 2004; Hernandez et al., 2009**). In the wavelength region of 200-700 nm, 72% transmission of light through PLA films is noticed as shown in Figure 2.11. This specifies that most of the UV-B and visible radiation pass through PLA films. After reinforcement of GR in the PLA matrix, the transparency of PLA films declines with an increase in the loading of GR (wt %). For the PLA-GR-0.5 sample, maximum reduction in the transparency is 53% in comparison with neat PLA. This is an advantage provided by GR filler, such that the PLA-GR composite films can find application in the storage of food products containing light sensitive materials such as lipids, flavors, vitamins, and pigments. The contact transparency images for PLA and PLA-

SP composites are illustrated in Figure 2.11 (b). At higher loadings of GR (0.5 wt%), the contact transparency of the composites is reduced as compared with neat PLA.

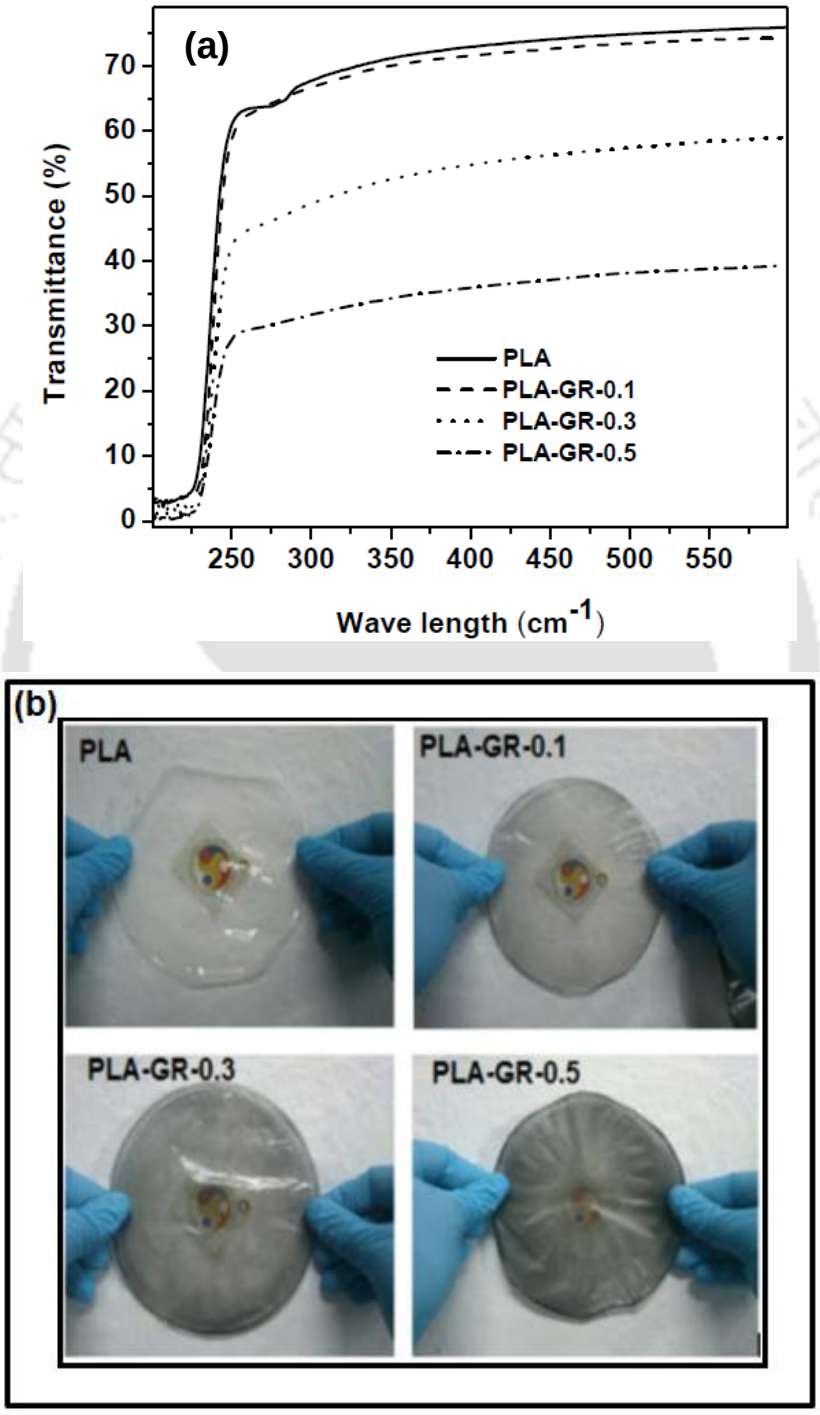

Figure 2.11. (a) Transparency measurements and (b) contact transparency for PLA and PLA-GR composites

2.4.3.7. Mechanical properties

The tensile strength and elongation-at-break (%) for PLA and PLA-GR composites are presented in Figure 2.12. The tensile strength of the PLA-GR composites is found to be higher for 0.1 wt% loading (40 MPa) of GR when compared with neat PLA (33 MPa). The PLA-GR-0.1 composite exhibits the highest tensile strength of 40 MPa as compared to PLA-GR-0.3 (37 MPa) and PLA-GR-0.5 (31 MPa). The gradual decline in the tensile strength values for further loadings explicates that addition as well as dispersion of GR in the PLA matrix are the dominant factors to enhance the mechanical properties. Therefore, it is clear that noticeable aggregation and the quality of dispersion become inferior at higher loading of GR (>0.1%). As a result, a slight decrease in tensile strength is observed for the PLA composites. The improved tensile strength of the PLA-GR-0.1 sample is an indication of good adhesion between PLA and the filler. It also reveals that the stress applied is transferred from PLA matrix to the GR. The elongation at break value obtained for 0.1 wt% of GR content is 51%, which is higher than that of neat PLA. This implies that the ductility of PLA is effectively improved with the incorporation of GR. GR acts as a bridge to prolong the fracture process of PLA composites and thereby reduces the sudden risk of failure. At further loadings of GR (0.3 and 0.5 wt%), elongation at break values display the downturn of around ~41% and 45%, respectively. This is because, defects induced by the agglomeration of GR sheets account for greater brittleness of the PLA matrix. However, GR reinforced in the PLA matrix demonstrates a positive impact on the tensile strength as well as elongation at break properties at lower GR loadings (0.1 wt%) in comparison with the PLA-EG composites produced by **Murariu et al.** (**2010**). In their study, it was reported that the addition of EG in the PLA matrix showed a negative impact on the above properties at all the loadings (wt%) of EG due to the aggregation of graphene stacks. Hence, it is clear that the sonication process utilized in the present study to separate the graphene plays an effective role in enhancing the strength and ductility of the PLA composites.

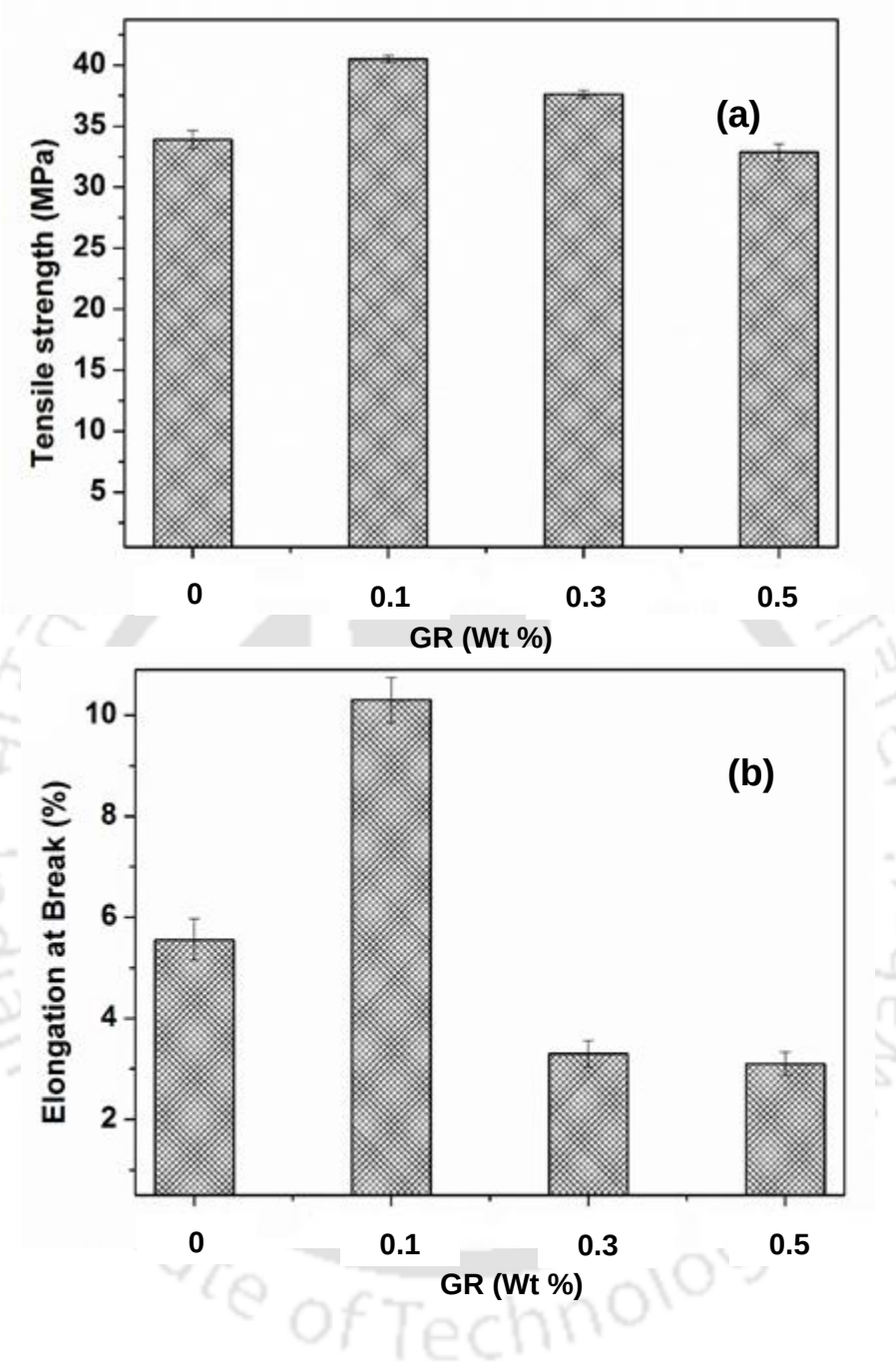

Figure 2.12. (a) Tensile strength and (b) elongation at break for PLA and PLA-GR nanocomposites

2.4.3.8. Film permeability

For semicrystalline polymers, like PLA, oxygen barrier characteristics are directed by permeation and diffusion of oxygen molecules through the amorphous phase of polymer film. To enhance the barrier properties of PLA, inclusion of impermeable barriers that reduces the gas permeation by creating the tortuous pathway is important. In the current investigation, the influence of graphene on inhibition of oxygen transport through PLA films is examined at various temperatures (25-45 °C) and the results are presented in Table 2.5. The permeation of oxygen is reduced by 22% (25 °C) after incorporating 0.1 wt% GR in the PLA matrix. This is attributed to the tortuous path effect generated by the exfoliated GR nanosheets, which hinders the oxygen transport in the PLA film. However, at higher loadings of GR, further improvement in oxygen permeation is not observed. This may be caused by the formation of GR aggregates at higher loadings. For both PLA and PLA-GR composite systems, oxygen permeation increases with increasing temperature, due to the fast diffusion of gas molecules through the PLA matrix at higher temperature. When 25 °C is taken as a point of comparison, 22% reduction in oxygen permeation is observed for PLA-GR-0.1 over neat PLA. At 45 °C, the oxygen permeation for PLA composite containing 0.1 wt% GR is reduced about 40%. This indicates that the addition of GR acts as an effective impermeable barrier for oxygen transport even at higher temperature.

Table 2.5. Effect of graphene content on oxygen permeability (OP) of PLA-GR composite films

Sample Name	Temperature (°C)	Oxygen permeability (cc mm/ m^2 day bar)	% Reduction in oxygen Permeability
PLA	25	23	-
	35	33	-
	45	51	-
PLA-GR-0.1	25	18	22
	35	22	33
	45	31	40
PLA-GR-0.3	25	20	13
	35	23	30
	45	35	32
PLA-GR-0.5	25	22	4
	35	30	9
	45	40	14

2.5. Conclusions

The optimum condition for thermal exfoliation of EG is determined as 750 °C. The formation of monolayer GR is verified by TEM analysis. No diffraction peak corresponding to graphene is observed from the XRD patterns of PLA-GR composites prepared with 30 min sonication due to exfoliation of GR in the PLA matrix. The TGA analysis reveals that the thermal stability of PLA-GR-0.5 composites improves about 31 °C when 10% weight loss is taken as a point of comparison. The presence of GR greatly improves the melting temperature of about 4-5 °C as well as the crystallization ability of PLA during the non-isothermal crystallization processes. This indicates that GR acts as an effective nucleating agent in enhancing the crystallization behavior of PLA. In the UV-B and visible radiation region (200-700 nm), 53% reduction in the transparency for PLA films is observed after reinforcement of GR. The tensile strength of PLA-GR composites is found to be maximum (40 MPa) for 0.1 wt% loading of GR in comparison with

neat PLA, which is an indication of good adhesion between PLA and the filler. The presence of GR in the PLA matrix reduces the oxygen permeation by 22% (25 °C) and 40% (45 °C).

CHAPTER 3

Synthesis and Characterization of Sucrose Palmitate Reinforced PLA Nanocomposites

This chapter investigates the use of a food additive, sucrose palmitate as eco-friendly filler for the fabrication of PLA based nanocomposites. TEM analysis reveals the uniform dispersion of SP filler in the PLA matrix. DSC and XRD results confirm that the incorporated biofiller acts as a nucleating agent and partially contributes towards the crystallinity of PLA-SP nanocomposites. Enhancement in the tensile strength and elongation at break up to 25% and 56% respectively is obtained. The best positive influence for the oxygen barrier is observed for the PLA-SP nanocomposite film where the reduction in oxygen permeability by 69% is achieved in comparison with neat PLA. This part of work has been published in ***Journal of Applied Polymer Science****, 2015, 132, 41320-41330.*

3.1. Introduction

In terms of food packaging applications, it is important to understand not only the physical and mechanical properties of filler materials, but also their compatibility with food during storage become a foremost pre-requisite factor (**Garlotta et al., 2001**). Hence, exploration of non-toxic substances approved for food contact needs to be prospected as fillers. Few attempts were made to produce PLA composite systems based on bio fillers that are non-toxic in nature (**Lu et al., 2009; Koutsomitopoulou et al., 2014; Fortunati et al., 2014; Bonilla et al., 2013; Fortunati et al., 2012; Lee et al., 2009; Zhu et al., 2012; Goriparthi et al., 2012; Wang et al., 2014**). The effect of different bio fillers such as starch (**Lu et al., 2009**), olive pit powder (**Koutsomitopoulou et al., 2014**), limonene (**Fortunati et al., 2014**), chitosan (**Bonilla et al., 2013**), cellulose nanocrystals (**Fortunati et al., 2012**), kenaf fibres (**Lee et al., 2009**), soy protein (**Zhu et al., 2012**), jute fibres (**Goriparthi et al., 2012**), cellulose actetate butyrate (**Wang et al., 2014**) on the thermal, mechanical and gas barrier properties of PLA are investigated. In this regard, U.S food and drug administration (FDA) approved food additive, sucrose palmitate (SP) is chosen as eco-friendly filler for the fabrication of PLA nanocomposites (**Corma et al., 2007**). Sucrose palmitate is nonionic as well as amphiphilic in nature, characterized by the presence of hydrophilic head (sugar) and hydrophobic tail (ester) moieties (**Corma et al., 2007**). Besides, SP being readily biodegradable and nontoxic, the antimicrobial, mechanical and barrier properties exhibited by the same make it ideal candidate for the storage of food (**Corma et al., 2007**). In general, the expected improvements in the final product are directly dependent on the dispersion of the nanoparticles in the polymer matrix which manipulate physical or chemical interaction between the matrix and the reinforcing phases. The optimization of dispersion and interactions of nanoparticles in polymer matrices plays a key role for the development of high quality nanocomposites. Therefore, the influence of the biofiller on

morphological, thermal, mechanical and barrier properties of PLA composites are examined in this chapter.

3.2. Experimental

3.2.1. Materials

Sucrose palmitate manufactured by Sisterna (Netherlands) was used as a filler material. Poly(lactic acid) (PLA) grade 2003D obtained from Nature Works® (USA) was used as a polymer matrix. Chloroform obtained from Merck (India) Ltd., was used as the solvent for fabrication of poly(lactic acid)-sucrose palmitate (PLA-SP) nanocomposites films.

3.2.2. Synthesis of PLA-SP composites

PLA-SP composites were fabricated by solution-casting method as follows: ~0.95 g of PLA was mixed in 50 mL of chloroform and subsequently the mixture was stirred for 2 h in order to completely dissolve the PLA. Likewise above, various concentrations of sucrose palmitate (1, 3, 5, 10, 15, 30 wt % with respect to PLA) was dispersed in chloroform with continuous stirring for 1 h. Subsequently, this solution containing dispersed SP was transferred into PLA-chloroform mixture under vigorous stirring. PLA-SP solution was casted on teflon petriplates and further dried under ambient condition for 24 h. The dried composite films were peeled off carefully from the petriplates. The resulting films were finally oven dried under vacuum for 12 h at 40°C and stored in airtight bags at room temperature for further characterizations. All the samples are designated as SP, PLA, PLA-SP-1, PLA-SP-3, PLA-SP-5, PLA-SP-10, PLA-SP-15 and PLA-SP-30 for sucrose palmitate, PLA, PLA/sucrose palmitate 1 (wt%), PLA/sucrose palmitate 3 (wt%), PLA/sucrose palmitate 5 (wt%), PLA/sucrose palmitate 10 (wt%), PLA/sucrose palmitate 15 (wt%) and PLA/sucrose palmitate 30 (wt%), respectively. The thickness of the fabricated films was measured using film thickness meter (Indi 1652). Twenty measurements were taken on each film and the average thickness of the films is found to be 60 ± 5 µm.

3.3. Characterization

3.3.1. Thermogravimetric analysis (TGA)

Thermogravimetric analysis was performed on a Mettler Toledo thermo gravimetric analyzer (TGA/SDTA 851® model). Samples (10.5± 0.3 mg) were placed in 900 µl crucible and heated from 25 to 700 °C in a 60 ml/min flow of N_2 at a heating rate of 20 °C/min.

3.3.2. Differential scanning calorimetry (DSC)

Thermal properties and crystallization behavior of PLA and PLA-SP nanocomposites were studied using a differential scanning calorimetry (Mettler Toledo-1 series). Samples (10±0.5 mg) were hermetically sealed in aluminum pans and heated from 25 to 180 °C at a heating rate of 5 °C/min in an inert atmosphere (N_2 flow, 50 mL/min). All the samples were first heated from 25 to 180 °C and held at this temperature for 5 min to eliminate the effect of the thermal and processing history. Glass transition temperature (T_g), cold crystallization temperature (T_{cc}), the enthalpy change at T_{cc} (ΔH_{cc}), melting temperature (T_m) and the enthalpy of fusion at T_m (ΔH_m) of pure PLA and nanocomposites films were determined from the DSC thermograph during second heating cycle. The T_g was obtained from the midpoint of heat changes from the DSC curves. The percentage crystallinity (% X_c) of PLA was calculated according to the following relation (**Garlotta et al., 2001**).

$$\%X_c = \frac{\left(\Delta H_m - \Delta H_{cc}\right)}{\left(\Delta H_{mp}\right)} \times 100 \qquad (3.1)$$

Where, ΔH_m is enthalpy of fusion at melting temperature T_m, ΔH_{cc} is the enthalpy of fusion at cold crystallization temperature T_{cc}. ΔH_{mp} is the heat of fusion of a perfect PLA crystal which is 93.6 J/g (**Garlotta et al., 2001**).

3.3.3. X-ray diffraction analysis (XRD)

XRD analysis of neat PLA and its nanocomposite films was carried out under air atmosphere at room temperature on a Bruker A8 advance instrument using Cu-Kα (λ= 0.15406 nm) radiation operating at 40 kV and 40 mA. The diffraction data were recorded in the 2θ range of 1 - 50° with a scanning rate of 0.05° s^{-1} and 0.5 s step size**.**

3.3.4. Fourier transform infrared spectroscopy (FTIR)

FT-IR spectra for pure PLA and composite films were recorded between 4000 and 450 cm^{-1} region using spectroscopic quality KBr powder with a Shimadzu IR affinity-1 model spectrometer.

3.3.5. Morphological analyses

The dispersion of SP in PLA matrix was visually observed using transmission electron microscopy (JEOLJEM 2100), operated at 200kV. By direct casting of polymer composite solution over the carbon-coated copper TEM grid, images of the nanocomposite were obtained. The morphology of SP and dispersion of SP in the PLA matrix was pictoriated using field-emission scanning electron microscopy (FESEM) (Zeiss Sigma model).

3.3.6. UV-visible spectrophotometry

Transparency measurements were carried out using a UV-Visible spectrophotometer (Make: Perkin Elmer, Model: Lambda 35). The wavelength range for the measurements was varied between 200-600 nm with a scan rate of 50 nm/min and a spectral bandwidth of 2 nm.

3.3.7. Mechanical testing

The uni-axial tensile properties (modulus, tensile strength, elongation at break) were measured at room temperature with a 50 kN load cell on a tensile tester. The cross -head speed was set at

5 mm/min. Specimens used in this method were prepared according to ASTM standard D 882-12. Three specimens of each sample were tested and the average results were reported.

3.3.8. Oxygen permeability measurements

The oxygen permeability of PLA and PLA-SP composites was measured using a PBI-Dansensor (Ringsted, Denmark) OPT 5000 oxygen permeability tester at 23±0.03 °C and 50±2% relative humidity. Dry nitrogen containing less than 0.1 ppm oxygen (Alphagaz 2, Air-Liquid Denmark, Ballerup, Denmark) was used as carrier gas and 99.995% pure oxygen (Air-Liquid Denmark) was used as a test gas. Inlet pressure was maintained at ~ 4 Kg/cm^2. At least three replicate tests were performed for each samples.

3.4. Results and discussion

3.4.1. Thermogravimetric analysis

Thermo graphs shown in Figure 3.1(a) indicate the weight loss profile in two stages: first stage of weight loss ~100 °C is due to evaporation of adsorbed moisture. The second stage of thermal degradation process of PLA that occurs in the temperature regime of 300-375 °C can be mainly due to intra-molecular trans-esterification (backbitting reaction) (**Garlotta et al., 2001; Fan et al., 2004; Taubner et al., 2001; Wang et al., 2005; Wang et al., 2008; Yu et al., 2003**). From the TGA profiles, the onset of degradation (T_{onset}) that corresponds to 10 wt% loss is determined by extrapolating the peak of degradation of the samples. Similar to neat PLA, PLA-SP composites also exhibit two stages of degradation. When 10% weight loss is taken as a point of comparison, T_{onset} of the composites for PLA is 301 °C and it declines to 288 °C for 1 wt % of SP content. As the SP content increases from 3 to 10 wt%, T_{onset} reduces from 278 to 249 °C (see Table 3.1). The possible reason is the contribution of thermal decomposition profile of SP. It can be observed from the TGA curves that SP is thermally stable up to 180 °C. Hence, with increasing the concentration of SP content in the PLA matrix, sucrose content also increases in

turn leading to early onset degradation of PLA composites. However, thermal decomposition of SP occurs via three stages. First stage of thermal degradation is due to the adsorbed moisture. The second region of weight loss observed from 180-240 °C reflects splitting of glycosidic bridge between glucose and fructose groups present in the sucrose (**Hosseini et al., 2005; Predoi et al., 2010**). The third region of weight loss of SP observed at 240 °C corresponds to the decomposition of ester groups present in the palmitate tail (**Fang et al., 2011; Li et al., 2009**).

The decomposition temperatures at 50% weight loss for neat PLA, 1, 3, 5, and 10 wt% PLA-SP composites are 348, 347, 336, and 316 °C, respectively (see Table 3.1). The temperature of 50% weight loss of PLA is comparable with PLA composites (SP: 1 wt % and 3 wt %). In rest of the composites, a considerable difference in weight loss can be seen. This is because of the excess water released during sucrose hydrolysis that induces autocatalytic cleavage of ester groups (**Antheunis et al., 2010; Janorkar et al., 2004**). Another important thermal property is the temperature corresponding to the maximum rate of weight loss ($T_{max.}$), which is defined as the peak value of the first derivative of the TGA curve. The first derivative curves for SP, neat PLA, and PLA-SP composites are depicted in Figure 3.1(b). All the samples (neat PLA and PLA composites) demonstrate a single peak in the DTG curves indicating that the main degradation of these materials proceed in one step. It can be noticed that there is no change in the $T_{max.}$ value (357 °C) for neat PLA and its composites (up to 5 wt% of SP loading). In the case of 10 wt% of SP reinforcement in the PLA matrix, $T_{max.}$ shifts to lower temperature (324 °C) (see Table 3.1). The downturn exhibited is probably due to the increased acidic sites created during the degradation of higher loadings of SP in the PLA matrix (**Janorkar et al., 2004; Kelly et al., 1978**). Moreover, it can be observed from Figure 3.1(a and b), the thermal stability of PLA-SP-10 is drastically reduced in comparison with PLA-SP-5. Hence, PLA-SP-5 is considered as optimum loading and further characterizations are carried out only up to 5 wt% SP loading.

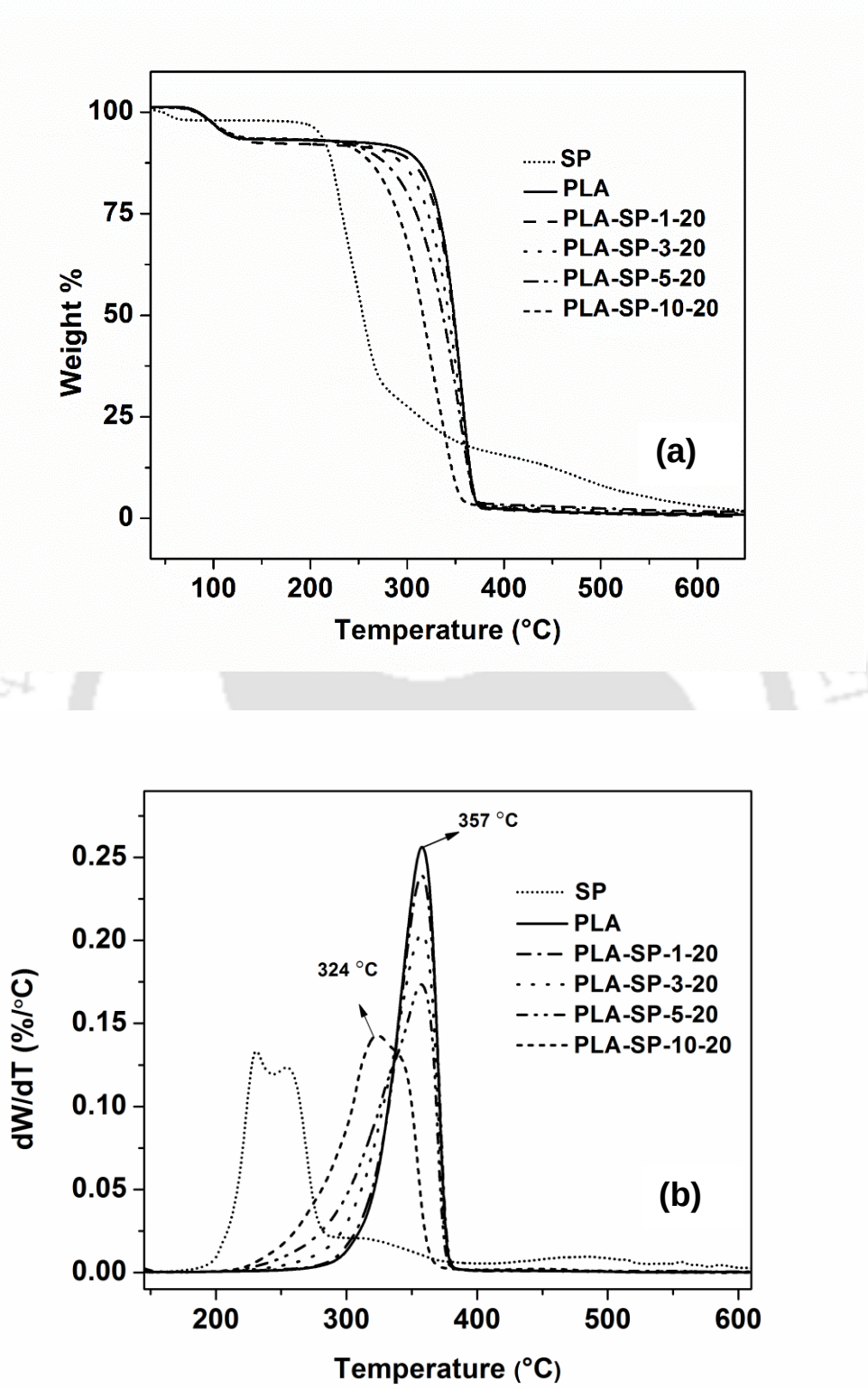

Figure 3.1. (a) TGA curves and (b) DTG curves for SP, PLA and PLA-SP composites

Table 3.1. TGA and DTG results for PLA and PLA-SP composites

S:No	Sample name	$T_{10\%}$ (°C)	$T_{50\%}$ (°C)	T_{max} (°C)
1	SP	219	254	244
2	PLA	301	348	357
3	PLA-SP-1	288	347	357
4	PLA-SP-3	278	343	357
5	PLA-SP-5	261	336	357
6	PLA-SP-10	249	316	324

3.4.2. Differential scanning calorimetry

DSC analysis is carried out to evaluate crystallization and melting behaviors of PLA and PLA-SP composites. DSC second heating thermographs of neat PLA and PLA nanocomposites are shown in Figure 3.2. In the present study, the influence of addition of nano biofiller (SP) on the crystalline morphology of PLA is slightly positive effect, which can be seen from Table 3.2. The melting region of PLA provides unimodal endothermic peak, (T_m=149 °C), which indicates the presence of PLA in *α*-crystalline form (**Ravi et al., 2014**). Incorporation of the biofiller does not result in bimodal endothermic melting peaks for PLA nanocomposites (see Figure.3.2). Unimodal endotherms reveal the melting of stable crystals of PLA formed due to the absence of heterogeneous distribution of the crystals as well as uniform crystal thickness developed in PLA after reinforcement of the SP filler (**Bharadwaj et al., 2006**). Addition of biofiller in PLA matrix shifts T_m to slightly higher value. The shift in T_m indicates that the addition of the SP filler did not lower the molecular weight of PLA. The current result specifies that the SP acts as a better nucleating agent by enhancing the T_m, in contrast to the recently reported reinforcements such as organically modified montmorillonite (MMT-TAC) (**Wang et al., 2012**), nickel-containing layered double hydroxides (LDH) (**Shan et al., 2012**) and nanoclay (**Vasanthan et al., 2011**), used for developing PLA composites. The decrease in the T_m values of about ~6, 8, 1, and 3 °C, is reported for the respective fillers in comparison with neat PLA. The reduction in the heat of

fusion for melting peaks is observed when the SP content increases. This phenomenon is attributed to the strong hydrogen bonding interaction between SP and PLA (**Ali et al., 2011**).

Several studies reported that lower values of T_g for PLA composites could be attributed to the presence of short chain molecules due to filler induced PLA degradation and reduced macromolecular interactions (**Peng et al., 2011; Liu et al., 2009**). Interestingly, in the present study, T_g (61 °C) remains unaltered for the PLA composites indicating that the reinforcement of SP does not induce the formation of short chain PLA molecules. Because nanocomposite films are prepared by solution casting techniques at room temperature instead of melt extrusion where degradation generally occurs if the material exposed for longer time. It can be seen from the DSC curves that in comparison with neat PLA, the cold crystallization temperature (T_{cc}) increases significantly by 6, 14, 14 °C for 1, 3, 5 wt% loading of SP, respectively. The increase in T_{cc} is due to the fact that the addition of SP suppresses the diffusion rate leading to the slower migration of the polymer chains to the surface of the nucleus (**Katiyar et al., 2010, Zhang et al., 2012**). The higher T_{cc} values with broadening of its peak width obtained for the composites signify that the crystallization rate becomes slower than that of neat PLA; both homogeneous and heterogeneous crystallization take place within the composites (**Katiyar et al., 2010**). The increase in T_{cc} could be further considered due to the nucleation effect of SP incorporated in the PLA matrix (**Goffin et al., 2011**). Another reason for enhancement in the crystallization temperature for the PLA composites may be the formation of ordered *α*-form of PLA crystals during cold crystallization process (**Pan et al., 2012**).

DSC analysis of nanocomposite films provides data on ΔH_{cc} and $\Delta H_{m,}$ from which useful insight into interactions between PLA and SP can be inferred (**Ali et al., 2011**). It is noticed from Table 3.2, that ΔH_{cc} and ΔH_m for PLA-SP-1 are slightly higher in comparison with neat PLA. This is indicative of stable crystals of PLA formed during crystallization process and hence, slight enhancement in the percentage crystallinity is observed for 1 wt% SP incorporation. In contrast,

ΔH_{cc} and ΔH_m gradually decreases with further increase in the SP content, which is due to the melting of PLA crystallites (**Zeng et al., 2011**). Due to this fact, at higher loadings, despite of enhancement in crystallization temperature, crystallization peaks are broaden leading to decrease in percentage crystallinity when compared with 1 wt% loading of SP. DSC results reveal that there is a slight improvement in the crystallinity of the PLA at very low concentration of SP.

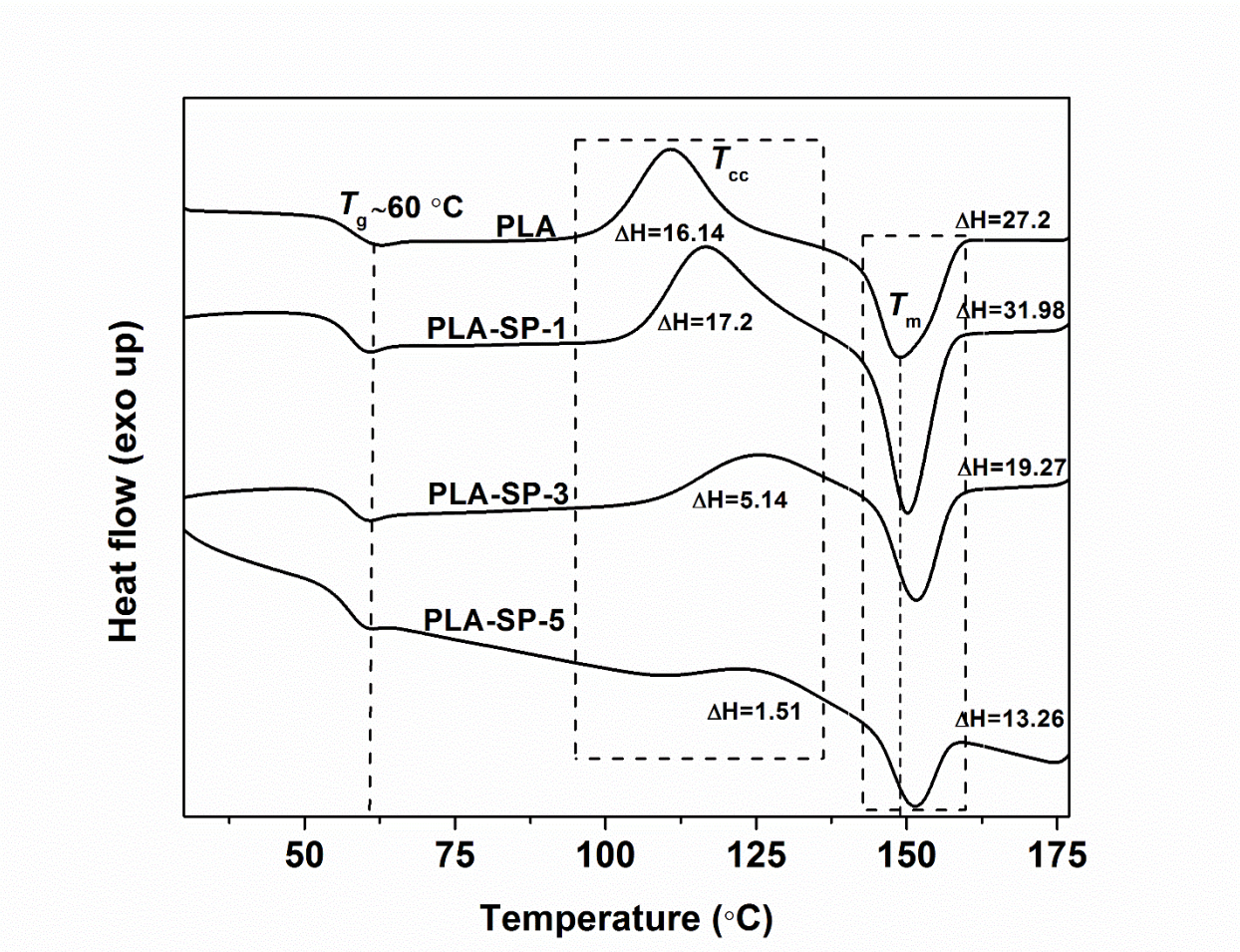

Figure 3.2. DSC second heating curves for PLA and PLA-SP composites at the heating rate of 5 °C/min

Table 3.2. DSC results for PLA and PLA-SP composites

S:No	Sample	T_g (°C)	T_{cc} (°C)	T_m (°C)	ΔH_c (J/g)	ΔH_m (J/g)	X_c (%)
1	PLA	61	110	149	16.14	27.20	~12
2	PLA-SP-1	60	117	150	17.20	31.98	~16
3	PLA-SP-3	60	125	152	5.14	19.27	~15
4	PLA-SP-5	60	125	152	1.51	13.16	~12

3.4.3. XRD analysis

XRD analysis as shown in Figure 3.3 was performed to understand the addition of SP on the crystalline structure of PLA. The crystal structure of PLA has been the topic of extensive studies. In general, depending on the preparation conditions, two crystal structures may be obtained for PLA: a pseudoorthorhombic *α*-structure and a less stable *β*-orthorhombic structure (**Krikorian et al., 2003**). The structural analysis of neat PLA displays the most intense peak at 2θ =16.7° corresponding to the reflections from (1 1 0) and/or (2 0 0) planes of orthorhombic *α*-crystalline phase. The less intense peaks appeared at 2θ =15.1°, 19.1° and 21.5° are from the (0 1 0), (2 0 3) and (2 1 0) planes of *α*-phase, respectively (**Zhang et al., 2012; Barrau et al., 2011**). The PLA diffraction pattern presented herein matches closely with the *α*-crystalline structure. XRD analysis of SP shows a sharp intense crystalline peak at 2θ =2.27°, corresponding to the palmitate ester tail present in the biofiller. The less intense diffraction peaks at 4.53° and 22.4° are attributed to the head group of sucrose palmitate (**Fang et al., 2011**).

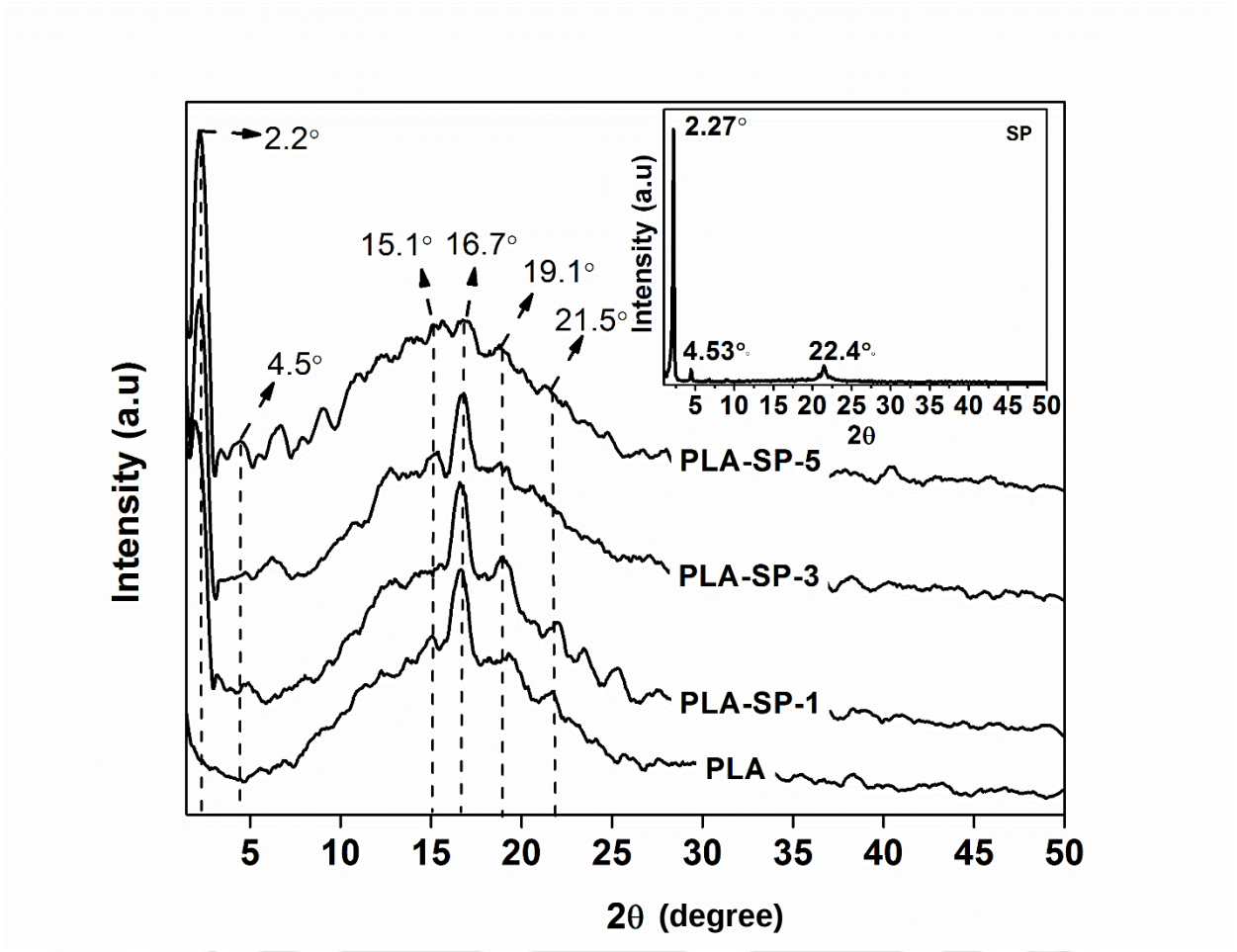

Figure 3.3. XRD patterns of SP, PLA and PLA-SP composites

The nanocomposite diffraction intensities are vertically offset for clarity of presentation. The peak at 2θ =4.53° corresponding to the head group of sucrose palmitate is not identified at low SP content, due to their relatively low concentration of SP in the PLA composites. The intensity of the crystalline peak corresponding to the palmitate ester group increases with an increase in the SP concentration. This increased intensity is due to the more diffracted X-rays from the dispersion of the additional reinforcing agent in the PLA matrix (**Barrau et al., 2011**). For all the nanocomposites, the peak position (2θ =16.7°) corresponding to the crystal structure of PLA is not altered. It is clear that lattice parameters are not altered by the addition of SP (**Desantis et**

al., 1968; Brizzolara et al., 1996; Hoogsteen et al., 1990). The reflection representing the crystal structure of PLA is present in all the bio-nanocomposite indicating that the incorporation of SP is not significantly disrupted the crystal structure within the PLA matrix (**Desantis et al., 1968; Brizzolara et al., 1996; Hoogsteen et al., 1990**). However, it can be seen from Figure 3.3 that the intensity of the peak (2θ= 16.7°) corresponding to the crystal structure of PLA increases for the PLA-SP-1 sample. This supports the increase in amount of crystallinity (**Krikorian et al., 2003**) as discussed in DSC analysis. The presence of a shoulder at around 2θ =19.1° for PLA-SP nanocomposite elucidates that SP has the ability to act as a nucleating agent, by increasing the crystallinity of the composite system (**Fortunati et al., 2012**).

3.4.4. Morphology of PLA nanocomposite films

The morphological feature of SP is examined by FE-SEM as depicted in Figure 3.4(a). The images reveal that the SP exhibits a plate-like structure. The dispersed SP platelets (1 wt%) within PLA matrix can also be seen from TEM micrographs in Figure 3.4(b and c). The presence of SP in the PLA matrix is shown by circle. The average particle size of the reinforced SP in the PLA matrix is found to be 50.84±11.98 nm. In the TEM micrograph, the sheet-like particles (dark portion indicated in circles) represent the bio-filler, SP and the bright areas represent the PLA matrix. The appearance of homogeneously dispersed SP in the composite system is visualized from the TEM image. The uniform dispersion of SP in the PLA matrix can also be observed from the FE-SEM images for PLA and PLA-SP nanocomposites as shown in Figure 3.5. It is indicative from the FE-SEM image (inset) pictoriated at higher magnification for PLA-SP-5 nanocomposites that plate like structure of SP filler is homogenously dispersed in the PLA matrix without agglomeration.

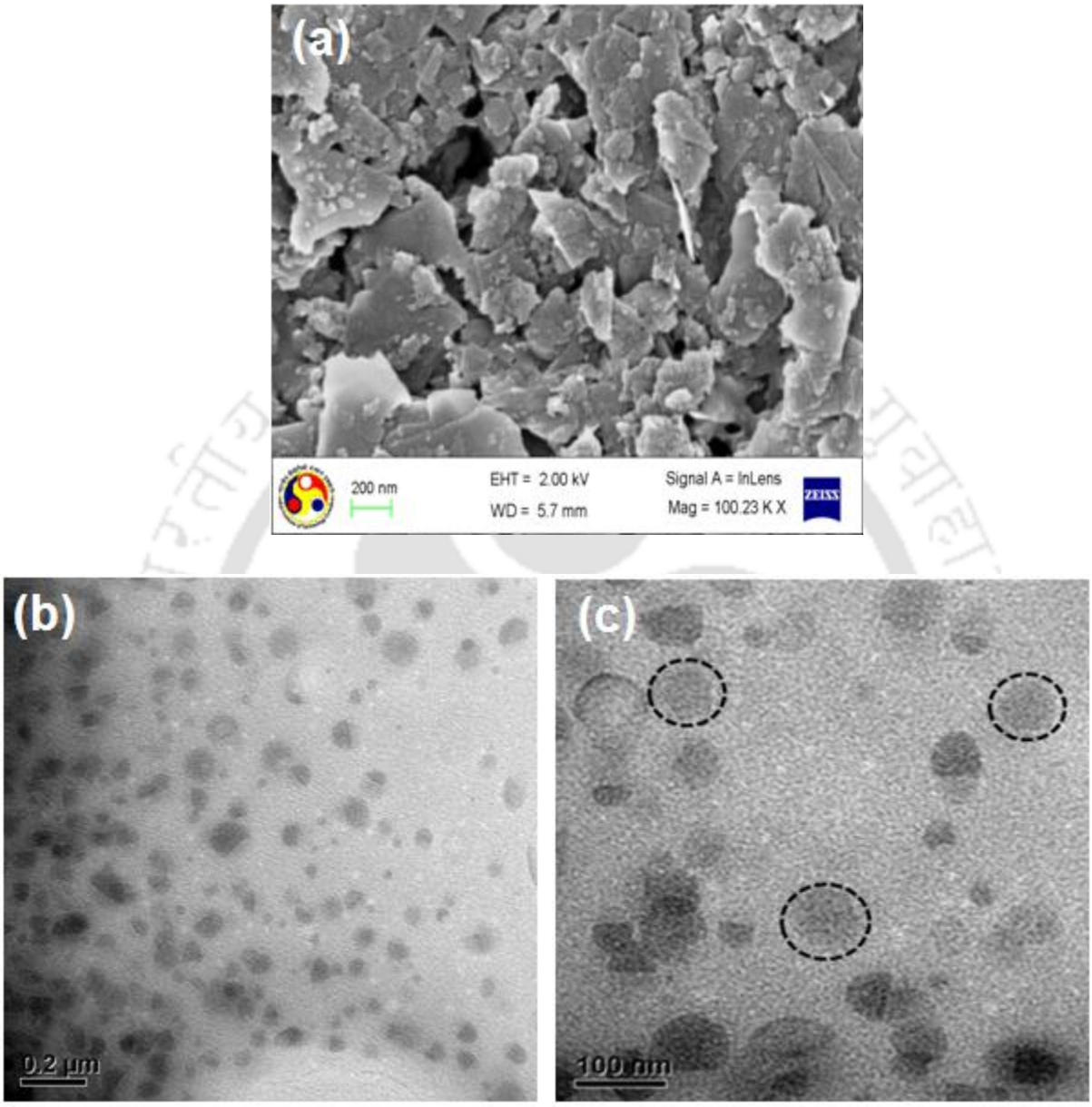

Figure 3.4. FESEM images of SP (a) and TEM images of PLA-SP-1 at different magnifications (b, c)

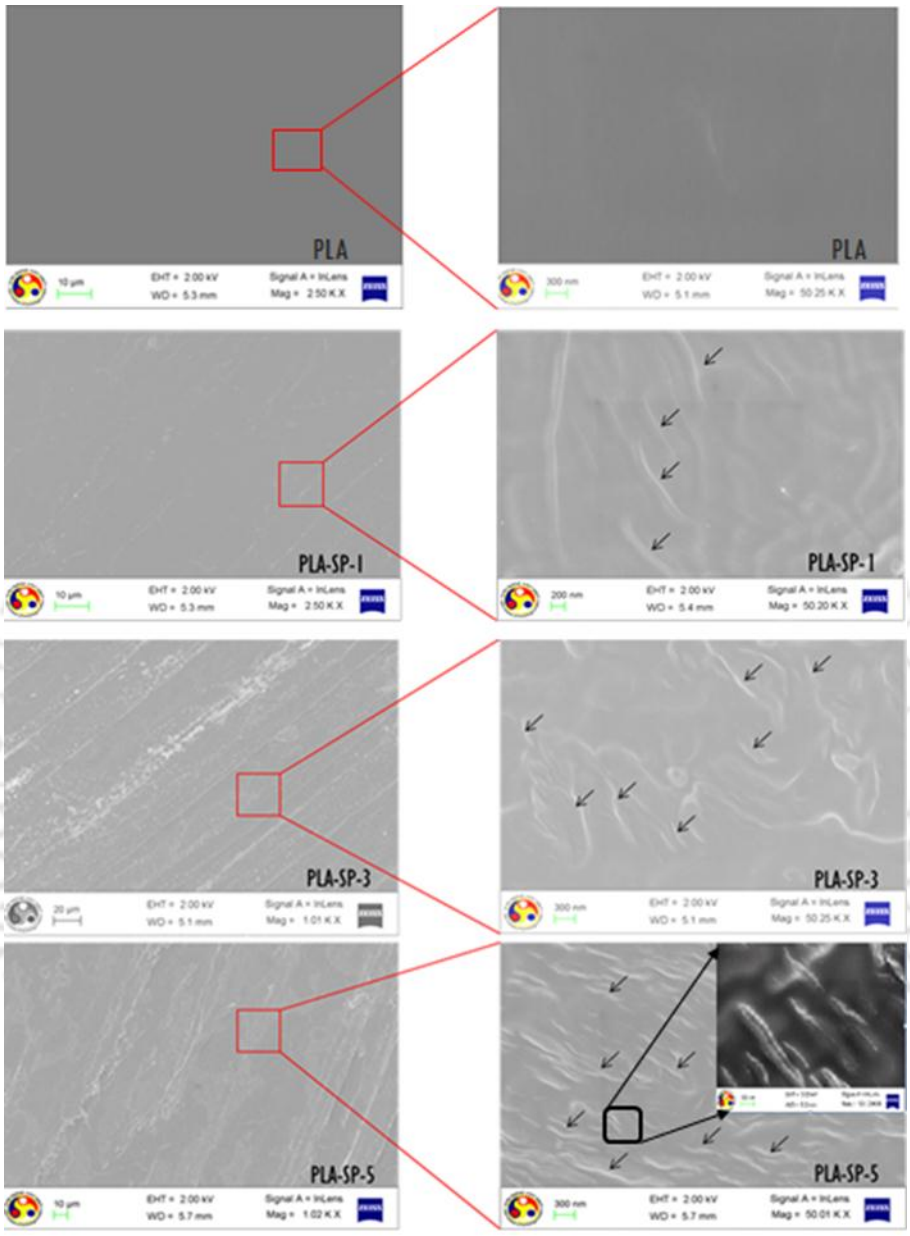

Figure 3.5. FE-SEM images of PLA and PLA-SP nanocomposites

3.4.5. Transparency

From Figure. 3.6 (a), it can be observed that, 63% (at 250 nm) and 66% (at 300 nm) of UV light are transmitted in the neat PLA film, respectively. This indicates that most of the UV-B radiation (315-280nm) passes through PLA film (**Auras et al., 2004; Hernandez et al., 2009**). In case of PLA-SP-5 nanocomposite film, the reduction in the UV-B transmittance of 32% and 30% at 250 and 300 nm, respectively, is noticed in comparison with neat PLA. At 575 nm, the visible light transmittance for neat PLA, and PLA-SP-5 films is observed to be 72% and 63%, respectively which is 12.5% reduction in transmittance when compared with neat PLA. This is an advantage provided by SP filler, such that the optical clarity remains very close to that of the neat PLA film, with only a slight decrease in transparency with an increase in SP (wt%) loadings. The contact transparency images for PLA and PLA-SP composites are also illustrated in Figure 3.6 (b). As observed, all the PLA-composite films illustrate almost a similar contact transparency in comparison with neat PLA. This observation specifies that there exists a better compatibility between the filler and PLA matrix (**Sun et al., 2012**).

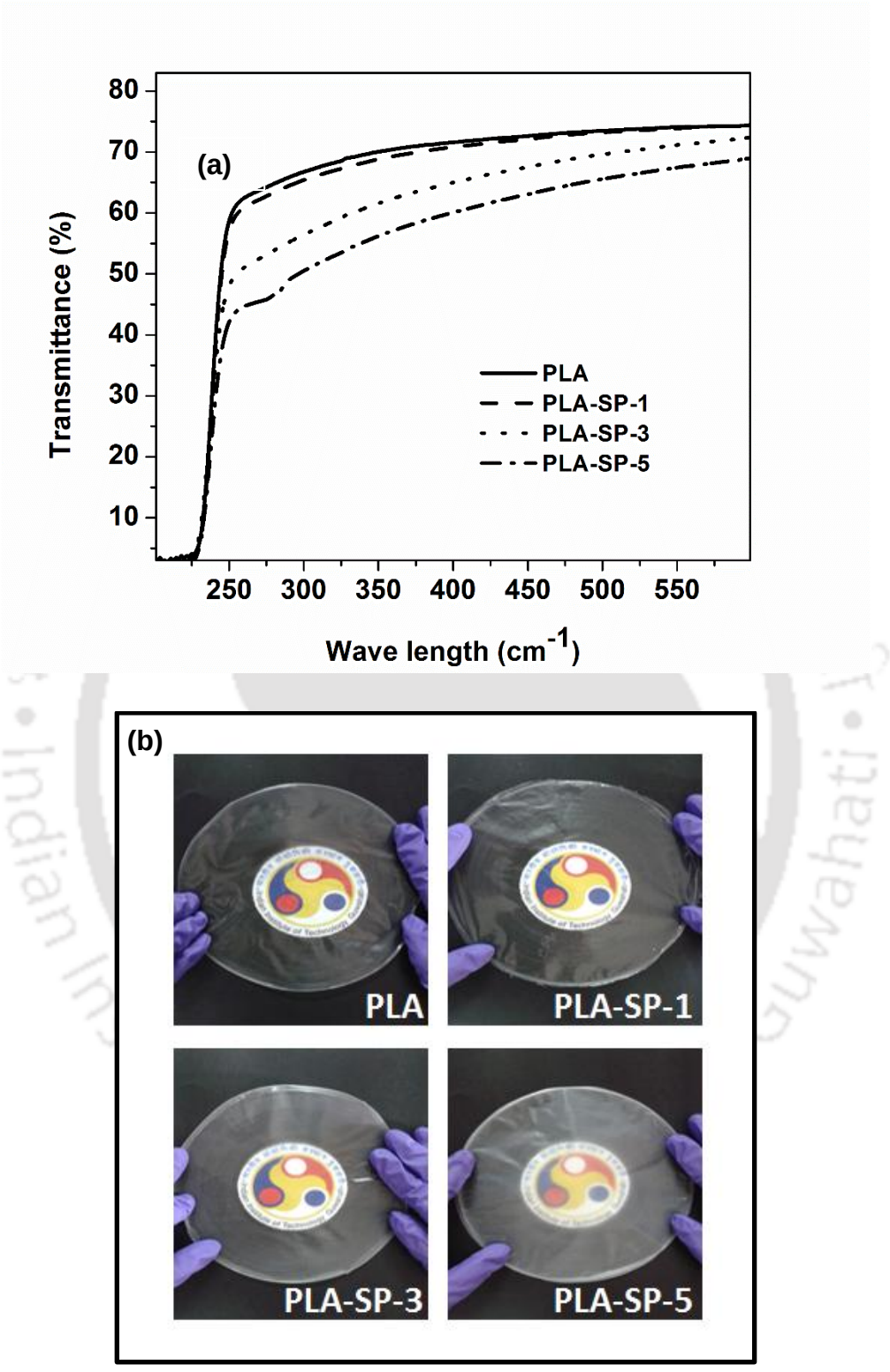

Figure 3.6. (a) Transparency measurements and (b) Contact transparency images for PLA and PLA-SP composites

3.4.6. Fourier transform infrared spectroscopy

Figure 3.7 depicts the FTIR spectra of SP, PLA and PLA-SP composites. In the case of PLA, a band observed around 3500 cm^{-1} corresponds to the stretching of hydroxyl groups present as end group in PLA backbone (**Vasanthan et al., 2011**). The strong bands at 3000 and 2937 cm^{-1} correspond to the asymmetric and symmetric mode of C-H stretching, respectively. An absorption band present in the region of 1700-1800 cm^{-1} is attributed to the carbonyl group present in the ester linkage of the PLA matrix (**Pamula et al., 2001**). The existence of CH_3 band in the PLA is characterized by the presence of peak at 1456 cm^{-1}. The appearance of band at 1386 cm^{-1} is assigned to the C-H deformation (**Pamula et al., 2001**). The band present around 1083 cm^{-1} is due to the C-O asymmetric stretching of ester groups (**Mai et al., 2012**). The stretching frequency observed at 956 and 922 cm^{-1} is mainly attributed to the rocking mode of CH_3 (**Vasanthan et al., 2011; Pamula et al., 2001; Mai et al., 2012**). In the FTIR spectrum of SP, the strong absorption band found in the region of 3500-3200 cm^{-1} characterizes the O-H stretching of the free hydroxyl groups of SP. The stretching bands at 2917 and 2845 cm^{-1} are assigned to the methylene and terminal methyl groups of palmitate chain of SP, respectively. The band at 1058 cm^{-1} corresponds to the C-O-C stretching vibration of SP (**Predoi et al., 2010; Bharadwaj et al., 2006**).

It can be observed from the FTIR spectra of PLA-SP nanocomposites that the hydroxyl region is exhibited in the range of 3600-3200 cm^{-1} upon addition of SP in the PLA matrix (**Grapnuer et al., 2008; Cheng et al., 2009**). When the carbonyl region (1700-1800 cm^{-1}) of PLA and PLA-SP composites are closely visualized, the corresponding peak become broadened and split into two small peaks (1753 and 1746 cm^{-1}) for PLA-SP composites. This reveals the existence of intermolecular interaction between PLA and SP (**Grapnuer et al., 2008; Cheng et al., 2009**). As the SP loading increases in the PLA matrix, the content of methylene and terminal methyl groups of palmitate in the PLA composites also increases. This fact is well revealed by the

increase in the intensity of the bands (2845 cm^{-1}) corresponding to terminal methyl groups of palmitate chain of SP (**Grapnuer et al., 2008; Cheng et al., 2009**). The increase in sharpness preceded by the decrease in broadness of the corresponding band region (3200-2800 cm^{-1}) in comparison with pure PLA also supports the above statement.

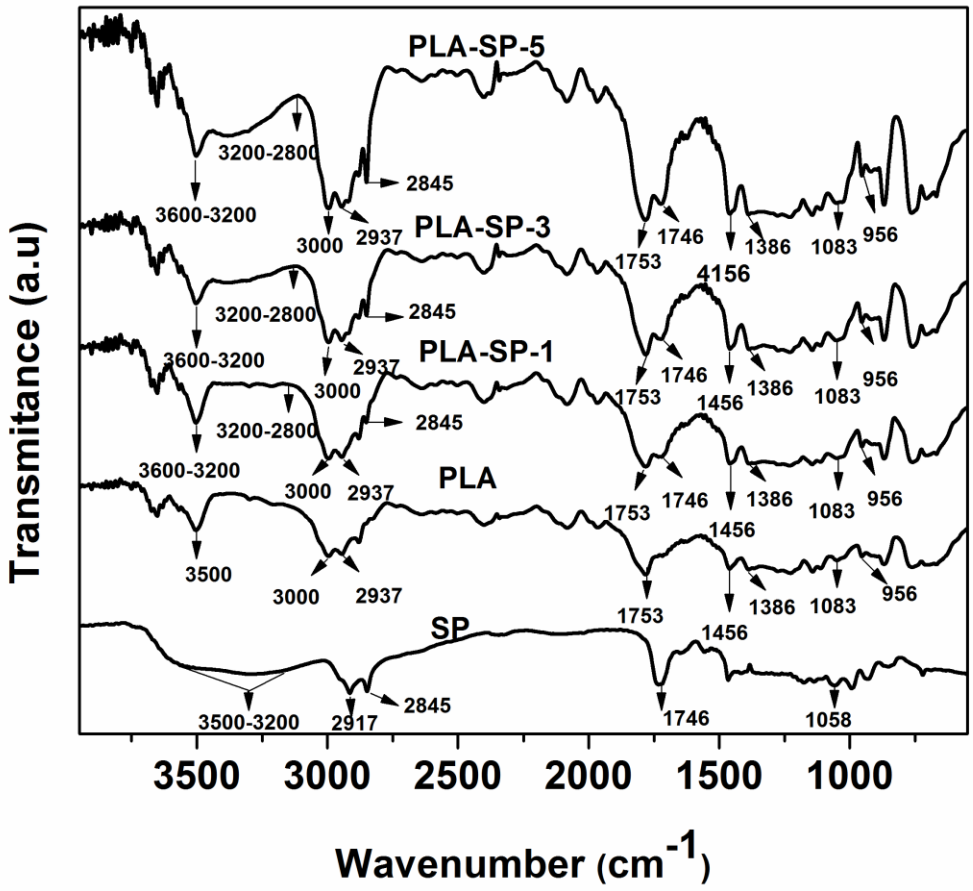

Figure 3.7. FTIR spectra of SP, PLA and PLA-SP composites

3.4.7. Mechanical properties

Figure 3.8 shows the effect of SP content on the mechanical properties of PLA matrix. It can be seen from Figure 3.8(a) that the tensile strength of PLA composites increases with an increase in the SP content. The PLA-SP-5 composite demonstrates a maximum tensile strength and modulus of 44 MPa, 2.2 GPa, respectively over neat PLA (tensile strength of 34 MPa and

modulus of 2 GPa). The addition of SP improves the tensile strength, which is an indication of good adhesion between PLA and the filler. The obtained results are consistent with results reported by **Graupner et al.** (**2008**) for PLA- cotton fiber composites. As can be seen from Figure 3.8(b), the incorporation of SP in the PLA matrix enhances the tensile modulus for PLA composites, indicating the reinforcing action of the filler. In comparison with neat PLA, the increased modulus of PLA-SP composites can also be associated with the restrictions of molecular mobility and deformability imposed by the presence of SP. Figure 3.8(c) shows the elongation at break of PLA and PLA-SP composites. The value obtained at 5 wt% of SP content is 56% higher than that of neat PLA. It implies that the ductility of PLA is effectively improved by the incorporation of SP. This behaviour is due to the plasticization effect provided by hydrophobic moieties of SP reinforced in the PLA matrix. The results also indicate that SP acts as a bridge to prolong the fracture process of PLA composites and thereby reduces the sudden risk of failure. Enhancement in the elongation at break values obtained in the present study is comparable to the PLA-chicken feather fiber composites (~55%) reported by **Cheng et al.** (**2009**). However, drop in the tensile strength and elongation at break (%) is also reported for PLA-starch (**Lu et al., 2009**) and PLA-soy protein (**Zhu et al., 2012**). It was discussed that both the tensile strength and elongation at break (%) of these composites decreased due to the lack of affinity between the filler and PLA (**Lu et al., 2009; Zhu et al., 2012**).

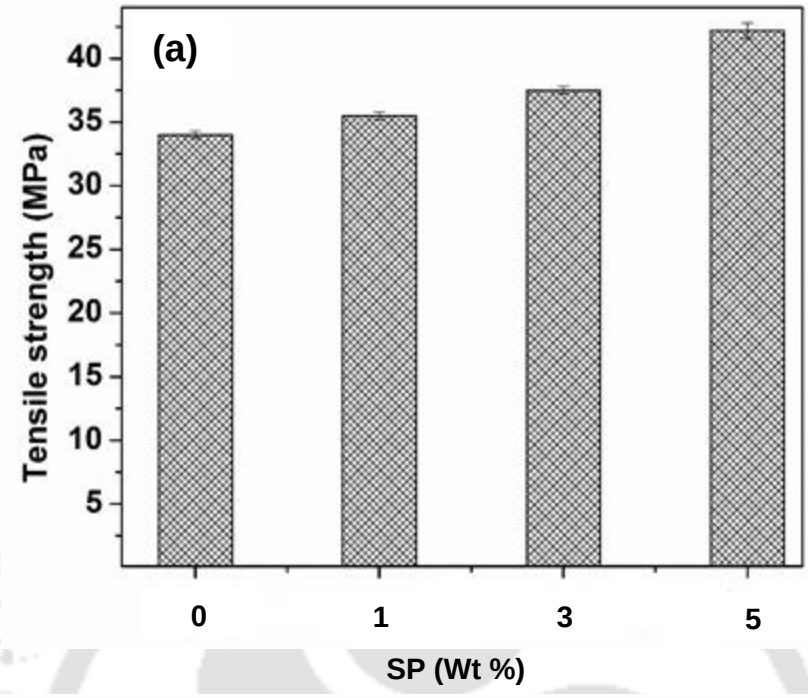

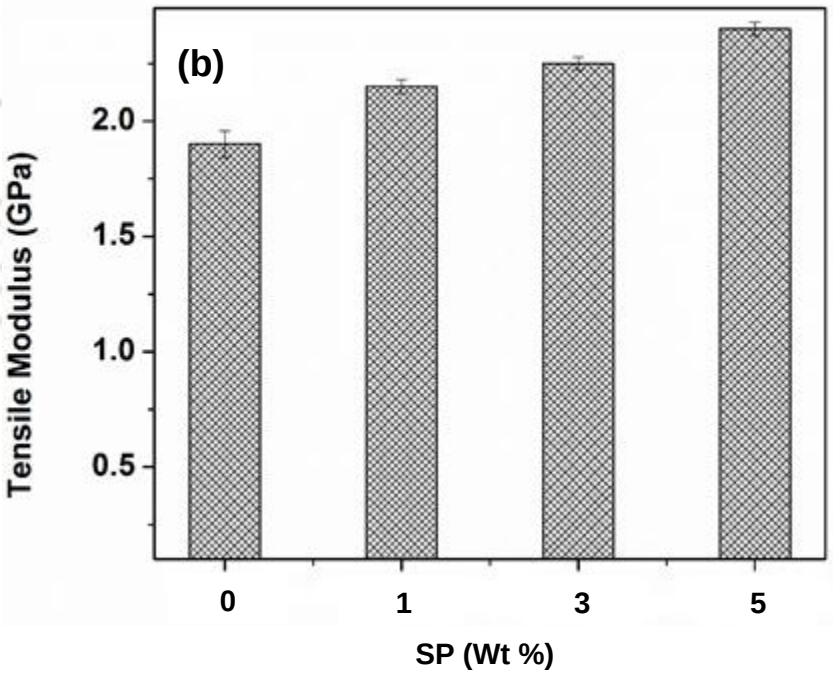

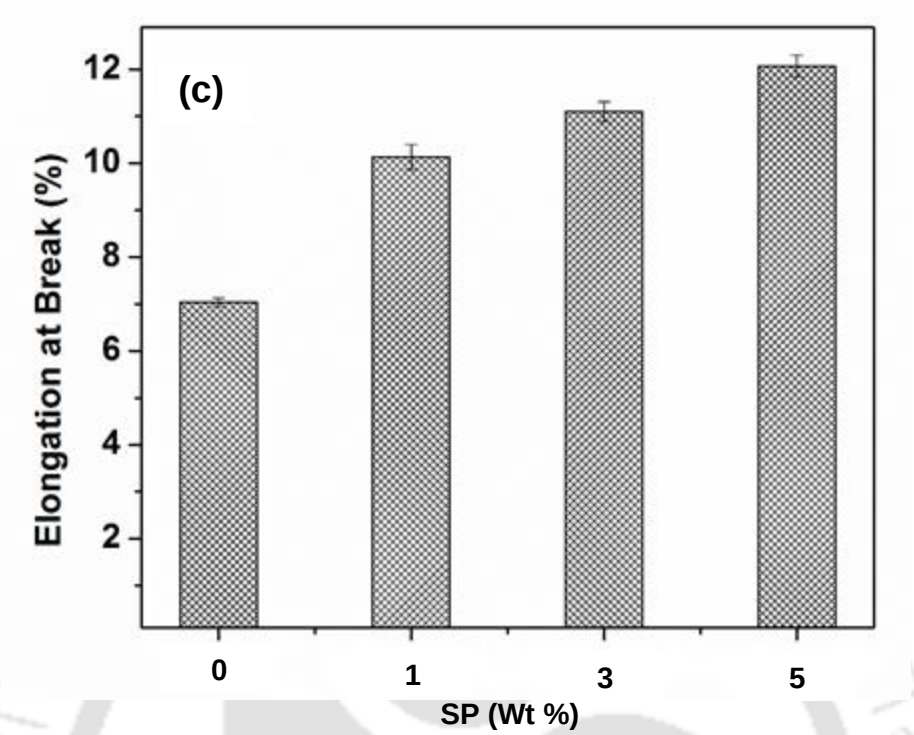

Figure 3.8. (a) Tensile strength (b) Tensile modulus and (c) Elongation at break for PLA and PLA-SP composites

3.4.8. Film permeability

One of the main functions of the films for food packaging is to decrease the oxygen transmission between the food and the surrounding atmosphere. Hence, oxygen permeability (OP) becomes a significant physical parameter to be considered. In a view to know the effect of novel filler, "SP' in terms of barrier properties, oxygen permeation studies are performed beyond 5 wt% SP loading (i.e. 15 wt% and 30 wt% SP). Figure. 3.9 shows the OP values of PLA and PLA nanocomposites reinforced with SP. Nanocomposites display reduction in the OP values with respect to PLA film and the OP values reduce drastically when the SP content increases. This underlines the positive effect of SP in increasing the barrier properties of PLA. The best positive influence is confirmed for the PLA-SP-30 nanocomposite films where the reduction in OP by ~69% is noticed as comparison with PLA (Figure. 3.9).

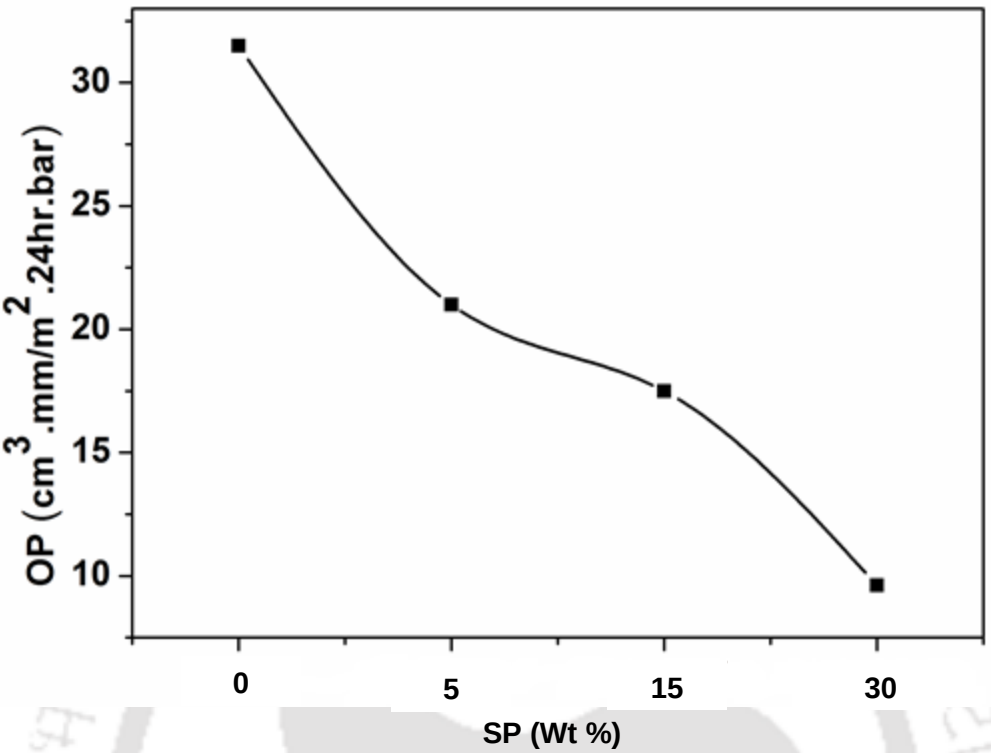

Figure 3.9. Oxygen permeability measurements for PLA and PLA-SP composites

It is well known that the transport properties of gases through PLA films are strongly influenced by tortuousity of their path, which is dependent on several factors including shape and aspect ratio of the filler, degree of exfoliation or dispersion, filler loading and orientation, adhesion to the matrix, moisture activity, filler-induced crystallinity, polymer chain immobilization, filler-induced solvent retention and porosity (**Sanchez et al., 2008**). In our case, dispersion of SP to a higher extent in the PLA matrix as shown in TEM analysis and good adhesion between SP with PLA matrix via intra molecular hydrogen bonding as revealed in FTIR analysis results in a more efficient barrier effect. The reduction in OP of 15.95% and 7.97% are reported for butylated hydroxytoluene (BHT)/poly(ethylene glycol) (PEG 400) and α-tocopherol/BHT/PEG 400 blended PLA films (**Byun et al., 2010**), respectively. Around 47-62% reduction of OP for PLA/closite-B composite is also reported in a previous study (**Katiyar et al., 2011**). However, for food packaging applications, consideration of compatibility of filler with food during storage becomes

a pre-requisite factor. In comparison with literature data (**Byun et al., 2010; Katiyar et al., 2011**), a significant enhancement in the oxygen barrier effects for PLA-SP nanocomposites is evidenced and also the filler chosen in the current work is a food additive which has definite compatibility with food during storage. Highly dispersed state of SP in the PLA matrix increases the distance (tortuous path) that the oxygen molecules have to travel through the PLA matrix and the same is reflected in terms of barrier effects. High oxygen barrier effects and transparent nature of the films induced by food additive SP promises that PLA-SP nanocomposite films can be used as potential materials for food packaging applications.

3.5. Conclusions

The incorporation of SP has brought considerable improvements in the mechanical and barrier properties of PLA. From the DSC analysis, it is observed that crystallization takes place in PLA through homogeneous crystallization. PLA-SP nanocomposites exhibit both homogeneous as well as heterogeneous crystallization, which confirms the nucleation effect of SP. The higher T_c values obtained for the composites indicate that crystallization rate becomes dependent on filler loading. Uniform dispersion of SP in the PLA matrix identified through morphological analyses shows a profound impact on the mechanical and barrier properties. In terms of mechanical properties, SP indeed improves the elongation at break (%) due to its plasticizing property. The best positive effect is observed for PLA-SP composites, where the reduction in OP by 69% is noticed in comparison with neat PLA. This effect in terms of barrier properties is due to increase in the tortuous path, which can be correlated to the uniform dispersion of SP in the PLA matrix evidenced in morphological studies.

CHAPTER 4

Crystallization Studies of Graphene and Sucrose Palmitate Reinforced PLA Nanocomposites

This chapter investigates the effect of sucrose palmitate (SP) and graphene (GR) on the crystallization kinetics of poly(lactic acid) (PLA). The non isothermal cold crystallization kinetic study for PLA, PLA-SP and PLA-GR nanocomposites was carried out using differential scanning calorimetry (DSC) at different heating rates of 2.5, 5, 7.5 and 10 °C/min. The obtained kinetic data were analyzed using crystallization kinetic models such as Avrami and Tobin methods. The decreasing trend obtained in the Avrami as well as Tobin exponent (n and n_T, respectively) with respect to neat PLA revealed the nucleating effect of both the reinforcements. Polarized optical microscopy (POM) was used to observe the growth of the spherulites in the PLA, PLA-GR and PLA-SP nanocomposites. With respect to addition of GR and SP in the PLA matrix, the reduction in the nucleation induction time and increment in the number of nucleation sites were reflected in the POM analysis.

4.1. Introduction

Crystallization is considered as one of the prime factors that shows a profound impact on the key characteristics such as mechanical and barrier effects of PLA. As processing of polymers are carried out under dynamic conditions in practical cases; it is essentially worth to understand the crystallization behaviour of PLA in the presence of graphene and sucrose palmitate under non-isothermal conditions (**Mubarak et al., 2001; Liu et al., 2010**). After incorporation of any filler (or additive) in the polymer matrix, investigating the crystallization behavior of the resultant composite systems becomes essential. This is because of the incorporated additives affecting the crystallization process of polymers via two ways. First, the additives can act as nucleating agents leading to an enhancement in crystallization temperature, which have a positive response on the crystallization characteristics. Second, additives can impede the movement and diffusion of molecular chains of polymer to the surface of the growing nucleus of crystallites in the composite system. This phenomenon may lead to a reduction in crystallization temperature, which has a negative response to the crystallization process. In view of this, the current chapter is focused on investigation of non-isothermal cold crystallization behavior of PLA, PLA-GR and PLA-SP nanocomposites using differential scanning calorimetry under the dynamic heating regime (2.5, 5, 7.5 and 10 °C/min). Further, the experimental crystallization data are analyzed using Avrami and Tobin models to derive information about the mechanism of the nucleation process in PLA, PLA-SP and PLA-GR nanocomposites. In addition to this, crystallization rate parameter (CRP) is determined for PLA, PLA-SP and PLA-GR nanocomposites using the Avrami parameters (*n* and *K*). The influence of fillers (SP and GR) as a nucleating agent and its impact on morphology as well as growth rate of spherulites is studied by polarized optical microscopy (POM) under isothermal crystallization temperature (120 °C) at different intervals (5, 10, 15 and 20 min) of the cold crystallization process.

4.2. Experimental

4.2.1. Materials

The chemicals used for the synthesis of PLA-SP and PLA-GR nanocomposites are discussed in section 3.2.1 and 2.2.1, respectively.

4.2.2. Synthesis of PLA-SP and PLA-GR nanocomposites

The synthesis procedure for the fabrication of PLA-SP and PLA-GR nanocomposites is discussed in section 3.2.2 and 2.2.3, respectively.

4.3. Characterization

4.3.1. Differential scanning calorimetry

Crystallization behavior of PLA, PLA-SP and PLA-GR nanocomposites were studied using a differential scanning calorimetry (Mettler Toledo-1 series). Samples (10±0.5 mg) were hermetically sealed in aluminum pans and heated from 25 to 180 °C at various heating rates of 2.5, 5, 7.5 and 10 °C/min in an inert atmosphere (N_2 flow, 50 mL/min). All the samples were first heated from 25 to 180 °C and held at this temperature for 5 min in order to eliminate the effect of thermal and processing history. Glass transition temperature (T_g), cold crystallization temperature (T_{cc}), the enthalpy change at T_{cc} (ΔH_{cc}), melting temperature (T_m) and the enthalpy of fusion at T_m (ΔH_m) for pure PLA, PLA-SP and PLA-GR nanocomposite films were determined from the DSC thermograph during the second heating cycle.

4.3.2. Polarized optical microscopy

The nucleation and spherulite growth in PLA, PLA-SP and PLA-GR nanocomposites were observed using Leica DM 2500P polarizing optical microscope fitted with a QICAM FAST1394 camera. The Linkam LTS420 temperature control stage was used to study the morphological changes of the film at isothermal crystallization temperature (120 °C). PLA, PLA-SP and PLA-GR nanocomposite films with the thickness of about 60 μm were first melted at 180 °C for 5 min in order to erase thermal histories, and immediately transferred to the temperature of 120 °C for isothermal crystallization. The micrographs of growing

spherulites were pictoriated at a specific interval of time before the impingement of spherulites.

4.4 Theory

4.4.1. Relative degree of crystallinity

In order to determine the relative degree of crystallinity ($X(t)$), as a function of crystallization time, the exotherms that correspond to cold crystallization of PLA, PLA-SP and PLA-GR nanocomposites is integrated. $X(t)$ as a function of temperature is given by the following equation.

$$X(t) = \frac{\int_{T_0}^{T} \left(\frac{dH_C}{dT} \right) dT}{\int_{T_0}^{T_\infty} \left(\frac{dH_C}{dT} \right) dT} \tag{4.1}$$

where, T_0 and T_∞ denotes the onset and final cold crystallization temperature, respectively (**Pei et al., 2010; Vasanthan et al., 2011**). The crystallization time (t) and the respective temperature (T) are related by the following expression:

$$t = \frac{T - T_0}{\phi} \tag{4.2}$$

where, ϕ is the heating rate (**Pei et al., 2010; Vasanthan et al., 2011**).

4.4.2. Crystallization half time

The half-time of crystallization ($t_{1/2}$) is defined as the time required to achieve 50% of the crystallization process. Determination of crystallization half-time is of prime importance in understanding the kinetics of crystallization process and is obtained using the following expression (**Ravari et al., 2013; Qiu et al., 2011; Tsuji et al., 2009**):

$$t_{1/2} = \left(\frac{\ln 2}{k} \right)^{1/n} \tag{4.3}$$

4.4.3. Avrami model

The kinetic parameters corresponding to the non-isothermal crystallization process of PLA, PLA-SP and PLA-GR nanocomposites are determined using the "Avrami model", which is expressed as follows:

$$X(t) = 1 - \exp\left(-kt^{n}\right) \tag{4.4}$$

The eq. (4.4) is expressed in the non-linear form as

$$\log\left[-\ln\left(1 - X(t)\right)\right] = \log k + n \log t \tag{4.5}$$

where, $X(t)$ refers to the relative crystallinity at any time "t", n corresponds to the Avrami exponent, k is the overall kinetic constant (**Bao et al., 2013**). The Avrami exponent (n) and the crystallization rate constant (k) are determined using the slope and intercept values obtained from the linear plot of log [- ln (1 - $X(t)$)] versus log t.

4.4.4. Tobin model

The Tobin equation is given by the following expression:

$$X_t = \frac{K_T t^{n_T}}{1 + K_T t^{n_T}} \tag{4.6}$$

where, X_t refers to the relative crystallinity at time 't', whereas, K_T and n_T are the Tobin parameters related to crystallization rate constant and exponent, respectively (**Han et al., 2013**). The type of nucleation and growth mechanism associated with the non-isothermal crystallization process of PLA, PLA-SP and PLA-GR nanocomposites are derived from the values of Tobin exponent (n_T). The eq. (4.6) is rearranged as follows:

$$\log\left(\frac{X_t}{1 - X_t}\right) = \log K_T + n_T \log t \tag{4.7}$$

4.5. Results and discussion

4.5.1. Influence of sucrose palmitate on the non-isothermal cold crystallization kinetics of PLA

Figure 4.1 shows the non-isothermal crystallization and melting behaviors of neat PLA and PLA-SP nanocomposites investigated by DSC at various heating rates (2.5, 5, 7.5, and 10). The curves show an exothermic cold crystallization peak at about 100-121°C for neat PLA films, and at 105-125 °C for PLA-SP nanocomposites. The curves also present an endothermic peak related to melting at about 148-151°C for neat PLA and PLA-SP nanocomposites. It can be seen from Figure 4.1 that crystallization temperatures (T_{cc}) shift gradually to the higher temperature side with respect to heating rates for both PLA and PLA-SP nanocomposites. This indicates that PLA requires excess time for crystallization at a higher heating rate (shown in Figure 4.2(a)). This phenomenon is related to the lower heat conductivity of the PLA, which delays crystallization with increasing heating rates (**Ravari et al., 2013**). For a lower heating rate (2.5 °C/min), two melting peaks for both PLA and PLA-SP composites are observed. The melting peak that corresponds to the lower temperature is ascribed to the melting process of imperfect crystalline structures of PLA formed during the primary phase of the cold crystallization process. The higher temperature melting peak is attributed to the melting of the perfect crystalline structure of PLA formed at the later phase of the cold crystallization process as a result of increased thickness of lamellae (**Yasuniwa et al., 2008; Kong et al., 2003; Fukushima et al., 2009; Fortunati et al., 2012**). In contrast, for a heating rate of 5 °C/min, the disappearance of the double melting peak is observed for both PLA and PLA-SP nanocomposites. With the further increase in the heating rate i.e. 10 °C/min, the cold crystallization peak of PLA and PLA-SP nanocomposites becomes very small and hard to detect, demonstrating the formation of less perfect crystal structures due to faster heating process (**Ravari et al., 2013; Nofar et al., 2011**). The T_g values for all the samples with a constant heating rate remain similar, but the T_g for each material increases with the rise in the heating rate, owing to thermal delay (shown in Figure 4.2(b)) (**Ravari et**

al., 2013; Nofar et al., 2011). The enthalpy of cold crystallization (ΔH_{cc}) decreases for both PLA and PLA-SP composites with an increase in the heating rate. Because PLA molecular chains do not possess sufficient time to relax before the formation of crystal structures when subjected to faster heating process (**Ravari et al., 2013; Nofar et al., 2011**). The melting enthalpy (ΔH_m) also varies at a same pace as ΔH_{cc} indicating that melting behaviors mainly arise due to melting of crystal structures formed during the cold crystallization process (**Ravari et al., 2013; Nofar et al., 2011).**

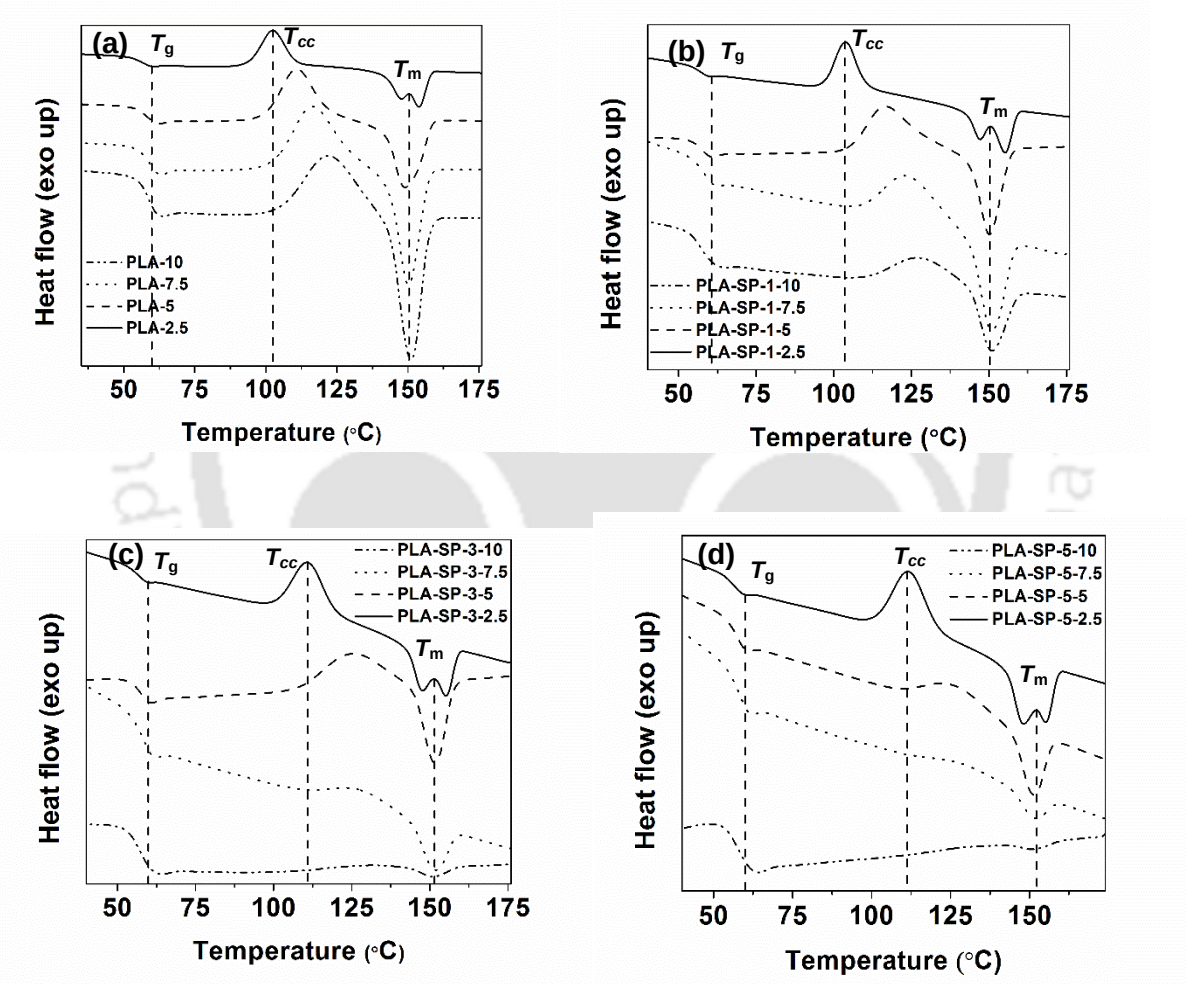

Figure 4.1. DSC thermographs at different heating rates of 2.5, 5, 7.5 and 10 °C/min for (a) neat PLA, (b) PLA-SP-1, (c) PLA-SP-3 and (d) PLA-SP-5 nanocomposites

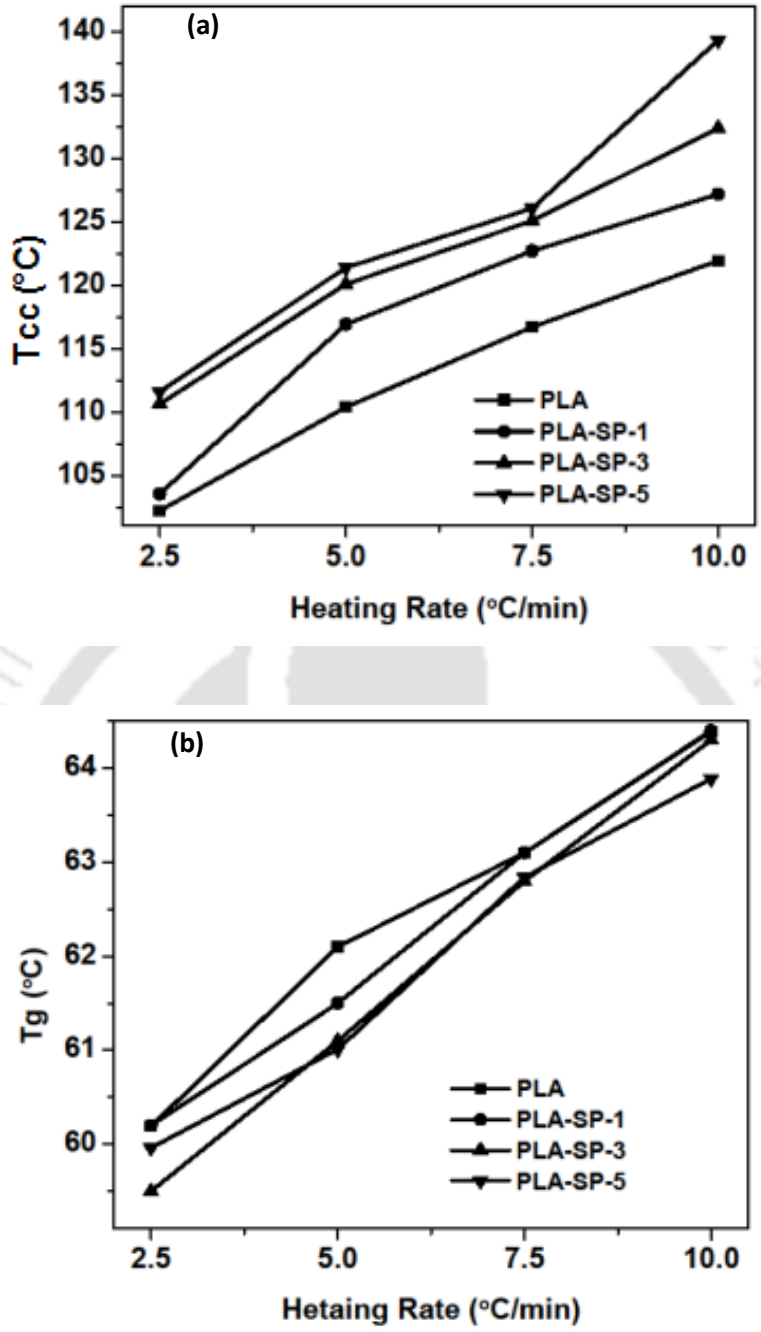

Figure 4.2. Variation of T_{cc} (a) and T_g (b) with respect to heating rate

The plots of relative crystallinity versus crystallization time for neat PLA and PLA-SP nanocomposites are portrayed in Figure 4.3. The relative crystallinity curves of both PLA and its nanocomposites obtained at various heating rates exhibit sigmoidal shape characteristic curves, which are attributed to the impingement of spherulites at the later stage of the crystallization process (**Liu et al., 2010; Wang et al., 2012**). From these curves, the lag effects of heating rates on the crystallization process can be observed. Figure 4.3 also

shows that at higher heating rates, PLA matrices have a shorter time of crystallization. This means that crystallization rates increased with the incorporation of SP (**Ravari et al., 2013; Wu et al., 2007**).

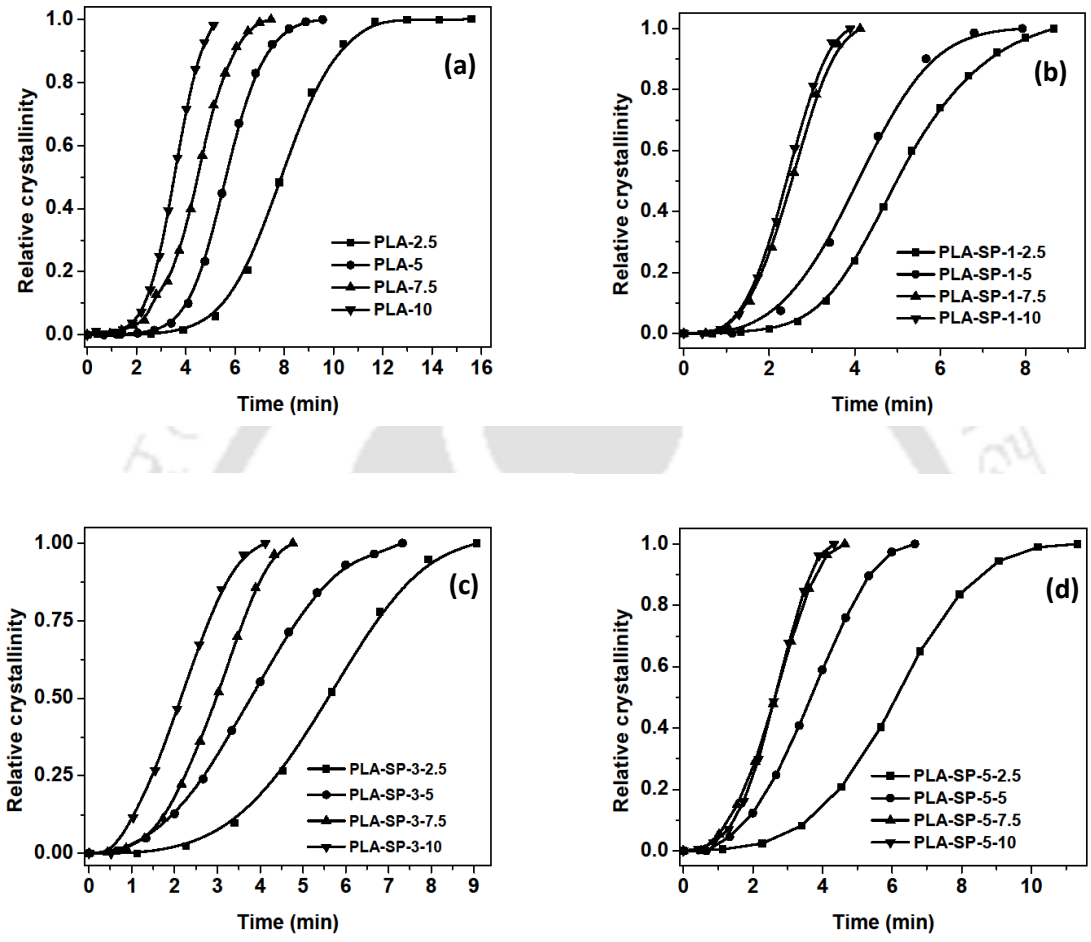

Figure 4.3. Relative crystallinity versus crystallization time at different heating rates for (a) neat PLA, (b) PLA-SP-1, (c) PLA-SP-3 and (d) PLA-SP-5 nanocomposites

In general, shorter the $t_{1/2}$ values, faster will be the crystallization process. With increasing the heating rate, $t_{1/2}$ values for both PLA and its composites exhibit decreasing trends indicating shorter crystallization completion times. Moreover, the $t_{1/2}$ values for PLA-SP nanocomposites are observed to be lower in comparison with neat PLA. This is due to the acceleration of the overall cold crystallization process after reinforcement of SP. However, the higher $t_{1/2}$ values observed for PLA and PLA-SP nanocomposites at lower heating rates

may be attributed to the secondary crystallization process. The variation of $t_{1/2}$ with ϕ for neat PLA and its composites is clearly seen from Figure 4.4. From the Figure, one can distinctly interpret the influence of ϕ and SP loading on the overall crystallization rate of PLA nanocomposites. It can be noticed that the $1/t_{1/2}$ value shoots up for PLA-SP nanocomposites when compared to neat PLA. Hence, it becomes mandatory to discuss the effect of SP and its content (wt %) on the crystallization performance of PLA. Nucleation and growth are the two important aspects associated with the overall crystallization process of polymers (**Yi et al., 2007**)**.** The SP incorporated in the PLA matrix may engage in two distinct or contending functions influencing the crystallization process. On one hand, SP may involve in providing nucleation effect in order to fasten the non-isothermal crystallization process of PLA. On the other hand, there is a possibility that PLA chains will be present in an exceedingly intertwined during the melt state. Therefore, while due course of the crystallization process, PLA molecular segments must overwhelm definite energy barriers in order to migrate and bind onto the surface of the growing crystal front. The SP may serve as a cross-linking agent that obstructs the migration of PLA molecular fragments. This in turn hampers the growth of crystalline structures by restraining the nearby molecular segments of polymer during strong synergistic interactions exist between PLA and SP. There is a significant difference in the $1/t_{1/2}$ values between PLA and PLA-SP-1 nanocomposite. This is due to the predominant nucleation effect induced by 1 wt% loading of SP enhancing the crystallization of PLA. However, further increase in the $1/t_{1/2}$ values for higher loadings of SP is not observed. Although SP might contribute in providing additional nucleation spots at higher loadings, the presence of more SP content may also create a much more appreciable detention consequence on the crystal growth process of PLA. Since the detention effect masks the nucleation effect, the overall crystallization rate is observed to be slow down at higher loadings of SP.

Zhang et al. (**1994**) introduced a method to evaluate the crystallization rate parameter (CRP), which describes the effect of filler on the crystallization rate of polymer quantitatively.

Figure 4.4 shows the plot of $1/t_{1/2}$ versus ϕ for both PLA and its nanocomposites. The CRP is obtained from the slope of a linear plot of $1/t_{1/2}$ versus ϕ. The values of CRP are found to be 0.0272, 0.0276, 0.0313, and 0.0335 for PLA, PLA-SP-1, PLA-SP-3 and PLA-SP-5, respectively. The CRP values obtained for PLA-SP nanocomposites point out that SP slightly enhances the cold crystallization of PLA matrix.

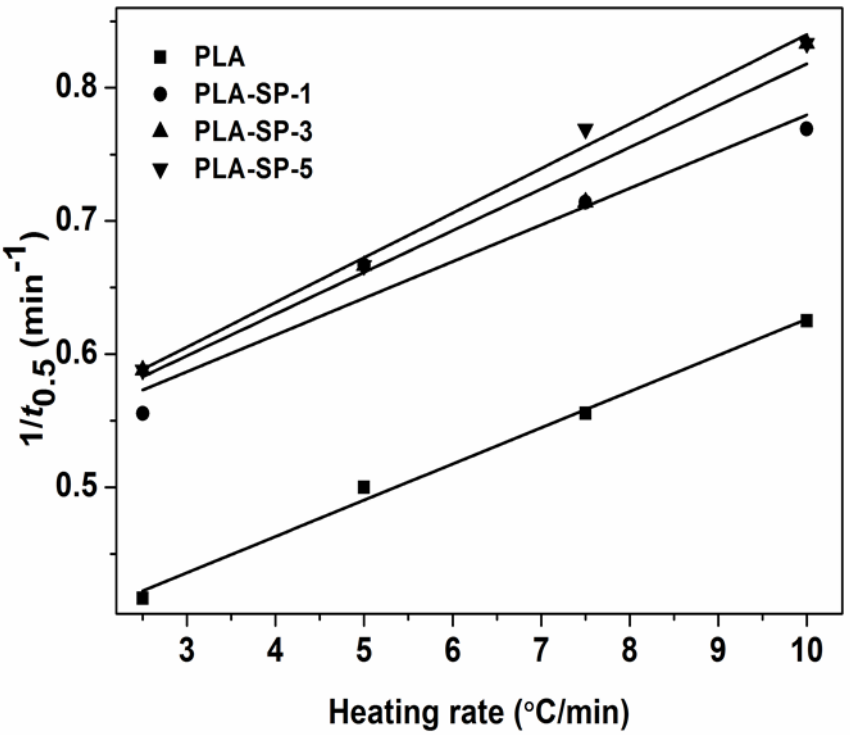

Figure 4.4. Effect of SP loading on the crystallization rate parameter (CRP)

A typical relative crystallinity curves for neat PLA, PLA-SP-1, PLA-SP-3 and PLA-SP-5 are shown in Figure 4.3(a-d) and the corresponding Avrami plots for the same are presented in Figure 4.5(a-d). It can be noticed from Figure 4.5(a-d), good linearity is obtained for all the plots. This suggests that the theory seems to be helpful to appropriately elucidate the non-isothermal crystallization of PLA nanocomposite systems.

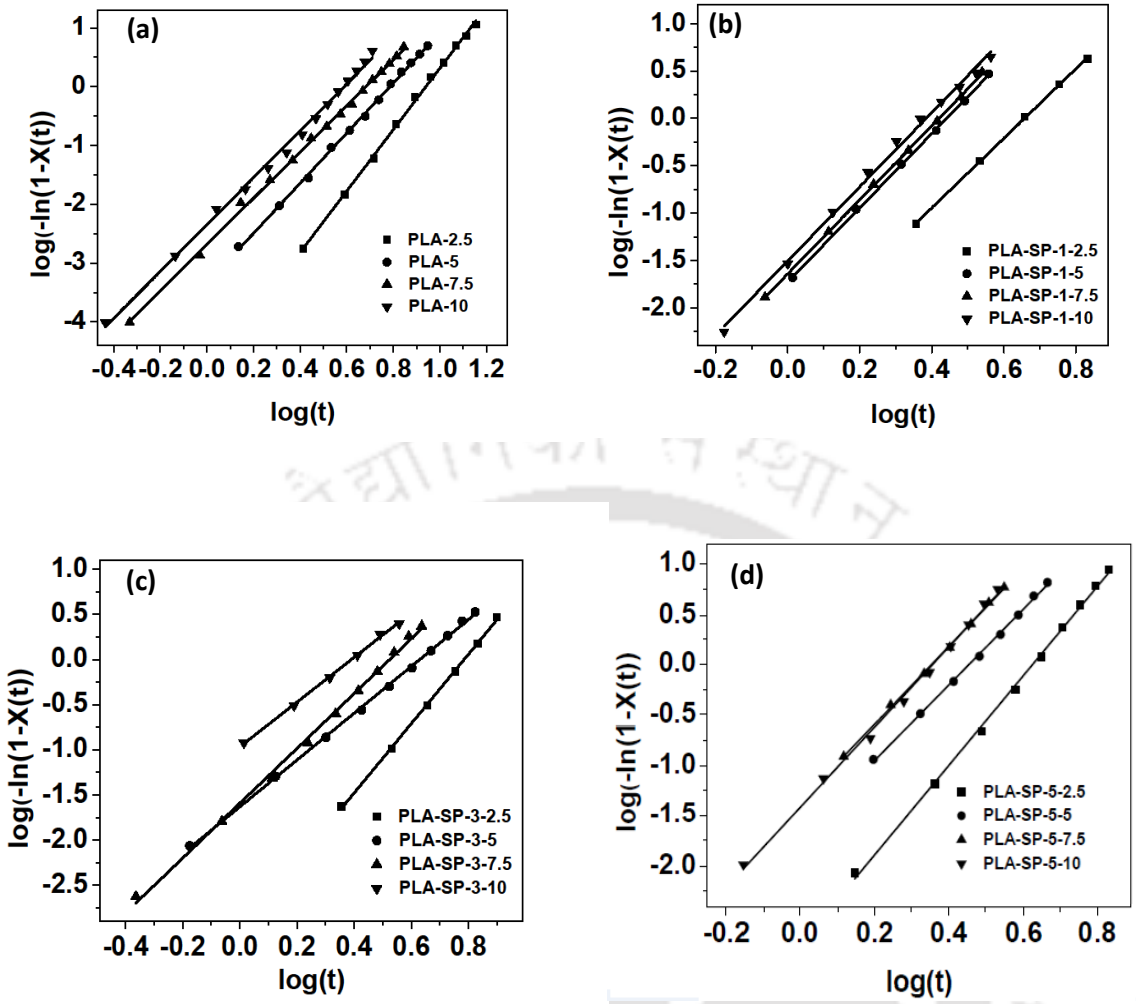

Figure 4.5. Avrami plots for non-isothermal cold crystallization of (a) PLA, (b) PLA-SP-1, (c) PLA-SP-3 and (d) PLA-SP-5 nanocomposites

In the current work, *n* values (presented in the Table 4.1) for neat PLA lie in the range of 4-5, which is in accordance with literature data (**Fortunati et al., 2012; Nofar et al., 2011**). This suggests that the 3-dimensional (3D) growth of PLA crystals takes place during the non-isothermal cold crystallization process and crystal growth is in disk-like nature by homogeneous nucleation. The *n* values for PLA-SP nanocomposites are found to be in the range of ~2.5-4, which is slightly lower in comparison with neat PLA. This is ascribed to the faster crystallization process that does not provide adequate time for the crystals to grow in three dimensions, which results in the heterogeneous nucleation process (**Fortunati et al., 2012; Nofar et al., 2011**).

Table 4.1. Avrami model parameters for PLA and PLA-SP nanocomposites

S:No	Sample	*n*				log(*k*)			
		2.5 °C/min	5 °C/min	7.5 °C/min	10 °C/min	2.5 °C/min	5 °C/min	7.5 °C/min	10 °C/min
1	PLA	4.8	4.2	3.9	4	-4.9	-3.3	-2.6	-2.3
2	PLA-SP-1	3.9	3.9	3.9	3.7	-2.4	-1.7	-1.6	-1.5
3	PLA-SP-3	3.8	3.3	2.5	2.4	-3	-1.6	-1.5	-1.3
4	PLA-SP-5	3.8	3.5	2.9	2.7	-2.8	-1.7	-1.4	-1.3

The Avrami model used for studying the crystallization kinetics of PLA and PLA-SP nanocomposites is merely appropriate for investigating the early phase of the crystallization process. This is due to the fact that the Avrami model does not involve in describing the growth site impingement as well as the secondary crystallization process. In order to investigate the phase-transformation kinetics with growth site impingement in the non-isothermal crystallization kinetics of PLA and PLA-SP nanocomposites, Tobin model is utilized. The Tobin exponent (n_T), provides information about the type of nucleation and growth mechanism involved in the non-isothermal crystallization process. Tobin plots for PLA and PLA-SP nanocomposites obtained for different heating rates are shown in Figure 4.6(a-d), in which $\log\left(\frac{X_t}{1-X_t}\right)$ is plotted against $\log t$. Tobin parameters (n_T and K_T) are determined from the slope and intercept of the linear fit, respectively and the same is summarized in Table 4.2.

It can be observed from Table 4.2, that the Tobin exponent, 'n_T' value for PLA is in the range of 4-6. It decreases with respect to heating rate and the obtained value is comparable with literature data (**Han et al., 2013**). Tobin parameter, K_T, exhibits the increasing trend with an increase in the heating rate, which points out the faster crystallization process. In

case of PLA-SP nanocomposites, the 'n_T' values show decreasing trend with respect to the heating rate. However, the values are found to be in the range of ~3-5, which is relatively smaller in comparison with neat PLA, irrespective of the heating rate. This difference in the 'n_T' values suggests that the reinforcement of SP in the PLA matrix alters the crystallization process of PLA. It is also seen from Table 4.2, that the 'K_T' values obtained for PLA-SP nanocomposites are higher when compared to neat PLA. This phenomenon indicates that the SP accelerates the non-isothermal crystallization process of PLA. The findings of the Tobin model discussed above are similar to the trend obtained for Avrami parameters. Hence, the Tobin parameters also describe the same physical significance analogous to that of Avrami model (**Maiti et al., 2012**).

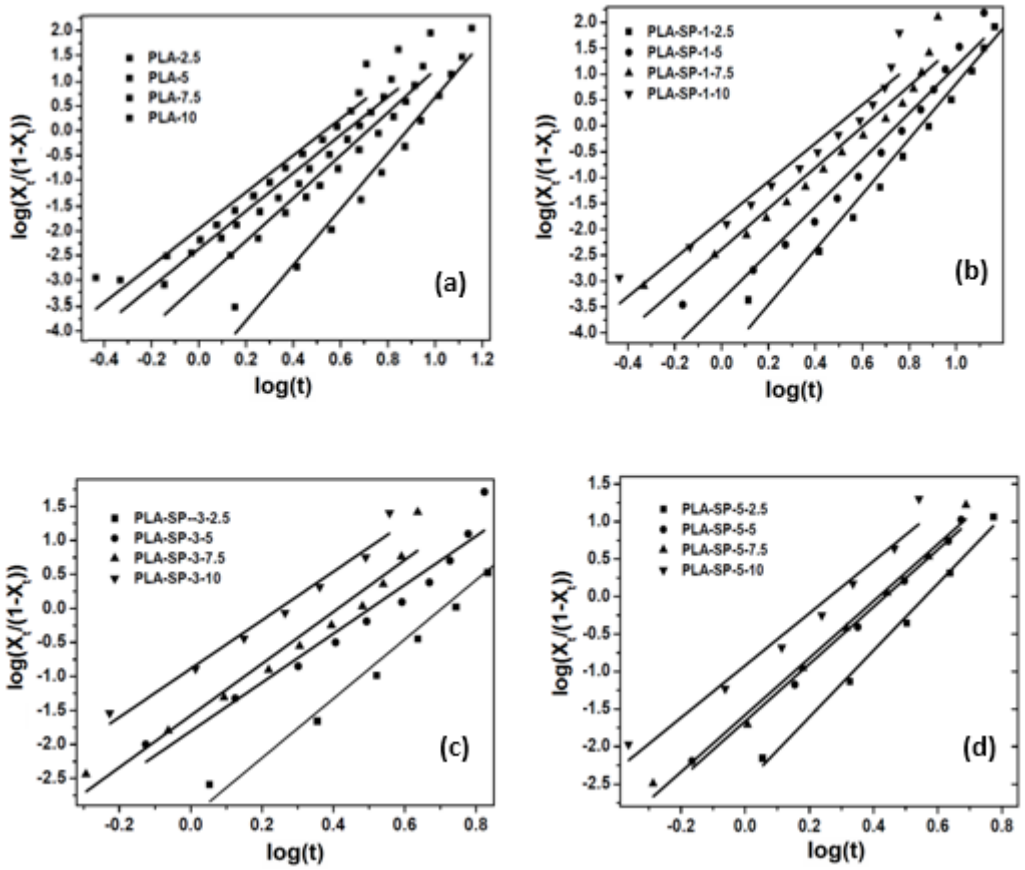

Figure 4.6. Tobin plots for non-isothermal cold crystallization of (a) PLA, (b) PLA-SP-1, (c) PLA-SP-3 and (d) PLA-SP-5 nanocomposites

Table 4.2. Tobin model parameters for PLA and PLA-SP nanocomposites

S:No	Sample	n_T				Log(K_T)			
		2.5 °C/min	5 °C/min	7.5 °C/min	10 °C/min	2.5 °C/min	5 °C/min	7.5 °C/min	10 °C/min
1	PLA	6.0	4.6	4.1	3.9	-5.0	-3.0	-2.3	-1.9
2	PLA-SP-1	5.3	4.5	3.9	3.7	-4.5	-3.3	-2.2	-1.8
3	PLA-SP-3	4.3	3.6	3.8	3.5	-3.1	-1.8	-1.6	-1.3
4	PLA-SP-5	4.4	3.8	3.7	3.5	-2.5	-1.7	-1.6	-1.1

The influence of SP as a nucleation agent on the crystallization behavior of PLA matrix is performed using a polarized optical microscope as shown in Figure 4.7. PLA and PLA-SP nanocomposites are heated up to 180 °C and the hot stage containing samples are maintained at the same temperature for a time span of 5 min to remove thermal history. Optical micrographs are pictoriated in the 0, 5^{th}, 10^{th}, 15^{th} and 20^{th} min at 120 °C after cooled from melt state at 180 °C for PLA and PLA-SP composites. In the current study, the process of nucleation and growth control the overall crystallization kinetics of PLA. After incorporation of SP in the PLA matrix, an increase in the overall crystallization rate of PLA occurs. This is reflected through the diminution of the nucleation induction period followed by an increment in additional primary nucleation sites. For the PLA-SP nanocomposites, the nucleation density of PLA spherulites is found to increase at 5 min, 10 min, 15 min and 20 min in comparison with neat PLA (see Figure 4.7). In addition to this, an appreciable increase in the nucleation density with respect to SP loading is noticed, which signifies the better dispersion of SP in the PLA matrix. Therefore, more crystals have the ability to undergo nucleation and subsequently grow in the enhanced surface area of the interfaces owing to increment in the number of nucleating sites.

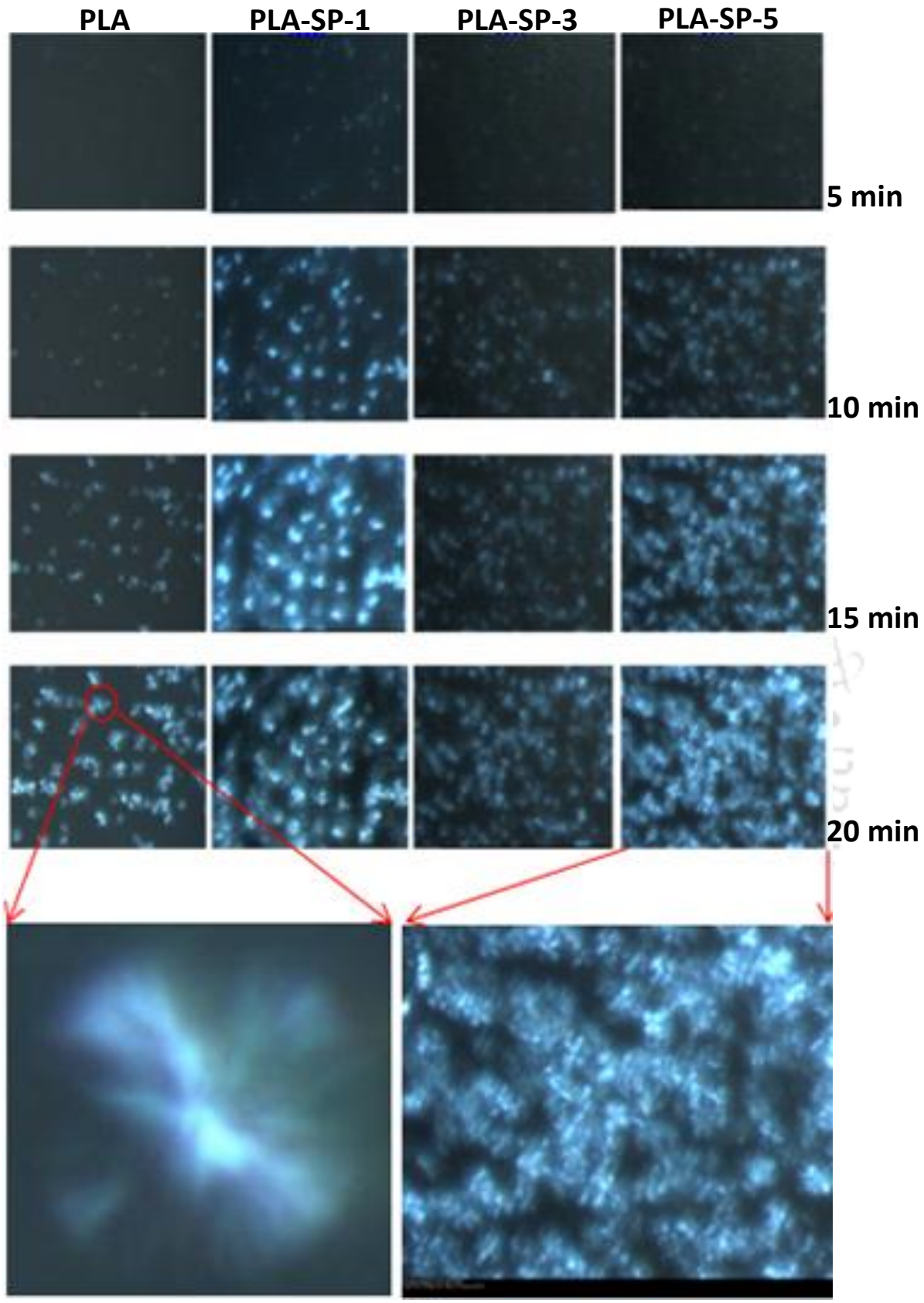

Figure 4.7. Optical microscopy images of PLA and PLA-SP nanocomposites with respect to time at 120 °C

For neat PLA and PLA-SP composites, the radial spherulite growth rates are measured as a function of time. Figure 4.8 represents the variation of spherulite radius with time at 120 °C. For both PLA and PLA-SP composites, the size of the spherulites amplifies linearly with respect to time. This conveys that the growth rate is not dependent on the spherulite diameter. In case, if it is considered that all the crystallizable species are not eliminated from the growing spherulite phase, they are expected to escalate on the surface of the growing crystal front. This in turn may consequently impede the migration of the crystallizable species from the melt phase to the growing front. This phenomenon leads to a deflection from linear spherulite growth after a certain diameter of spherulite attained. As such, no deflection from linearity for growth of spherulites is noticed in the PLA-SP nanocomposite system (Figure 4.8), it can be inferred that the SP is not eliminated during the spherulite growth process. Similar results are reported for PLA-carbon nanotubes (CNT) nanocomposites by **Xu et al.** (**2011**).

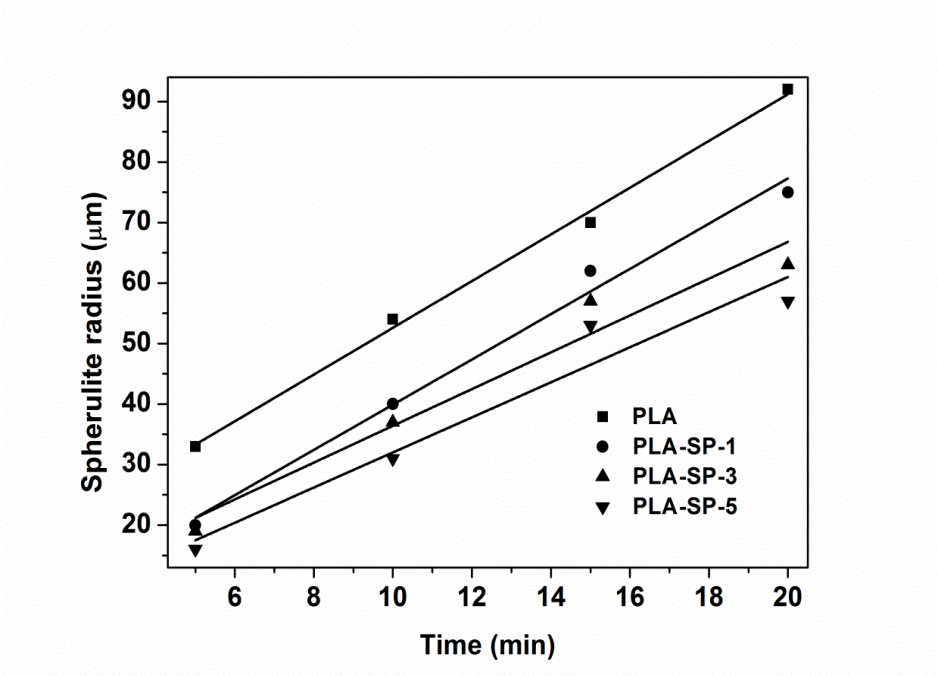

Figure 4.8. Variation of spherulite radius versus time for PLA and PLA-SP nanocomposites

4.5.2. Influence of graphene on the non-isothermal cold crystallization kinetics of PLA

The DSC thermographs for neat PLA and PLA-GR nanocomposites obtained at different heating regime (2.5, 5, 7.5 and 10 °C/min) are analyzed for understanding the non-isothermal crystallization and melting behaviors (Figure 4.9). Both PLA and PLA-GR nanocomposites display similar T_g value for a single heating rate. However, the shift in the T_g values is observed for each sample with increasing heating rate, which is attributed to thermal delay (**Ravari et al., 2013; Yasuniwa et al., 2008**). A cold crystallization exotherm is observed in the temperature range of 99-120 °C for neat PLA and 100-126 °C for PLA-GR nanocomposites. The steady shift in the T_{cc} to the greater temperature values with the rise in heating rate can be observed for PLA and PLA-GR nanocomposites (Figure 4.9). This is ascribed to the lower heat transfer coefficient, which prolongs the time required for the cold crystallization process at higher heating rate (**Nofar et al., 2011**). A peak corresponding to melting endotherm is noticed for all the samples in the temperature ranging from 150-156 °C (Figure 4.9). Interestingly, it is observed that all the samples exhibited a double melting endotherm for a heating rate of 2.5 °C/min. The endotherm observed at lower and higher temperature corresponds to the melting phenomenon of imperfect and perfect crystalline structures of PLA developed at the primary and secondary phase of the cold crystallization process, respectively (**Fukushima et al., 2009; Fortunati et al., 2012**). However, the bimodal melting endotherm is not noticed for both PLA and PLA-GR nanocomposites in case of further heating rates.

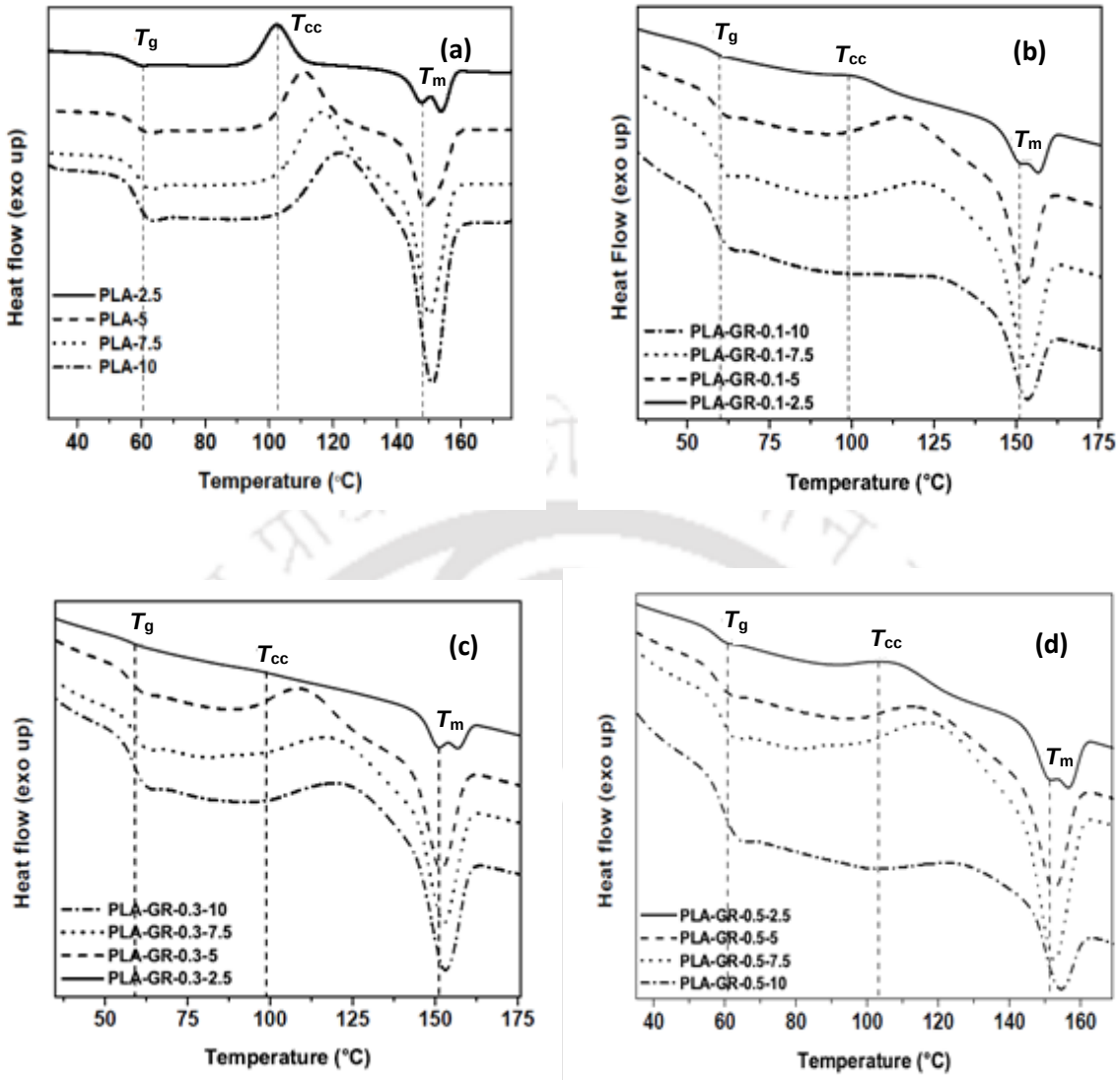

Figure 4.9. DSC thermographs at different heating rates of 2.5, 5, 7.5 and 10 °C/min for (a) neat PLA, (b) PLA-GR-0.1, (c) PLA-GR-0.3 and (d) PLA-GR-0.5 nanocomposites

The values of relative crystallinity are plotted as a function of crystallization time for both neat PLA as well as PLA-GR nanocomposites and the same is portrayed in Figure 4.10. The Figure displays a characteristic sigmoidal shaped relative crystallinity curves for all the samples at different heating regime. This discloses the phenomenon of impingement of spherulites that occurred at the advanced phase of the cold crystallization process (**Wang et al., 2012**). In addition to this, in case of greater heating rates, the lag effects are not experienced on the crystallization behavior of both PLA and PLA-GR nanocomposites.

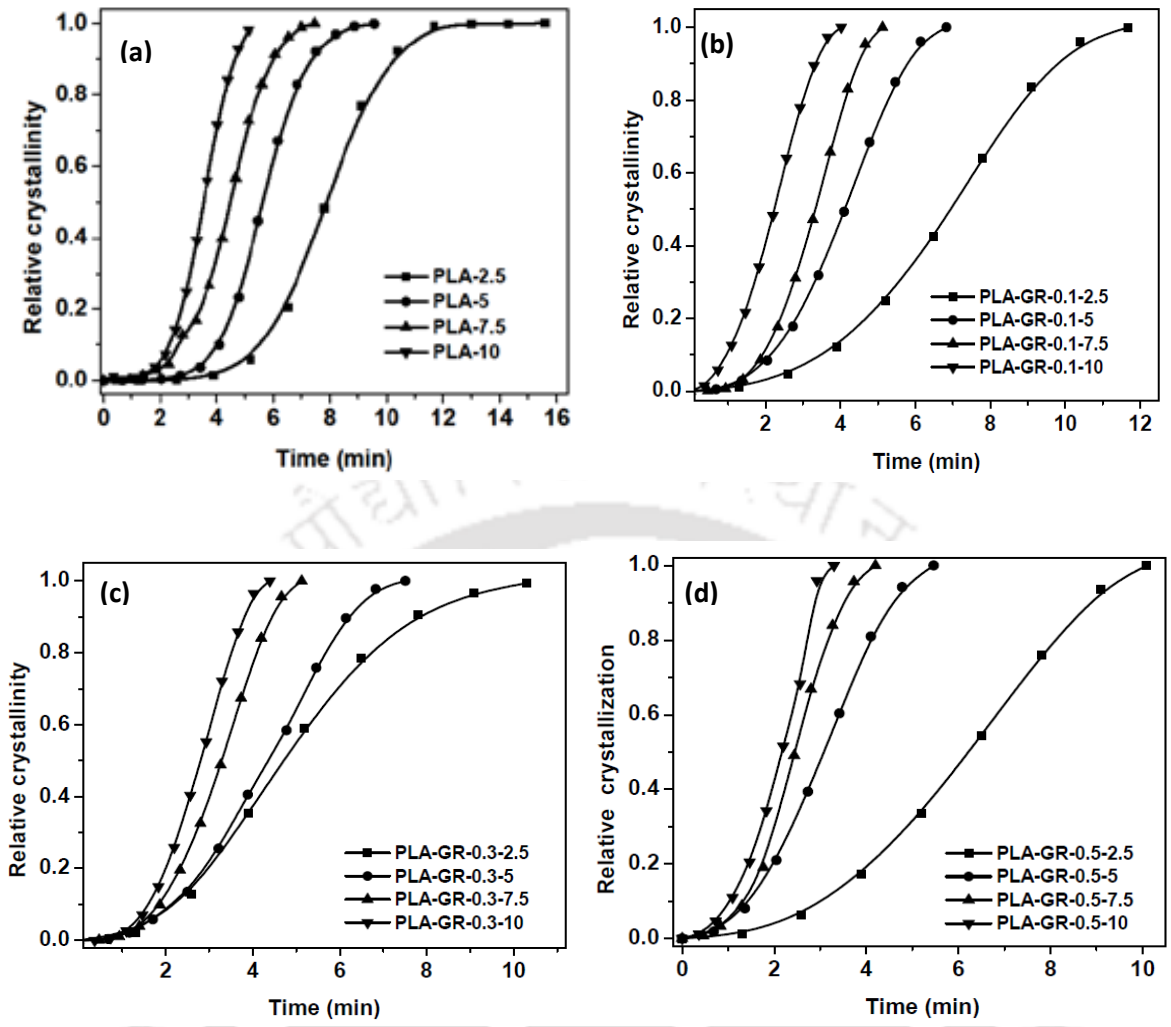

Figure 4.10. Relative crystallinity versus crystallization time at different heating rates for (a) neat PLA, (b) PLA-GR-0.1, (c) PLA-GR-0.3 and (d) PLA-GR-0.5 nanocomposites

The $t_{1/2}$ values obtained for both PLA as well as PLA-GR nanocomposites exhibit downturn with respect to increase in heating rates. This is attributed to the faster crystallization completion periods with progress in the heating rate. Also, the $t_{1/2}$ values obtained for PLA-GR nanocomposites are noticed to be relatively lower in comparison with neat PLA for all the heating rates. The possible reason for this might be due to the fact that the addition of GR in the PLA matrix accelerates the cold crystallization rate on the whole. The greater $t_{1/2}$ values obtained at the lower heating rate for both PLA and nanocomposite films result from the secondary crystallization phenomenon. In order to study the influence of GR towards the crystallization process, $1/t_{1/2}$ versus ϕ is plotted for PLA and PLA-GR nanocomposites as

shown in Figure 4.11. One can see that $1/t_{1/2}$ value increases significantly for PLA-GR-0.1 as compared to neat PLA. This increment corresponds to the prominent effect of nucleation ability of GR that stimulates the crystallization process of PLA. A much profound impact on the $1/t_{1/2}$ values is not evidenced thereafter with further GR loadings in the PLA matrix. However, the increasing trend obtained in the $1/t_{1/2}$ values is ascribed to the nucleation effect of GR resulting in a faster rate of the crystallization process in PLA. Further, crystallization rate parameter (CRP) is calculated from the slope of the linear plots shown in Figure 4.11 in order to derive quantitative information about the influence of GR on the crystallization rate of PLA. The CRP value for PLA, PLA-GR-0.1, PLA-GR-0.3 and PLA-GR-0.5 is determined to be 0.0272, 0.0372, 0.0404 and 0.0413, respectively. The increasing trend obtained in the CRP values of PLA-GR nanocomposites as compared to neat PLA confirms that reinforcement of GR indeed fastens the cold crystallization process in PLA.

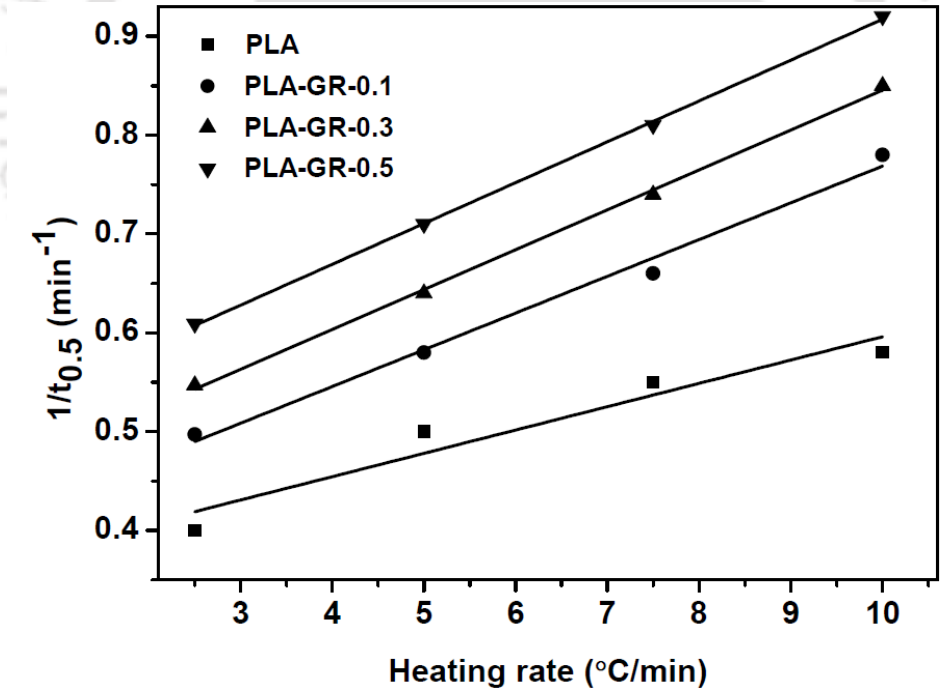

Figure 4.11. Effect of GR loading on the crystallization rate parameter (CRP)

The relative crystallinity curves corresponding to neat PLA, PLA-GR-0.1, PLA-GR-0.3 and PLA-GR-0.5 are presented in Figure 4.10(a-d) and the respective Avrami plots for the same are depicted in Figure 4.12(a-d). The linear behaviour exhibited by these plots specifies that

the Avrami model adequately elucidates the cold crystallization process of PLA under non-isothermal conditions. The '*n*' values corresponding to Avrami exponent for both PLA and PLA-GR nanocomposites are presented in Table 4.3. It is observed that the *n* values show a decreasing trend with respect to GR loadings in comparison with neat PLA irrespective of the heating rate. The greater '*n*' values observed in case of neat PLA is ascribed to the homogeneous nucleation, which is responsible for 3-dimensional (3D) growth of PLA crystals (**Liao et al., 2007**). In contrast, the relatively lower '*n*' values noticed for PLA-GR nanocomposites suggest that heterogeneous nucleation accelerate the crystallization rate. This also indicates that PLA crystals do not possess enough time for its growth in three dimensions in the latter case (**Liao et al., 2007**).

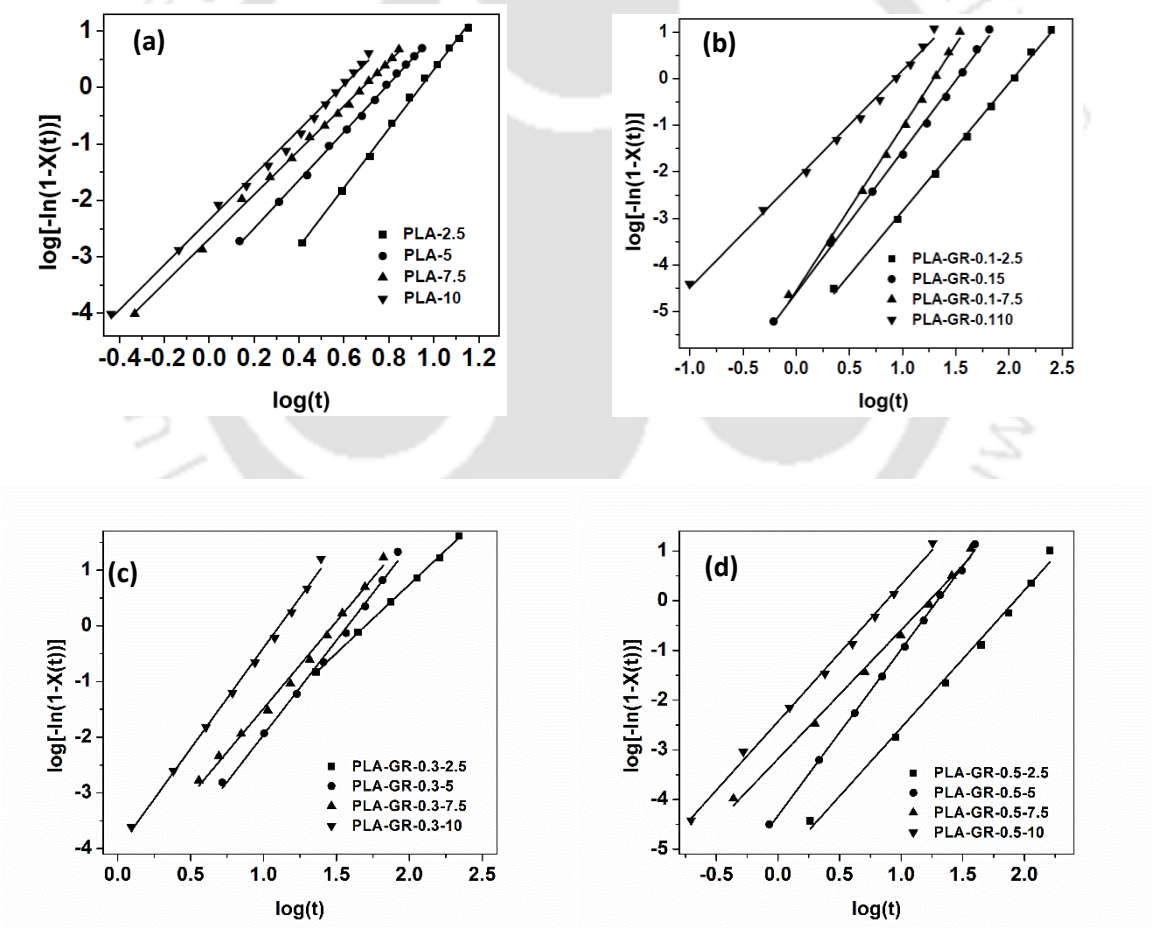

Figure 4.12. Avrami plots for non-isothermal cold crystallization of (a) PLA, (b) PLA-GR-0. 1, (c) PLA-GR-0.3 and (d) PLA-GR-0.5 nanocomposites

Table 4.3. Avrami model parameters for PLA and PLA-GR nanocomposites

Sample name	*n*				Log(*k*)			
	2.5 °C/min	**5 °C/min**	**7.5 °C/min**	**10 °C/min**	**2.5 °C/min**	**5 °C/min**	**7.5 °C/min**	**10 °C/min**
PLA	4.8	4.2	3.9	4.0	-4.9	-3.3	-2.6	-2.3
PLA-GR-0.1	4.2	3.9	3.7	3.6	-3.3	-2.5	-1.9	-1.3
PLA-GR-0.3	4.0	3.4	3.2	3.2	-2.76	-1.85	-1.5	-1.15
PLA-GR-0.5	3.9	3.3	3.2	2.9	-2.3	-1.5	-1.2	-1.01

The growth site impingement and the secondary crystallization that usually occur during the crystallization process of PLA and PLA-GR nanocomposites cannot be described by Avrami model. This is due to the fact that the Avrami model accounts only for the investigation of the initial stage of crystallization progression. Therefore, in order to have an insight into the phase transformation kinetics with growth site impingement, a model proposed by Tobin is utilized for studying the non-isothermal crystallization kinetics of PLA and PLA-GR nanocomposites. The plot of $\log\left(\frac{X_t}{1-X_t}\right)$ versus $\log t$ for PLA and PLA-GR nanocomposites for the dynamic heating regime is presented in Figure 4.13(a-d). The parameters associated with the crystallization rate (K_T) and Tobin exponent (n_T) are calculated from the slope and intercept values obtained from the linear fit, respectively and is reported in Table 4.4.

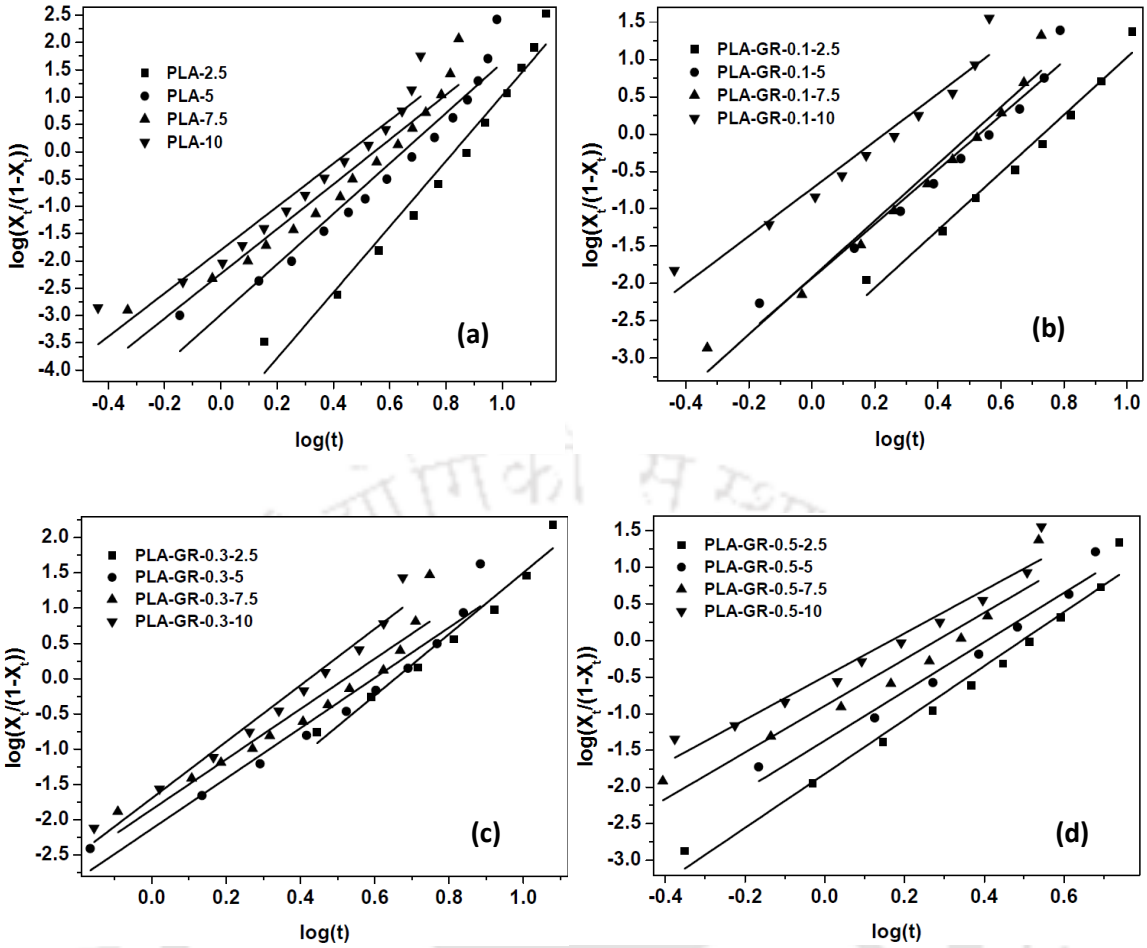

Figure 4.13. Tobin plots for non-isothermal cold crystallization of (a) PLA, (b) PLA-GR-0.1, (c) PLA-GR-0.3 and (d) PLA-GR-0.5 nanocomposites

Table 4.4. Tobin model parameters for PLA and PLA-GR nanocomposites

Sample name	n_T				Log(K_T)			
	2.5 °C/min	5 °C/min	7.5 °C/min	10 °C/min	2.5 °C/min	5 °C/min	7.5 °C/min	10 °C/min
PLA	6.0	4.6	4.1	3.9	-5.0	-3.0	-2.3	-1.9
PLA-GR-0.1	3.76	3.65	3.84	2.77	.2.73	-1.99	-1.92	-0.61
PLA-GR-0.3	4.36	3.57	3.56	4.00	-2.85	-2.13	-1.85	-1.69
PLA-GR-0.5	3.67	3.35	3.17	2.94	-1.82	-1.36	-0.89	-0.49

The Tobin exponent (n_T) values for neat PLA are obtained in the range of ~4-6 (Table 4.4) and the same exhibits a decreasing trend with increasing heating rate. This is accordance with the values reported in the literature (**Han et al., 2013**). The crystallization rate parameter, 'K_T' values corresponding to the Tobin model to demonstrate increasing tendency with respect to heating rate, suggesting the acceleration in the non-isothermal crystallization process of PLA. For PLA-GR nanocomposites, the 'n_T' values are found to be in the range of ~3-4 and are comparatively smaller than PLA for all the heating rates studied. The significant variation between the 'n_T' values for PLA and PLA-GR nanocomposites would have been resulted due to the alteration in the crystallization process of PLA. In addition to this, the 'K_T' values obtained in case of PLA-GR nanocomposites show greater deviation from that of the crystallization rate parameter values calculated for PLA, irrespective of the heating rate. This underlines the fact that the addition of GR in the PLA matrix leads to noteworthy enhancement in the non-isothermal crystallization progression of PLA. The overall trend noticed in the 'K_T' and 'n_T' values for both the PLA and PLA-GR nanocomposites are in accordance with the trend followed in case of Avrami parameters. This reveals that the physical meaning of Tobin parameters remains the same as the Avrami model.

The influence of GR on the crystallization characteristics of PLA is further explored using polarized optical microscopy (POM) observations under isothermal conditions. Prior recording the images, the neat PLA and PLA-GR nanocomposite samples are subjected to heating up to the melting temperature (180 °C) and held under the same environment for a period of 5 min to erase thermal history. Thereafter, the POM images are pictoriated for PLA and PLA-GR nanocomposites at an isothermal crystallization temperature of 120 °C in various intervals of time (0, 5th, 10th, 15th and 20th min), while cooling from the melt and the respective images are shown in Figure 4.14. With the addition of GR in the PLA matrix, advancement in the overall crystallization process of PLA is evidenced, which in turn, is

confirmed by the reduction in the induction period of nucleation process. In addition to this, the dramatic increase in the number of primary nucleation spots with respect to GR loadings is also visualized. Hence, it can be concluded that GR acts as an effective nucleating agent and thereby, fastens the rate of crystallization.

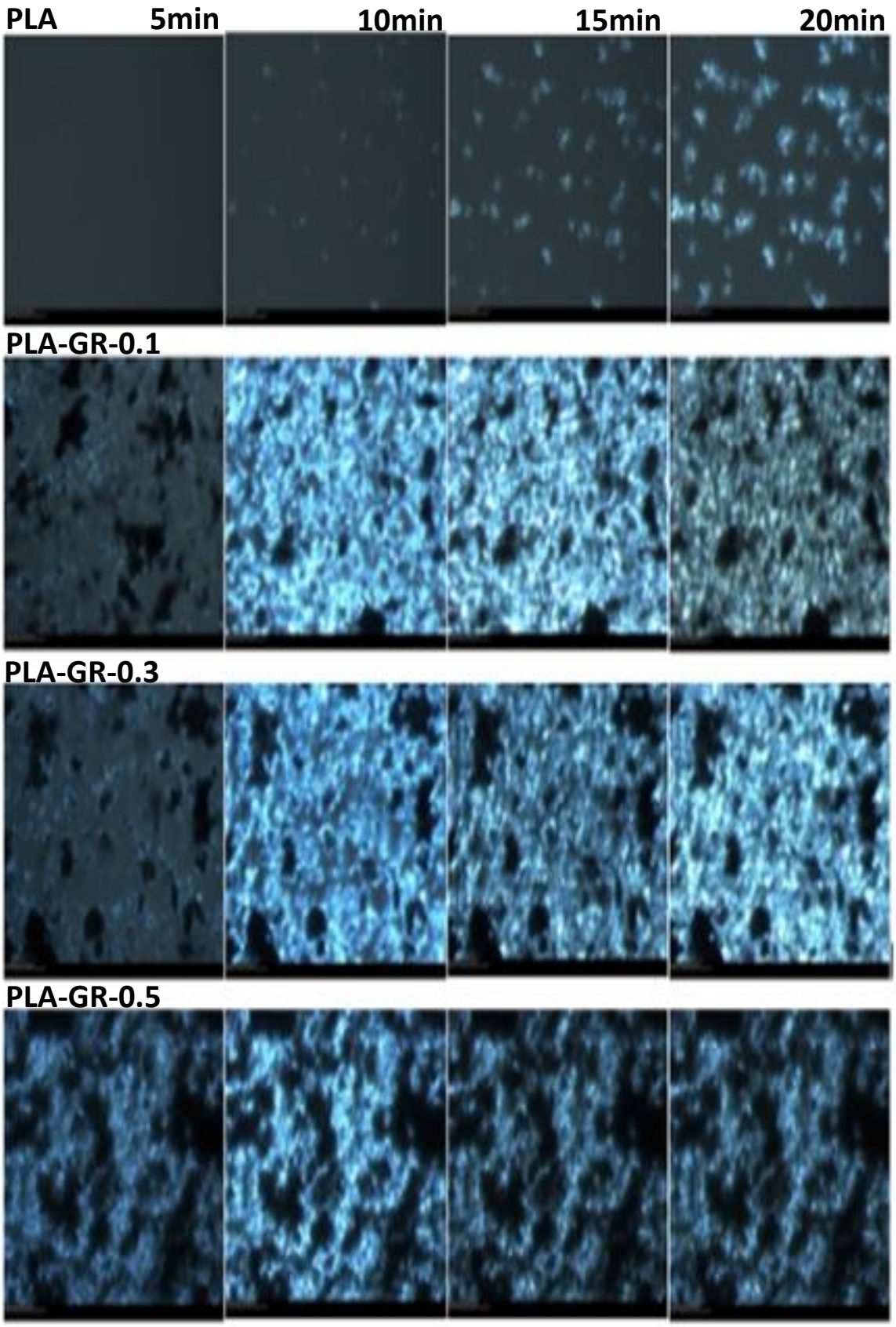

Figure 4.14. Optical microscopy images of PLA and PLA-GR nanocomposites with respect to time at 120 °C

4.6. Conclusions

The enhancement in the crystallization process with respect to the heating rate is observed for both PLA and PLA-SP nanocomposites. This phenomenon is further confirmed by the increasing trend obtained for 'K_T' values of Tobin model, with an increase in the heating rate. Furthermore, $1/t_{0.5}$ value and CRP increase with respect to SP loading that signifies an enhancement in the crystallization rate of PLA. The nucleation density amplifies significantly in the PLA matrix with an increase in the SP content (wt %), which is verified by POM studies. The radial spherulite growth rate increases linearly with time, confirming that the growth rate is not dependent on the spherulite diameter. For both PLA and PLA-GR nanocomposites, the crystallization exotherm shifts to higher temperature side with respect to the heating rate, which is indicative of the faster rate of crystallization process. The crystallization rate parameter values of PLA-GR nanocomposites obtained by both Avrami and Tobin models show increasing trend with respect to neat PLA demonstrating the nucleation effect of GR. The similar physical significance provided by both the models suggests the suitability of the same in predicting the crystallization kinetic behavior of PLA and PLA-GR nanocomposites. The nucleating ability of GR in the PLA matrix is revealed by the reduction in the nucleation induction period, which is observed by POM studies.

CHAPTER 4

Crystallization Studies of Graphene and Sucrose Palmitate Reinforced PLA Nanocomposites

This chapter investigates the effect of sucrose palmitate (SP) and graphene (GR) on the crystallization kinetics of poly(lactic acid) (PLA). The non isothermal cold crystallization kinetic study for PLA, PLA-SP and PLA-GR nanocomposites was carried out using differential scanning calorimetry (DSC) at different heating rates of 2.5, 5, 7.5 and 10 °C/min. The obtained kinetic data were analyzed using crystallization kinetic models such as Avrami and Tobin methods. The decreasing trend obtained in the Avrami as well as Tobin exponent (n and n_T, respectively) with respect to neat PLA revealed the nucleating effect of both the reinforcements. Polarized optical microscopy (POM) was used to observe the growth of the spherulites in the PLA, PLA-GR and PLA-SP nanocomposites. With respect to addition of GR and SP in the PLA matrix, the reduction in the nucleation induction time and increment in the number of nucleation sites were reflected in the POM analysis.This part of work has been published in ***Journal of Polymer Research***, **2015**, 175, 1-14 and ***Polymer Bulletin****,* **2015***,* DOI 10.1007/s00289-015-1468-3.

4.1. Introduction

Crystallization is considered as one of the prime factors that shows a profound impact on the key characteristics such as mechanical and barrier effects of PLA. As processing of polymers are carried out under dynamic conditions in practical cases; it is essentially worth to understand the crystallization behaviour of PLA in the presence of graphene and sucrose palmitate under non-isothermal conditions (**Mubarak et al., 2001; Liu et al., 2010**). After incorporation of any filler (or additive) in the polymer matrix, investigating the crystallization behavior of the resultant composite systems becomes essential. This is because of the incorporated additives affecting the crystallization process of polymers via two ways. First, the additives can act as nucleating agents leading to an enhancement in crystallization temperature, which have a positive response on the crystallization characteristics. Second, additives can impede the movement and diffusion of molecular chains of polymer to the surface of the growing nucleus of crystallites in the composite system. This phenomenon may lead to a reduction in crystallization temperature, which has a negative response to the crystallization process. In view of this, the current chapter is focused on investigation of non-isothermal cold crystallization behavior of PLA, PLA-GR and PLA-SP nanocomposites using differential scanning calorimetry under the dynamic heating regime (2.5, 5, 7.5 and 10 °C/min). Further, the experimental crystallization data are analyzed using Avrami and Tobin models to derive information about the mechanism of the nucleation process in PLA, PLA-SP and PLA-GR nanocomposites. In addition to this, crystallization rate parameter (CRP) is determined for PLA, PLA-SP and PLA-GR nanocomposites using the Avrami parameters (*n* and *K*). The influence of fillers (SP and GR) as a nucleating agent and its impact on morphology as well as growth rate of spherulites is studied by polarized optical microscopy (POM) under isothermal crystallization temperature (120 °C) at different intervals (5, 10, 15 and 20 min) of the cold crystallization process.

4.2. Experimental

4.2.1. Materials

The chemicals used for the synthesis of PLA-SP and PLA-GR nanocomposites are discussed in section 3.2.1 and 2.2.1, respectively.

4.2.2. Synthesis of PLA-SP and PLA-GR nanocomposites

The synthesis procedure for the fabrication of PLA-SP and PLA-GR nanocomposites is discussed in section 3.2.2 and 2.2.3, respectively.

4.3. Characterization

4.3.1. Differential scanning calorimetry

Crystallization behavior of PLA, PLA-SP and PLA-GR nanocomposites were studied using a differential scanning calorimetry (Mettler Toledo-1 series). Samples (10±0.5 mg) were hermetically sealed in aluminum pans and heated from 25 to 180 °C at various heating rates of 2.5, 5, 7.5 and 10 °C/min in an inert atmosphere (N_2 flow, 50 mL/min). All the samples were first heated from 25 to 180 °C and held at this temperature for 5 min in order to eliminate the effect of thermal and processing history. Glass transition temperature (T_g), cold crystallization temperature (T_{cc}), the enthalpy change at T_{cc} (ΔH_{cc}), melting temperature (T_m) and the enthalpy of fusion at T_m (ΔH_m) for pure PLA, PLA-SP and PLA-GR nanocomposite films were determined from the DSC thermograph during the second heating cycle.

4.3.2. Polarized optical microscopy

The nucleation and spherulite growth in PLA, PLA-SP and PLA-GR nanocomposites were observed using Leica DM 2500P polarizing optical microscope fitted with a QICAM FAST1394 camera. The Linkam LTS420 temperature control stage was used to study the morphological changes of the film at isothermal crystallization temperature (120 °C). PLA, PLA-SP and PLA-GR nanocomposite films with the thickness of about 60 μm were first melted at 180 °C for 5 min in order to erase thermal histories, and immediately transferred to the temperature of 120 °C for isothermal crystallization. The micrographs of growing

spherulites were pictoriated at a specific interval of time before the impingement of spherulites.

4.4 Theory

4.4.1. Relative degree of crystallinity

In order to determine the relative degree of crystallinity ($X(t)$), as a function of crystallization time, the exotherms that correspond to cold crystallization of PLA, PLA-SP and PLA-GR nanocomposites is integrated. $X(t)$ as a function of temperature is given by the following equation.

$$X(t) = \frac{\int_{T_0}^{T} \left(\frac{dH_C}{dT} \right) dT}{\int_{T_0}^{T_\infty} \left(\frac{dH_C}{dT} \right) dT} \tag{4.1}$$

where, T_0 and T_∞ denotes the onset and final cold crystallization temperature, respectively (**Pei et al., 2010; Vasanthan et al., 2011**). The crystallization time (t) and the respective temperature (T) are related by the following expression:

$$t = \frac{T - T_0}{\phi} \tag{4.2}$$

where, ϕ is the heating rate (**Pei et al., 2010; Vasanthan et al., 2011**).

4.4.2. Crystallization half time

The half-time of crystallization ($t_{1/2}$) is defined as the time required to achieve 50% of the crystallization process. Determination of crystallization half-time is of prime importance in understanding the kinetics of crystallization process and is obtained using the following expression (**Ravari et al., 2013; Qiu et al., 2011; Tsuji et al., 2009**):

$$t_{1/2} = \left(\frac{\ln 2}{k} \right)^{1/n} \tag{4.3}$$

4.4.3. Avrami model

The kinetic parameters corresponding to the non-isothermal crystallization process of PLA, PLA-SP and PLA-GR nanocomposites are determined using the "Avrami model", which is expressed as follows:

$$X(t) = 1 - \exp\left(-kt^{n}\right) \tag{4.4}$$

The eq. (4.4) is expressed in the non-linear form as

$$\log\left[-\ln\left(1 - X(t)\right)\right] = \log k + n \log t \tag{4.5}$$

where, $X(t)$ refers to the relative crystallinity at any time "t", n corresponds to the Avrami exponent, k is the overall kinetic constant (**Bao et al., 2013**). The Avrami exponent (n) and the crystallization rate constant (k) are determined using the slope and intercept values obtained from the linear plot of log [- ln (1 - $X(t)$)] versus log t.

4.4.4. Tobin model

The Tobin equation is given by the following expression:

$$X_t = \frac{K_T t^{n_T}}{1 + K_T t^{n_T}} \tag{4.6}$$

where, X_t refers to the relative crystallinity at time 't', whereas, K_T and n_T are the Tobin parameters related to crystallization rate constant and exponent, respectively (**Han et al., 2013**). The type of nucleation and growth mechanism associated with the non-isothermal crystallization process of PLA, PLA-SP and PLA-GR nanocomposites are derived from the values of Tobin exponent (n_T). The eq. (4.6) is rearranged as follows:

$$\log\left(\frac{X_t}{1 - X_t}\right) = \log K_T + n_T \log t \tag{4.7}$$

4.5. Results and discussion

4.5.1. Influence of sucrose palmitate on the non-isothermal cold crystallization kinetics of PLA

Figure 4.1 shows the non-isothermal crystallization and melting behaviors of neat PLA and PLA-SP nanocomposites investigated by DSC at various heating rates (2.5, 5, 7.5, and 10). The curves show an exothermic cold crystallization peak at about 100-121°C for neat PLA films, and at 105-125 °C for PLA-SP nanocomposites. The curves also present an endothermic peak related to melting at about 148-151°C for neat PLA and PLA-SP nanocomposites. It can be seen from Figure 4.1 that crystallization temperatures (T_{cc}) shift gradually to the higher temperature side with respect to heating rates for both PLA and PLA-SP nanocomposites. This indicates that PLA requires excess time for crystallization at a higher heating rate (shown in Figure 4.2(a)). This phenomenon is related to the lower heat conductivity of the PLA, which delays crystallization with increasing heating rates (**Ravari et al., 2013**). For a lower heating rate (2.5 °C/min), two melting peaks for both PLA and PLA-SP composites are observed. The melting peak that corresponds to the lower temperature is ascribed to the melting process of imperfect crystalline structures of PLA formed during the primary phase of the cold crystallization process. The higher temperature melting peak is attributed to the melting of the perfect crystalline structure of PLA formed at the later phase of the cold crystallization process as a result of increased thickness of lamellae (**Yasuniwa et al., 2008; Kong et al., 2003; Fukushima et al., 2009; Fortunati et al., 2012**). In contrast, for a heating rate of 5 °C/min, the disappearance of the double melting peak is observed for both PLA and PLA-SP nanocomposites. With the further increase in the heating rate i.e. 10 °C/min, the cold crystallization peak of PLA and PLA-SP nanocomposites becomes very small and hard to detect, demonstrating the formation of less perfect crystal structures due to faster heating process (**Ravari et al., 2013; Nofar et al., 2011**). The T_g values for all the samples with a constant heating rate remain similar, but the T_g for each material increases with the rise in the heating rate, owing to thermal delay (shown in Figure 4.2(b)) (**Ravari et**

al., 2013; Nofar et al., 2011). The enthalpy of cold crystallization (ΔH_{cc}) decreases for both PLA and PLA-SP composites with an increase in the heating rate. Because PLA molecular chains do not possess sufficient time to relax before the formation of crystal structures when subjected to faster heating process (**Ravari et al., 2013; Nofar et al., 2011**). The melting enthalpy (ΔH_m) also varies at a same pace as ΔH_{cc} indicating that melting behaviors mainly arise due to melting of crystal structures formed during the cold crystallization process (**Ravari et al., 2013; Nofar et al., 2011).**

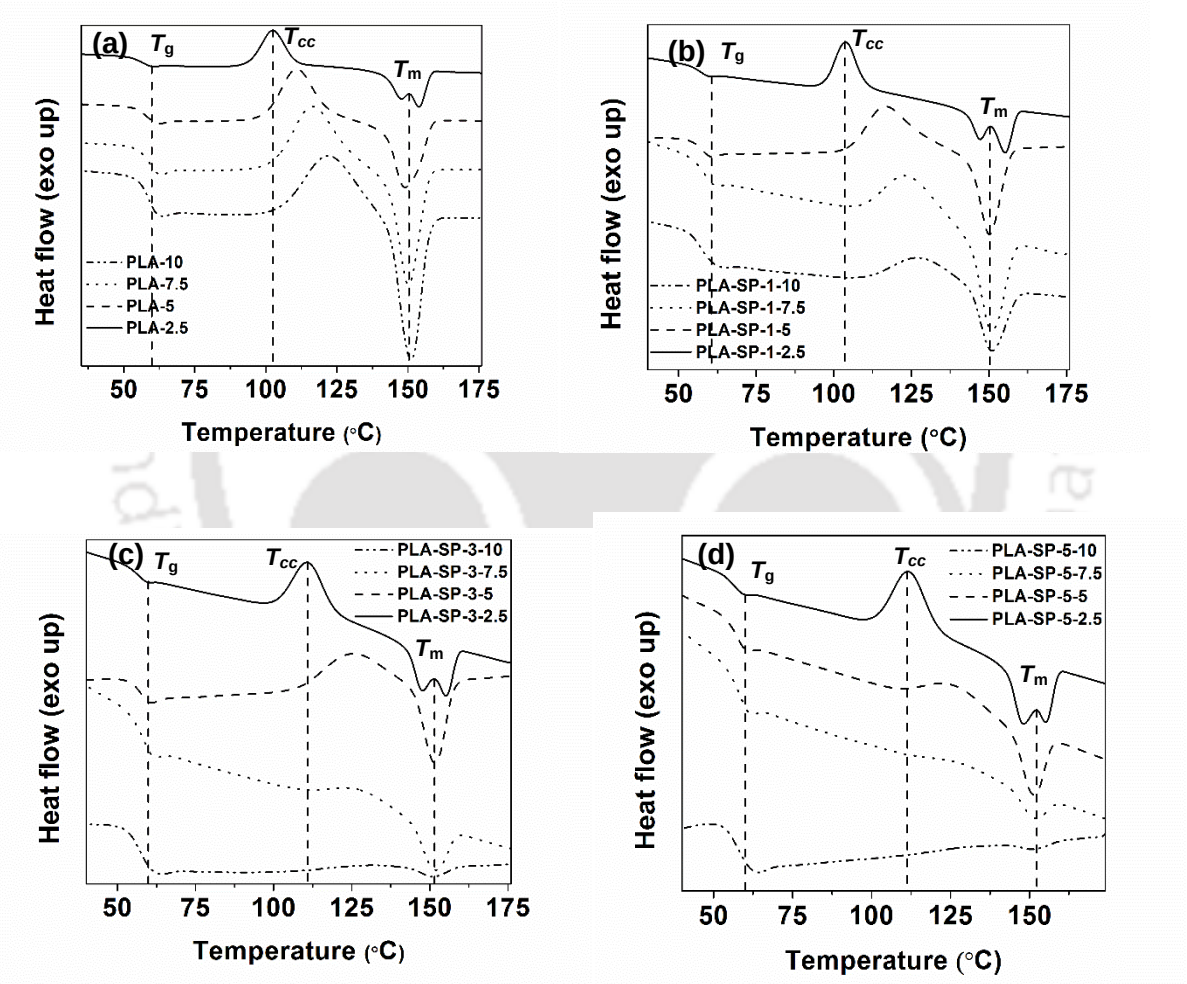

Figure 4.1. DSC thermographs at different heating rates of 2.5, 5, 7.5 and 10 °C/min for (a) neat PLA, (b) PLA-SP-1, (c) PLA-SP-3 and (d) PLA-SP-5 nanocomposites

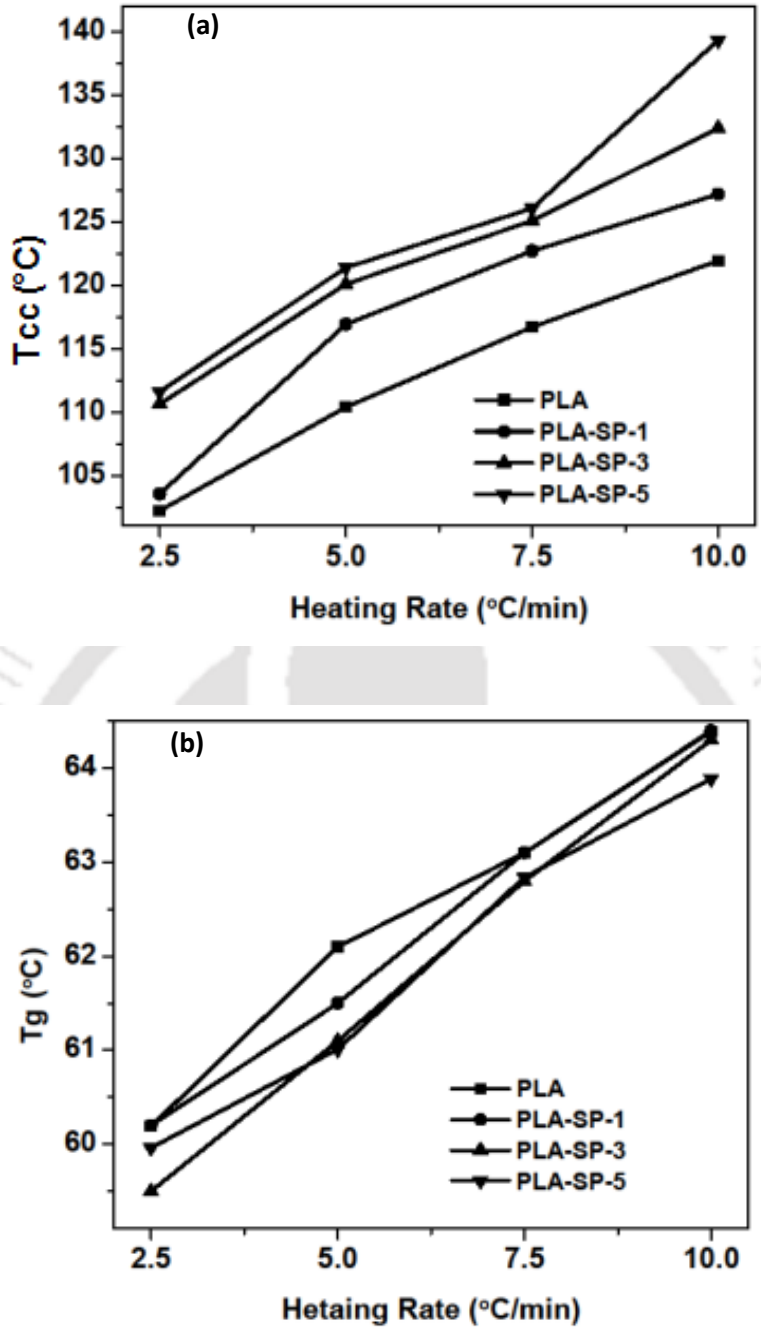

Figure 4.2. Variation of T_{cc} (a) and T_g (b) with respect to heating rate

The plots of relative crystallinity versus crystallization time for neat PLA and PLA-SP nanocomposites are portrayed in Figure 4.3. The relative crystallinity curves of both PLA and its nanocomposites obtained at various heating rates exhibit sigmoidal shape characteristic curves, which are attributed to the impingement of spherulites at the later stage of the crystallization process (**Liu et al., 2010; Wang et al., 2012**). From these curves, the lag effects of heating rates on the crystallization process can be observed. Figure 4.3 also

shows that at higher heating rates, PLA matrices have a shorter time of crystallization. This means that crystallization rates increased with the incorporation of SP (**Ravari et al., 2013; Wu et al., 2007**).

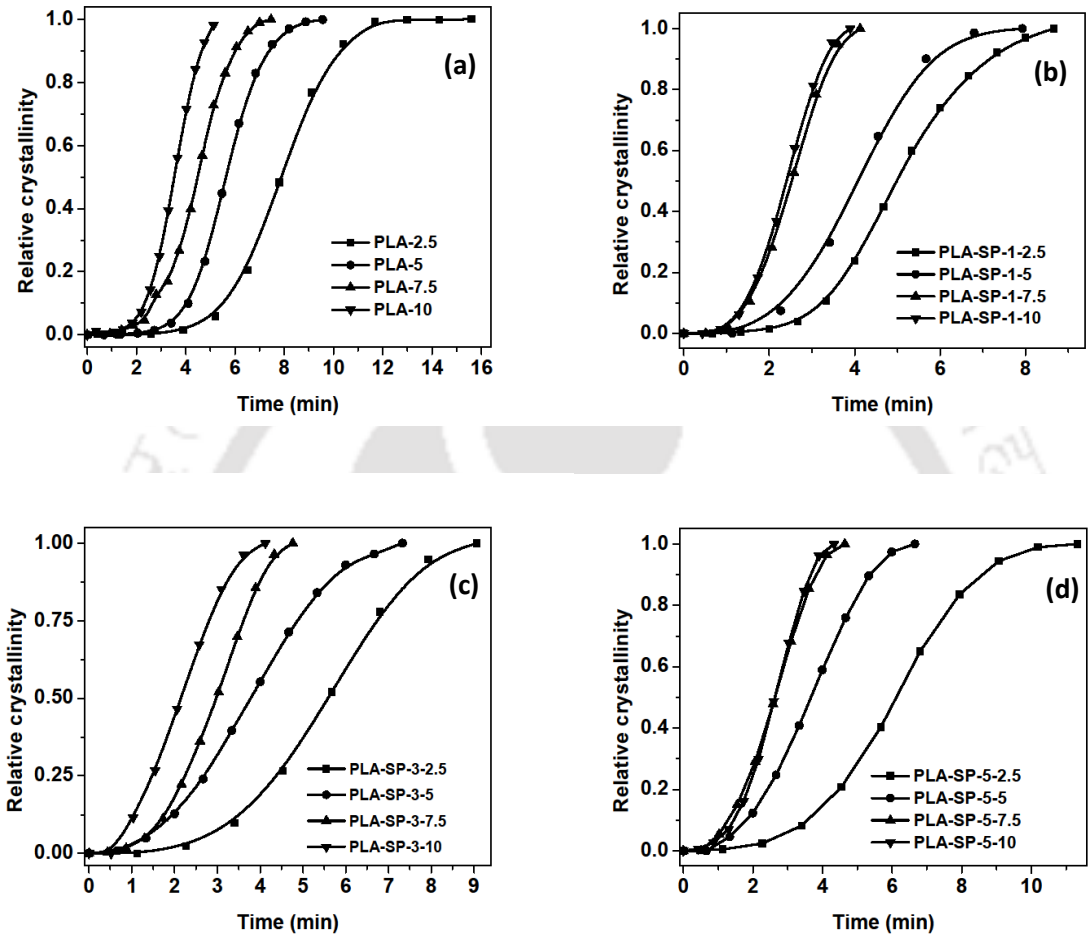

Figure 4.3. Relative crystallinity versus crystallization time at different heating rates for (a) neat PLA, (b) PLA-SP-1, (c) PLA-SP-3 and (d) PLA-SP-5 nanocomposites

In general, shorter the $t_{1/2}$ values, faster will be the crystallization process. With increasing the heating rate, $t_{1/2}$ values for both PLA and its composites exhibit decreasing trends indicating shorter crystallization completion times. Moreover, the $t_{1/2}$ values for PLA-SP nanocomposites are observed to be lower in comparison with neat PLA. This is due to the acceleration of the overall cold crystallization process after reinforcement of SP. However, the higher $t_{1/2}$ values observed for PLA and PLA-SP nanocomposites at lower heating rates

may be attributed to the secondary crystallization process. The variation of $t_{1/2}$ with ϕ for neat PLA and its composites is clearly seen from Figure 4.4. From the Figure, one can distinctly interpret the influence of ϕ and SP loading on the overall crystallization rate of PLA nanocomposites. It can be noticed that the $1/t_{1/2}$ value shoots up for PLA-SP nanocomposites when compared to neat PLA. Hence, it becomes mandatory to discuss the effect of SP and its content (wt %) on the crystallization performance of PLA. Nucleation and growth are the two important aspects associated with the overall crystallization process of polymers (**Yi et al., 2007**)**.** The SP incorporated in the PLA matrix may engage in two distinct or contending functions influencing the crystallization process. On one hand, SP may involve in providing nucleation effect in order to fasten the non-isothermal crystallization process of PLA. On the other hand, there is a possibility that PLA chains will be present in an exceedingly intertwined during the melt state. Therefore, while due course of the crystallization process, PLA molecular segments must overwhelm definite energy barriers in order to migrate and bind onto the surface of the growing crystal front. The SP may serve as a cross-linking agent that obstructs the migration of PLA molecular fragments. This in turn hampers the growth of crystalline structures by restraining the nearby molecular segments of polymer during strong synergistic interactions exist between PLA and SP. There is a significant difference in the $1/t_{1/2}$ values between PLA and PLA-SP-1 nanocomposite. This is due to the predominant nucleation effect induced by 1 wt% loading of SP enhancing the crystallization of PLA. However, further increase in the $1/t_{1/2}$ values for higher loadings of SP is not observed. Although SP might contribute in providing additional nucleation spots at higher loadings, the presence of more SP content may also create a much more appreciable detention consequence on the crystal growth process of PLA. Since the detention effect masks the nucleation effect, the overall crystallization rate is observed to be slow down at higher loadings of SP.

Zhang et al. (**1994**) introduced a method to evaluate the crystallization rate parameter (CRP), which describes the effect of filler on the crystallization rate of polymer quantitatively.

Figure 4.4 shows the plot of $1/t_{1/2}$ versus ϕ for both PLA and its nanocomposites. The CRP is obtained from the slope of a linear plot of $1/t_{1/2}$ versus ϕ. The values of CRP are found to be 0.0272, 0.0276, 0.0313, and 0.0335 for PLA, PLA-SP-1, PLA-SP-3 and PLA-SP-5, respectively. The CRP values obtained for PLA-SP nanocomposites point out that SP slightly enhances the cold crystallization of PLA matrix.

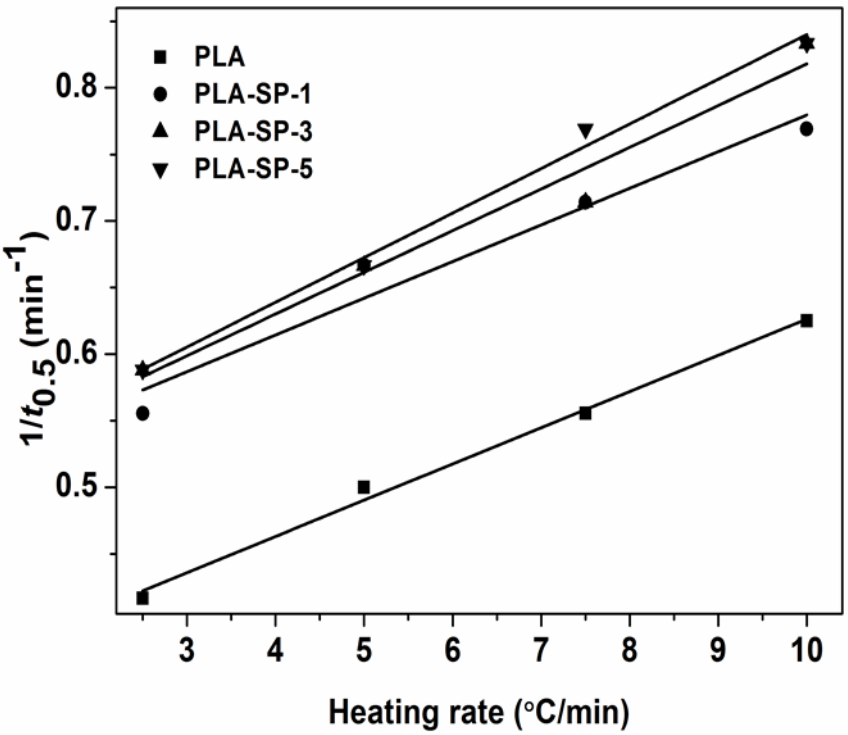

Figure 4.4. Effect of SP loading on the crystallization rate parameter (CRP)

A typical relative crystallinity curves for neat PLA, PLA-SP-1, PLA-SP-3 and PLA-SP-5 are shown in Figure 4.3(a-d) and the corresponding Avrami plots for the same are presented in Figure 4.5(a-d). It can be noticed from Figure 4.5(a-d), good linearity is obtained for all the plots. This suggests that the theory seems to be helpful to appropriately elucidate the non-isothermal crystallization of PLA nanocomposite systems.

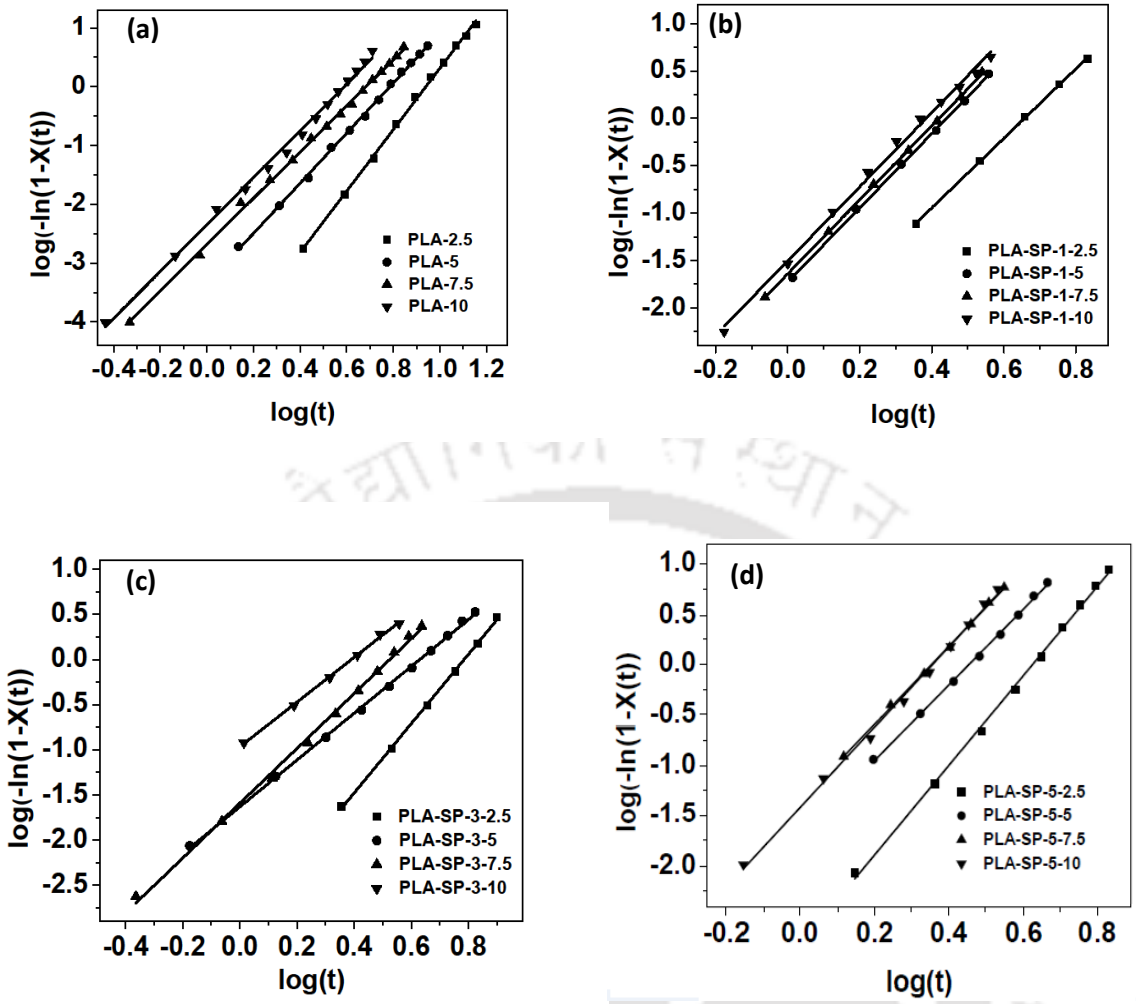

Figure 4.5. Avrami plots for non-isothermal cold crystallization of (a) PLA, (b) PLA-SP-1, (c) PLA-SP-3 and (d) PLA-SP-5 nanocomposites

In the current work, *n* values (presented in the Table 4.1) for neat PLA lie in the range of 4-5, which is in accordance with literature data (**Fortunati et al., 2012; Nofar et al., 2011**). This suggests that the 3-dimensional (3D) growth of PLA crystals takes place during the non-isothermal cold crystallization process and crystal growth is in disk-like nature by homogeneous nucleation. The *n* values for PLA-SP nanocomposites are found to be in the range of ~2.5-4, which is slightly lower in comparison with neat PLA. This is ascribed to the faster crystallization process that does not provide adequate time for the crystals to grow in three dimensions, which results in the heterogeneous nucleation process (**Fortunati et al., 2012; Nofar et al., 2011**).

Table 4.1. Avrami model parameters for PLA and PLA-SP nanocomposites

S:No	Sample	*n*				log(*k*)			
		2.5 °C/min	5 °C/min	7.5 °C/min	10 °C/min	2.5 °C/min	5 °C/min	7.5 °C/min	10 °C/min
1	PLA	4.8	4.2	3.9	4	-4.9	-3.3	-2.6	-2.3
2	PLA-SP-1	3.9	3.9	3.9	3.7	-2.4	-1.7	-1.6	-1.5
3	PLA-SP-3	3.8	3.3	2.5	2.4	-3	-1.6	-1.5	-1.3
4	PLA-SP-5	3.8	3.5	2.9	2.7	-2.8	-1.7	-1.4	-1.3

The Avrami model used for studying the crystallization kinetics of PLA and PLA-SP nanocomposites is merely appropriate for investigating the early phase of the crystallization process. This is due to the fact that the Avrami model does not involve in describing the growth site impingement as well as the secondary crystallization process. In order to investigate the phase-transformation kinetics with growth site impingement in the non-isothermal crystallization kinetics of PLA and PLA-SP nanocomposites, Tobin model is utilized. The Tobin exponent (n_T), provides information about the type of nucleation and growth mechanism involved in the non-isothermal crystallization process. Tobin plots for PLA and PLA-SP nanocomposites obtained for different heating rates are shown in Figure 4.6(a-d), in which $\log\left(\frac{X_t}{1-X_t}\right)$ is plotted against $\log t$. Tobin parameters (n_T and K_T) are determined from the slope and intercept of the linear fit, respectively and the same is summarized in Table 4.2.

It can be observed from Table 4.2, that the Tobin exponent, 'n_T' value for PLA is in the range of 4-6. It decreases with respect to heating rate and the obtained value is comparable with literature data (**Han et al., 2013**). Tobin parameter, K_T, exhibits the increasing trend with an increase in the heating rate, which points out the faster crystallization process. In

case of PLA-SP nanocomposites, the 'n_T' values show decreasing trend with respect to the heating rate. However, the values are found to be in the range of ~3-5, which is relatively smaller in comparison with neat PLA, irrespective of the heating rate. This difference in the 'n_T' values suggests that the reinforcement of SP in the PLA matrix alters the crystallization process of PLA. It is also seen from Table 4.2, that the 'K_T' values obtained for PLA-SP nanocomposites are higher when compared to neat PLA. This phenomenon indicates that the SP accelerates the non-isothermal crystallization process of PLA. The findings of the Tobin model discussed above are similar to the trend obtained for Avrami parameters. Hence, the Tobin parameters also describe the same physical significance analogous to that of Avrami model (**Maiti et al., 2012**).

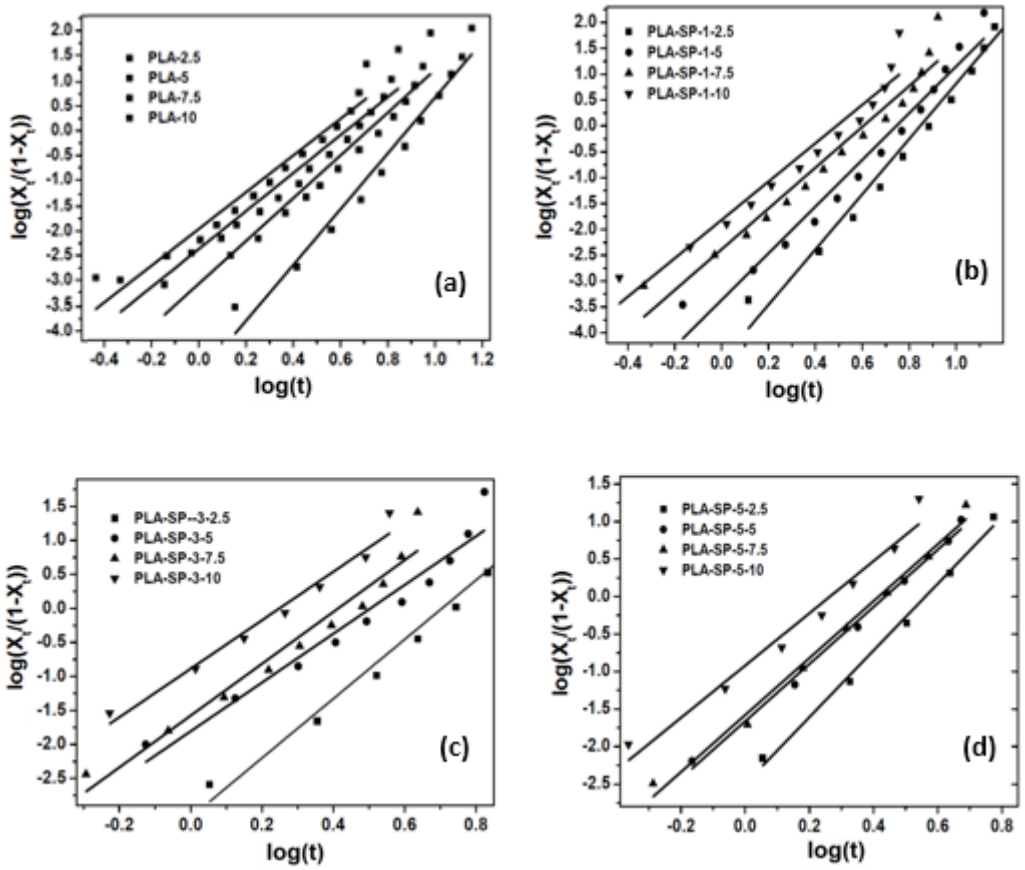

Figure 4.6. Tobin plots for non-isothermal cold crystallization of (a) PLA, (b) PLA-SP-1, (c) PLA-SP-3 and (d) PLA-SP-5 nanocomposites

Table 4.2. Tobin model parameters for PLA and PLA-SP nanocomposites

S:No	Sample	n_T				Log(K_T)			
		2.5 °C/min	5 °C/min	7.5 °C/min	10 °C/min	2.5 °C/min	5 °C/min	7.5 °C/min	10 °C/min
1	PLA	6.0	4.6	4.1	3.9	-5.0	-3.0	-2.3	-1.9
2	PLA-SP-1	5.3	4.5	3.9	3.7	-4.5	-3.3	-2.2	-1.8
3	PLA-SP-3	4.3	3.6	3.8	3.5	-3.1	-1.8	-1.6	-1.3
4	PLA-SP-5	4.4	3.8	3.7	3.5	-2.5	-1.7	-1.6	-1.1

The influence of SP as a nucleation agent on the crystallization behavior of PLA matrix is performed using a polarized optical microscope as shown in Figure 4.7. PLA and PLA-SP nanocomposites are heated up to 180 °C and the hot stage containing samples are maintained at the same temperature for a time span of 5 min to remove thermal history. Optical micrographs are pictoriated in the 0, 5^{th}, 10^{th}, 15^{th} and 20^{th} min at 120 °C after cooled from melt state at 180 °C for PLA and PLA-SP composites. In the current study, the process of nucleation and growth control the overall crystallization kinetics of PLA. After incorporation of SP in the PLA matrix, an increase in the overall crystallization rate of PLA occurs. This is reflected through the diminution of the nucleation induction period followed by an increment in additional primary nucleation sites. For the PLA-SP nanocomposites, the nucleation density of PLA spherulites is found to increase at 5 min, 10 min, 15 min and 20 min in comparison with neat PLA (see Figure 4.7). In addition to this, an appreciable increase in the nucleation density with respect to SP loading is noticed, which signifies the better dispersion of SP in the PLA matrix. Therefore, more crystals have the ability to undergo nucleation and subsequently grow in the enhanced surface area of the interfaces owing to increment in the number of nucleating sites.

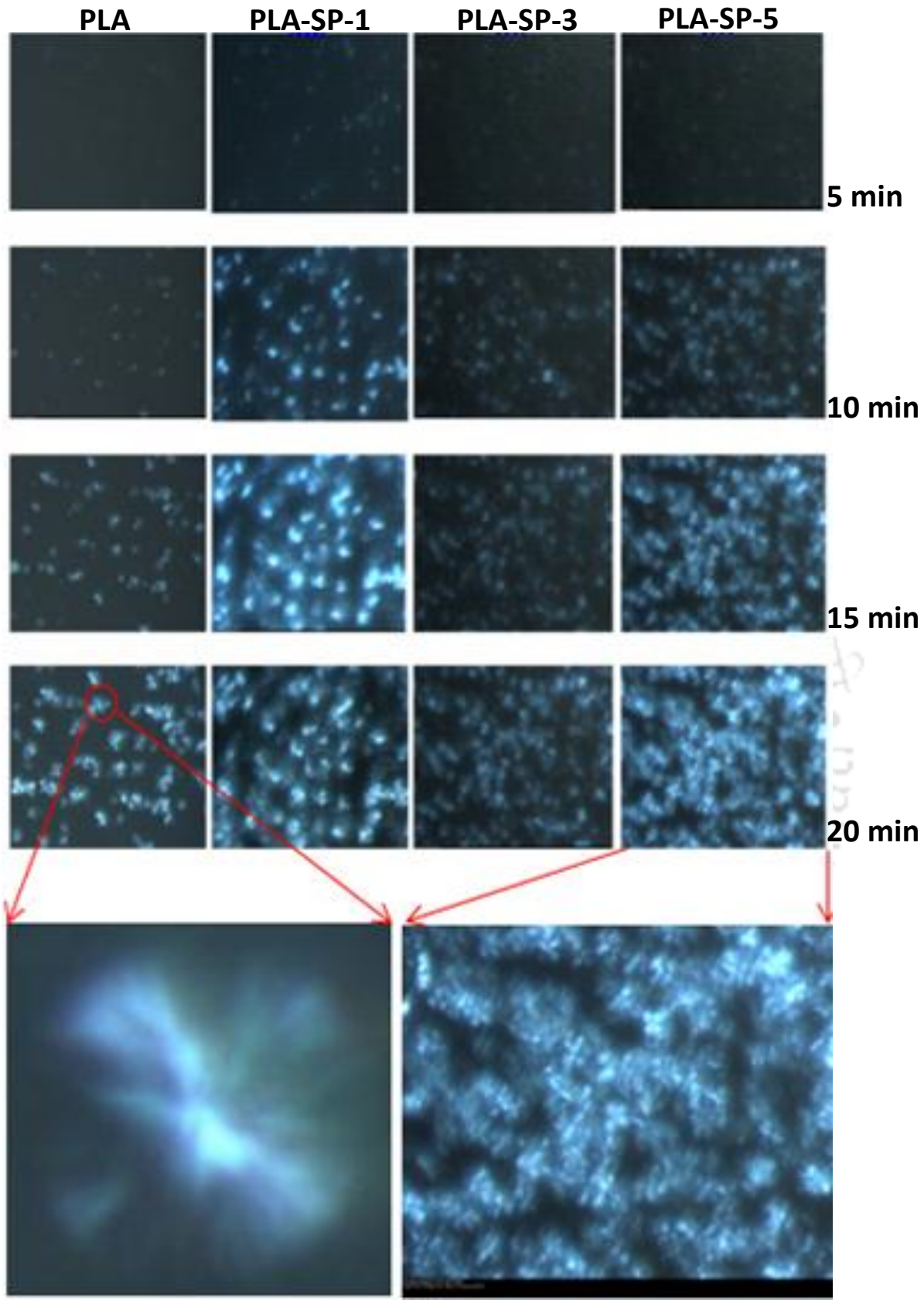

Figure 4.7. Optical microscopy images of PLA and PLA-SP nanocomposites with respect to time at 120 °C

For neat PLA and PLA-SP composites, the radial spherulite growth rates are measured as a function of time. Figure 4.8 represents the variation of spherulite radius with time at 120 °C. For both PLA and PLA-SP composites, the size of the spherulites amplifies linearly with respect to time. This conveys that the growth rate is not dependent on the spherulite diameter. In case, if it is considered that all the crystallizable species are not eliminated from the growing spherulite phase, they are expected to escalate on the surface of the growing crystal front. This in turn may consequently impede the migration of the crystallizable species from the melt phase to the growing front. This phenomenon leads to a deflection from linear spherulite growth after a certain diameter of spherulite attained. As such, no deflection from linearity for growth of spherulites is noticed in the PLA-SP nanocomposite system (Figure 4.8), it can be inferred that the SP is not eliminated during the spherulite growth process. Similar results are reported for PLA-carbon nanotubes (CNT) nanocomposites by **Xu et al.** (**2011**).

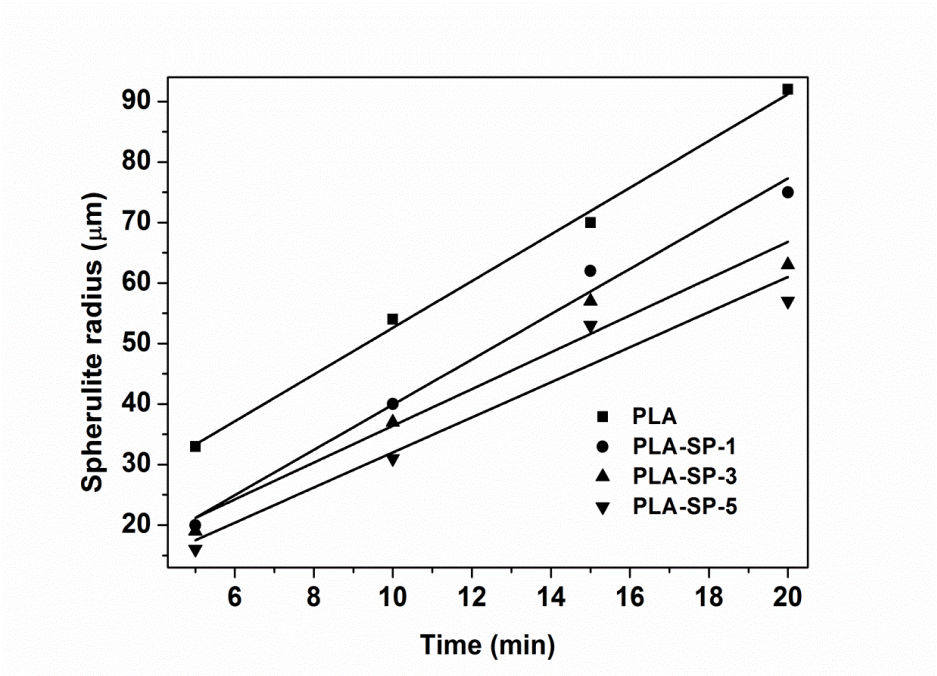

Figure 4.8. Variation of spherulite radius versus time for PLA and PLA-SP nanocomposites

4.5.2. Influence of graphene on the non-isothermal cold crystallization kinetics of PLA

The DSC thermographs for neat PLA and PLA-GR nanocomposites obtained at different heating regime (2.5, 5, 7.5 and 10 °C/min) are analyzed for understanding the non-isothermal crystallization and melting behaviors (Figure 4.9). Both PLA and PLA-GR nanocomposites display similar T_g value for a single heating rate. However, the shift in the T_g values is observed for each sample with increasing heating rate, which is attributed to thermal delay (**Ravari et al., 2013; Yasuniwa et al., 2008**). A cold crystallization exotherm is observed in the temperature range of 99-120 °C for neat PLA and 100-126 °C for PLA-GR nanocomposites. The steady shift in the T_{cc} to the greater temperature values with the rise in heating rate can be observed for PLA and PLA-GR nanocomposites (Figure 4.9). This is ascribed to the lower heat transfer coefficient, which prolongs the time required for the cold crystallization process at higher heating rate (**Nofar et al., 2011**). A peak corresponding to melting endotherm is noticed for all the samples in the temperature ranging from 150-156 °C (Figure 4.9). Interestingly, it is observed that all the samples exhibited a double melting endotherm for a heating rate of 2.5 °C/min. The endotherm observed at lower and higher temperature corresponds to the melting phenomenon of imperfect and perfect crystalline structures of PLA developed at the primary and secondary phase of the cold crystallization process, respectively (**Fukushima et al., 2009; Fortunati et al., 2012**). However, the bimodal melting endotherm is not noticed for both PLA and PLA-GR nanocomposites in case of further heating rates.

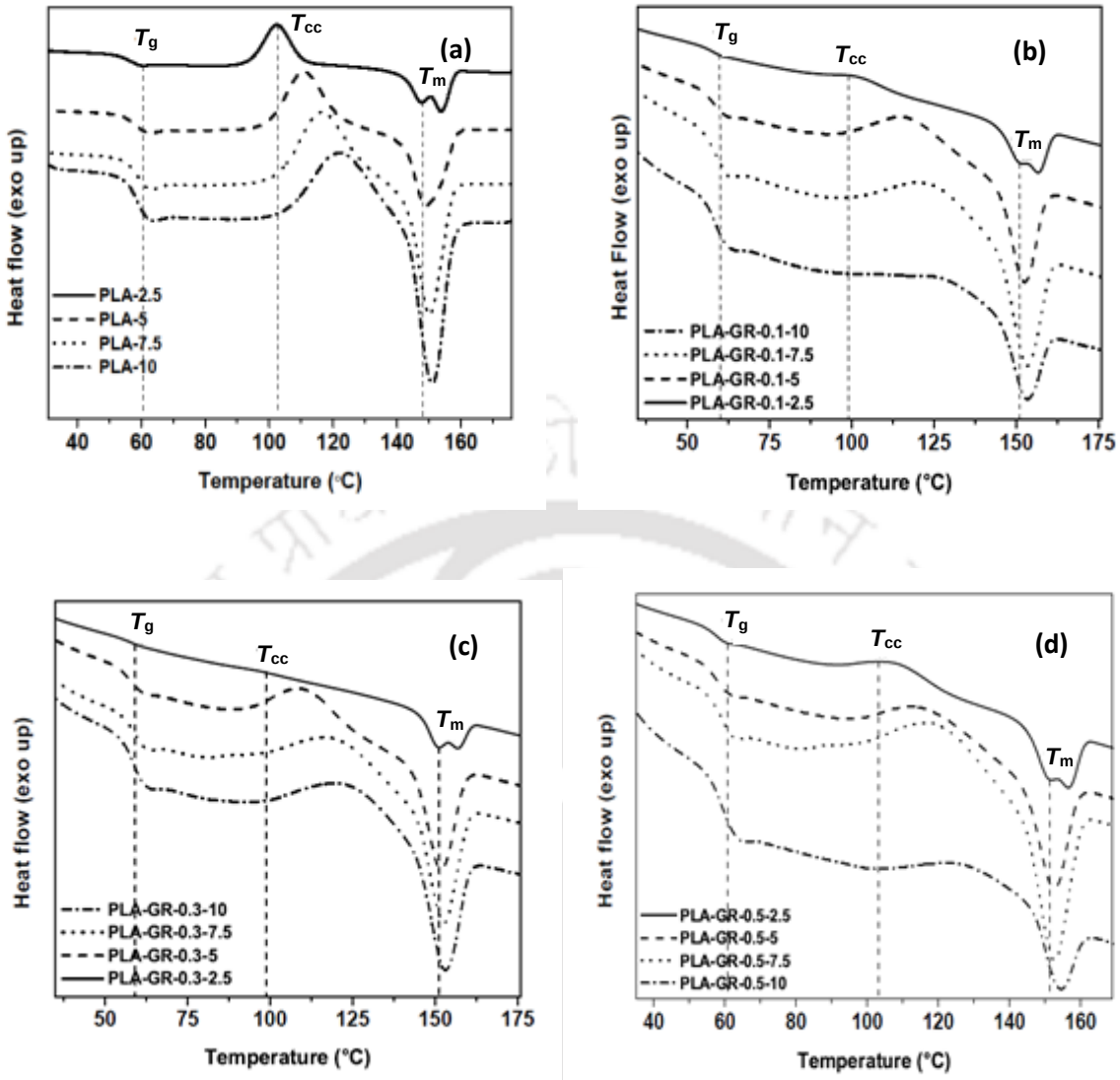

Figure 4.9. DSC thermographs at different heating rates of 2.5, 5, 7.5 and 10 °C/min for (a) neat PLA, (b) PLA-GR-0.1, (c) PLA-GR-0.3 and (d) PLA-GR-0.5 nanocomposites

The values of relative crystallinity are plotted as a function of crystallization time for both neat PLA as well as PLA-GR nanocomposites and the same is portrayed in Figure 4.10. The Figure displays a characteristic sigmoidal shaped relative crystallinity curves for all the samples at different heating regime. This discloses the phenomenon of impingement of spherulites that occurred at the advanced phase of the cold crystallization process (**Wang et al., 2012**). In addition to this, in case of greater heating rates, the lag effects are not experienced on the crystallization behavior of both PLA and PLA-GR nanocomposites.

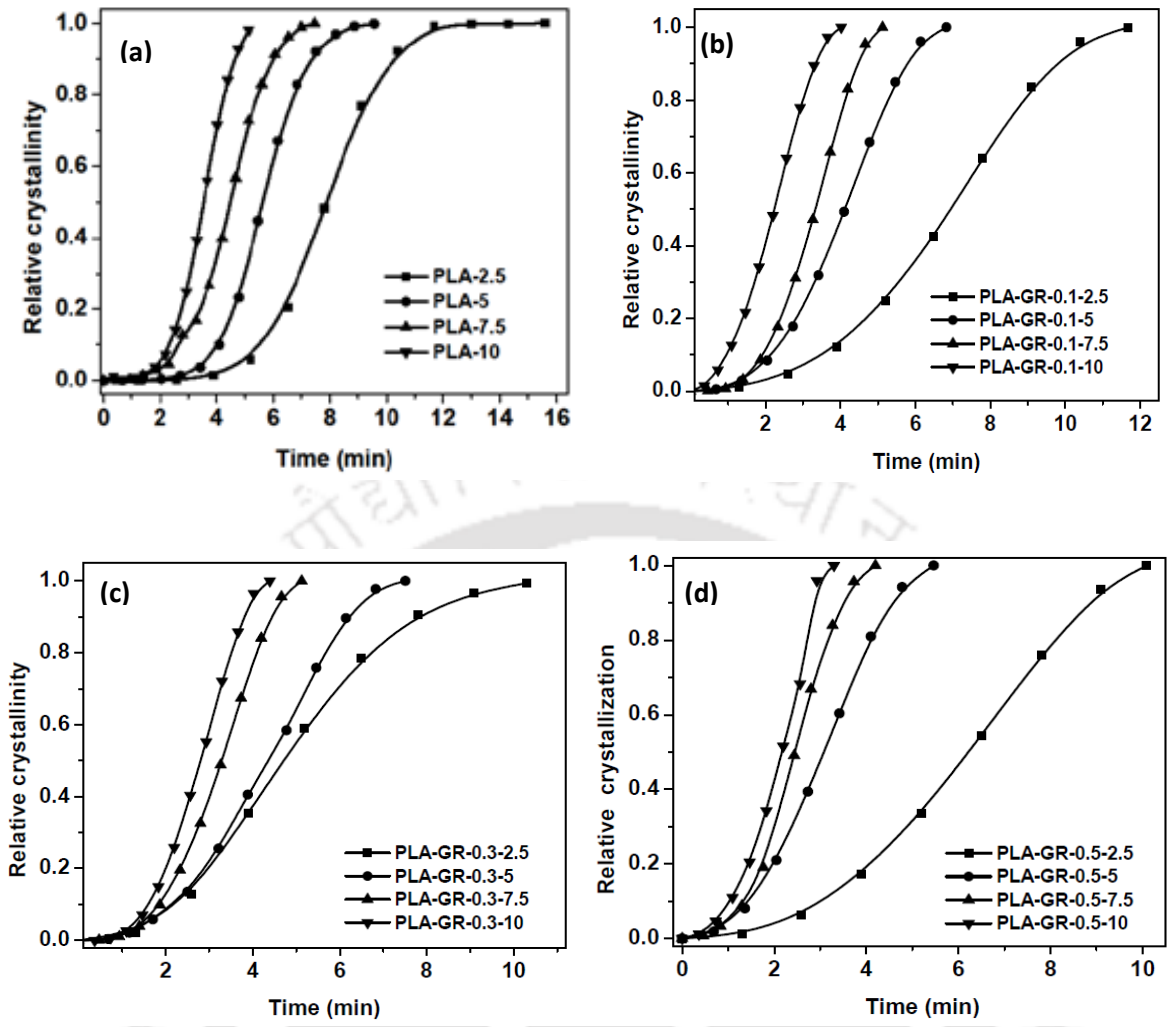

Figure 4.10. Relative crystallinity versus crystallization time at different heating rates for (a) neat PLA, (b) PLA-GR-0.1, (c) PLA-GR-0.3 and (d) PLA-GR-0.5 nanocomposites

The $t_{1/2}$ values obtained for both PLA as well as PLA-GR nanocomposites exhibit downturn with respect to increase in heating rates. This is attributed to the faster crystallization completion periods with progress in the heating rate. Also, the $t_{1/2}$ values obtained for PLA-GR nanocomposites are noticed to be relatively lower in comparison with neat PLA for all the heating rates. The possible reason for this might be due to the fact that the addition of GR in the PLA matrix accelerates the cold crystallization rate on the whole. The greater $t_{1/2}$ values obtained at the lower heating rate for both PLA and nanocomposite films result from the secondary crystallization phenomenon. In order to study the influence of GR towards the crystallization process, $1/t_{1/2}$ versus ϕ is plotted for PLA and PLA-GR nanocomposites as

shown in Figure 4.11. One can see that $1/t_{1/2}$ value increases significantly for PLA-GR-0.1 as compared to neat PLA. This increment corresponds to the prominent effect of nucleation ability of GR that stimulates the crystallization process of PLA. A much profound impact on the $1/t_{1/2}$ values is not evidenced thereafter with further GR loadings in the PLA matrix. However, the increasing trend obtained in the $1/t_{1/2}$ values is ascribed to the nucleation effect of GR resulting in a faster rate of the crystallization process in PLA. Further, crystallization rate parameter (CRP) is calculated from the slope of the linear plots shown in Figure 4.11 in order to derive quantitative information about the influence of GR on the crystallization rate of PLA. The CRP value for PLA, PLA-GR-0.1, PLA-GR-0.3 and PLA-GR-0.5 is determined to be 0.0272, 0.0372, 0.0404 and 0.0413, respectively. The increasing trend obtained in the CRP values of PLA-GR nanocomposites as compared to neat PLA confirms that reinforcement of GR indeed fastens the cold crystallization process in PLA.

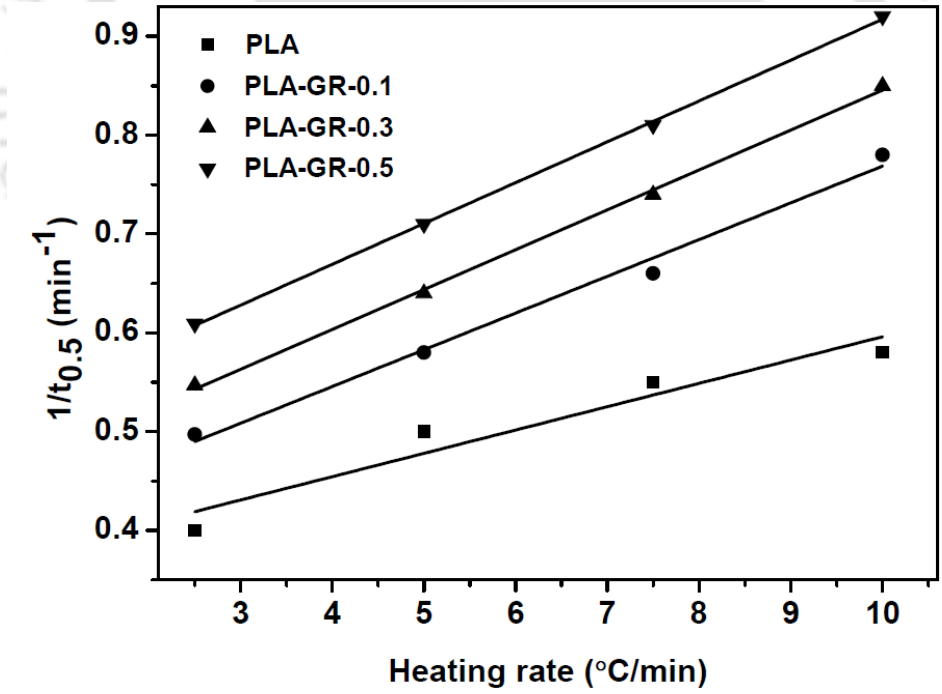

Figure 4.11. Effect of GR loading on the crystallization rate parameter (CRP)

The relative crystallinity curves corresponding to neat PLA, PLA-GR-0.1, PLA-GR-0.3 and PLA-GR-0.5 are presented in Figure 4.10(a-d) and the respective Avrami plots for the same are depicted in Figure 4.12(a-d). The linear behaviour exhibited by these plots specifies that

the Avrami model adequately elucidates the cold crystallization process of PLA under non-isothermal conditions. The '*n*' values corresponding to Avrami exponent for both PLA and PLA-GR nanocomposites are presented in Table 4.3. It is observed that the *n* values show a decreasing trend with respect to GR loadings in comparison with neat PLA irrespective of the heating rate. The greater '*n*' values observed in case of neat PLA is ascribed to the homogeneous nucleation, which is responsible for 3-dimensional (3D) growth of PLA crystals (**Liao et al., 2007**). In contrast, the relatively lower '*n*' values noticed for PLA-GR nanocomposites suggest that heterogeneous nucleation accelerate the crystallization rate. This also indicates that PLA crystals do not possess enough time for its growth in three dimensions in the latter case (**Liao et al., 2007**).

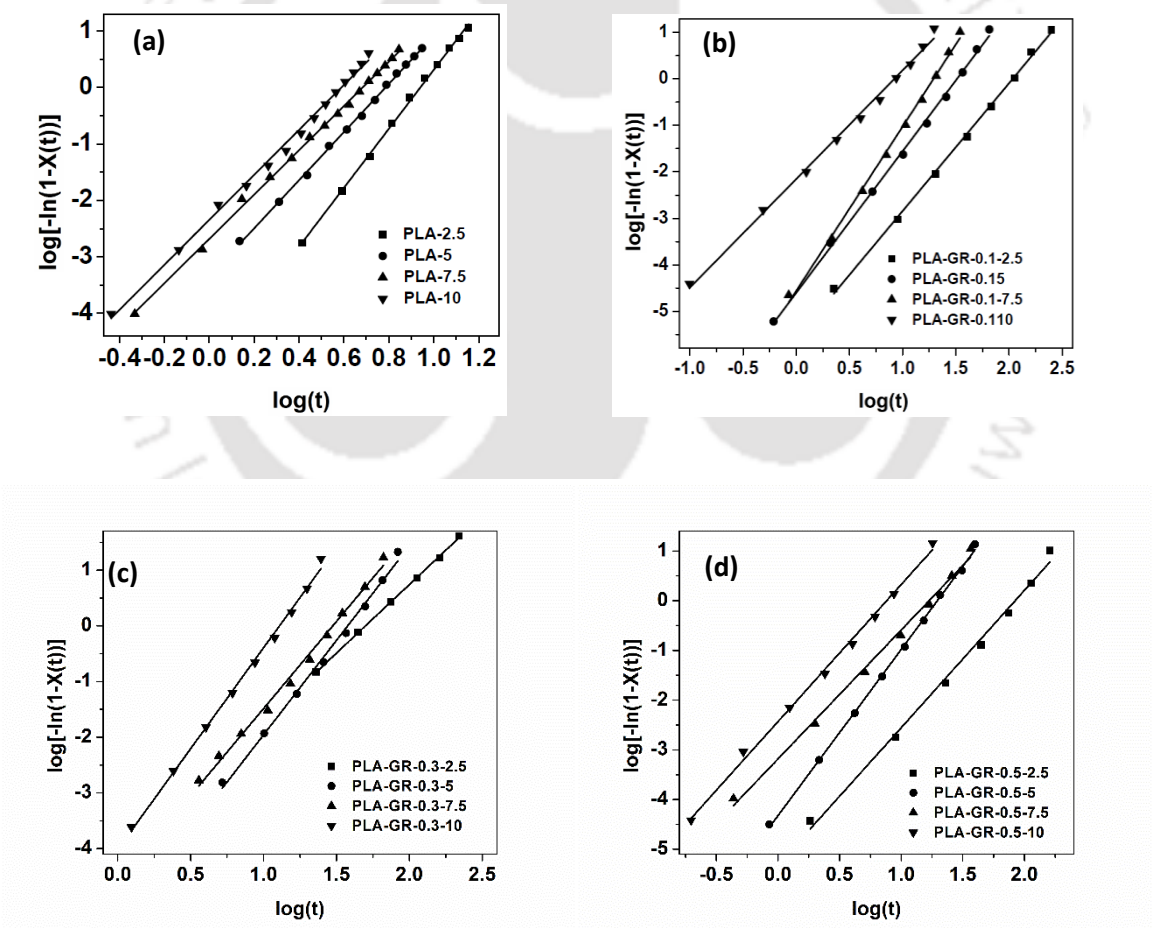

Figure 4.12. Avrami plots for non-isothermal cold crystallization of (a) PLA, (b) PLA-GR-0. 1, (c) PLA-GR-0.3 and (d) PLA-GR-0.5 nanocomposites

Table 4.3. Avrami model parameters for PLA and PLA-GR nanocomposites

Sample name	*n*				Log(*k*)			
	2.5 °C/min	**5 °C/min**	**7.5 °C/min**	**10 °C/min**	**2.5 °C/min**	**5 °C/min**	**7.5 °C/min**	**10 °C/min**
PLA	4.8	4.2	3.9	4.0	-4.9	-3.3	-2.6	-2.3
PLA-GR-0.1	4.2	3.9	3.7	3.6	-3.3	-2.5	-1.9	-1.3
PLA-GR-0.3	4.0	3.4	3.2	3.2	-2.76	-1.85	-1.5	-1.15
PLA-GR-0.5	3.9	3.3	3.2	2.9	-2.3	-1.5	-1.2	-1.01

The growth site impingement and the secondary crystallization that usually occur during the crystallization process of PLA and PLA-GR nanocomposites cannot be described by Avrami model. This is due to the fact that the Avrami model accounts only for the investigation of the initial stage of crystallization progression. Therefore, in order to have an insight into the phase transformation kinetics with growth site impingement, a model proposed by Tobin is utilized for studying the non-isothermal crystallization kinetics of PLA and PLA-GR nanocomposites. The plot of $\log\left(\frac{X_t}{1-X_t}\right)$ versus $\log t$ for PLA and PLA-GR nanocomposites for the dynamic heating regime is presented in Figure 4.13(a-d). The parameters associated with the crystallization rate (K_T) and Tobin exponent (n_T) are calculated from the slope and intercept values obtained from the linear fit, respectively and is reported in Table 4.4.

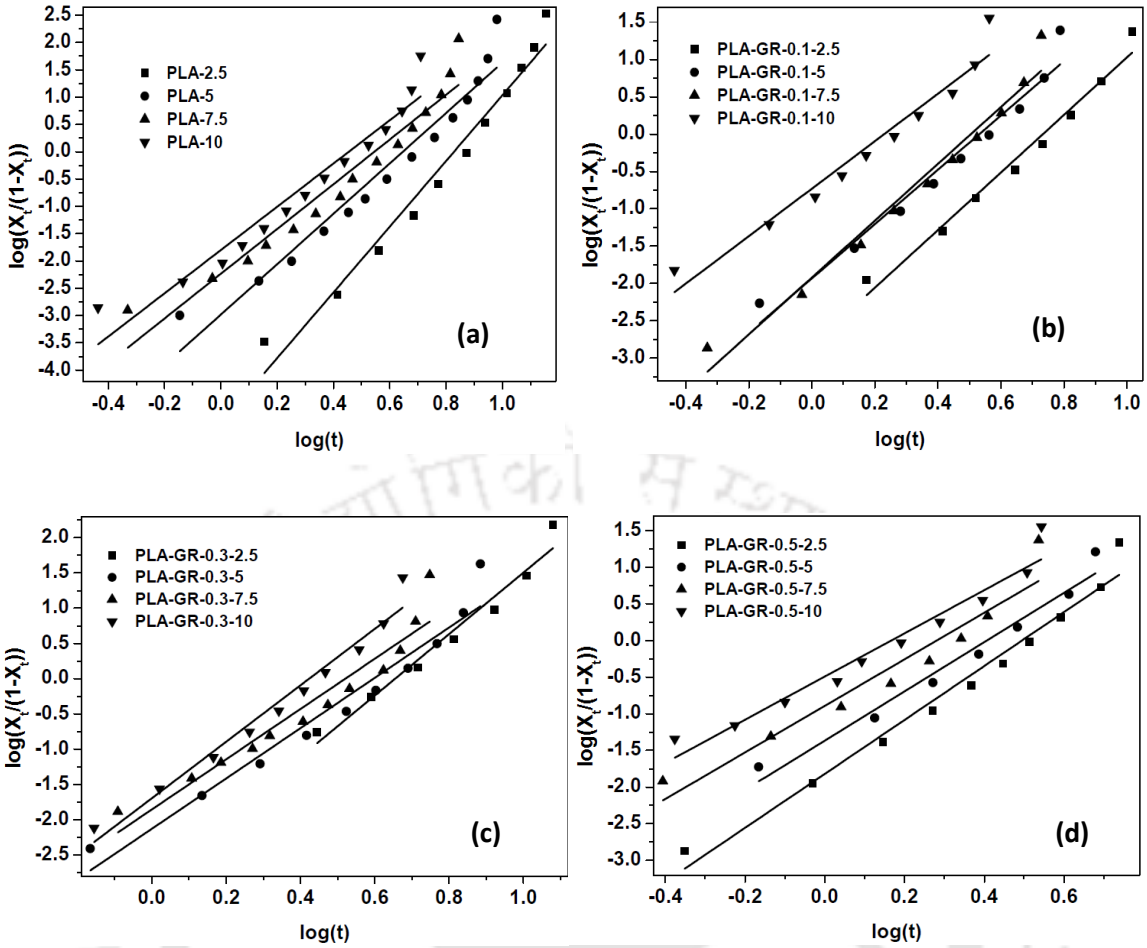

Figure 4.13. Tobin plots for non-isothermal cold crystallization of (a) PLA, (b) PLA-GR-0.1, (c) PLA-GR-0.3 and (d) PLA-GR-0.5 nanocomposites

Table 4.4. Tobin model parameters for PLA and PLA-GR nanocomposites

Sample name	n_T				Log(K_T)			
	2.5 °C/min	5 °C/min	7.5 °C/min	10 °C/min	2.5 °C/min	5 °C/min	7.5 °C/min	10 °C/min
PLA	6.0	4.6	4.1	3.9	-5.0	-3.0	-2.3	-1.9
PLA-GR-0.1	3.76	3.65	3.84	2.77	.2.73	-1.99	-1.92	-0.61
PLA-GR-0.3	4.36	3.57	3.56	4.00	-2.85	-2.13	-1.85	-1.69
PLA-GR-0.5	3.67	3.35	3.17	2.94	-1.82	-1.36	-0.89	-0.49

The Tobin exponent (n_T) values for neat PLA are obtained in the range of ~4-6 (Table 4.4) and the same exhibits a decreasing trend with increasing heating rate. This is accordance with the values reported in the literature (**Han et al., 2013**). The crystallization rate parameter, 'K_T' values corresponding to the Tobin model to demonstrate increasing tendency with respect to heating rate, suggesting the acceleration in the non-isothermal crystallization process of PLA. For PLA-GR nanocomposites, the 'n_T' values are found to be in the range of ~3-4 and are comparatively smaller than PLA for all the heating rates studied. The significant variation between the 'n_T' values for PLA and PLA-GR nanocomposites would have been resulted due to the alteration in the crystallization process of PLA. In addition to this, the 'K_T' values obtained in case of PLA-GR nanocomposites show greater deviation from that of the crystallization rate parameter values calculated for PLA, irrespective of the heating rate. This underlines the fact that the addition of GR in the PLA matrix leads to noteworthy enhancement in the non-isothermal crystallization progression of PLA. The overall trend noticed in the 'K_T' and 'n_T' values for both the PLA and PLA-GR nanocomposites are in accordance with the trend followed in case of Avrami parameters. This reveals that the physical meaning of Tobin parameters remains the same as the Avrami model.

The influence of GR on the crystallization characteristics of PLA is further explored using polarized optical microscopy (POM) observations under isothermal conditions. Prior recording the images, the neat PLA and PLA-GR nanocomposite samples are subjected to heating up to the melting temperature (180 °C) and held under the same environment for a period of 5 min to erase thermal history. Thereafter, the POM images are pictoriated for PLA and PLA-GR nanocomposites at an isothermal crystallization temperature of 120 °C in various intervals of time (0, 5th, 10th, 15th and 20th min), while cooling from the melt and the respective images are shown in Figure 4.14. With the addition of GR in the PLA matrix, advancement in the overall crystallization process of PLA is evidenced, which in turn, is

confirmed by the reduction in the induction period of nucleation process. In addition to this, the dramatic increase in the number of primary nucleation spots with respect to GR loadings is also visualized. Hence, it can be concluded that GR acts as an effective nucleating agent and thereby, fastens the rate of crystallization.

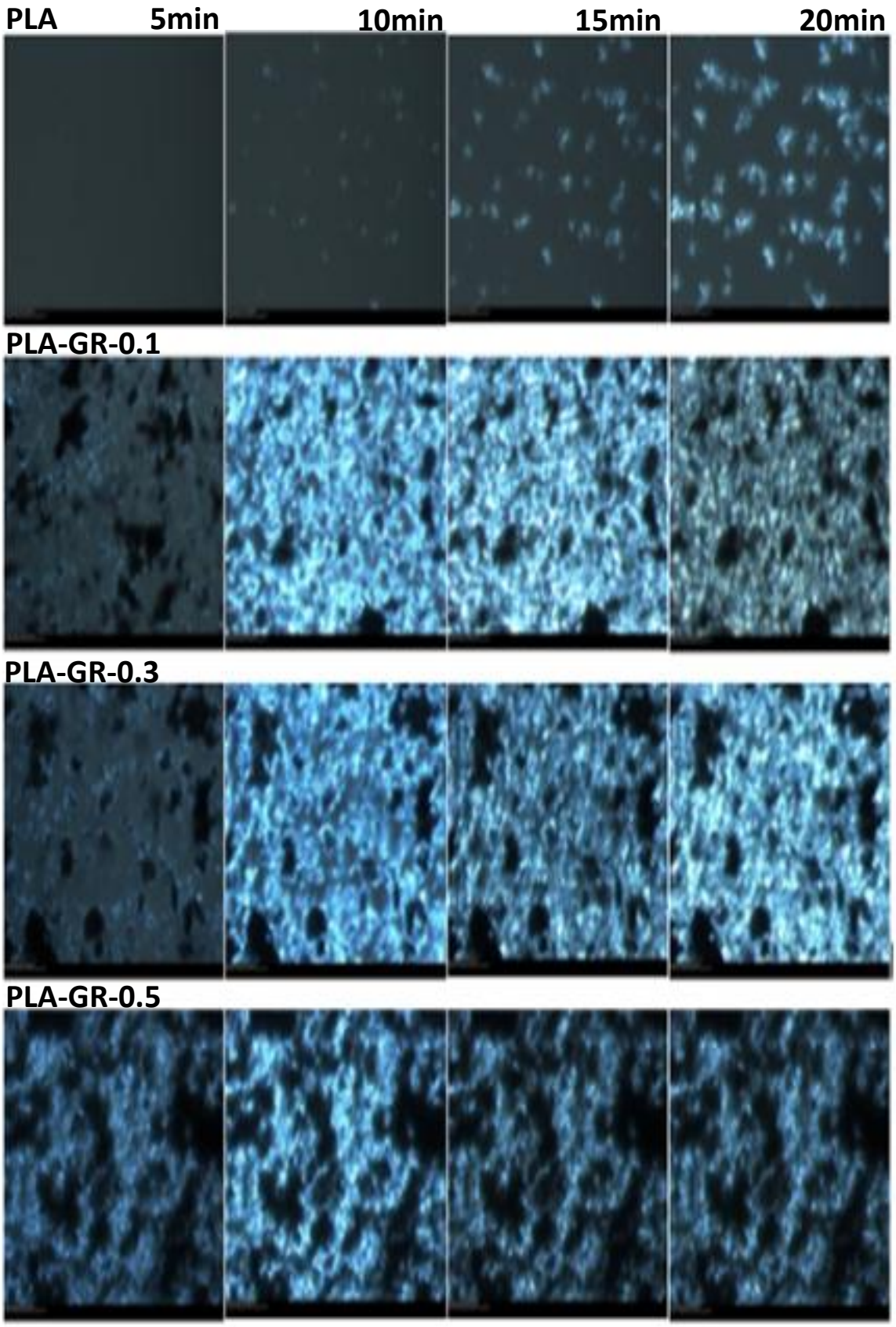

Figure 4.14. Optical microscopy images of PLA and PLA-GR nanocomposites with respect to time at 120 °C

4.6. Conclusions

The enhancement in the crystallization process with respect to the heating rate is observed for both PLA and PLA-SP nanocomposites. This phenomenon is further confirmed by the increasing trend obtained for 'K_T' values of Tobin model, with an increase in the heating rate. Furthermore, $1/t_{0.5}$ value and CRP increase with respect to SP loading that signifies an enhancement in the crystallization rate of PLA. The nucleation density amplifies significantly in the PLA matrix with an increase in the SP content (wt %), which is verified by POM studies. The radial spherulite growth rate increases linearly with time, confirming that the growth rate is not dependent on the spherulite diameter. For both PLA and PLA-GR nanocomposites, the crystallization exotherm shifts to higher temperature side with respect to the heating rate, which is indicative of the faster rate of crystallization process. The crystallization rate parameter values of PLA-GR nanocomposites obtained by both Avrami and Tobin models show increasing trend with respect to neat PLA demonstrating the nucleation effect of GR. The similar physical significance provided by both the models suggests the suitability of the same in predicting the crystallization kinetic behavior of PLA and PLA-GR nanocomposites. The nucleating ability of GR in the PLA matrix is revealed by the reduction in the nucleation induction period, which is observed by POM studies.

CHAPTER 5

Thermal Degradation Kinetic Studies of Sucrose Palmitate and Graphene Reinforced PLA Nanocomposites

*This chapter focuses on investigation of the influence of graphene (GR) and sucrose palmitate (SP) on the thermal degradation behavior of poly(lactic acid) (PLA) nanocomposites. The thermal degradation behavior of the PLA nanocomposites was investigated by thermo-gravimetric analysis (TGA) using the dynamic heating regime. The apparent activation energies (E_a) of the thermal degradation of PLA and PLA nanocomposites were evaluated by Coats-Redfern, Flynn-Wall-Ozawa and Kissinger methods. The thermal degradation mechanism of PLA, PLA-GR and PLA-SP nano composites at a particular heating rate is also predicted using the Criado method. Part of this work has been published in "**International Journal of Biological Macromolecules**",* 2014, 65, 275-283, ***RSC Advances***, **2015**, 5, 28410-28423 *and* ***Journal of Polymer Research***, **2015**, 175, 1-14.

5.1. Introduction

In general, thermal degradation plays an extremely crucial role during processing of PLA composites (**Tudorachi et al., 2012; Li et al., 2009)**. Therefore, understanding the influence of the reinforcements on the thermal degradation behavior of the PLA composites become essentially important in determining how molten PLA should be processed without causing serious thermal decomposition. Thermogravimetric analysis (TGA) is one of the effective thermal analysis techniques to study the solid-state thermal degradation kinetics (**Wu et al., 2008; Wu et al., 2006**). Overall kinetics can be easily obtained by measuring the change in the mass of a composite material with time, based on the isothermal and non-isothermal decomposition profile of the TGA analysis (**Gotor et al., 2000; Perinovic et al., 2010**). Many solid-state kinetic models have been developed to describe the thermal degradation behavior of biopolymer based composites. Models with different approaches (model-fitting and model-free isoconversional) have been proposed to determine kinetic triplets i.e., activation energy (E_a), pre-exponential factor (A), and reaction order (n) (**Khawan et al., 2006**). The model-fitting approach involves fitting various models to conversion versus temperature curves and simultaneously determining the activation energy and pre-exponential factor. In general, model-fitting methods make use of only one TGA curve recorded at a certain heating rate to evaluate the kinetic parameters. Although model-fitting methods allow direct determination of kinetic triplet, these methods are associated with different reaction models that satisfactorily fit the kinetic data at the expense of drastic variations in the Arrhenius parameters. Hence, several researchers suggested that model-fitting methods produce unreliable kinetic parameters (**Khawan et al., 2006; Jankovic et al., 2008; Aboyade et al., 2012; Jankovic et al., 2007**). On the other hand, the model-free approach has gained popularity among the scientific communities due to its potential to estimate E_a values as a function of conversion without the previous assumption of a kinetic model (f (α)) (**Chrissafis et al., 2010**). In solid-state kinetic studies, the “apparent” E_a is defined as the excess energy obtained from the vibration of an

atom or molecule at certain temperature. This energy can also be related to the rupture of chemical bonds (**Bagg et al., 1969**). Since the E_a derived from TGA data is the sum of activation energies of chemical reactions and physical processes, the same is denoted as apparent activation energy throughout this study. To avoid the problems peculiar to model-fitting methods, isoconversional methods for estimating the activation energy are used. The three well-known representatives of model-free approaches, i.e., Coats-redfern (**Armentano et al., 2013**), Flynn-Wall-Ozawa (**Flynn et al., 1966**), Kissinger methods (**Kissinger et al., 1957**) are used to investigate the thermal degradation behavior of PLA, PLA-SP and PLA-GR nanocomposites. The thermal degradation mechanism associated with the PLA, PLA-SP and PLA-GR nanocomposites is also predicted using the Criado method.

5.2. Experimental

5.2.1. Materials

The chemicals used for the synthesis of PLA-SP and PLA-GR nanocomposites are discussed in section 3.2.1 and 2.2.1, respectively.

5.2.2. Synthesis of PLA-SP and PLA-GR nanocomposites

The synthesis procedure for the fabrication of PLA-SP and PLA-GR nanocomposites is discussed in section 3.2.2 and 2.2.3, respectively.

5.3. Characterization

Thermogravimetric analysis was performed on a Mettler Toledo thermo gravimetric analyzer (TGA/SDTA 851® model). Samples (10.5 ± 0.3 mg) were placed in 900 µl alumina crucibles. Samples were heated from 25 to 700 °C in a 60 ml/min flow of N_2 at heating rates of 10, 20, and 30 °C/min.

5.4. Theory

Kinetic studies of the degradation process were performed for better understanding of the thermal degradation behavior of PLA, PLA-SP and PLA-GR composites. The thermal degradation of polymers can be expressed by the following typical kinetic equation:

$$\frac{d\alpha}{dt} = kf(\alpha) \tag{5.1}$$

where, α is the conversion degree or the fraction decomposed [$\alpha = (w_0-w_t)/(w_0-w_f)$, w_0, w_t, and w_f are the initial, time t, and final weights of the polymer], dα/dt is the rate of conversion, k is the temperature-degradation rate constant, and $f(\alpha)$ is the differential expression of a kinetic model function, which depends on the particular degradation mechanism (**Wu et al., 2006; Khawan et al., 2006; Yuzay et al., 2010**).

The temperature dependent degradation rate constant (k) can be expressed in terms of Arrhenius equation as follows:

$$k = A\exp\left(\frac{-E_a}{RT}\right) \tag{5.2}$$

where, A is the pre-exponential factor (s^{-1}), E_a is the apparent activation energy of the degradation reaction (kJ/mol), R is the universal gas constant (8.314 J mol^{-1} K^{-1}), and T is the absolute temperature (K). Substituting k from Eq. (5.2) into Eq. (5.1), a general expression for the kinetic process under isothermal conditions can be derived and expressed as

$$\frac{d\alpha}{dt} = A\exp\left(\frac{-E_a}{RT}\right) f(\alpha) \tag{5.3}$$

In the present study, the thermal degradation kinetic study of PLA composites is carried out under non-isothermal conditions, where samples are heated with a constant heating rate, β=dT/dt. Hence, Eq. (5.3) is transformed into an equation describing the degradation reaction rate as a function of temperature and then expressed as follows:

$$\left(\frac{d\alpha}{dT}\right)=\frac{A}{\beta}\exp\left(\frac{-E_a}{RT}\right)f(\alpha) \tag{5.4}$$

Eqs. (5.3) and (5.4) are the fundamental expressions of analytical methods to calculate kinetic triplets on the basis of TGA data. The degradation reaction is assumed to be a simple n^{th} order reaction and kinetic model function, $f(\alpha)$, as $(1-\alpha)^n$, where n is the order of reaction (**Chrissafis et al., 2010; Flynn et al., 1966; Yuzay et al., 2010**).

Taking integration on both sides of the equation (5.4) and rearranging

$$g(\alpha)=\int_0^{\alpha}\frac{d\alpha}{f(\alpha)}=\frac{A}{\beta}\int_0^{T}e^{\frac{-E_a}{RT}}dT \tag{5.5}$$

where, $g(\alpha)$ is the integral function of conversion degree, α. The process of polymer degradation mainly obeys sigmoidal or deceleration functions.

5.4.1. Coats-Redfern method

Using eq. (5.5) and putting $f(\alpha)=(1-\alpha)^n$ and $x=E_a/RT$ and rearranging, we get:

$$g(\alpha)=\frac{ART^2}{\beta E_a}\left(1-\frac{2RT}{E_a}\right)\exp\left(\frac{E_a}{RT}\right) \tag{5.6}$$

$g(\alpha)$ can be written in different ways for different n values.

when $n=1, g(\alpha)=-\ln(1-\alpha)$ (5.7)

when $n\neq 1, g(\alpha)=\frac{1}{n-1}\left[(1-\alpha)^{1-n}-1\right]$ (5.8)

The combination of equations (5.7) and (5.8) and by rearrangement, we get:

$$n=1, \ln\left(\frac{-\ln(1-\alpha)}{T^2}\right)=\ln\left[\frac{AR}{\beta E_a}\left(1-\frac{2RT}{E_a}\right)\right]-\frac{E_a}{RT} \tag{5.9a}$$

$$n \neq 1, \ln\left(\frac{1-(1-\alpha)^{1-n}}{(1-n)T^2}\right) = \ln\left[\frac{AR}{\beta E_a}\left(1-\frac{2RT}{E_a}\right)\right] - \frac{E_a}{RT} \quad (5.9b)$$

Plotting the left hand side term versus $-1/T$ gives the straight line and activation energy is obtained from the slope of the straight line. The value of the pre-exponential factor, A is obtained from intercept of the straight line, by considering the expression $\left(1-\frac{2RT}{E_a}\right)$ inside the parenthesis as 1 (**Krishna et al., 2011; Poletto et al., 2012**). Analysis is done using only single heating data, which is different from other kinetic models where multiple heating data are required for analysis.

The Coats-Redfern method requires TG data with only one heating rate to calculate kinetic parameters such as activation energy (E_a), reaction order (n) and pre-exponential factor (A) (**Armentano et al., 2013**). In this study, TGA data of PLA composite samples with different GR and SP loadings are taken at a single heating rate (10 °C/min). For this method, a reaction order "n" is assumed and the assumed value is substituted in eq. (5.9a) and (5.9b). The plot of the left hand side of the eq. (5.9a) and (5.9b) versus $-1/T$ is fitted to calculate the R^2 values. This process is repeated until the best R^2 value is obtained.

5.4.2. Flynn-Wall-Ozawa method

The Flynn-Wall-Ozawa method (F-W-O) is one of the integral methods that can determine the activation energy for the thermal degradation reaction without any knowledge of reaction mechanisms. It represents a relatively simple method for determining the activation energy directly from data of weight loss versus temperature obtained at several heating rates. This method utilizes Doyle's linear approximation and is denoted by the following equation:

$$\log(\beta) = \left\{ \log \frac{AE}{g(\alpha)R} - 2.315 \right\} - \frac{0.457E_a}{RT} \quad (5.10)$$

where β, A, E_a, T, and R are the heating rate, the pre-exponential factor, the apparent activation energy, the absolute temperature, and the gas constant, respectively, and α is the conversion (fractional weight loss). The E_a can be calculated based on the slope of a plot of log (β) versus -1/T for timed value of conversion (α) (**Kim et al., 2000**).

5.4.3. Kissinger method

To relatively compare the activation energy of PLA and its composites, Kissinger method determining the kinetic parameter (E_a) at a fixed conversion rate is also employed. This method involves the temperature, T_{max} at the maximum weight loss rate $(\frac{d\alpha}{dt})_{max}$. The apparent activation energy can also be determined without a precise knowledge of the reaction mechanism, using the following equation:

$$\ln\left(\frac{\beta}{T_{max}^2}\right) = \left\{ \ln\frac{AR}{E_a} + \ln\left[n(1-\alpha_{max})^{n-1} \right] \right\} - \frac{E_a}{RT_{max}} \quad (5.11)$$

where, T_{max}, and α_{max} are the temperature corresponding to the inflection point of thermal degradation curves, which corresponds to the maximum weight loss and the conversion degree at the inflection point, n is the order of the reaction (**Khawan et al., 2006; Kissinger., 1957; Yuzay et al., 2010**). The E_a for decomposition can be obtained from the slope of the straight line when $\ln\left(\frac{\beta}{T_{max}^2}\right)$ is plotted against $\left(-\frac{1}{T_{max}}\right)$.

5.4.4. Criado Method

The mechanism of thermal degradation of PLA composites at a particular heating rate is predicted using the Criado method (**Criado et al., 1989**). The reaction mechanism is determined with the help of activation energy, pre-exponential factor and the apparent order of the reaction calculated using the Coats Redfern method. The Criado equation is given by

$$Z(\alpha) = \frac{\frac{d\alpha}{dt}}{\beta} \pi(x) T \tag{5.12}$$

where, $x = \frac{E_a}{RT}$ and $\pi(x)$ is an expression resulted by integration against temperature, that cannot be articulated using simple analysis formula. A relationship between $\pi(x)$ and $P(x)$ is reported elsewhere (**Flynn et al., 1997**) and is given as follows:

$$\pi(x) = xe^x P(x) \tag{5.13}$$

where, $P(x)$ is expressed as:

$$P(x) = \frac{e^{-x}}{x} \frac{x^3 + 18x^2 + 86x + 96}{x^4 + 20x^3 + 120x^2 + 240x + 120} \tag{5.14}$$

Combining equations (5.12), (5.13) and (5.14), the following relationship can be obtained

$$Z(\alpha) = f(a) g(\alpha) \tag{5.15}$$

Combining equation (5.4) with (5.15) provides the following relationship

$$Z(\alpha) = \frac{\beta}{A} g(\alpha) \frac{d\alpha}{dT} \exp\left(\frac{E_a}{RT}\right) \tag{5.16}$$

From the equations (5.12) and (5.13), the following relationship is obtained

$$Z(\alpha) = \frac{d\alpha}{dT} \frac{E_a}{R} \exp\left(\frac{E_a}{RT}\right) P(x) \tag{5.17}$$

The master $Z(\alpha) - \alpha$ curve of the different reaction mechanisms given in Table 5.1 is plotted using Eq.(5.16), and $Z(\alpha) - \alpha$ experimental curve is plotted using Eq. (5.17) (**Krishna et al., 2011)**. Thereafter, the master $Z(\alpha) - \alpha$ curve has been compared with the experimental $Z(\alpha) - \alpha$ curve for predicting the reaction mechanism of the thermal degradation process.

Table 5.1. Expression of g(*α*) for the most frequently used reaction mechanism of the solid state processes

Mechanism	g(*α*)	Solid state process
Sigmoidal function		
A_2	$[-\ln(1-\alpha)]^{1/2}$	Nucleation and growth Avrami Eq.(1)
A_3	$[-\ln(1-\alpha)]^{1/3}$	Nucleation and growth Avrami Eq.(2)
A_4	$[-\ln(1-\alpha)]^{1/4}$	Nucleation and growth Avrami Eq.(3)
Deceleration function		
R_2	$[-\ln(1-\alpha)^{1/2}]$	Phase boundary controlled reaction: contraction area
R_3	$[-\ln(1-\alpha)^{1/3}]$	Phase boundary controlled reaction: contraction area
D_1	α^2	One-D diffusion
D_2	$(1-\alpha)\ln(1-\alpha) + \alpha$	Two-D diffusion
D_3	$[1-(1-\alpha)^{1/3}]^2$	Three-D diffusion: Jander equation
D_4	$-\ln(1-\alpha)$	Three-D diffusion: Ginstlinge Brounshetein equation
F_1	$-\ln(1-\alpha)$	Random nucleation having one nucleus on individual particle
F_2	$1/(1-\alpha)$	Random nucleation having two nucleus on individual particle
F_3	$1/(1-\alpha)^2$	Random nucleation having two nucleus on individual particle

5.5. Results and discussion

5.5.1. Effect of sucrose palmitate on the thermal degradation kinetics of PLA

The non-isothermal TGA and DTG curves of PLA and PLA-SP composites at three different heating rates of 10, 20 and 30 °C/min in the nitrogen atmosphere are shown in Figure. 5.1 and Figure 5.2, respectively. The TGA curves reveal the different profiles depending on heating rate and loadings of the filler, SP. It can be seen from Figure. 5.1 that for all the samples, temperatures of all the degradation stages ($T_{10\%}$, $T_{50\%}$, T_{max}) increase progressively as the heating rate increases. The shift of the TGA curves to higher temperatures with increasing heating rate could be attributed to the short time provided for a sample to reach a given temperature at high heating rate (**Yuzay et al., 2010**). At constant heating rates, the TGA weight loss curves of PLA and PLA-SP composites attributed to the main degradation region imply a single stage degradation of PLA and its composites (**Yuzay et al., 2010**).

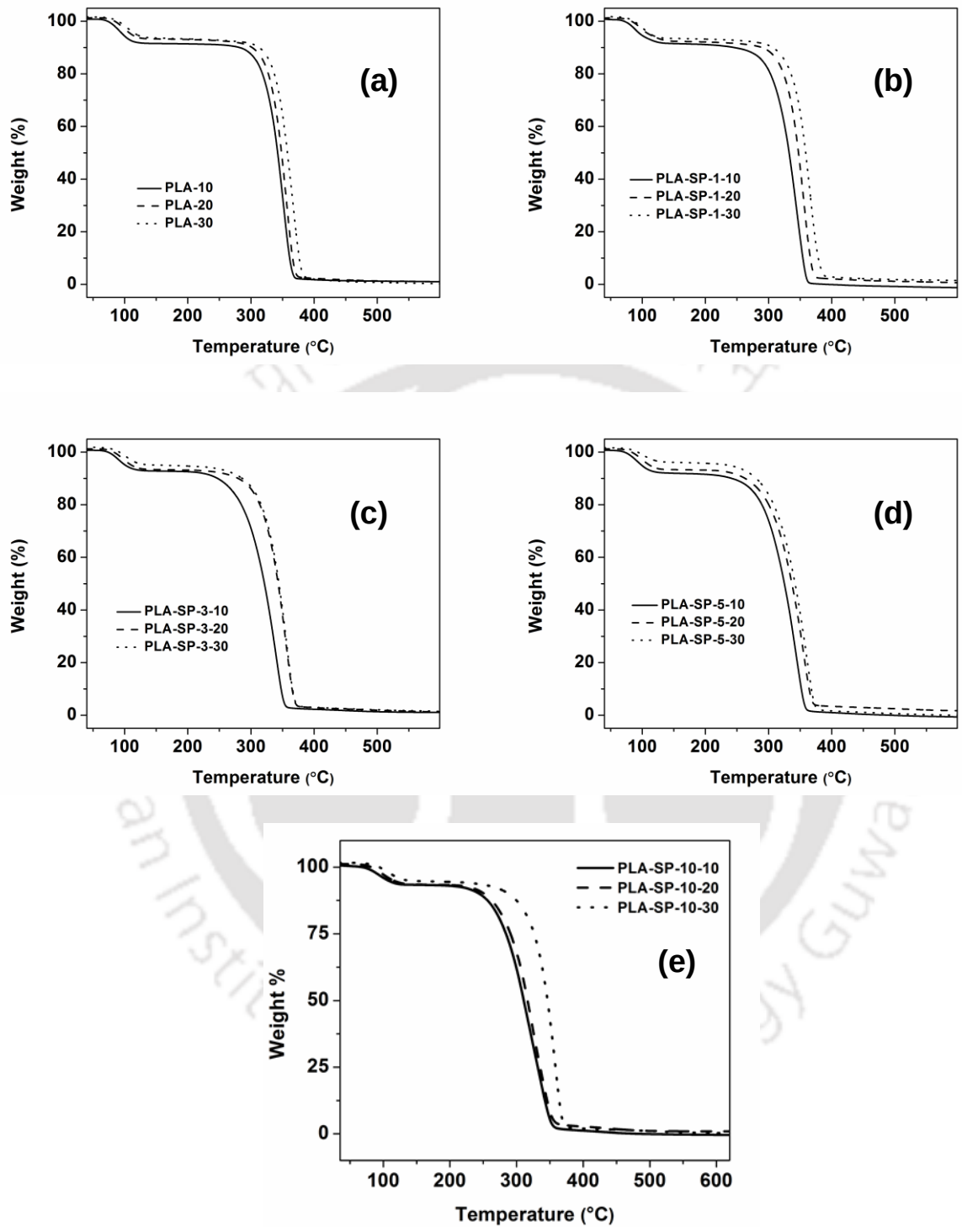

Figure 5.1. TGA curves at different heating rates (10, 20 and 30 °C/min) for (a) PLA, (b) PLA-SP-1, (c) PLA-SP-3, (d) PLA-SP-5 and (e) PLA-SP-10

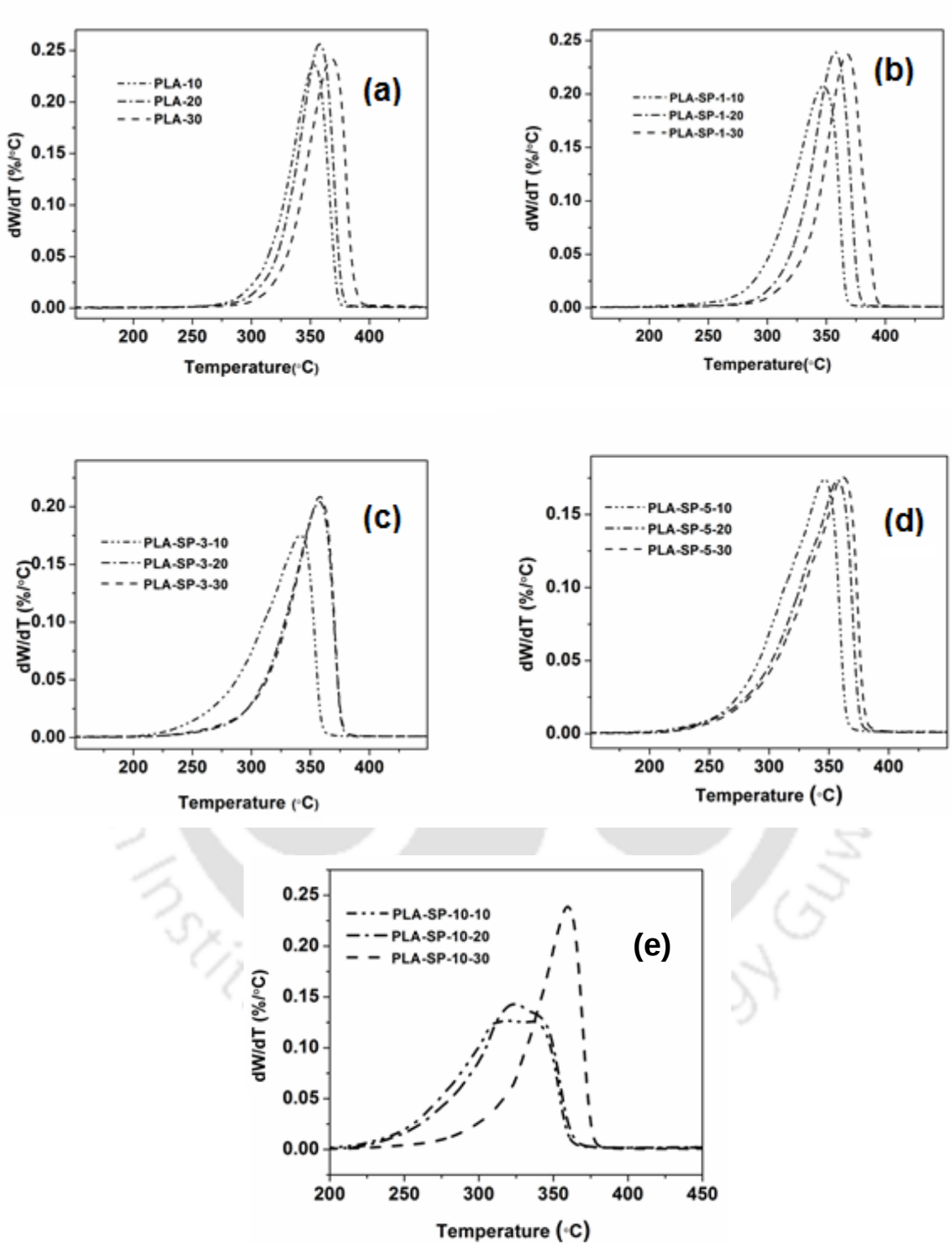

Figure 5.2. DTG curves at different heating rates (10, 20 and 30 °C/min) for (a) PLA, (b) PLA-SP-1, (c) PLA-SP-3, (d) PLA-SP-5 and (e) PLA-SP-10

In the thermal degradation process of PLA-SP composites, the first step involved in the degradation is primarily the decomposition of sucrose moieties present in the SP. It is well documented that the thermal decomposition of sucrose in aqueous environment occurs via hydrolysis (**Kelly et al., 1978; Mauch et al., 1971; Richards et al., 1978**). It is also to be noted that during sucrose hydrolysis, protonation of the oxygen molecule of the glycosidic bond between the glucose and fructose moieties takes place resulting in the splitting of the glycosidic linkage. When the thermal degradation of sucrose occurs in aqueous environment, the hydrogen ion (H^+) required for this step will be provided by water. Since water is highly dissociated at higher temperatures, and hence it can provide a medium which is more conductive for catalysis (pKa =14 at 24 °C and 12.23 at 100 °C), accelerating hydrolysis (**Kelly et al., 1978**). However, in the present study, thermal decomposition of sucrose takes place in the absence of an aqueous medium. Hence, the H^+ required for sucrose hydrolysis will be derived from the dissociation of sucrose molecule itself at higher temperatures (**Kelly et al., 1978; Richards et al., 1978**). In addition, another possible source of H^+ could be hydrogen bonded water molecules on the sucrose crystals. Kelly and Brown reported that pKa values of sucrose decreased to 11.07 at 90 °C from 12.43 at 20 °C, indicating that sucrose has acidic properties at elevated temperatures (**Kelly et al., 1978**). **Simkovic et al.** (**2003**) also confirmed by gas chromatography/mass spectrometry analysis (GC/MS), that the splitting of glycosidic bond is the most prominent primary reaction of sucrose thermal decomposition in the absence of an aqueous environment. This fact further reveals that sucrose hydrolysis can occur in the absence of an aqueous medium. The H^+ ions released during the thermal decomposition of sucrose will initiate the hydrolysis of alkyl ester (palmitate) that leads to the formation of alkyl groups with acid terminals (**Song et al., 2012**).

Then the released H^+ ions diffuse into the amorphous regions of the PLA matrix (**Antheunis et al., 2009; Jong et al., 2001**). The ester bonds in the PLA backbone are hydrolyzed in the

amorphous domains in the presence of H^+ (**Antheunis et al., 2009; Jong et al., 2001; Burkersroda et al., 2002**). This random chain scission process easily hydrolyzes the ester groups of PLA backbone resulting in the formation of oligomers with carboxylic acid terminal groups (**Vert et al., 1999; Pistner et al., 1993; Grizzi et al., 1995**). The terminal carboxylic acid groups of PLA oligomers further catalyzes the ester hydrolysis, which generally leads to a faster rate of degradation as the PLA degrades (autocatalysis) (**Gorrasi et al., 2013; Luo et al., 2012; Huang et al., 2012**). From the TGA analysis (Figure 5.1), it can be seen that the onset of thermal degradation process of the PLA-SP composites decreases with an increase of the SP content in the PLA matrix. This decreasing trend can be explained by the fact that higher loading of SP (wt %) in the PLA matrix leads to the production of relatively higher concentration of acidic sites, thus initiating the early onset of degradation of PLA. Therefore, the prevalence of presumably higher concentration of acidic sites in the PLA matrix, which is released by the higher loadings (10 wt %) of SP accelerates the autocatalytic chain-end hydrolysis of PLA oligomers (**Gorrasi et al., 2013; Luo et al., 2012; Huang et al., 2012**). Higher the SP concentration, higher will be the terminal carboxyl groups for lower molecular weight intermediates, which further accelerate the unzipping depolymerization and intermolecular ester exchange (**Liu et al., 2006; Zhou et al., 2009**). In general, chain-end hydrolysis is usually suggested to be faster than the random chain scission reactions (**Nostrum et al., 2004**). Henceforth, PLA with higher loadings of SP degrades at a much greater rate when compared to lower SP contents. Based on this hypothesis, the possible mechanism for the degradation of PLA-SP composites is presented in Figure 5.3. The cartoon shows the thermal degradation process for PLA-SP composites at lower and higher SP contents in the PLA matrix. At higher SP loading, relatively high concentration of H^+ released during the thermal decomposition of sucrose accelerates the hydrolysis of ester bonds in the PLA matrix. This further fastens the random chain scission process leading to formation of higher content of carboxylic acid terminal groups. This results in the faster degradation rate of PLA in comparison to lower loading of SP.

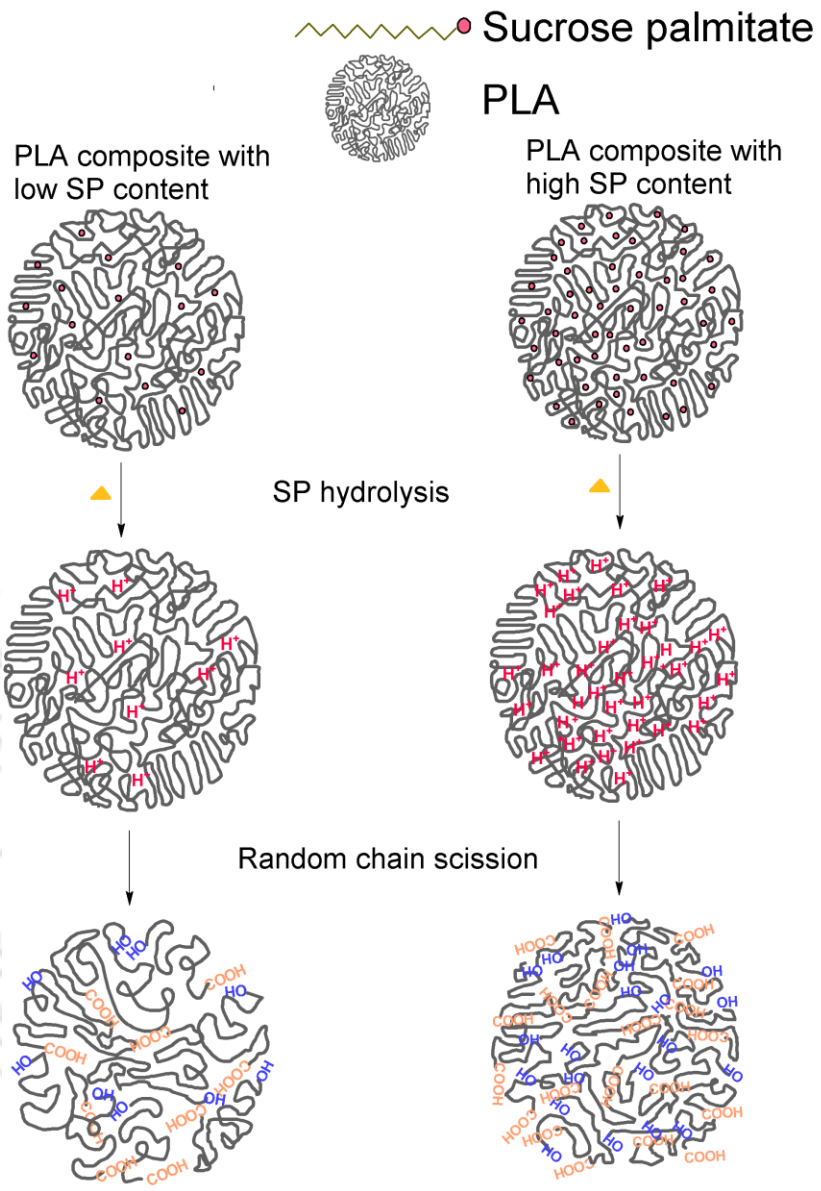

Figure 5.3. Possible mechanism for thermal degradation of PLA-SP composites

Figure 5.4 shows the linear fitted graph for neat PLA and PLA-SP composites for various "*n*" values. The calculated reaction order at the best R^2 value is considered as the reaction order for that sample (Table 5.2). Then the activation energy and the pre-exponential factor are obtained from the slope and intercept of the fitted straight line. The activation energy of neat PLA and

PLA-SP composite samples containing 1, 3, 5 and 10 wt% SP is 125, 74, 68 60 and 46 kJ/mol, respectively.

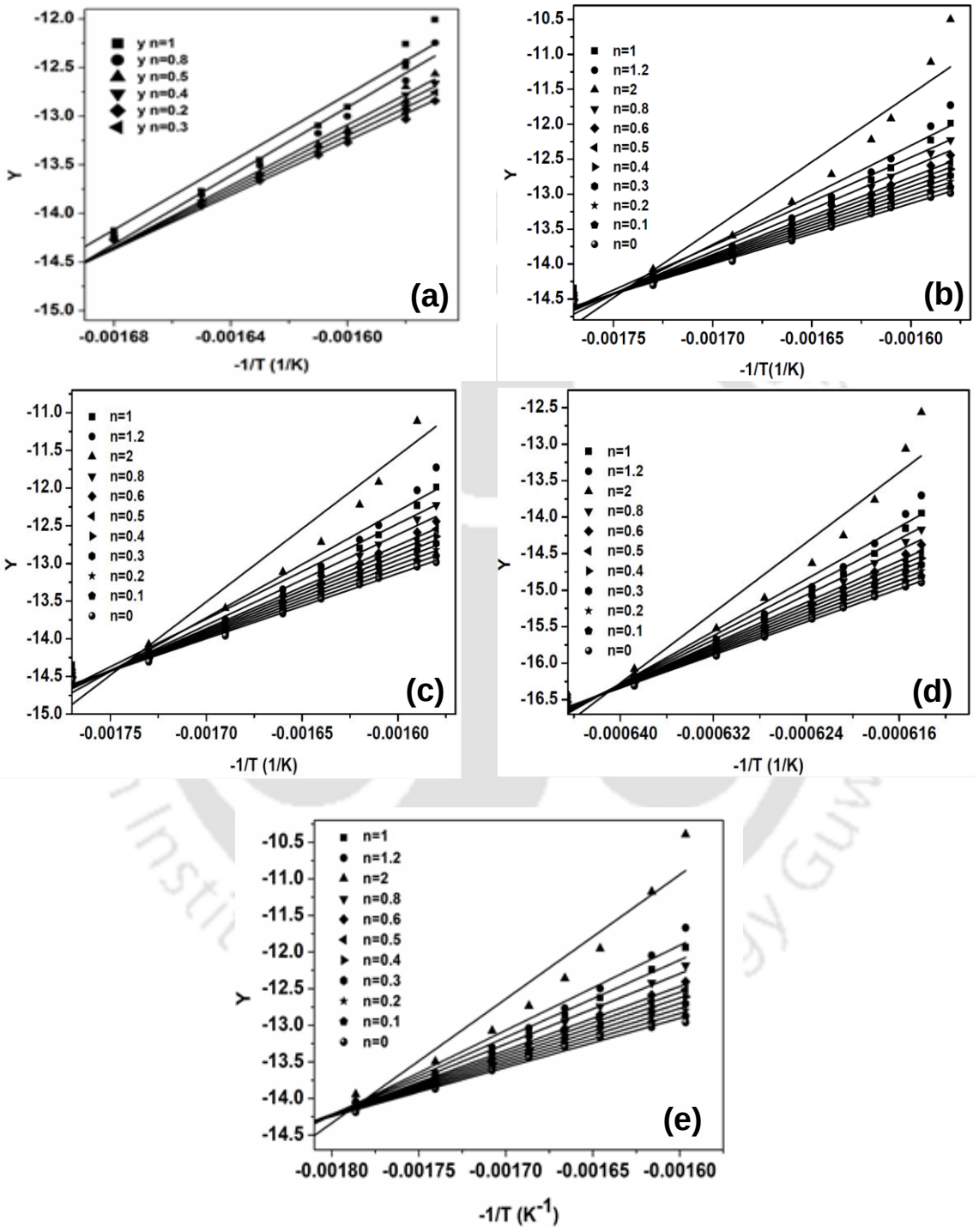

Figure 5.4. Coats-Redfern plots for (a) neat PLA, (b) PLA-SP-1, (c) PLA-SP-3, (d) PLA-SP-5 and (e) PLA-SP-10

Table 5.2. Activation energy, reaction order and regression co-efficient values obtained for PLA and PLA-SP nanocomposites using the Coats-Redfern method

S:No	Sample	E_a (kJ/mol)	*n*	R^2
1	PLA	125	0.4	0.994
2	PLA-SP-1	74	0.3	0.995
3	PLA-SP-3	68	0.2	0.991
4	PLA-SP-5	60	0.2	0.998
5	PLA-SP-10	46	0.3	0.997

In case of Kissinger's method, the plot of ln (β/T^2_{max}) against -1/T_{max} provides straight lines as shown in Figure 5.5. The obtained slopes of various straight lines were used to calculate the corresponding apparent activation energy (Table 5.3). As can be seen from Figure 5.5, smooth relativity of the various fitted straight lines demonstrates the feasibility of Kissinger's method.

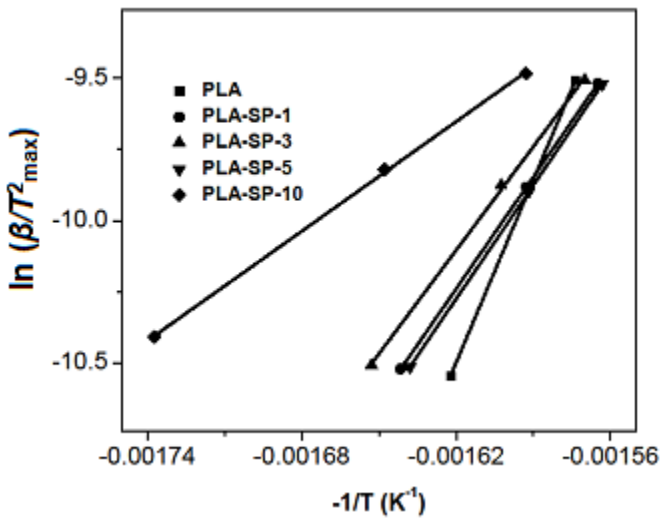

Figure 5.5. Kissinger's plot for PLA and PLA-SP composites

Table 5.3. Activation energy and regression co-efficient for PLA and its composites obtained by Kissinger and Flynn-Wall-Ozawa method

S:No	Sample name	Kissinger method		F-W-O method	
		E_a (kJ/mol)	R^2	E_a (kJ/mol)	R^2
1	PLA	177	0.999	170	0.995
2	PLA-SP-1	109	0.994	115	0.998
3	PLA-SP-3	105	0.999	111	0.997
4	PLA-SP-5	94	0.984	108	0.995
5	PLA-SP-10	53	0.999	83	0.997

Figure 5.6(a-e) displays the plots of log (β) against -1/T obtained using F-W-O method. It can be observed that the straight lines obtained at different α values for pure PLA and PLA-SP composites are nearly parallel. This proves that F-W-O method is well applicable to the investigated system in the conversion degree studied (**Chrissafis et al., 2010; Fan et al., 2004; Kim et al., 2000**). The plots of activation energy as a function of conversion (α) using F-W-O method for pure PLA and PLA-SP composites are also shown in Figure 5.7. The activation energy for the thermal degradation of both PLA and its composites varies with conversion throughout the degradation process. This reveals that the thermal degradation of both PLA and composites do not proceed through the simple process (**Yang et al., 2002; Chen et al., 2007**). It can be seen from Figure 5.7, that the E_a value of PLA increases in the conversion range of 0.1-0.7 and stays constant until complete decomposition. A similar behavior was also observed by **Li et al.,** (**2009**) for PLA sample and the E_a value (177 kJ/mol) obtained for PLA in the present study is also in accordance with the data reported by **Li et al.,** (**2009**). As evidenced, the activation energy of the composites decreases after incorporation of SP in the PLA matrix, which is consistent with TGA profiles. However, there is no significant variation in the activation energies among different PLA-SP (1, 3, 5 wt %) composites except PLA-SP-10.

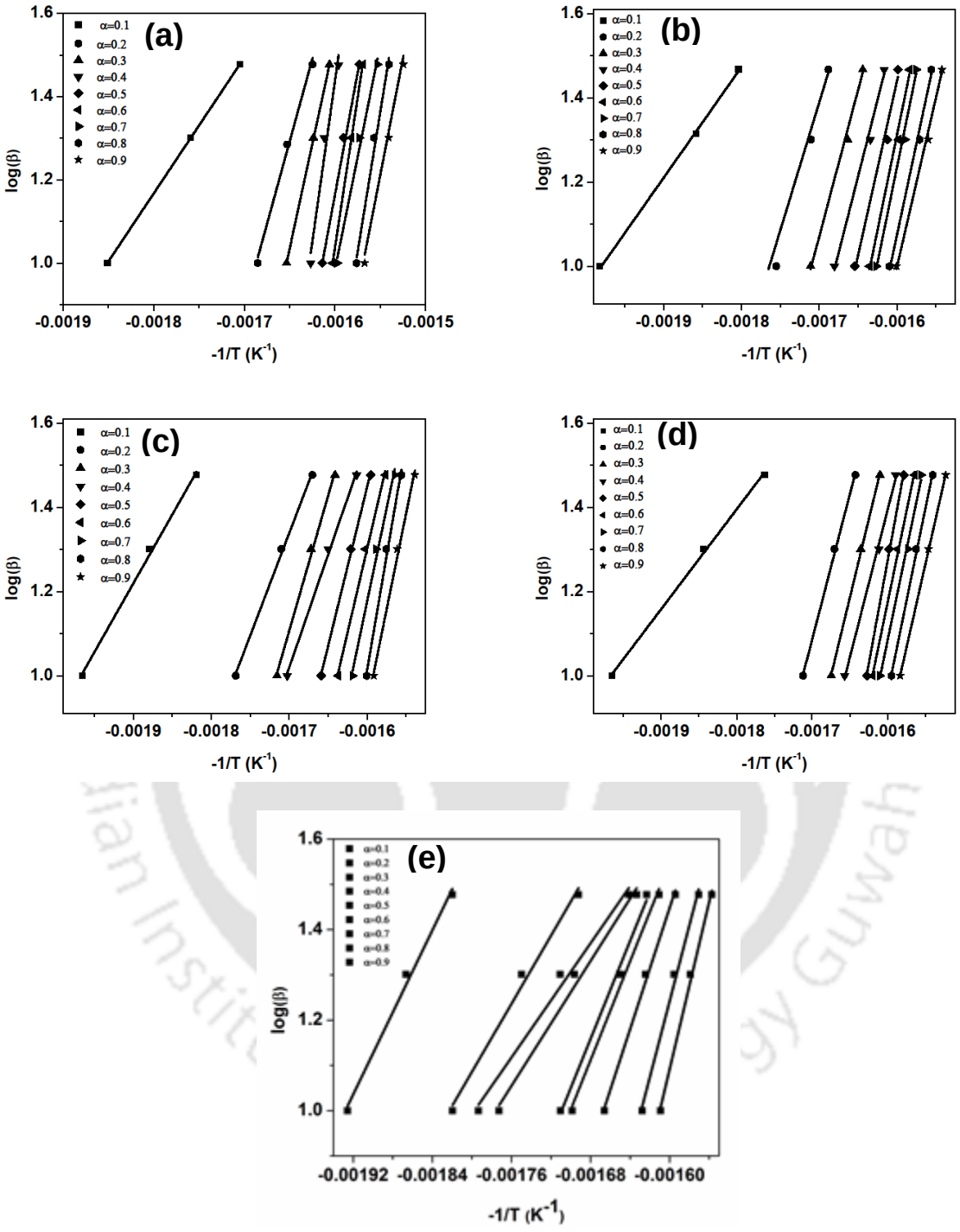

Figure 5.6. Flynn-Wall-Ozawa plots for (a) PLA, (b) PLA-SP-1, (c) PLA-SP-3, (d) PLA-SP-5 and (e) PLA-SP-10

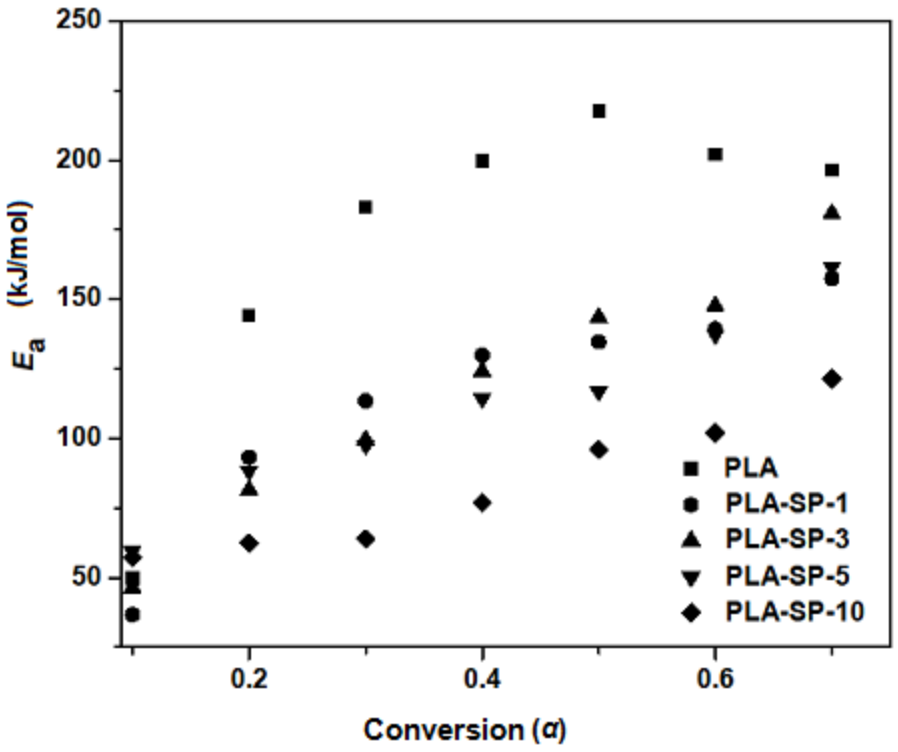

Figure 5.7. Conversion versus activation energy for PLA and PLA-SP composites

The E_a values obtained from both the methods were found to follow a similar trend with respect to increase in loadings of the filler, SP. The E_a values obtained from Kissinger method is in good agreement with the F-W-O method. However, a slight variation in the E_a values obtained by both the methods can be observed for PLA and PLA-SP composites. This is due to the fact that the F-W-O method provides activation energies for different conversion levels, while the Kissinger method is applicable to the maximum rate of conversion (only one data point) at which T_{max} appears. The regression coefficient (R^2) values obtained in the range of 0.9-0.999 for both the methods further proves the applicability of these methods for predicting the thermal degradation behavior of PLA and PLA-SP composites (**Chen et al., 2007; Chrissafis et al., 2010**).

The $Z(\alpha)-\alpha$ master and experimental curves for neat PLA and PLA-SP composites can be seen from Figure 5.8(a-d). The overlapping of experimental curves of neat PLA with the master curve, $Z(F_1)$ can be seen from Figure 5.8(a). This suggests that the thermal degradation process of neat PLA follows the F_1 reaction mechanism. This in turn, indicates that random nucleation becomes the rate controlling step associated with the nucleation process in case of lower α values (0.1-0.55). After the addition of SP in the PLA matrix, during the initial phase, the thermal degradation process proceeds via F_1 reaction mechanism for all the PLA-SP composite samples. With respect to progress in the degradation process, the system, however, slowly changes towards A_3 mechanism (which involves both nucleation and growth) at higher *α* value (0.7-0.95). This might be possibly due to the shift in the thermal degradation mechanism at higher temperature conditions.

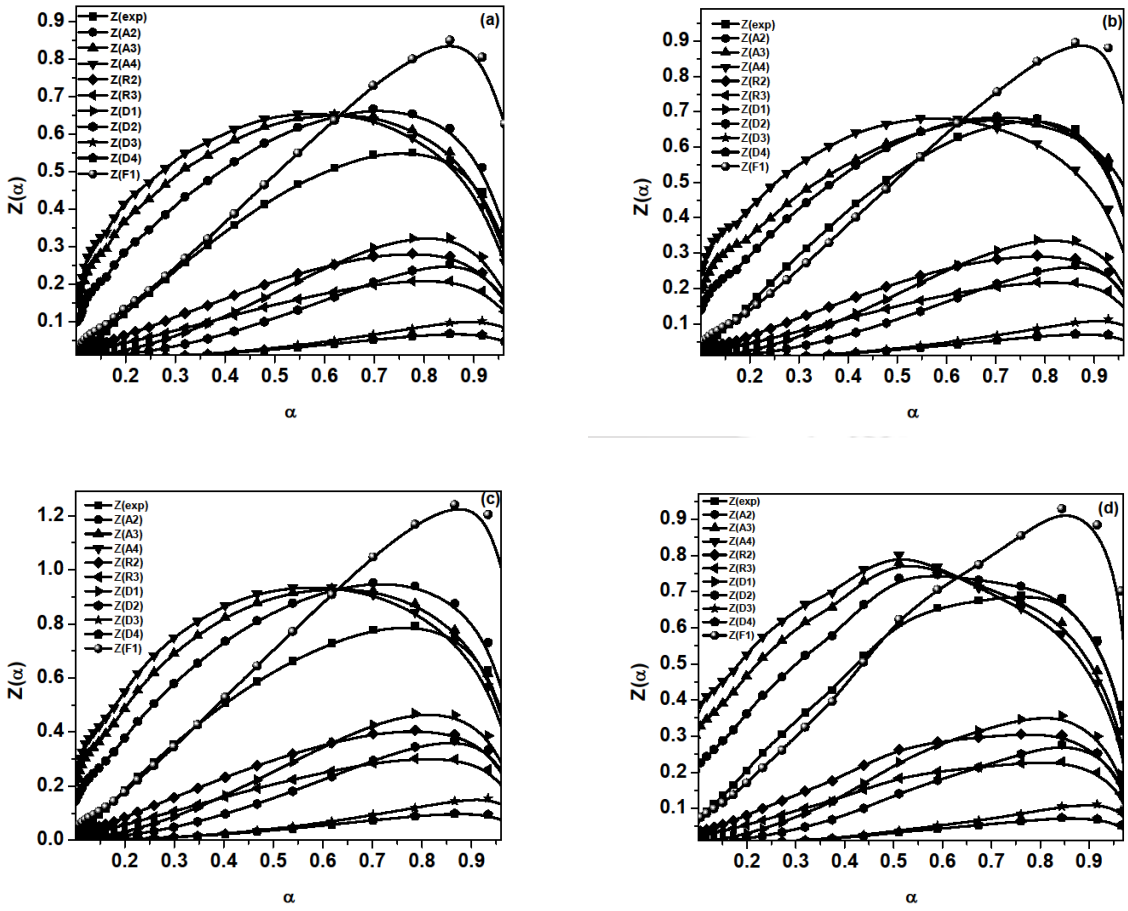

Figure 5.8. Determination of the thermal degradation reaction mechanism by plots of Z(α) versus α using Criado method for (a) neat PLA, (b) PLA-SP-1, (c) PLA-SP-3 and (d) PLA-SP-5

5.5.2. Effect of graphene on the thermal degradation kinetics of PLA

The non-isothermal TGA and DTG curves of PLA and PLA-GR composites at three different heating rates of 10, 20 and 30 °C/min in the nitrogen atmosphere are shown in Figure 5.9 and 5.10, respectively. The TGA curves shown in Figure 5.9 reveal that the thermal stability of PLA increases with increasing GR content irrespective of the heating rate. The DTG plots reveal the different profiles depending on heating rate and wt% loadings of GR. It can be seen from Figure 5.10, that for all the samples, temperatures corresponding to a maximum stage of degradation

(T_{max}) increase progressively with increasing the heating rate. The shift of the DTG curves to higher temperatures with increasing heating rate could be attributed to the short time provided for a sample to reach a given temperature at a high heating rate (**Wu et al., 2006**).

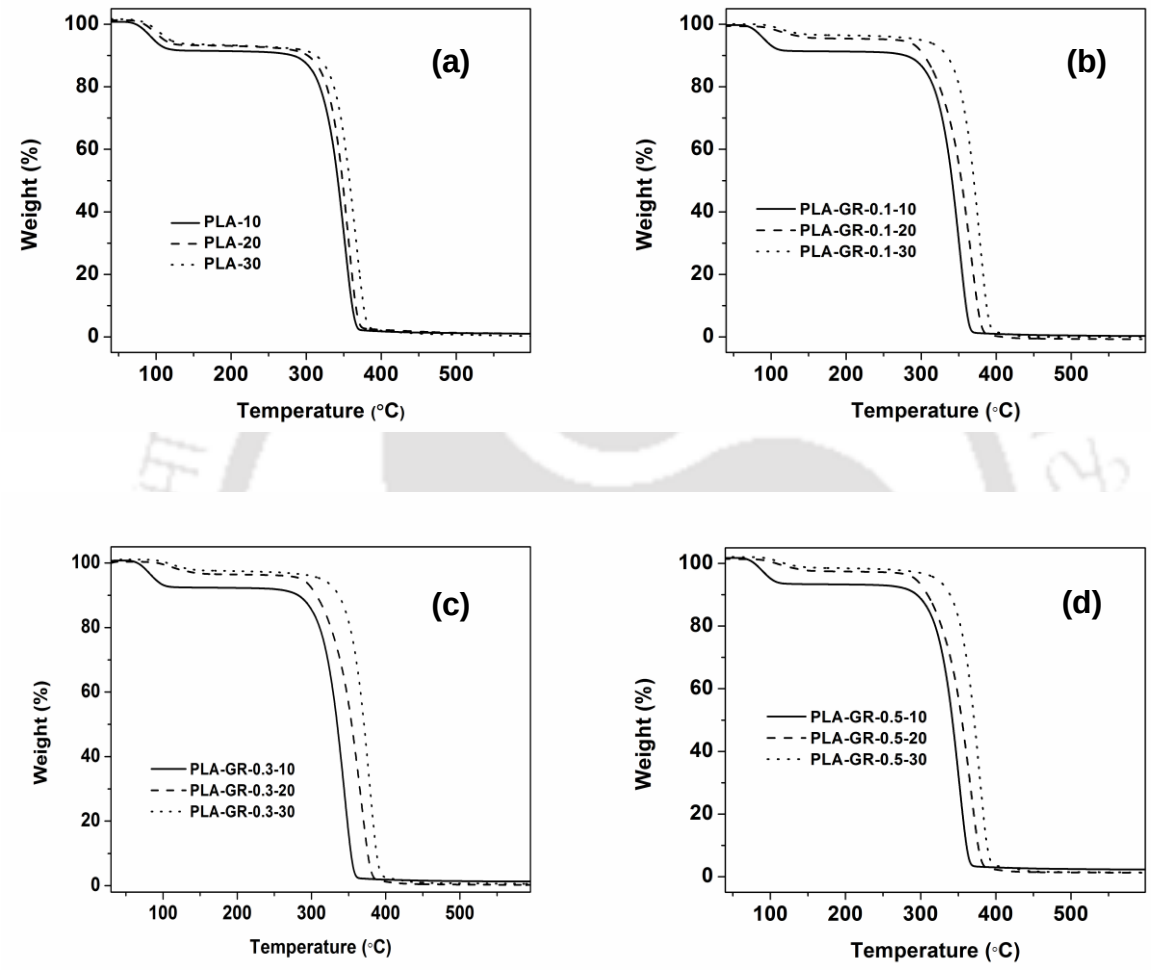

Figure 5.9. TGA curves at different heating rates (10, 20, 30 °C) for (a) PLA, (b) PLA-GR-0. 1, (c) PLA-GR-0.3 and (d) PLA-GR-0.5 nanocomposites

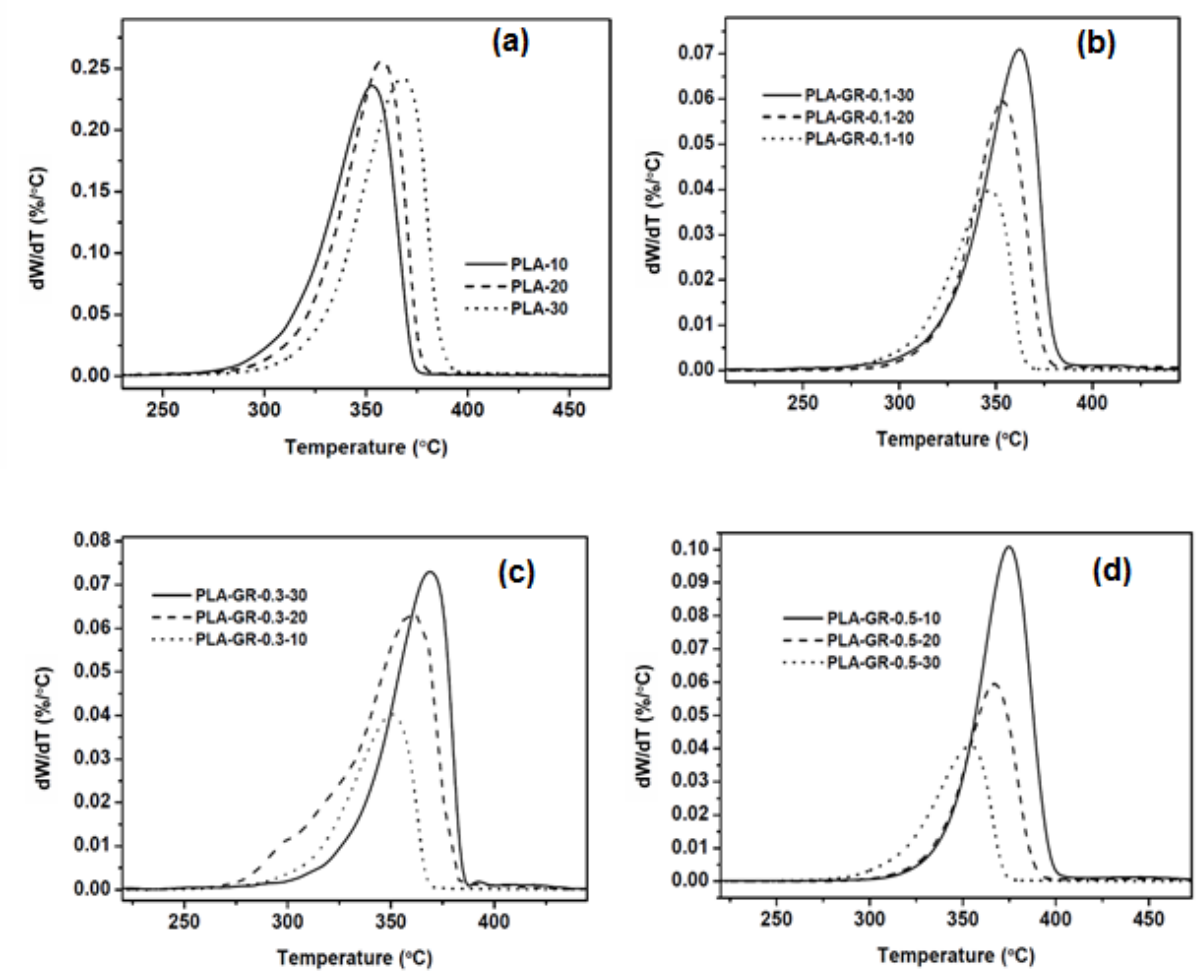

Figure 5.10. DTG curves at different heating rates (10, 20, 30 °C) for (a) PLA, (b) PLA-GR-0. 1, (c) PLA-GR-0.3 and (d) PLA-GR-0.5 nanocomposites

Figure 5.11 shows the linear fitted graph for neat PLA and PLA-GR composites for various "*n*" values. The calculated reaction order at the best R^2 value is considered as the reaction order for that sample (Table 5.4). Then the activation energy and the pre-exponential factor are obtained from the slope and intercept of the fitted straight line. The activation energy of neat PLA and PLA-GR composite samples containing 0.1, 0.3 and 0.5 wt% GR is 125, 129, 137, and 146 kJ/mol, respectively. This clearly indicates that GR acts as an effective nucleating agent and enhances the thermal properties of PLA matrix.

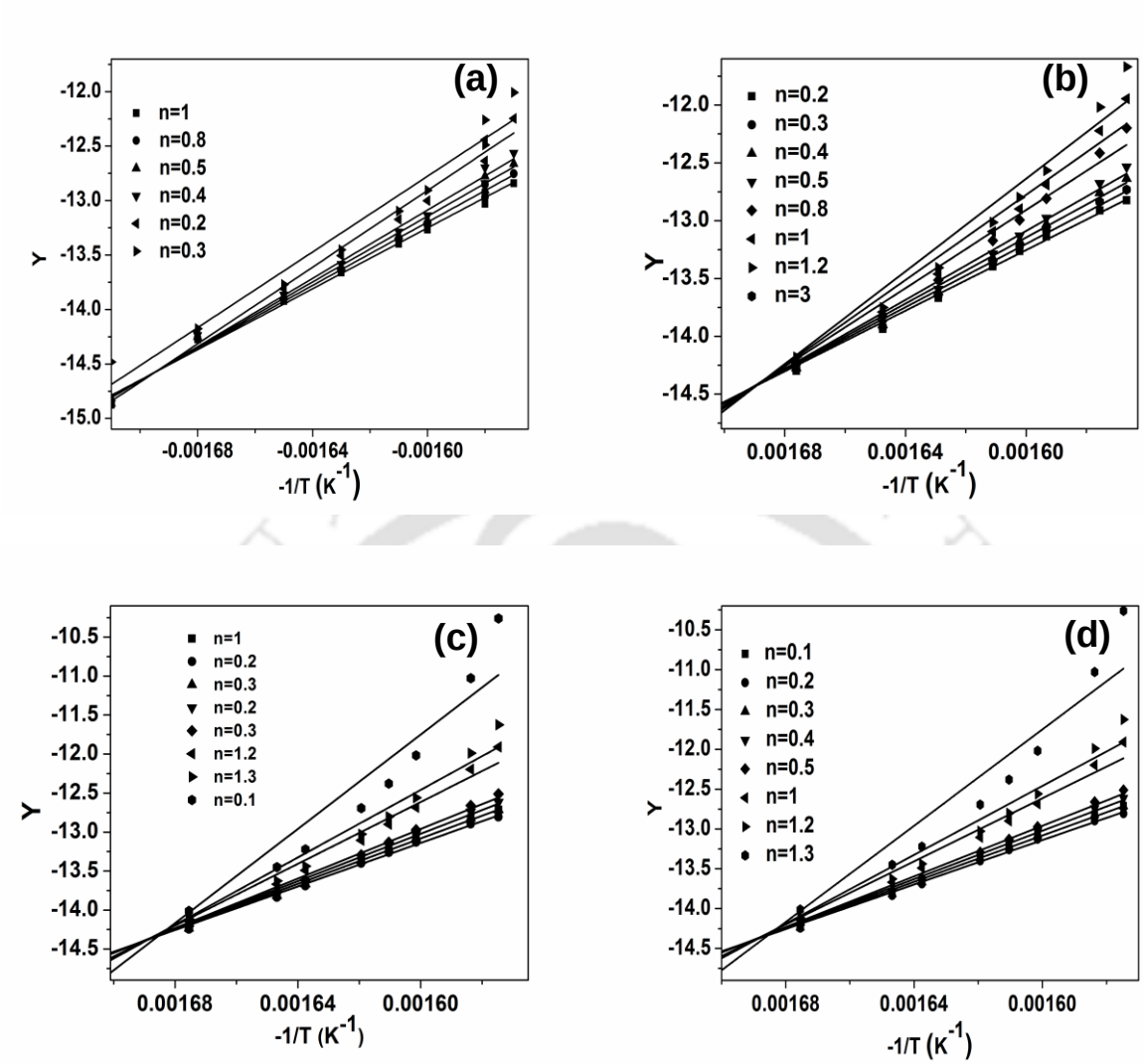

Figure 5.11. Coats-Redfern plots for (a) neat PLA, (b) PLA-GR-0.1, (c) PLA-GR-0.3, and (d) PLA-GR-0.5

Table 5.4. Activation energy, reaction order and regression co-efficient values obtained for PLA and PLA-GR nanocomposites using the Coats-Redfern method

S:No	Sample	E_a (kJ/mol)	*n*	R^2
1	PLA	125	0.4	0.994
2	PLA-GR-0.1	129	0.4	0.997
3	PLA-GR-0.3	137	0.2	0.995
4	PLA-GR-0.5	146	0.3	0.998

In Kissinger's method, the plot of ln (β/T^2_{max}) against $1/T_{max}$ provides straight lines as shown in Figure. 5.12. The apparent activation energy is calculated from the slopes corresponding to various straight lines (Figure 5.12) and the same is presented in Table 5.5. As can be seen from Figure 5.12, smooth relativity of the various fitted straight lines shows the feasibility of Kissinger's method. The E_a values obtained from Kissinger method is 177, 179, 181, and 184 kJ/mol for PLA, PLA-GR-0.1, PLA-GR-0.3 and PLA-GR-0.5 respectively. The regression coefficient (R^2) values obtained in the range of 0.9-0.999 further evidences the applicability of this method for envisaging the thermal degradation behavior of PLA and PLA-GR composites.

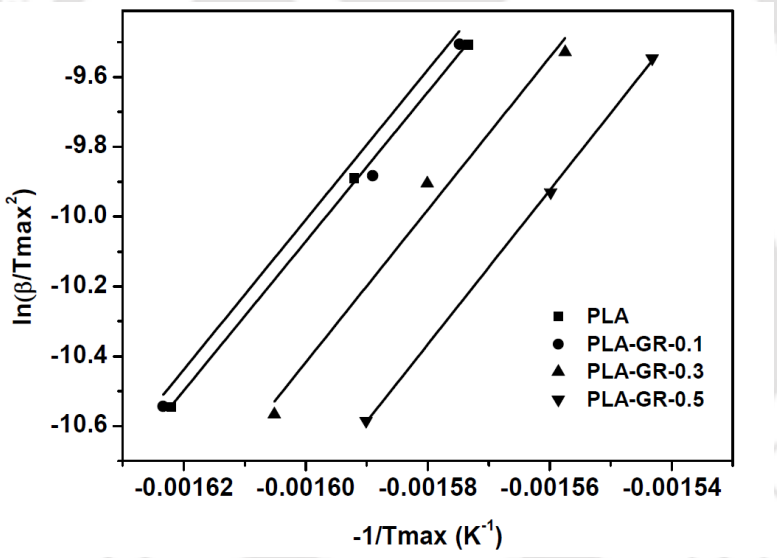

Figure 5.12. Kissinger plot for PLA and PLA-GR nanocomposites

Table 5.5. Activation energy and regression co-efficient for PLA and PLA-GR composites obtained by Kissinger method and Flynn-Wall-Ozawa method

S:No	Sample name	Kissinger method		F-W-O method	
		E_a (kJ/mol)	R^2	E_a (kJ/mol)	R^2
1	PLA	177	0.999	170	0.995
2	PLA-GR-0.1	179	0.999	178	0.997
3	PLA-GR-0.3	181	0.986	185	0.998
4	PLA-GR-0.5	184	0.997	188	0.996

Figure. 5.13(a-d) displays the plots of log (β) against -1/T obtained using F-W-O method. The parallel straight lines can be noticed for both PLA and PLA-GR composites at different α values. This indicates the well suitability of F-W-O method for investigating the thermal degradation kinetics at all levels of conversion degree (**Chrissafis et al., 2010; Fan et al., 2004; Kim et al., 2000**). The plots of activation energy as a function of conversion (α) using the F-W-O method for neat PLA and PLA-GR composites can be seen from Figure 5.14. Variation in the activation energy for both PLA and PLA-GR nanocomposites with respect to conversion can be noticed all through the thermal degradation process. This reveals that the thermal degradation of both PLA and composites do not proceed through the simple process (**Yang et al., 2002; Chen et al., 2007**). The activation energy value (177 kJ/mol) obtained for neat PLA is in accordance with the literature data reported by **Li et al.,** (**2009**). Increment in the activation energy after the addition of GR in the PLA matrix can be noticed. This indicates that the reinforcement improves the thermal stability of PLA. The E_a values obtained from Kissinger and F-W-O methods are in good agreement with each other. The slight variation arises in the E_a values obtained by both the methods, because, the F-W-O method provides activation energies for various levels of conversion, whereas, the Kissinger method can be applied to only maximum rate of conversion.

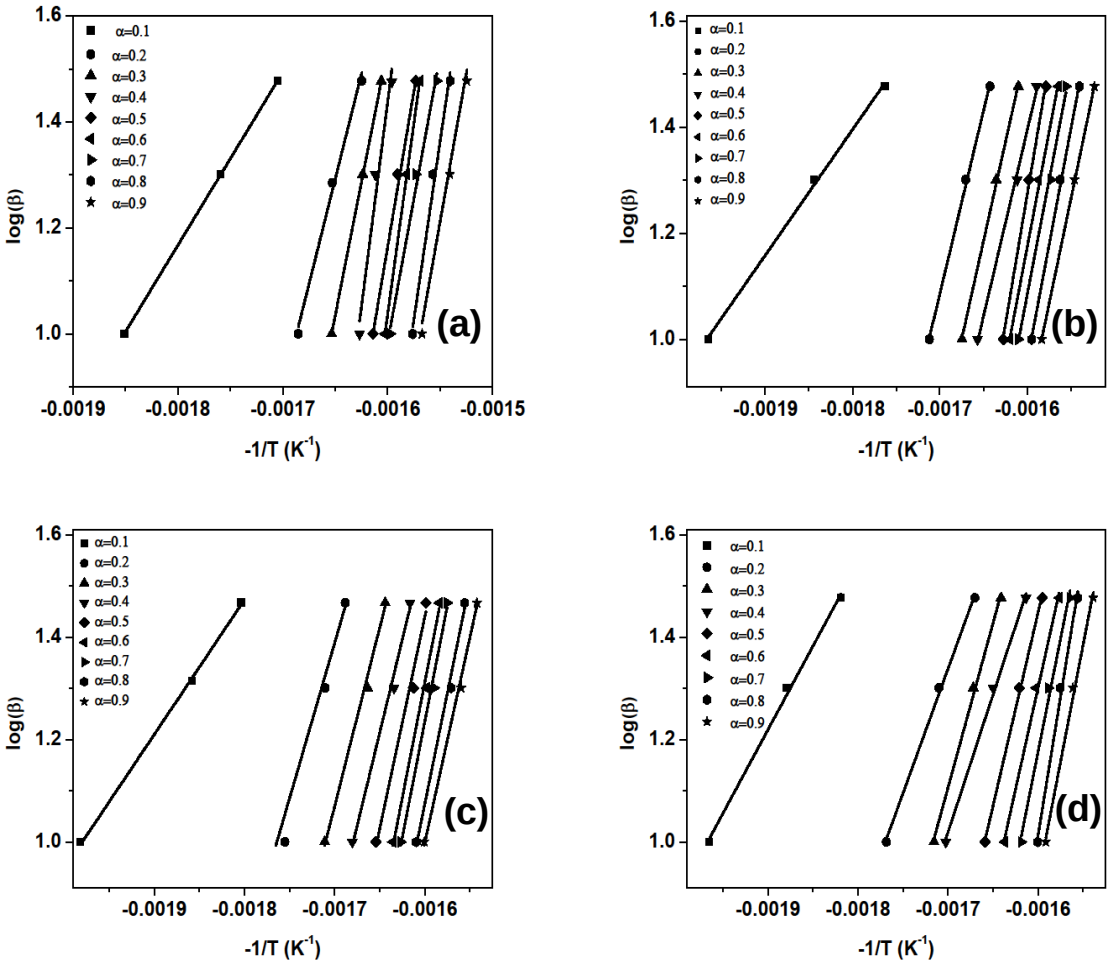

Figure 5.13. Flynn-Wall-Ozawa plots (a) PLA, (b) PLA-GR-0.1, (c) PLA-GR-0.3 and (d) PLA-GR-0.5

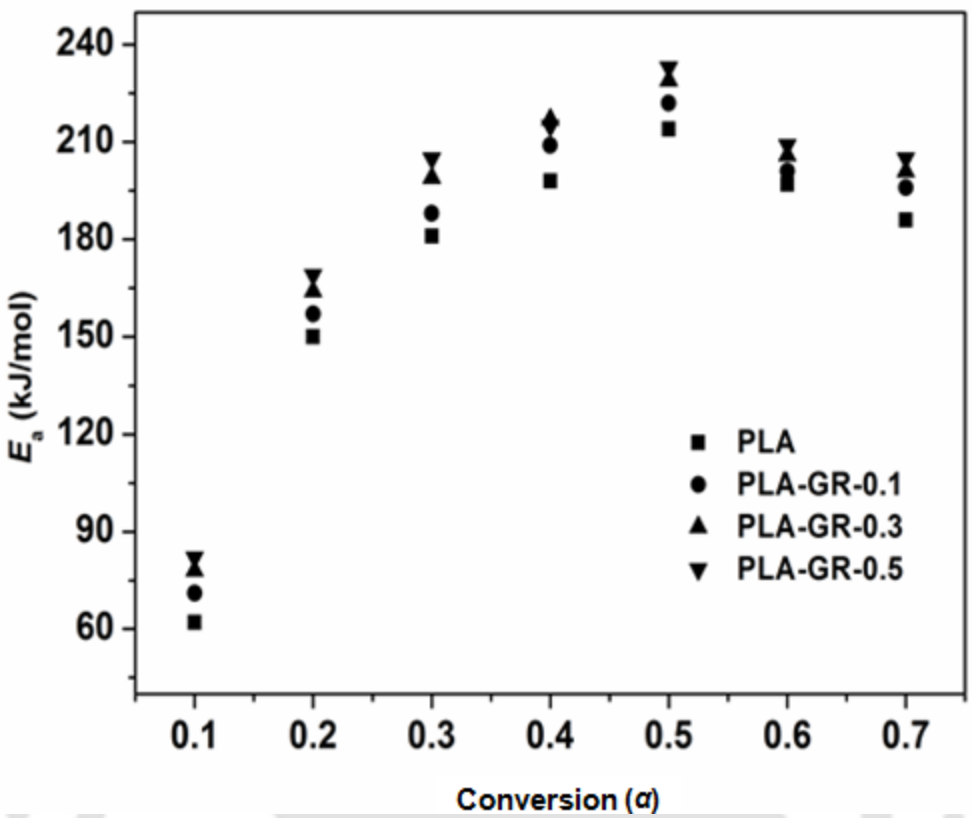

Figure 5.14. Conversion versus activation energy for PLA and PLA-GR composites

The kinetic parameters obtained for 10 °C/min heating rate using the Coats-Redfern method are substituted in the Eqs. (5.16) and (5.17). Figure 5.15 (a-d) illustrates the $Z(\alpha)-\alpha$ master and experimental curves for neat PLA and PLA-GR composite samples with 0.1, 0.3 and 0.5 wt% GR. It is apparent that the experimental curves of neat PLA (Figure. 5.15(a)) overlaps with the master curves of $Z(F_1)$, suggesting that the thermal degradation process of neat PLA follows the F_1 reaction mechanism. This indicates that random nucleation is the rate controlling step associated with the nucleation process at lower α values (0.1-0.55). After adding GR, at the initial phase, the thermal degradation process proceeds via F_1 reaction mechanism for all PLA composite samples. With further progress in the degradation reaction, the system, however, slowly changes towards A_3 mechanism (which involves both nucleation and growth) at higher α

value (0.7-0.95). This might be possibly due to the shift in the thermal degradation mechanism at higher temperature conditions.

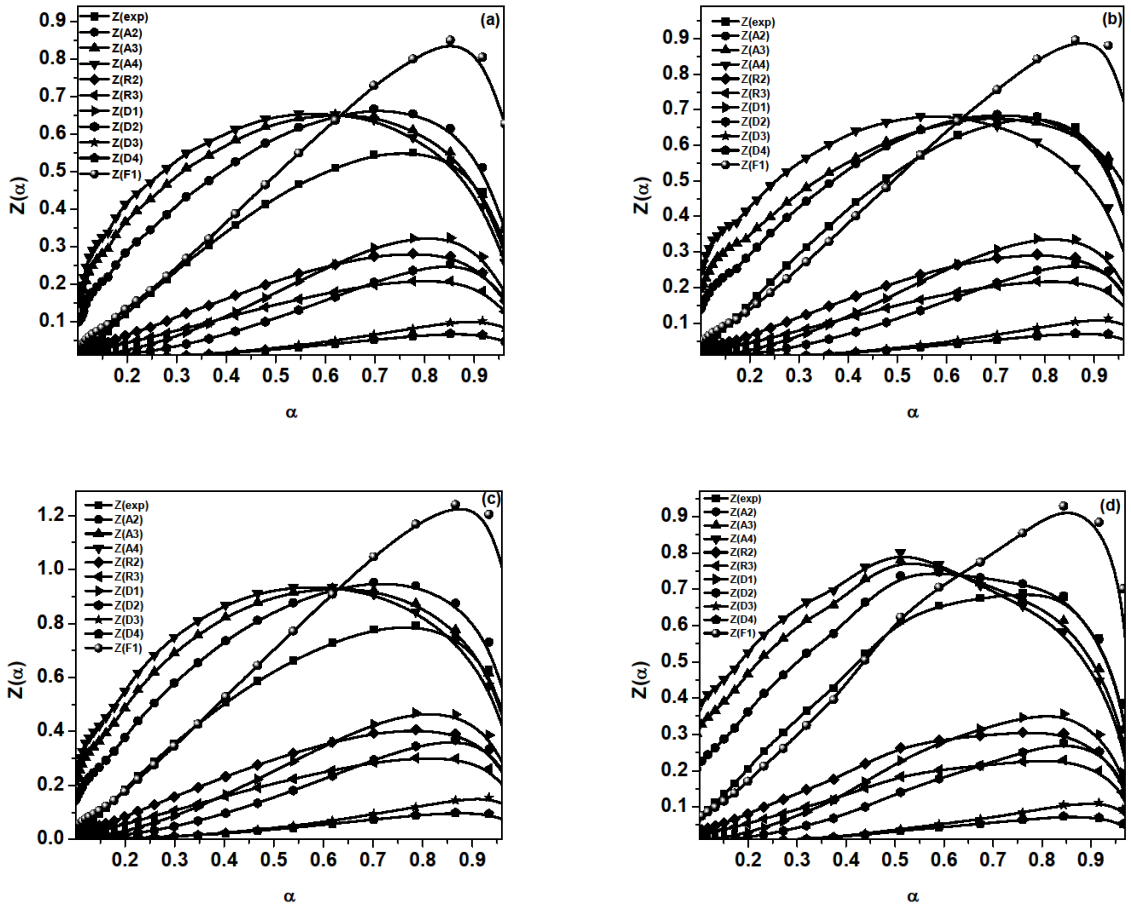

Figure 5.15. Determination of the thermal degradation reaction mechanism by plots of Z(α) versus α using Criado method for (a) neat PLA, (b) PLA-GR-0.1, (c) PLA-GR- 0.3, and (d) PLA-GR-0.5

5.6. Conclusions

Thermal degradation kinetics of PLA-SP and PLA-GR composites were investigated using Coats-Redfern, Kissinger and Flynn-Wall-Ozawa methods. The activation energy for the thermal degradation of both PLA and its composites was evaluated as a function of conversion throughout the degradation process by F-W-O method. The variation in the activation energy obtained with respect to conversion suggests that the thermal degradation of both PLA and composites occurs through complex mechanism. The activation energy values obtained for PLA and its composites by all the three methods are found to be in good agreement. In case of PLA-SP composites, a decrease in the activation energy is observed with incorporation of SP. After the addition of GR in the PLA matrix, the thermal stability of PLA is enhanced, which is evidenced by the increment in the activation energy. Criado method reveals that the PLA-GR and PLA-SP composites follow the F_1 and A_3 nucleation mechanism at lower (0.1-0.6) and higher (0.7-0.95) level of conversion, respectively.

CHAPTER 6

Hydrolytic Degradation Studies of Sucrose Palmitate and Graphene Reinforced PLA Nanocomposites

This chapter discusses the influence of sucrose palmitate (SP) and graphene (GR) on the hydrolytic degradation behavior of poly(lactic acid) (PLA) nanocomposites. The influence of temperature and pH of the solution on the hydrolytic degradation behavior of PLA and its nanocomposites was investigated. The variation in the crystallinity of PLA and PLA composites subjected to the hydrolytic degradation process was verified by XRD and DSC analysis. The morphological changes that occurred during the degradation process were pictoriated using scanning electron microscopy (SEM). Thermo-gravimetric analysis confirmed the loss of thermal stability of the neat PLA as well as composites after hydrolytic degradation process.

6.1. Introduction

After the disposal of packaging material, it is highly desirable that the same should be degraded at a rapid pace owing to environmental concerns (**Marsh et al., 2007**). The two important sequential steps that are associated with the biodegradation process include (i) hydrolysis reaction through which molecular weight of the polymer decreases and (ii) subsequent assimilation of the same by microbes (**Ndazi et al., 2011**). Therefore, it is clear that water is likely to be the PLA's most interactive molecule, after completion of its life cycle. This in turn, indicates that understanding the hydrolytic degradation behaviour of any biopolymer is the most encouraging way to understand the biodegradation process. A series of literature reported that PLA has exhibited an excellent hydrolytic degradation behaviour (**Chen et al., 2013a; Zhou et al., 2008; Gaona et al., 2012; Andersson et al., 2013; Kaitlyn et al., 2011; Proikakis et al.; 2005; Olewink et al., 2007**). However, any filler incorporated in the PLA matrix is expected to certainly have implications in the hydrolytic degradation behaviour of the resultant nanocomposite material. In this regard, the present work aims to study the effect of two different reinforcements, i.e., sucrose palmitate (SP) and graphene (GR) on the hydrolytic degradation behaviour of PLA. The hydrolytic degradation experiments for PLA, PLA-SP and PLA-GR nanocomposites are carried out under different pH (acidic, neutral and basic) and temperature (35 and 55 °C) conditions. Thereafter, the variation in the crystalline behaviour of PLA, PLA-SP and PLA-GR nanocomposites is investigated using differential scanning calorimetry (DSC) and X-ray diffraction analysis. The influence of hydrolytic degradation on the thermal stability of the PLA, PLA-SP and PLA-GR nanocomposite sample is examined using thermo gravimetric analysis (TGA). Further, the morphological changes induced by the hydrolytic degradation process for PLA, PLA-SP and PLA-GR nanocomposite are pictoriated using SEM. The transparency of the PLA, PLA-SP and PLA-GR nanocomposite samples before and after hydrolytic degradation is analyzed using UV-visible spectrophotometer.

6.2. Experimental

6.2.1. Materials

The chemicals used for the synthesis of PLA-SP and PLA-GR nanocomposites are discussed in section 3.2.1 and 2.2.1, respectively.

6.2.2. Synthesis of PLA-SP and PLA-GR nanocomposites

The synthesis procedure for the fabrication of PLA-SP and PLA-GR nanocomposites is discussed in section 3.2.2 and 2.2.3, respectively.

6.2.3. Hydrolytic degradation process

PLA, PLA-SP-5 and PLA-GR-0.1 nanocomposite samples were subjected to hydrolytic degradation process at two different temperatures (35 ± 1 °C and 55 ± 1 °C) with three different pH solutions, i.e. acidic (pH≈2), neutral (pH≈7) and basic (pH≈12). The pH of the solution was adjusted using HCl or NaOH. After placing the sample in the above solutions, the same was taken off from the container at a regular interval of time, washed with water and finally dried at 35 °C for a time period of 6 h. Thereafter, the weight change between before and after degradation was calculated in order to determine the residual weight fraction (ϕ). The following relationship was used for the calculation of the residual weight fraction (ϕ) as a function of degradation time (t).

$$\phi = \frac{W_t}{W_0} \times 100\% \qquad (6.1)$$

where, W_0 and W_t correspond to the dry weight (g) of the sample prior to the degradation process and the dry weight (g) of the sample after certain time (t) of degradation process, respectively. Samples subjected to hydrolytic degradation were designated as PLA-pH-T-t, PLA-SP-5-pH-T-t and PLA-GR-0.1-pH-T-t, where, pH refers to the acidic (A), neutral (N) and basic (B) conditions under which the degradation process was performed. The symbols, “T” and “t” refer to the temperature condition and time adopted for the hydrolytic degradation process, respectively.

6.3. Characterization

6.3.1. X-ray diffraction (XRD) analysis

The influence of hydrolytic degradation on the crystalline behaviour of PLA, PLA-SP-5 and PLA-GR-0.1 nanocomposite before and after degradation was studied using X-ray diffractometer (Bruker A8 advance). The XRD analysis was done under an air atmosphere at room temperature using Cu-Kα (λ= 0.15406 nm) radiation and the instrument was operated at 40 kV and 40 mA. The diffraction data were obtained in the 2θ range of 1-50° with a scanning rate of 0.05° s^{-1} and 0.5 s step size**.** The following relationship was used for the calculation of percentage crystallinity (% X_c)

$$X_c = \frac{\sum A_{crystalline}}{\sum A_{crystalline} + \sum A_{amorphous}} \quad (6.2)$$

where, $A_{crystalline}$ and $A_{amorphous}$, refer to the area under crystalline and amorphous fractions, respectively.

6.3.2. Differential scanning calorimetry (DSC)

The variation in the thermal and crystallization behaviour of PLA, PLA-SP-5 and PLA-GR-0.1 nanocomposite before and after hydrolytic degradation was investigated using a differential scanning calorimetty (Mettler Toledo-1 series). All the samples were heated from the temperature ranging from 30 to 180 °C at a heating rate of 5 °C/min, under N_2 flow of 50 mL/min. First, all the samples were heated from 30 to 180 °C and held isothermally at 180 °C in order to erase the thermal history. DSC thermographs resulted during the second heating cycle were used for interpretation of glass transition temperature (T_g), cold crystallization temperature (T_{cc}), the enthalpy change at T_{cc} (ΔH_{cc}), melting temperature (T_m) and the enthalpy of fusion at T_m (ΔH_m).

6.3.3. Thermogravimetric analysis (TGA)

The thermal degradation profile of PLA, PLA-SP-5 and PLA-GR-0.1 nanocomposite before and after hydrolytic degradation was obtained using thermo gravimetric analyzer. The

analysis was performed on a Mettler Toledo thermo gravimetric analyzer (TGA/SDTA 851® model). All the samples were heated from 40 to 600 °C, at a heating rate of 20 °C/min, with N_2 flow of 60 mL/min.

6.3.4. Scanning electron microscopy (SEM)

The morphologies of PLA, PLA-SP-5 and PLA-GR-0.1 nanocomposite samples before and after degradation were monitored by scanning electron microscopy (SEM) using a Zeiss Sigma model (LEO1430VP).

6.3.5. UV-visible spectrophotometry

Transparency measurements for PLA, PLA-SP-5 and PLA-GR-0.1 nanocomposite samples before and after degradation process were carried out using UV-Visible spectrophotometer (Make: Perkin Elmer, Model: Lambda 35). For the measurements, the wavelength range was varied between 200 and 600 nm with a scan rate of 50 nm/min and a spectral bandwidth of 2 nm.

6.3.6. Gel permeation chromatography (GPC)

The weight average molecular weight (Mw), number average molecular weight (Mn) and polydispersity index (PDI) for PLA, PLA-SP-5 and PLA-GR-0.1 before and after being hydrolyzed, were measured by gel permeation chromatography (GPC). GPC was performed on a Perkin-Elmer series 200 system (10 μm PL gel 300x7.5 mm mixed-B and mixed-C column, linear polystyrene calibration) equipped with a refractive index (RI) detector. Chloroform (HPLC grade) was used as a mobile phase at the flow rate of 1 mL/min and the analysis was done at room temperature.

6.4. Results and discussion

6.4.1. Effect of sucrose palmitate on the hydrolytic degradation behaviour of PLA

6.4.1.1. Hydrolytic degradation behaviour

The residual weight fraction (ϕ) of PLA and PLA-SP-5 nanocomposite was measured as a function of degradation time at different pH and temperature conditions. It can be observed from Figure 6.1 that the residual weight fraction of PLA and PLA-SP-5 nanocomposite varies non-linearly with an increase in the degradation time for all the pH as well as temperature conditions studied. It can also be seen that both PLA and PLA-SP-5 nanocomposite exhibit similar trend with increasing the degradation period, i.e. ϕ values are noticed to exhibit a greater downturn in the shorter time range and vice versa, irrespective of pH and temperature conditions. In order to further understand the influence of pH and temperature on the hydrolytic degradation behaviour of PLA and PLA-SP-5 nanocomposite, the whole degradation process is segmented into three sections (see Figure 6.1). In the first region of degradation, ϕ values are observed to vary linearly with time, which is evident from the greater slope of the degradation curves as compared to other regions. In the second region of degradation, ϕ values vary slightly with time and the degradation rate is relatively slow as compared to the first region. In the final region of degradation, it is observed that the ϕ values almost remain constant with an increase in the degradation time.

Further, in case of PLA, the slope corresponding to the initial degradation region is observed to be greater for samples subjected to degradation at elevated temperature (55 °C), as compared to 35 °C. This is because, at relatively greater temperature, i.e. 55 °C, intensified mobility of molecular chains results in decreased activation energy for chain scission reaction (**Chen et al., 2013b; Olewnik et al., 2006**). It is apparent that the hydrolytic degradation rate is faster under basic pH conditions at both the temperatures in comparison with acidic as well as neutral pH conditions. Similar degradation behaviour is reported for PLA with respect to different pH conditions by **Chen et al.** (**2013b**) and **Olewnik et al.** (**2006**). It is explained that the possible reason for this might be due to the decisive role

played by terminal OH groups resulted during the hydrolytic degradation under basic conditions.

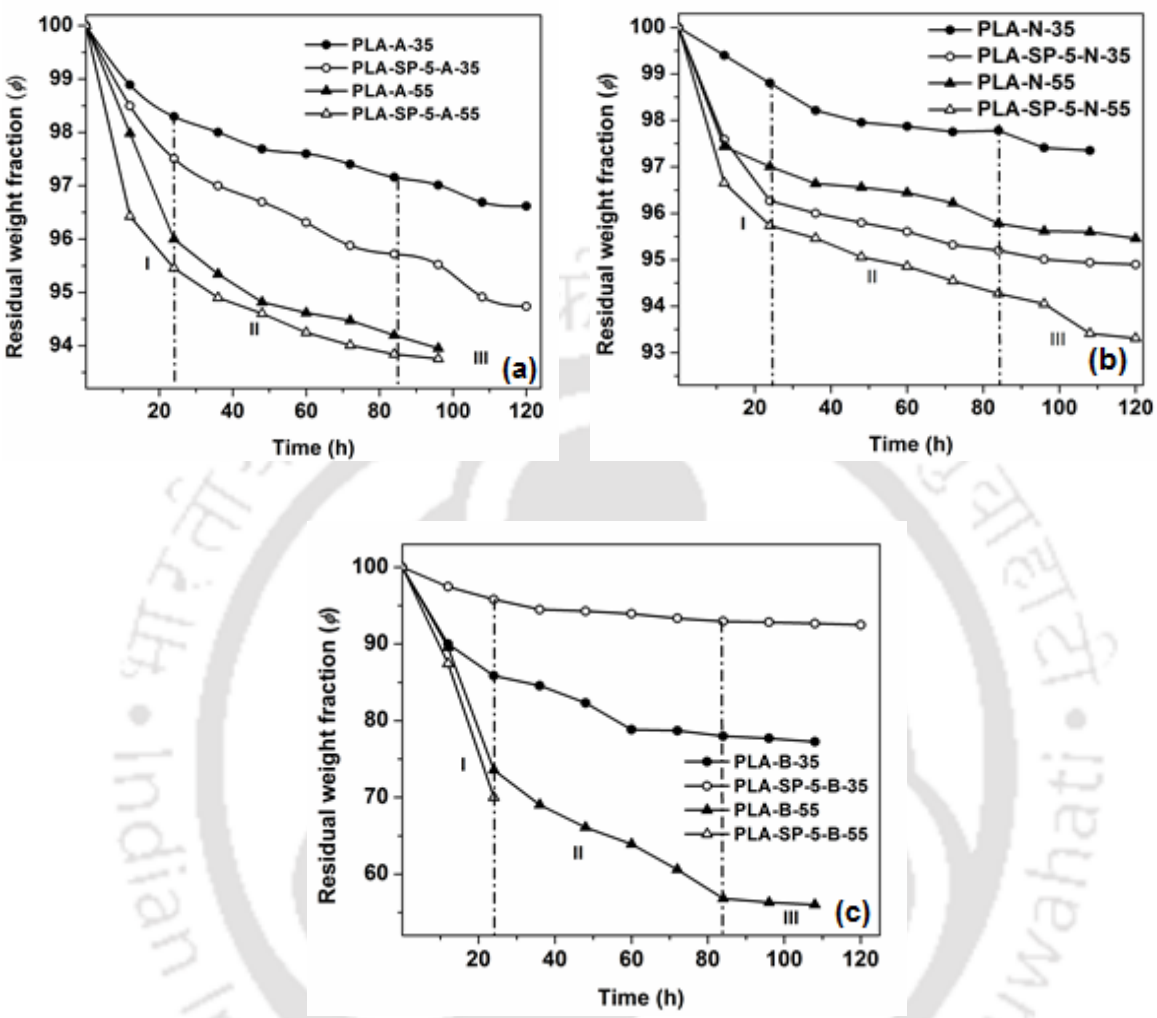

Figure 6.1. Residual weight fraction of PLA and PLA-SP-5 samples as a function of degradation time at (a) acid (b) neutral and (c) basic pH conditions

The PLA-SP-5 nanocomposite sample also exhibits the faster rate of degradation at elevated temperature (55 °C) throughout the entire degradation profile, irrespective of pH conditions. However, in comparison with PLA, PLA-SP-5 nanocomposite demonstrates slower and faster degradation rate at 35 and 55 °C, respectively, under basic pH condition. This peculiarity of the degradation phenomenon is due to the fact that the water diffuses easily inside the amorphous domain of PLA and initiates the degradation process (**Dias et al., 2012; Paul et al., 2005; Fernandez et al., 2013; Zhang et al., 2008**). After the addition

of SP in the PLA matrix, the slower degradation rate exhibited by PLA-SP-5 nanocomposite at 35 °C (see Figure 6.1(c)) may be due to the increase in hydrophobicity and crystallinity of the resultant nanocomposite material. However, at elevated temperature, due to the improvement in the mobility of PLA chains, water might diffuse into the interface between PLA and SP and initiate the hydrolysis of PLA, thereby, leading to oozing out of SP from PLA matrix. This is evident from XRD and FE-SEM results, which are discussed later in details.

6.4.1.2. DSC analysis

The second heating thermographs of PLA and PLA-SP-5 nanocomposite samples before and after degradation (108 h) at different pH and temperature are presented in Figure 6.2(a and b). Prior to the hydrolytic degradation process, the PLA sample exhibits the glass transition, crystallization and melting temperature at 62 °C, 110 °C and 149 °C, respectively. After the addition of SP in the PLA matrix, the T_g value remained constant, whereas, the T_{cc} and T_m values slightly shifted to higher temperature side. The shift in T_{cc} is due to the slower diffusion rate of polymer chains to the surface of the nucleus. The enhancement in the T_m value indicates that SP acts an effective nucleating agent.

It can be observed from the Figure 6.2(a), that PLA samples subjected to hydrolytic degradation at different pH and temperature conditions demonstrate a common endothermic peak in the glass transition region. The appearance of the glass transition region for all the samples is related to the melting behaviour of mesophase, in which the formation of locally ordered structure is induced **(Chen et al., 2012)**. The T_{cc} values for all the PLA samples are noticed to be shifted to the lower temperature side as compared to the PLA sample before degradation process **(Saha et al., 2006)**. This underlines the fact that the cold crystallization process of PLA is facilitated by the hydrolytic degradation process **(Chen et al., 2012)**. The improvement experienced in the cold crystallization process of PLA could have been resulted from the formation of less intensified and loose chain PLA entanglement with due course of the hydrolytic degradation process. Therefore, such type of entanglements

induced in the material is expected to possess greater mobility leading to promotion in the crystallinity of PLA. The much pronounced decrement in T_{cc} values are observed for PLA samples subjected to hydrolytic degradation under basic pH conditions. These results suggest that, hydrolytic degradation performed at basic pH conditions induces the faster degradation, which is evident from the improvement in the crystallinity observed in both DSC as well as XRD analysis **(Paul et al., 2005)**.

Like PLA samples, PLA-SP-5 nanocomposite also displays an endothermic peak in the glass transition region irrespective of various pH conditions and temperature studied. In case of PLA-SP-5 nanocomposite samples, decreasing trend in the cold crystallization temperature with respect to neutral, acidic and basic pH conditions (at different temperatures) is also observed. This indicates that the hydrolytic degradation of PLA-SP-5 nanocomposite sample under basic pH occurs at a much faster rate in comparison with acidic as well as neutral conditions. This reveals that the base solution easily attacks and hydrolyses the amorphous domains of PLA-SP-5 nanocomposite samples. This in turn, leads to greater loss of amorphous regions and increment of the crystalline domain in the nanocomposite material. Therefore, this phenomenon gives rise to improvement in the cold crystallization process of PLA-SP-5 nanocomposite. It can also be noticed from Figure 6.2(b) that the peak corresponding to melting region also decreases for all the PLA-SP-5 nanocomposite samples for which the degradation was carried out at acidic and basic pH conditions. In contrast, the melting peak for the PLA-SP-5 nanocomposite samples remain unaltered in the case of the hydrolytic degradation process done at neutral pH condition. The decrement observed in the melting peak of PLA-SP-5 nanocomposite samples treated at acidic and basic pH conditions is due to the reduction in the molecular weight of the samples. A similar phenomenon in the variation of T_{cc} and T_m values after hydrolytic degradation process is reported in the literatures **(Tsuji et al., 2010; Saha et al., 2006)**.

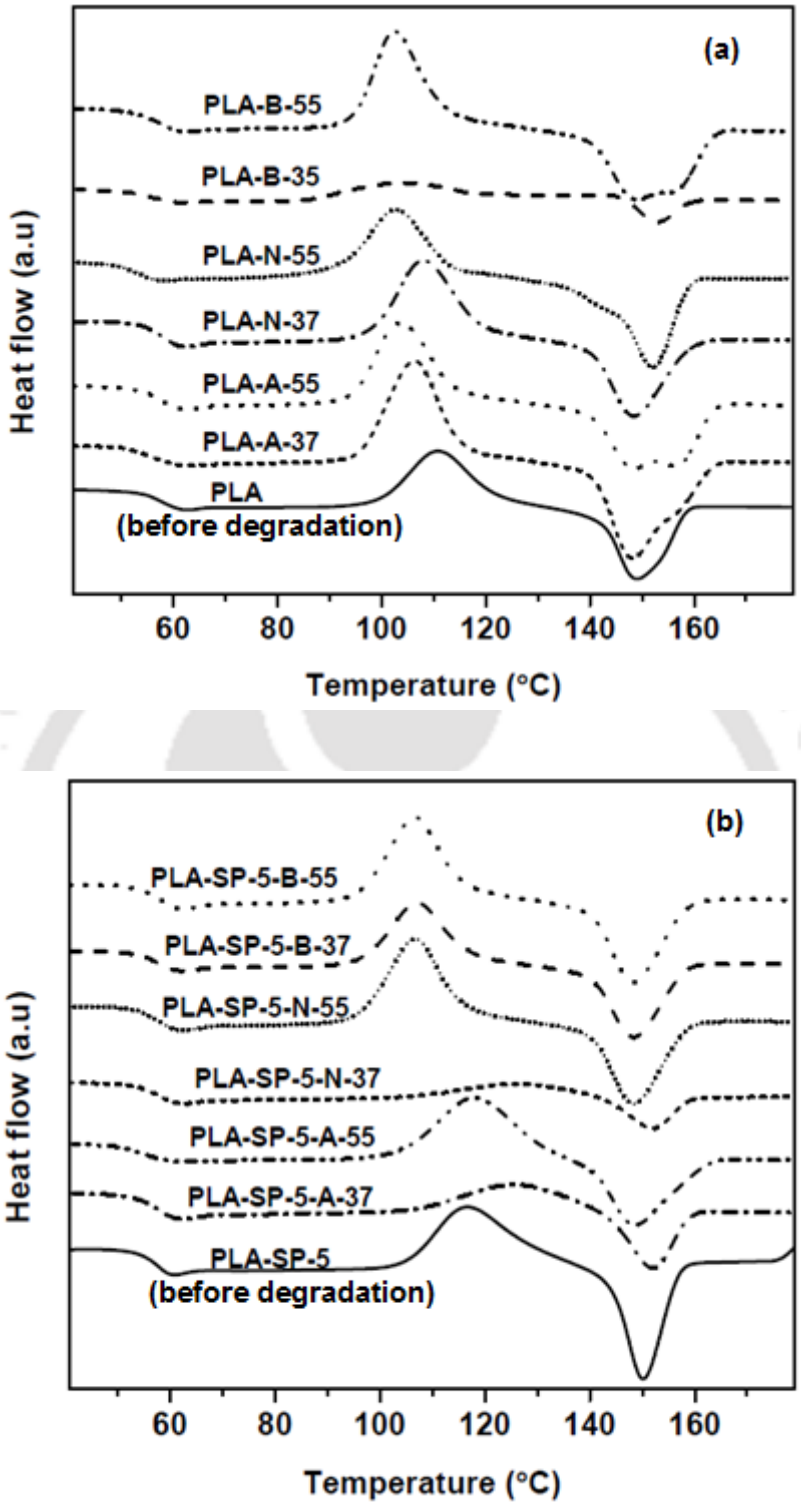

Figure 6.2. DSC thermographs for (a) PLA and (b) PLA-SP-5 (before and after hydrolytic degradation)

6.4.1.3. XRD analysis

The crystalline structure of PLA and PLA-SP-5 nanocomposite samples after degradation at basic pH was studied using XRD analysis as illustrated in Figure 6.3 and the crystallinity (%) of the respective samples is presented in Table 6.1. In the XRD pattern of the PLA sample (before degradation) depicted in Figure 6.3(a), the peak observed at 2θ = 16.7° corresponds to the semi-crystalline phase of PLA. The presence of a peak at 2θ = 16.7° is due to the reflections of (1 0 0) and (2 0 0) planes and this reveals the orthorhombic *α*-crystal form of PLA. The broad nature of the respective peak indicates that the PLA possesses low crystallinity (**Luo et al., 2012**). Under the basic pH condition studied, the intensity of the peak (2θ = 16.7°) corresponding to the crystalline structure of PLA increases with increasing the degradation time (36 and 108 h) as shown in Figure 6.3(a). The increment in crystallinity for PLA is further enhanced at higher degradation temperature (55 °C). This is because, at the initial stages of degradation, water firstly penetrates into the amorphous domains of PLA and hydrolyses the same. Thereafter, the hydrolyzed amorphous region diffuses out of the polymer matrix and this in turn leads to enhancement in the crystallinity (**Gorrasi et al., 2013; Oyama et al., 2009**).

It can be seen from the XRD pattern of PLA-SP-5 nanocomposite sample (before degradation) that the peak observed at 2θ = 2.27° reveals the presence of SP incorporated in the PLA matrix (Figure 6.3(b)). Interestingly, it can be noticed that the peak corresponding to SP tends to almost disappear after the degradation process. The reason for this behaviour can be inferred from the oozing out process of SP discussed earlier in the hydrolytic degradation behaviour section. A similar trend in the crystallinity behaviour exhibited by neat PLA with respect to degradation time is also evidenced for PLA-SP-5 nanocomposite too, as discussed earlier. This can be confirmed from the development of strong intensities of the diffraction peaks that corresponds to the (1 1 0), (2 0 0) as well as (2 0 3) crystal planes, with respect to degradation time, for both PLA and PLA-SP-5 nanocomposite. It can also be further noticed that, the presence of the relatively weak peak at 2θ = 22.27° is attributed to

the reflection of (0 1 5) plane of PLA, indicating the development of the more perfect crystalline structure with respect to degradation time, in case of both PLA and PLA-SP-5 nanocomposite **(Gorrasi et al., 2013)**. Further, for all the samples, the additional diffraction peaks observed at 2θ = 14.7°, 16.8°, 19.3° and 22.2° are ascribed to the reflections of (0 1 0), (1 1 0)/(2 0 0), (2 0 3) and (0 1 5) planes of α-crystalline form of PLA, respectively. At elevated temperature, it is unfeasible to obtain the XRD pattern for the PLA-SP-5 nanocomposite sample due to complete dissolution of PLA-SP-5 nanocomposite at basic pH after 36 h of the degradation process. This reveals the fact that the addition of SP in the PLA matrix leads to the faster degradation rate of nanocomposite system.

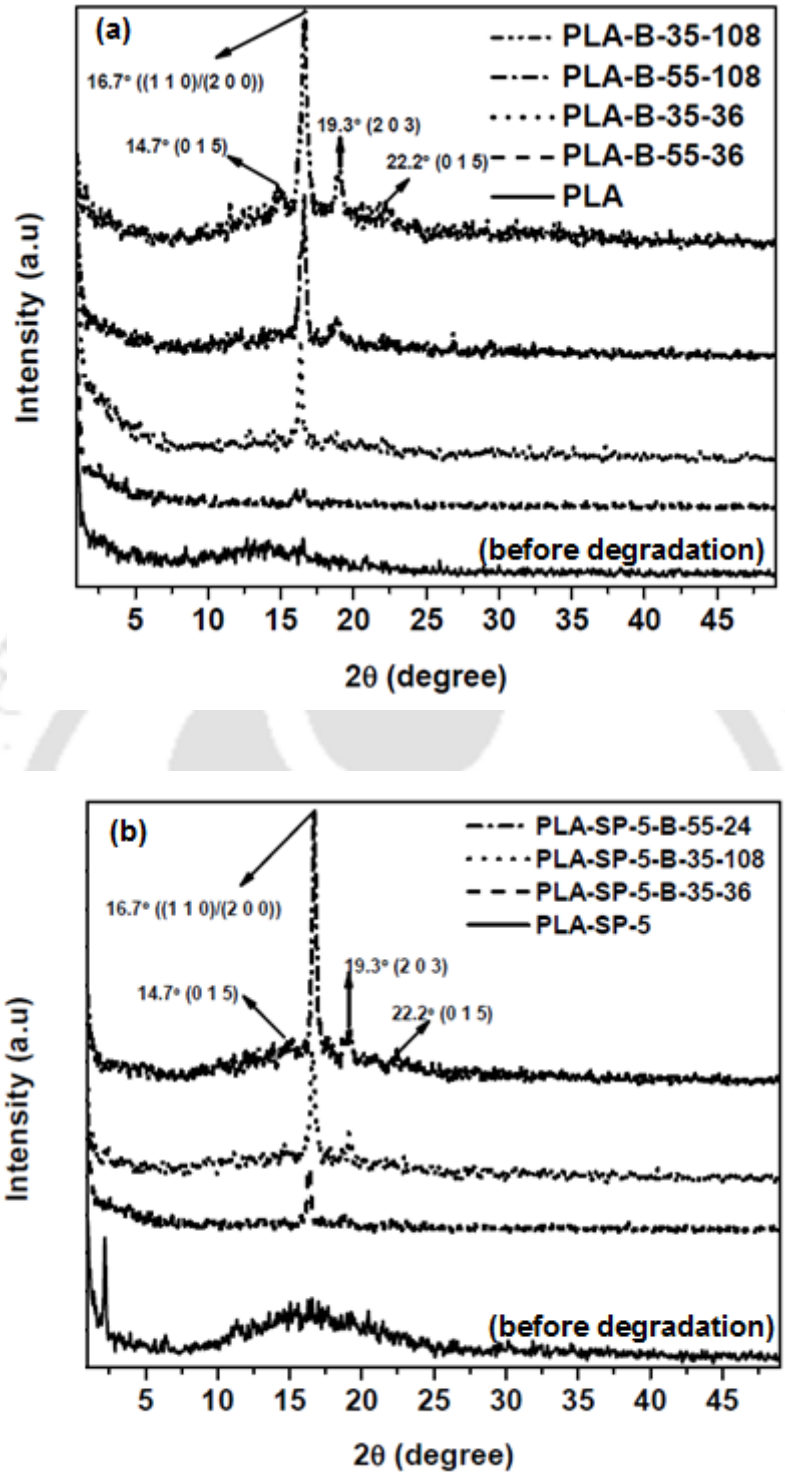

Figure 6.3. XRD patterns of (a) PLA and (b) PLA-SP-5 (before and after hydrolytic degradation)

Table 6.1. Crystallinity (%) of PLA and PLA-SP-5 samples (before and after degradation)

S:No	Sample name	Crystallinity (%)
1	PLA	12.5
2	PLA-B-35-108	39.2
3	PLA-B-55-108	50.1
4	PLA-SP-5	16.9
5	PLA-SP-5-B-35-108	45.6
6	PLA-GR-0.1-B-55-108	41

6.4.1.4. TGA analysis

The TGA curves for PLA and PLA-SP nanocomposite before and after degradation under different pH conditions are shown in Figure 6.4(a,b). The decomposition temperature for all the samples at 50% weight loss is presented in Table 6.2. It can be seen from Figure 6.4(a) that the neat PLA sample (before degradation) exhibits a single stage of weight loss in the temperature range of 307-402 °C. The temperature at 50% weight loss ($T_{50\%}$) from the TGA curve of PLA is extrapolated to be ~358 °C. After degradation time of 108 h, $T_{50\%}$ for PLA samples hydrolyzed under acidic, neutral and basic conditions at 35 °C is determined to be 353, 356 and 343 °C, respectively. With increasing in the hydrolytic degradation temperature, the $T_{50\%}$ further decreases to ~351, 354 and 313 °C for acidic, neutral and basic pH conditions, respectively. Comparative analysis of the $T_{50\%}$ values before and after degradation process under different pH and temperature conditions indicate that the PLA exhibits faster rate of hydrolytic degradation under basic pH conditions for the temperature of 55 °C **(Paula et al., 2011)**.

It can be observed from Figure 6.4(b) that the PLA-SP-5 nanocomposite (before degradation) also degrades by single step and shows weight loss in the temperature regime of 288-391°C. This specifies that the PLA-SP-5 nanocomposite undergoes thermal degradation relatively faster rate in comparison with neat PLA. The possible reason for this

is due to the fact that the bio-filler, SP exhibits thermal stability up to ~180 °C and the faster degradation phenomenon shown by PLA-SP-5 nanocomposite is discussed in detail in chapter 5. The decomposition temperature of PLA-SP-5 nanocomposite at 50% weight loss is determined to be ~338 °C. After hydrolytic degradation at 35 °C for 108 h, the decomposition temperature ($T_{50\%}$) of PLA-SP-5 sample is found to be 322, 336, 311 °C for acidic, neutral and basic pH conditions, respectively. At higher hydrolytic degradation temperature (55 °C), the decomposition temperature of the composite samples shows the downturn and the corresponding values are determined to be 313, 326, 306 °C in case of acidic (for 108 h), neutral (for 108 h) and basic pH (for 24 h), respectively. In the present case also, comparison of $T_{50\%}$ values for PLA-SP-5 nanocomposite before and after degradation process under acidic, neutral and basic pH conditions for both the temperatures indicate that basic pH and temperature condition of 55 °C favor the hydrolytic degradation process of PLA-SP-5 nanocomposite in comparison with other conditions studied **(Fukushima et al., 2011)**.

The thermal degradation profile of both PLA and PLA-SP-5 nanocomposite reveals that the addition of SP in the PLA matrix influences the faster rate of hydrolytic degradation process as compared to neat PLA under basic pH condition at 55 °C. It is important to note the variation in the $T_{50\%}$ values for PLA and PLA-SP-5 nanocomposite before and after degradation under basic pH at 35 °C. The difference between the $T_{50\%}$ value for PLA before and after degradation under the above mentioned condition is found to be 15 °C, whereas, in case of PLA-SP-5 nanocomposite, the difference is found to be 27 °C (see Table 6.2). From these values, it seems that PLA-SP-5 nanocomposite degrades at a much faster rate than that of neat PLA. This result is in contrast to the statement that PLA-SP-5 degrades at a slower rate under basic pH for the temperature condition of 35 °C in comparison with neat PLA, which is discussed in the hydrolytic degradation behaviour section earlier (section 6.4.1.1). The possible reason for the behaviour exhibited by PLA-SP-5 nanocomposite is due to the fact that with increasing temperature during the thermal degradation analysis,

decomposition of SP starts before PLA. H^+ ions released during the degradation of SP further triggers the autocatalytic cleavage of PLA backbone, which in turn leads to an earlier degradation of PLA-SP-5 nanocomposite in comparison with PLA, when subjected to TGA analysis.

Table 6.2. Decomposition temperature at 50% weight loss ($T_{50\%}$) for PLA and PLA-SP-5 nanocomposite samples

Sample name	$T_{50\%}$	Sample name	$T_{50\%}$
PLA	358	PLA-SP-5	338
PLA-A-35-108	353	PLA-SP-5-A-35-108	322
PLA-A-55-108	351	PLA-SP-5-A-55-108	313
PLA-B-35-108	343	PLA-SP-5-B-35-108	311
PLA-B-55-108	313	PLA-SP-5-B-55-24	306
PLA-N-35-108	356	PLA-SP-5-N-35-108	336
PLA-N-55-108	354	PLA-SP-5-N-55-108	326

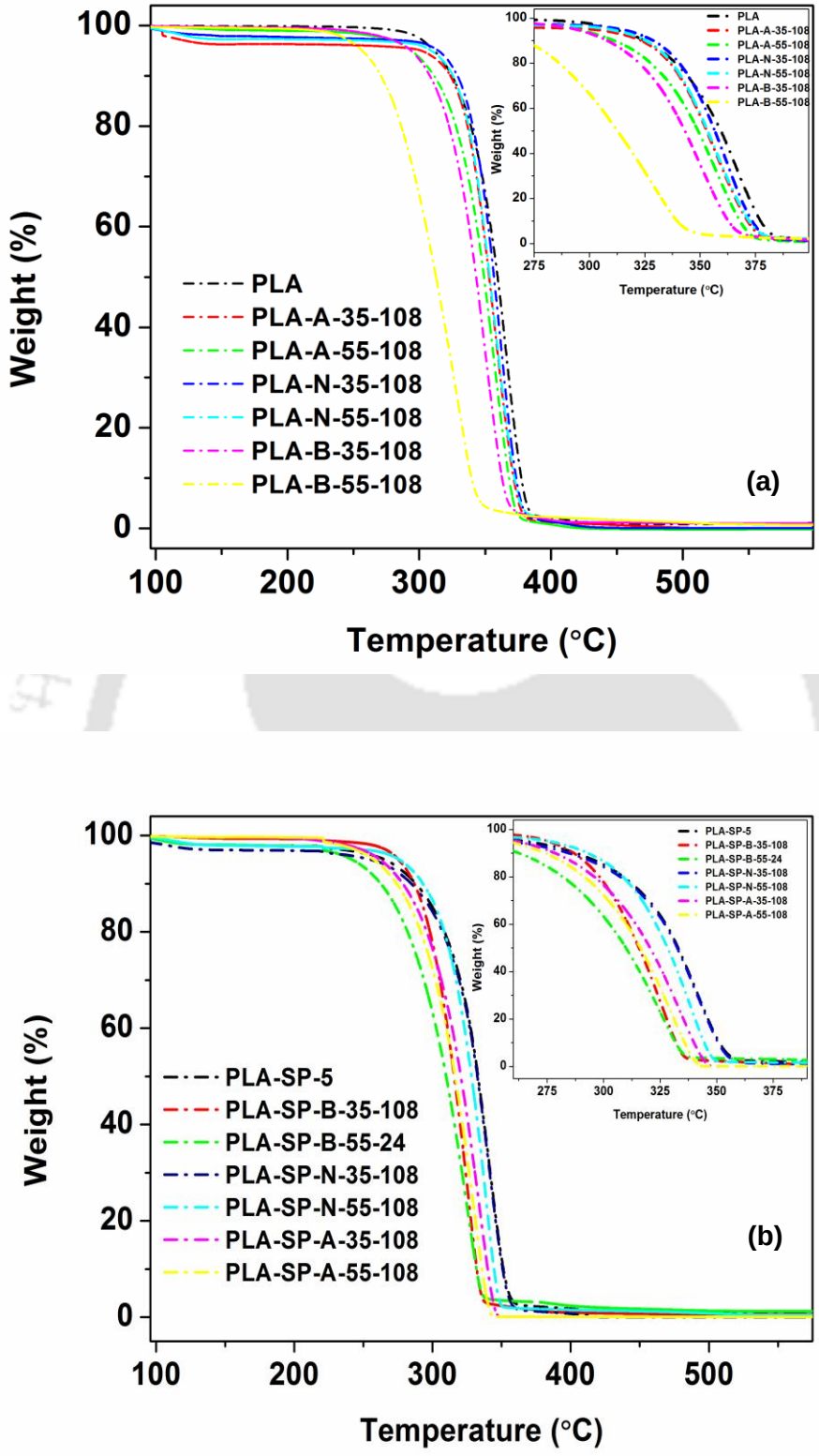

Figure 6.4. TGA thermographs of (a) PLA and (b) PLA-SP-5 sample (before and after hydrolytic degradation)

6.4.1.5. SEM analysis

The scanning electron microscopy images of PLA and PLA-SP-5 nanocomposite samples after degradation (under basic pH and two different temperatures) process are depicted in Figure 6.5(a-f). It can be observed from the Figure 6.5(a,d) that both PLA and PLA-SP-5 nanocomposite exhibit the smooth surface before the hydrolytic degradation process. Once the samples were subjected to degradation process, surface erosion can be seen distinctly in case of both PLA and PLA-SP-5 nanocomposite (Figure (b, c, e and f)). Apart from surface erosion, both PLA and PLA-SP nanocomposite are characterized by the presence of cavities (at 35 °C). In case of PLA, solvent enters into the amorphous domains first and initiates the hydrolysis reaction. As a consequence of the reaction, the amorphous domains leach out and enter into the base solution, resulting in the formation of cavities **(Joachim et al., 2004)**. In case of PLA-SP-5 nanocomposite, the solvent first enters the interface between PLA and SP, and initiates the hydrolysis at the interfacial region. With progress in the hydrolysis reaction, the bio-filler, SP tends to move away from the matrix towards the base solution **(Azwar et al., 2012)**. This can be corroborated with the disappearance of the peak corresponding to SP in the XRD analysis. At higher degradation temperature (55 °C), surface erosion and the number of cavities in the PLA and PLA-SP-5 nanocomposite samples are increased due to the faster degradation phenomenon **(George, et al., 2012)**.

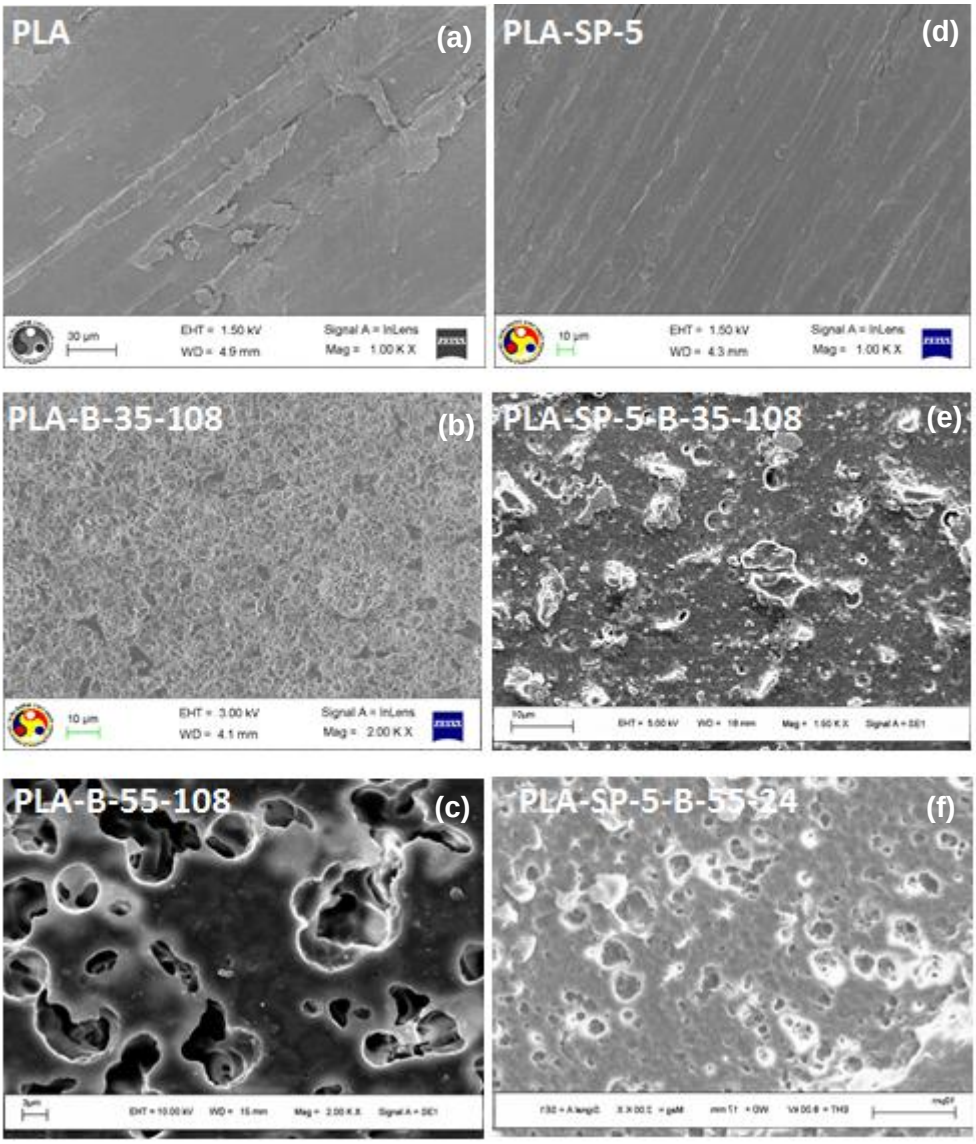

Figure 6.5. SEM images of PLA and PLA-SP-5 sample (before and after degradation)

6.4.1.6. Transparency measurements

The transparency measurements for PLA and PLA-SP-5 nanocomposite samples before as well as after hydrolytic degradation are performed using UV-visible spectrophotometer and the transmittance (%) values obtained in the wave length region of 575 nm is presented in Table 6.3. It can be observed from the Table that PLA shows the transmittance of around 72% in the visible light region (575 nm). When PLA is subjected to degradation under acidic conditions for 108 h at 35 °C, the transmittance value is found to be 21%. With increasing the degradation temperature to 55 °C, the transmittance value is further decreased to 4%.

After degradation under acidic conditions at 35 °C and 55 °C, the optical images of PLA were taken at several intervals of degradation as shown in Figure 6.6(a). It can be seen from the figure that at 35 °C, the appearance of the PLA samples remains almost invariant. In case of 55 °C and acidic conditions, PLA samples exhibit brittleness with due course of degradation. In addition to brittleness, the appearance of the sample changes to white color representing that crystallinity of the sample may be increased due to the faster degradation rate (**Gorrasi et al., 2013; Oyama et al., 2009**).

In case of neutral conditions, the transmittance value is found to be 54% for 108 h degraded PLA sample. This is comparatively higher than the value noticed at acidic pH conditions. A similar phenomenon in the transmittance (14% for 108 h) is perceived for the PLA samples in case of higher temperature (55 °C) under the same pH condition. The corresponding optical images are shown in Figure 6.6(b). In case of basic pH conditions at 35 and 55 °C, PLA samples display the drastic decline in the transmittance (0.5%) for 108 h of the degradation process. This suggests that the basic pH condition favors the opacity of the samples, due to increase in the crystallinity, as evidenced by XRD and DSC results. The respective optical images are shown in Figure 6.6(c).

It can be observed from the Table 6.3 that PLA-SP-5 nanocomposite sample exhibits the transmittance of 20, 32 and 0.5% under acidic, neutral and basic pH conditions (35 °C) for 108 h of degradation time. These results point out that an increase in the crystallinity of the samples due to degradation is directly reflected in terms of opacity. The color change observed in the samples indicates that the increased crystallinity defers the diffusion of light through the samples (Figure 6.6(a-c)). At higher degradation temperature (55 °C), it is not feasible to measure the transparency. This is because, after 24 h of degradation, the PLA-SP-5 nanocomposite films become thinner and highly dissociated into the base solution and the corresponding optical images are shown in Figure 6.6(a-c).

Table 6.3. Transmittance (%) for PLA and PLA-SP-5 nanocomposite at different pH and temperature conditions

Sample name	Transmittance (%)	Sample name	Transmittance (%)
PLA	72	PLA-SP-5	63
PLA-A-35-108	21	PLA-SP-5-A-35-108	20
PLA-A-55-108	4	PLA-SP-5-A-55-108	0.6
PLA-B-35-108	0.5	PLA-SP-5-B-35-108	0.5
PLA-B-55-108	0.5	PLA-SP-5-B-55-24	0.25
PLA-N-35-108	54	PLA-SP-5-N-35-108	32
PLA-N-55-108	14	PLA-SP-5-N-55-108	4.1

35 °C

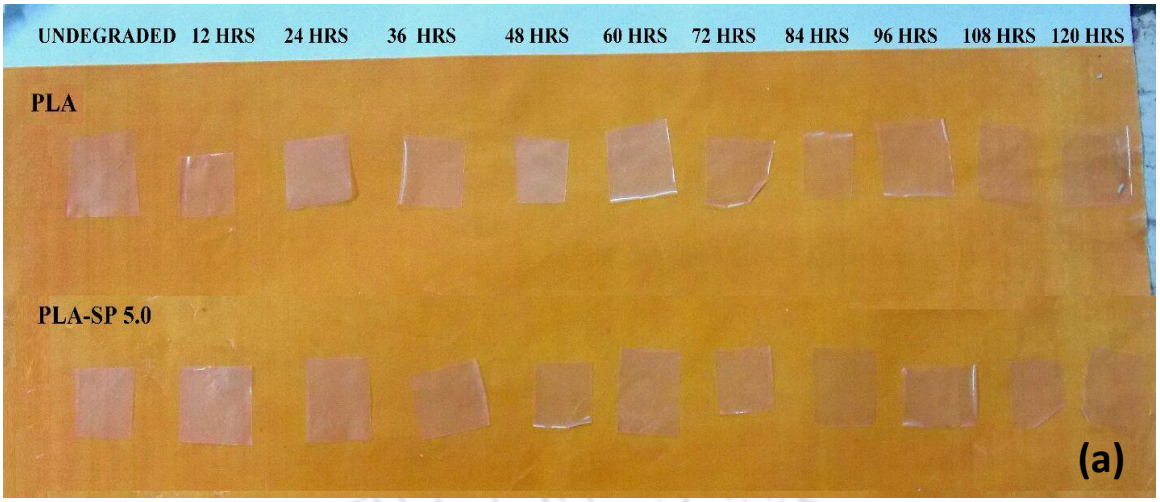

55 °C

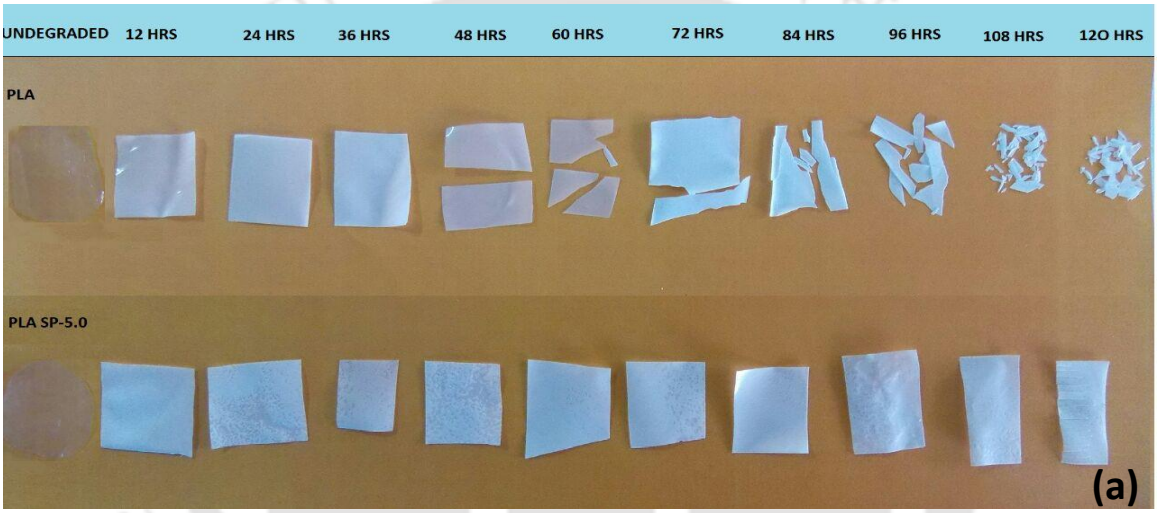

35 °C

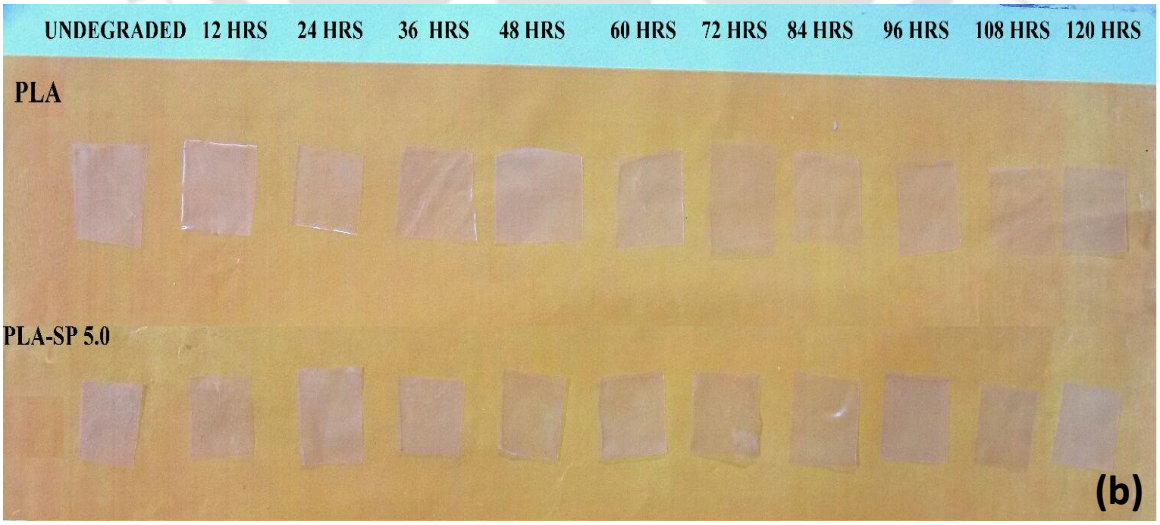

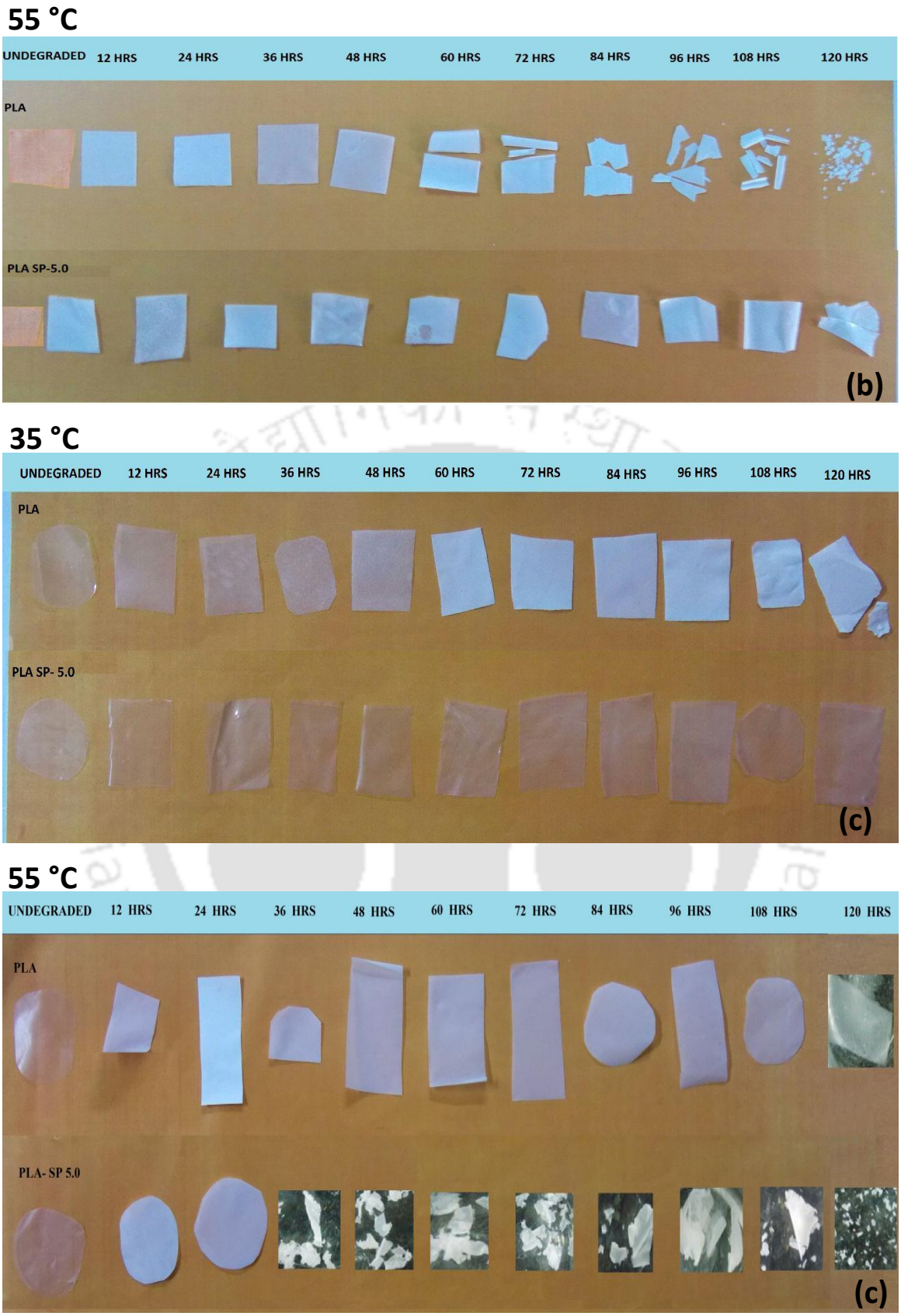

Figure 6.6. Optical images of PLA and PLA-SP-5 nanocomposite after degradation in (a) acidic (35 and 55 °C) (b) neutral (35 and 55 °C) and (c) basic (35 and 55 °C) pH conditions

6.4.1.7. GPC analysis

GPC analysis was employed to determine the polydispersive index (PDI), number average molecular weight (Mn) and weight average molecular weight (Mw) distribution of PLA and PLA-SP-5 nanocomposite samples after degradation process in basic pH conditions and the results are illustrated in Figure 6.7(a-c) and 6.8(a-c). It is well known that a maximum molecular weight decrement can occur in the samples which exhibited a higher percentage of residual weight loss **(Jong et al., 2001; Paul et al., 2005)**. Before degradation, neat PLA shows a Mn, Mw and PDI values of ~130000, 225000 and 1.6, respectively. For both the degradation temperature conditions, Mw values are observed to exhibit downturn by 27% at 35 °C and 34% at 55 °C, out of which, the maximum degradation is confirmed at the elevated temperature environment. This is attributed to the enhanced chain mobility of PLA molecular chain segments leading to the intensified chain end scission process. The increment in the PDI values for PLA also supports the reduction in the molecular weight evidenced.

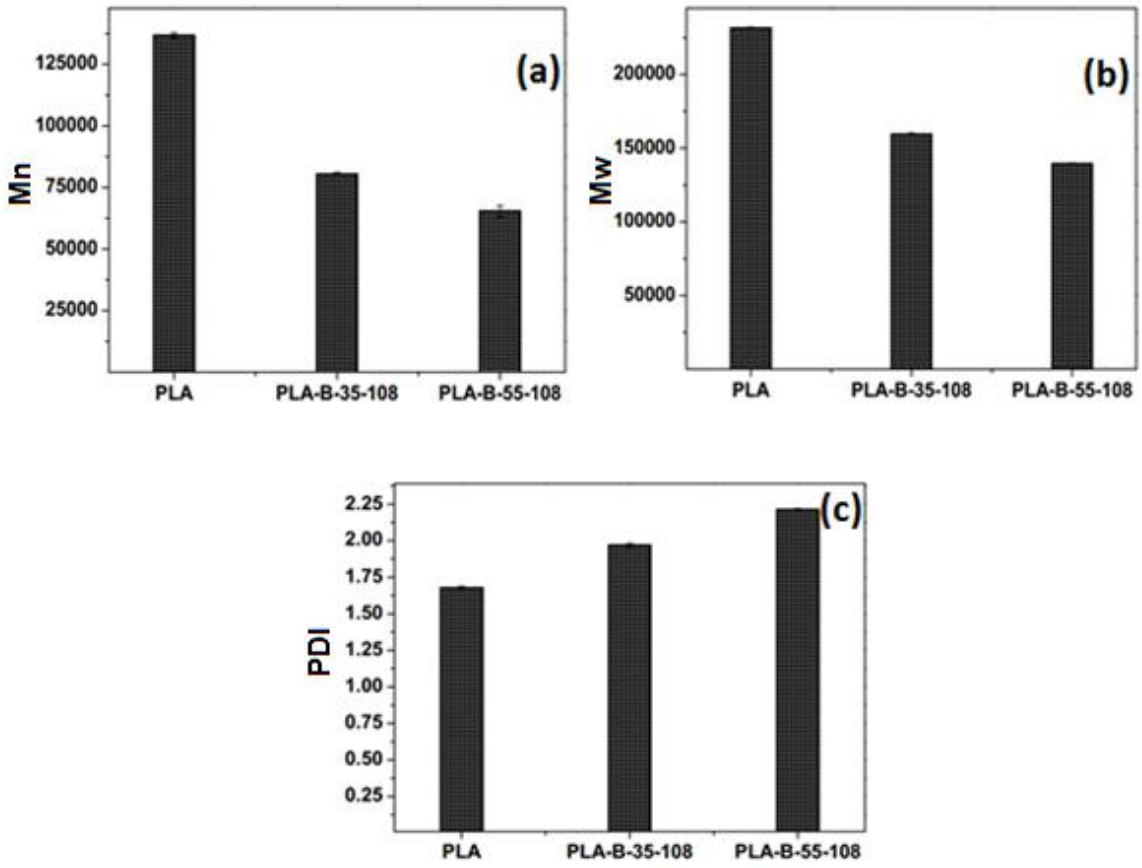

Figure 6.7. (a) Mn (b) Mw and (c) PDI for PLA samples (before and after degradation)

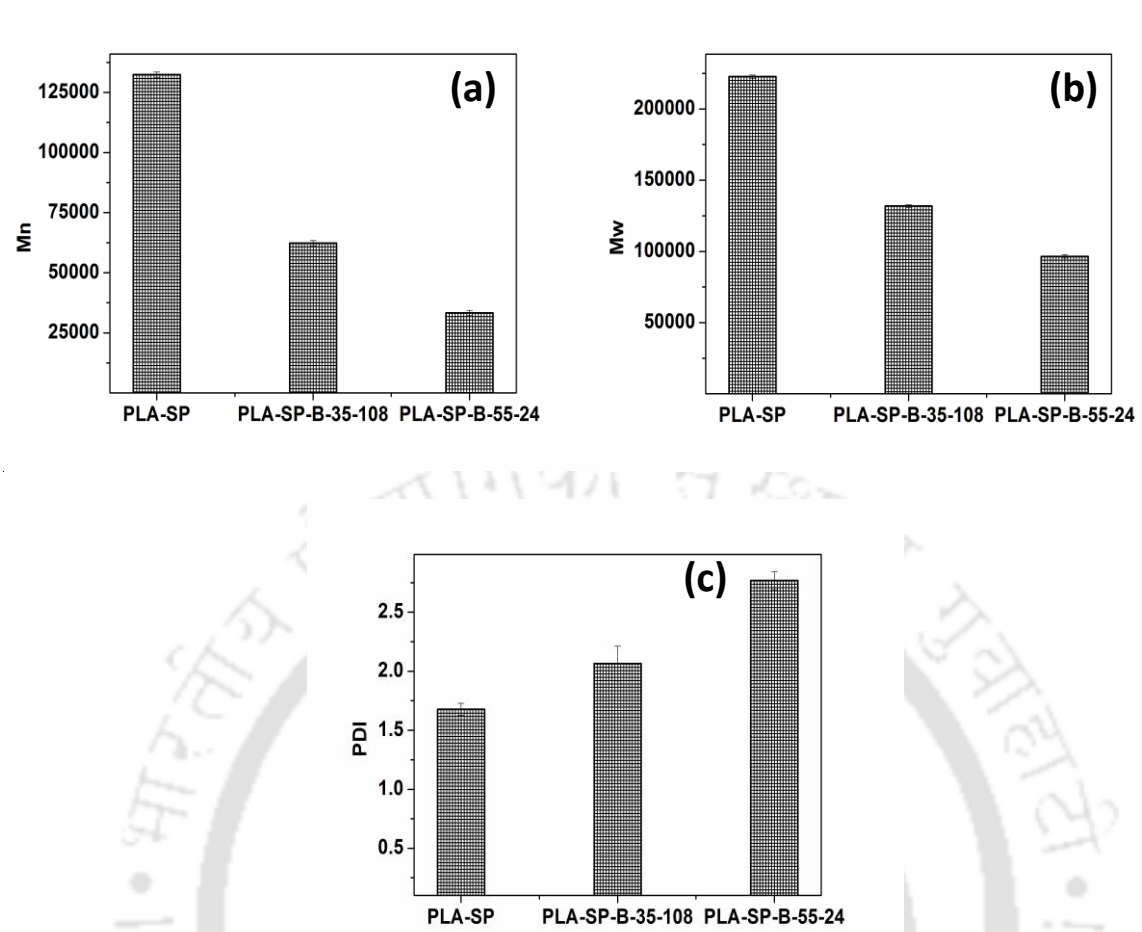

Figure 6.8. (a) Mn (b) Mw and (c) PDI for PLA-SP-5 samples (before and after degradation)

Similar behaviour is also observed for PLA-SP-5 nanocomposite sample. In case of PLA-SP-5 nanocomposite, decrement in the Mw values of ~44% at 35 °C and ~50% at 55 °C is noticed. The decrement (%) in the molecular weight for PLA-SP nanocomposite sample is comparable to that of the value reported in literature **(Langlois et al.; 2002)**. In addition to this, PLA-SP nanocomposite sample demonstrates greater reduction (%) in the molecular weight of ~32% as compared to neat PLA, at elevated temperature. This signifies that the presence of SP in the PLA matrix promotes the hydrolytic degradation process in a favorable manner.

6.4.2. Effect of graphene on the hydrolytic degradation behaviour of PLA

6.4.2.1. Hydrolytic degradation behaviour

With respect to degradation time, the residual weight fraction (ϕ) of PLA and PLA-GR-0.1 nanocomposite is calculated under different pH and temperature environments as shown in Figure 6.9. When the degradation time increases, the residual weight fraction is found to vary non-linearly for all the pH and temperature conditions studied. As evidenced from the figure, both PLA and PLA-GR-0.1 nanocomposites demonstrate higher weight loss in the initial degradation period for all the pH and temperature environments. It is also observed that except basic condition, the PLA displays a higher residual weight fraction as compared to PLA-GR-0.1 nanocomposites.

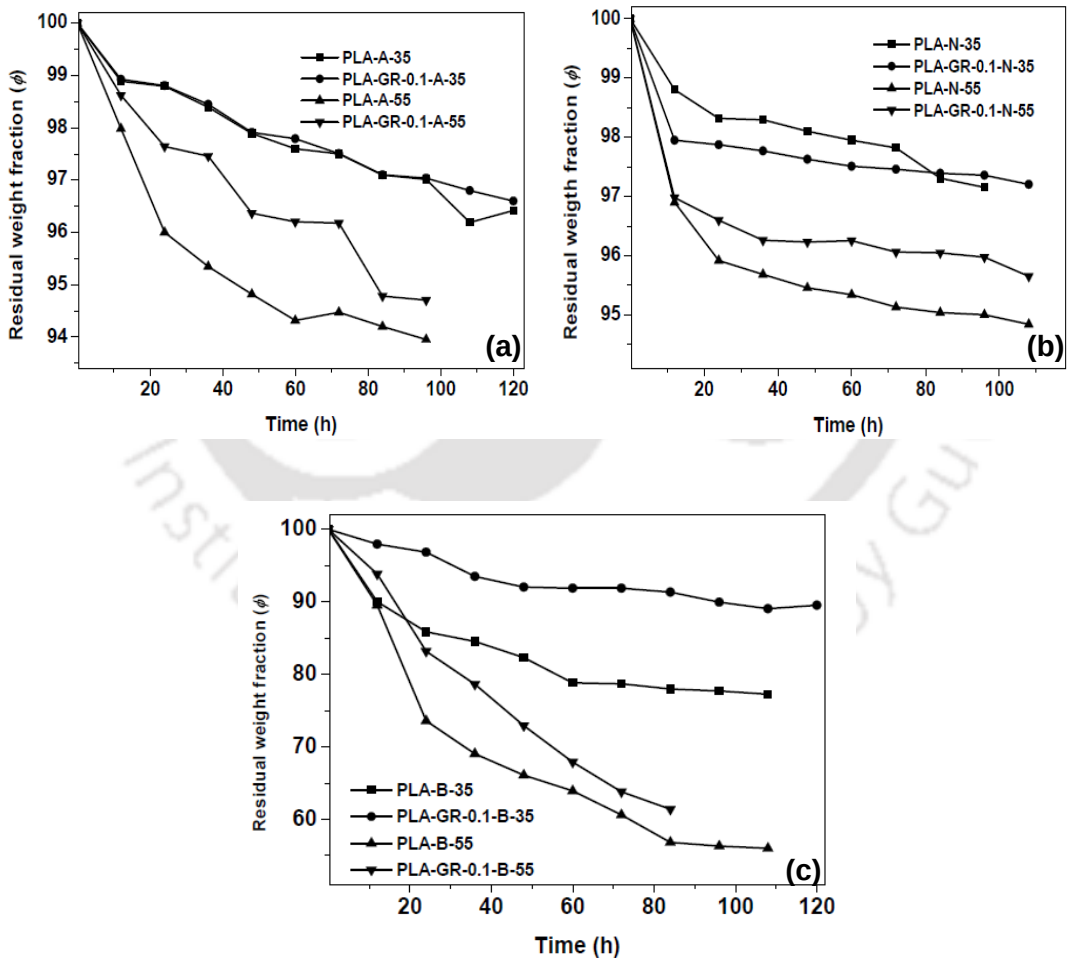

Figure 6.9. Residual weight fraction of PLA and PLA-GR-0.1 samples at (a) acid (b) neutral and (c) basic pH conditions

With respect to temperature, PLA demonstrates a greater degradation rate at elevated temperature condition (55 °C) than 35 °C. This is possibly due to the enhanced chain mobility and decrement in activation energy required for chain end scission (**Chen et al., 2013b; Olewnik et al., 2006**). Regarding pH conditions, PLA shows the enhanced degradation rate at basic pH conditions as compared to acidic and neutral pH conditions. The possible reason is that the end OH groups present in the PLA favor the hydrolytic degradation process under basic pH conditions (**Dias et al., 2012; Paul et al., 2005; Fernandez et al., 2013; Zhang et al., 2008**). A similar observation in terms of the hydrolytic degradation process is experienced for PLA-GR-0.1 nanocomposites with respect to temperature as well as pH conditions. However, it is apparent that after the addition of GR in the PLA matrix, the nanocomposite sample demonstrates a slower rate of degradation as compared to PLA for all pH and temperature conditions studied. This is because, incorporation of GR in the PLA matrix results in the improvement of hydrophobicity for the nanocomposite sample, which, in turn, hinders the diffusion of water inside the PLA matrix.

6.4.2.2. DSC analysis

Figures 6.10(a) and (b) represent the DSC thermographs of PLA and PLA-GR-0.1 nanocomposite, respectively. The thermographs were recorded for PLA and PLA-GR-0.1 nanocomposites under different pH and temperature conditions prior and after the degradation period. The PLA sample demonstrates the glass transition, crystallization and melting temperature of 62 °C, 110 °C and 149 °C, respectively. After the addition of GR in the PLA matrix, enhancement in the crystallinity is observed. The melting temperature of PLA is also improved by ~5 °C, whereas, the glass transition temperature remains unvaried after the reinforcement of GR.

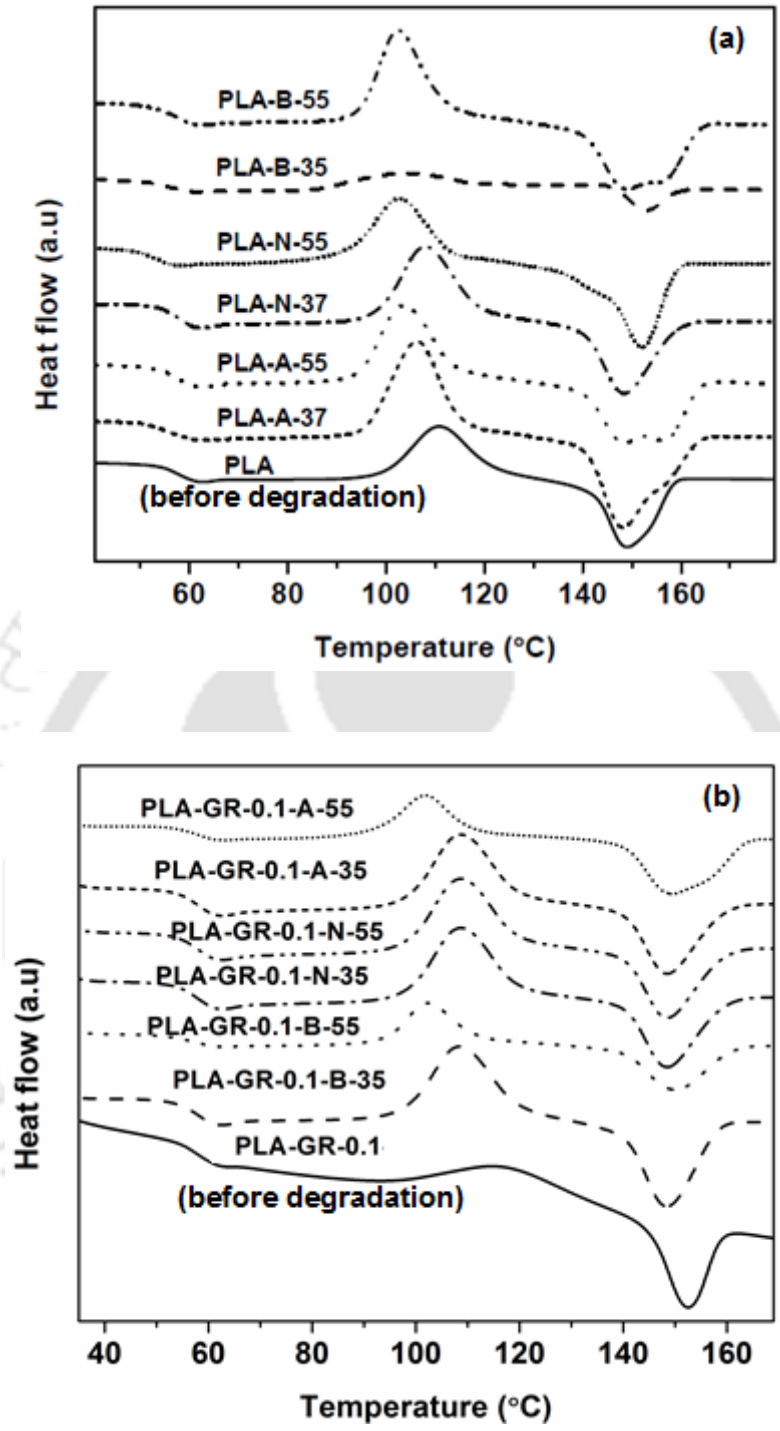

Figure 6.10. DSC thermographs for (a) PLA and (b) PLA-GR-0.1 (before and after hydrolytic degradation)

The glass transition peak, which is endothermic in nature, can be seen in all the PLA samples after hydrolytic degradation under different pH and temperature conditions (Figure 6.10(a)). The shift in the T_{cc} values to lower temperature is noticed for PLA samples (after

degradation process) when compared with the prior degradation process. The improvement observed in the cold crystallization process of PLA is due to the intensified chain mobility of loosely entangled PLA chains resulting in enhanced crystallinity (**Saha et al., 2006; Chen et al., 2012**). The significant reduction in the T_{cc} values are observed for PLA samples subjected to basic pH conditions, indicating the faster rate of degradation. Similar to neat PLA, PLA-GR-0.1 nanocomposite also displays a shift in the cold crystallization temperature to the lower side irrespective of pH and temperature conditions studied (Figure 6.10(b)). The shift is more significant for the samples subjected to basic pH conditions at elevated temperature, as compared to other conditions (acidic as well as neutral pH) at 35 °C. Similarly, the melting temperature is also shifted to lower temperature side, thus confirming the progress of the degradation process under different pH and temperature conditions (Figure 6.10(b)). These results are in accordance with the reported literature information (**Paul et al., 2005; Tsuji et al., 2010; Saha et al., 2006**).

6.4.2.3. XRD analysis

As evidenced that basic pH condition influences the hydrolytic degradation process of PLA and PLA-GR-0.1 nanocomposites greatly, XRD analysis was performed for both samples (before and after degradation process) to confirm the improvement in the crystallinity of the samples. The XRD pattern corresponding to neat PLA prior and after degradation process is depicted in Figure 6.11(a). Before the degradation process, PLA exhibits a semi crystalline peak at 2θ = 16.7°, confirming the α-crystalline phase of PLA (**Luo et al., 2012**). It is found that intensity of the crystalline peak increases with an increase in the degradation time. In addition to this, the elevated temperature condition also enhances the crystallinity of the PLA sample. The calculated percentage crystallinity values for PLA samples (before and after degradation process) also agree with the above results (see Table 6.4). The improvement in crystallinity is due to removal of amorphous domains from the samples with due course of degradation process (**Gorrasi et al., 2013; Oyama et al., 2009)**.

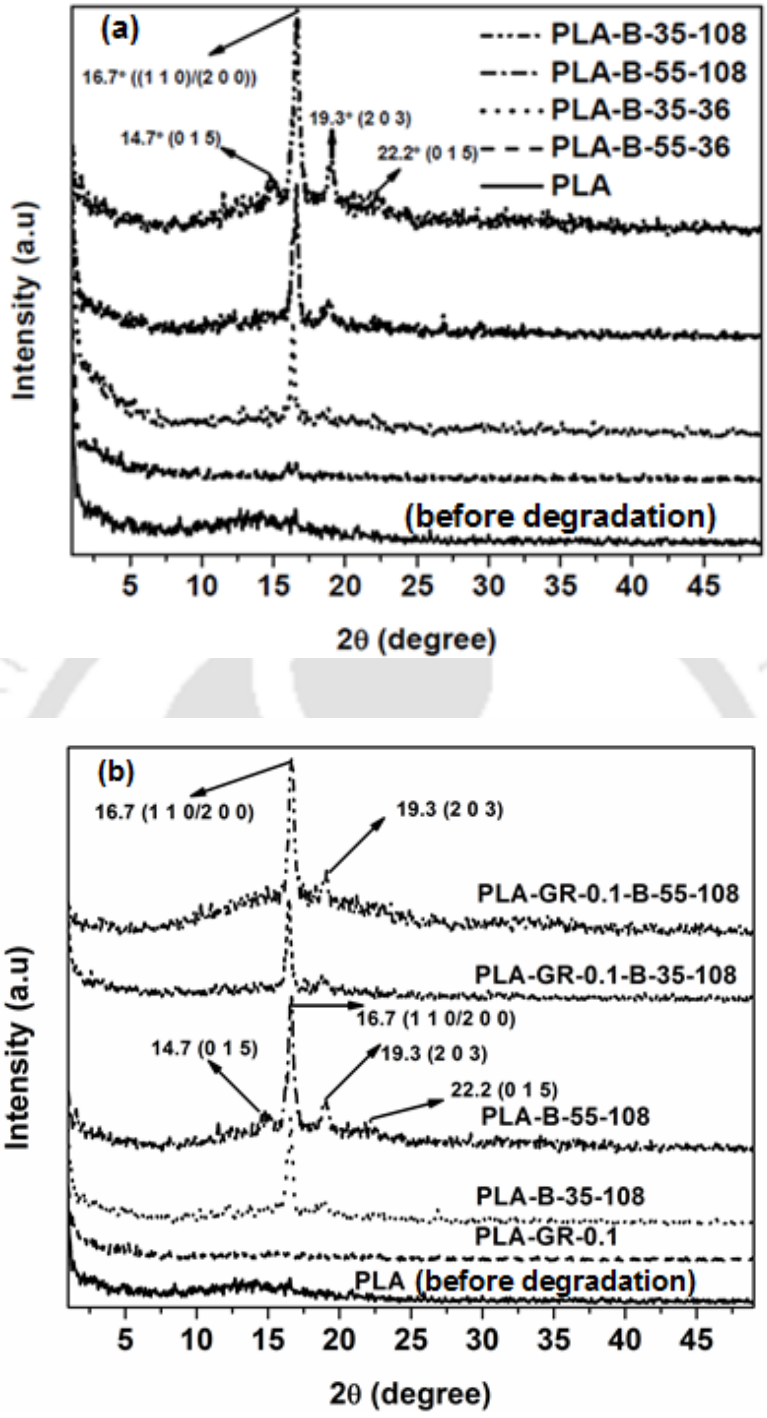

Figure 6.11. XRD patterns of (a) PLA and (b) PLA-GR-0.1 (before and after hydrolytic degradation)

The XRD patterns obtained for PLA-GR-0.1 nanocomposite samples subjected to basic pH at different temperatures are presented in Figure 6.11(b). All the samples display the presence of an intense crystalline peak at 2θ = 16.7° and extra diffraction peaks at 2θ = 14.7°, 16.8°, 19.3° and 22.2°, which correspond to the reflections of (0 1 0), (1 1 0)/(2 0 0), (2 0 3) and (0 1 5) planes of *α*-crystalline phase of PLA, respectively (**Gorrasi et al., 2013**). The improvement in the percentage crystallinity is more pronounced in case of PLA-GR-0.1 samples subjected to degradation at the elevated temperature (55 °C) for the time period of 108 h (Table 6.4).

Table 6.4. Crystallinity (%) of PLA and PLA-GR-0.1 (before and after degradation)

S:No	Sample name	Crystallinity (%)
1	PLA	12.5
2	PLA-B-35-108	39.2
3	PLA-B-55-108	50.1
4	PLA-GR-0.1	16.9
5	PLA-GR-0.1-B-35-108	34
6	PLA-GR-0.1-B-55-108	40

6.4.2.4. TGA analysis

TGA analysis was carried out for PLA and PLA-GR-0.1 nanocomposite samples after hydrolytic degradation process at various pH conditions for 108 h. The TGA curves of PLA and PLA-GR-0.1 nanocomposite samples are shown in Figure 6.12(a) and (b), respectively. A single stage of weight loss in the temperature regime of ~307-402 °C is noticed for PLA (before degradation) and temperature at which 50% weight loss ($T_{50\%}$) occurred is found to be ~358 °C. When the degradation progressed for 108 h under different pH conditions, the $T_{50\%}$ value for PLA samples shows decreasing trend. At 35 °C, the corresponding $T_{50\%}$ values for acidic, neutral and basic pH conditions are found to be ~353, 356 and 343 °C respectively. It is also observed that when the degradation temperature increases to 55 °C, $T_{50\%}$ value for PLA declines to ~351, 354 and 313 °C for acidic, neutral and basic pH

conditions, respectively. This makes clear that basic pH and elevated temperature conditions enhance the rate of degradation of PLA samples (**Paula et al., 2011**). In case of PLA-GR-0.1 nanocomposite samples, $T_{50\%}$ is found to be 2 °C higher as compared to neat PLA (before degradation). This indicates that the reinforcement of GR in the PLA matrix delayed the hydrolytic degradation process, which is due to the hydrophobic nature of the GR layers. However, after the degradation period of 108 h under different pH and temperature conditions, considerable changes in the thermal stability is not evidenced in comparison with neat PLA. The $T_{50\%}$ values exhibit similar trend like PLA under acidic, neutral and basic pH environment, irrespective of the temperature conditions.

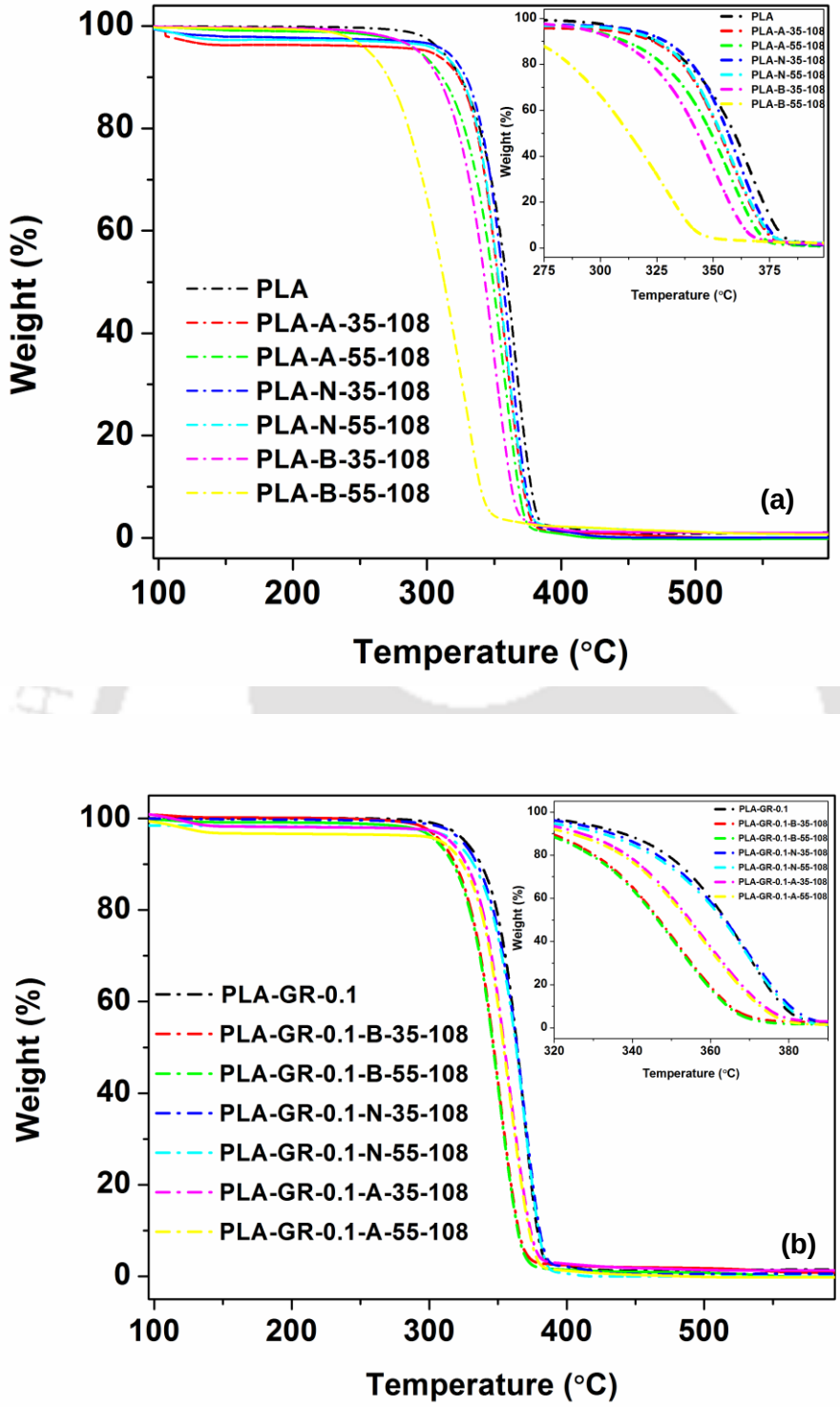

Figure 6.12. TGA thermographs of (a) PLA and (b) PLA-GR-0.1 (before and after hydrolytic degradation)

6.4.2.5. SEM analysis

The scanning electron microscopy images for PLA as well as PLA-GR-0.1 nanocomposite after degradation (under basic pH at two different temperatures) process is depicted in Figure 6.13(a-f). It is clear from the Figure 6.13(a,d) that both PLA and PLA-GR-0.1 nanocomposite exhibit the smooth surface before the hydrolytic degradation process. With due course of degradation, surface erosion and occurrence of cavities appear in the PLA samples that are subjected to degradation (Figure 6.13(b, c, e and f)). The observed cavities are due to the leaching of amorphous domains (**Joachim et al., 2004**). The leaching is found to be more prominent in case of samples subjected to hydrolytic degradation at 55 °C, indicating faster degradation process at elevated temperature (**George et al., 2012**). In case of PLA-GR-0.1 nanocomposite samples, despite surface erosion visualized, the presence of cavities is found to be rare as compared to neat PLA. This points out that the presence of GR in the PLA matrix affects the degradation process.

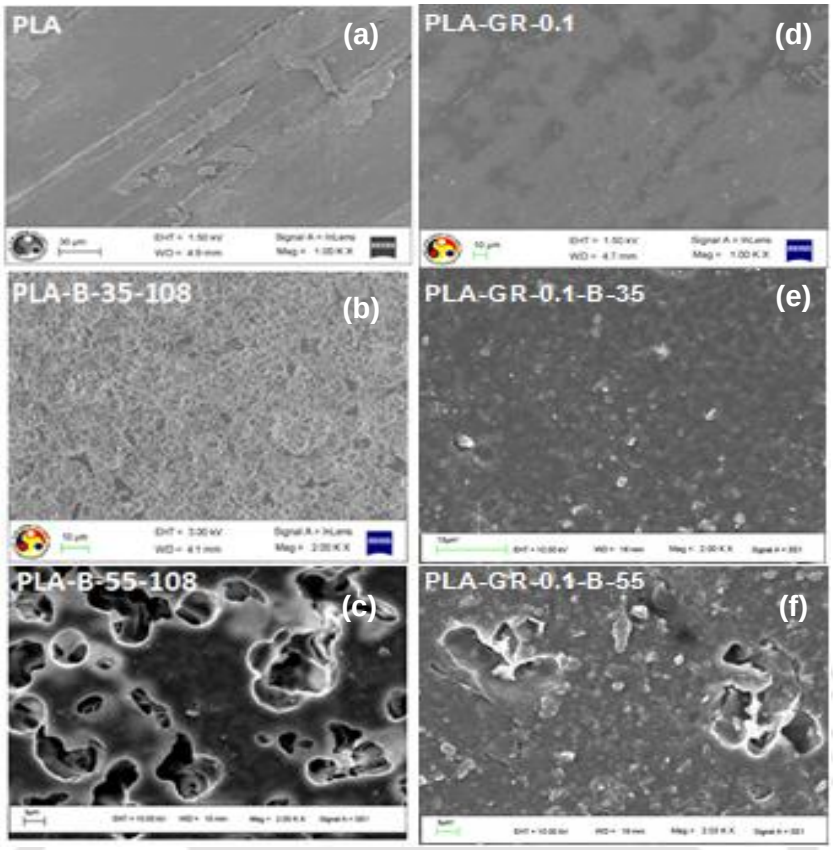

Figure 6.13. SEM images of (a) PLA and (b) PLA-GR-0.1 (before and after degradation)

6.4.2.6. Transparency measurements

Transmittance (%) results for both PLA and PLA-GR-0.1 nanocomposite samples after degradation process are presented in Table 6.5. The neat PLA demonstrates 72% transmittance in the visible light region. Under acidic pH conditions, PLA exhibits a transmittance value of 21% and 4% for the temperature condition of 35 °C and 55 °C, respectively after the degradation time of 108 h. The optical images of PLA subjected to degradation under acidic conditions at 35 °C and 55 °C pictoriated at various intervals of degradation can be seen from Figure 6.14(a). The appearance of PLA samples remains almost invariant under acidic pH conditions at 35 °C. With the rise in temperature (55 °C) and under acidic conditions, the PLA samples demonstrate brittleness after a certain degradation interval. Besides this, the appearance of the sample changes with increasing degradation duration. This is an indication of improvement in crystallinity of the samples because of the faster degradation rate. The transmittance values (54% and 14% at 35 and

55 °C, respectively) obtained in case of neutral pH conditions are found to be comparatively higher than that of acidic pH conditions. The corresponding optical images are shown in Figure 6.14 (b). Under basic pH conditions, PLA samples display the drastic reduction in the transmittance (0.5%) at both the temperature. This elucidates that basic pH condition influences the opacity of the samples, due to increase in the crystallinity, as evidenced by XRD and DSC results. The respective optical images are shown in Figure 6.14(c).

35 °C

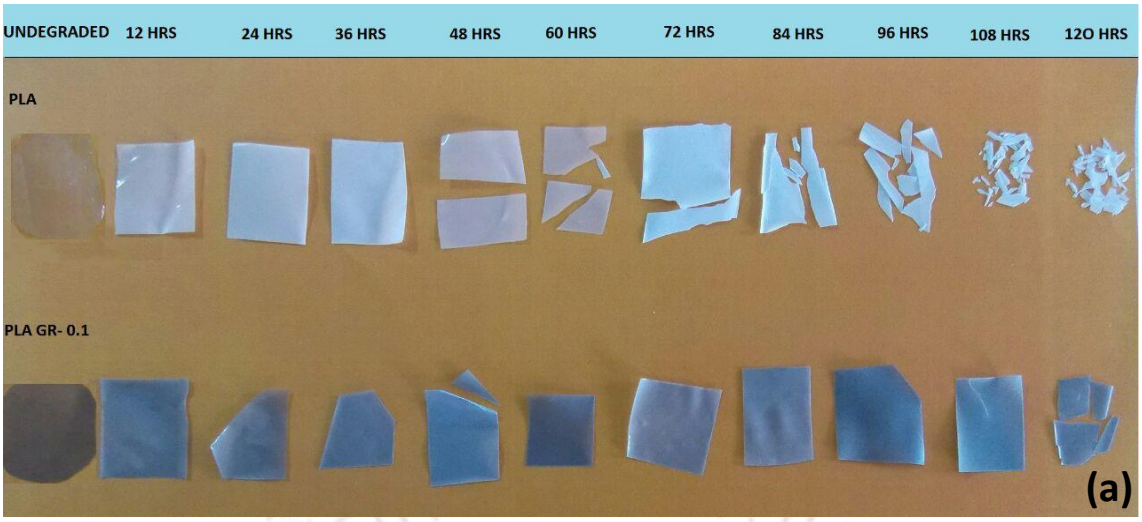

55 °C

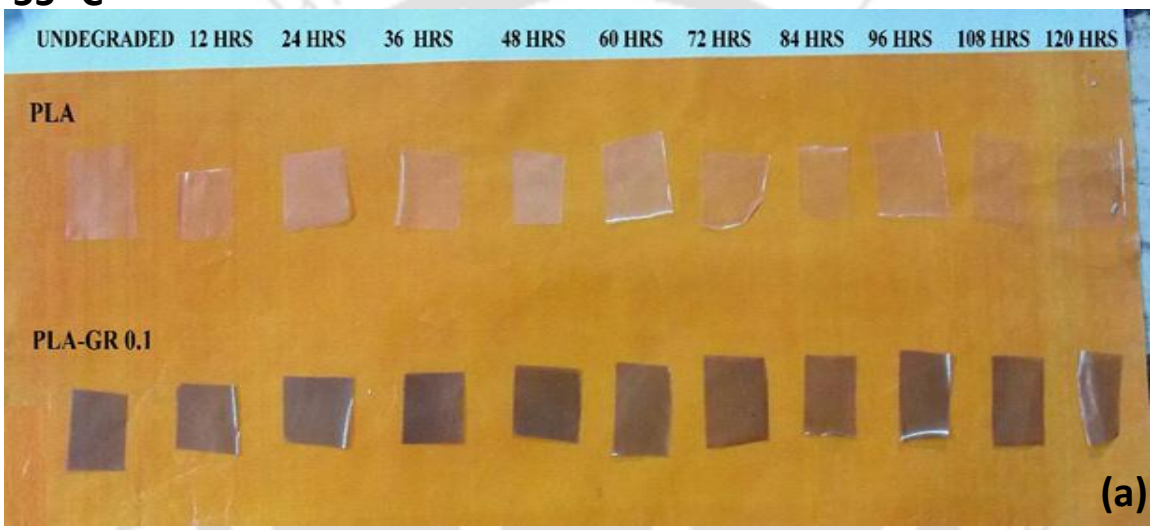

35 °C

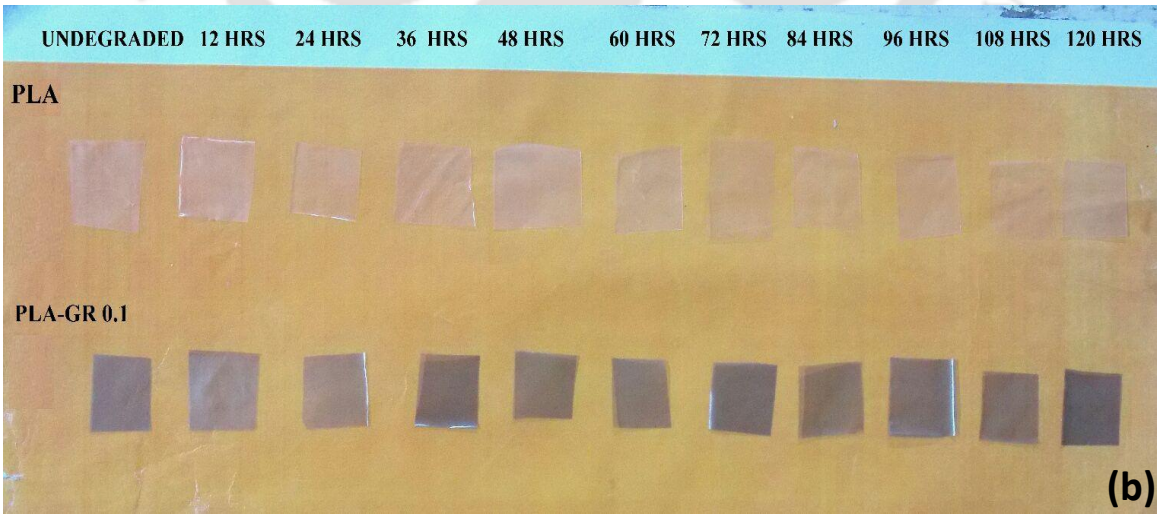

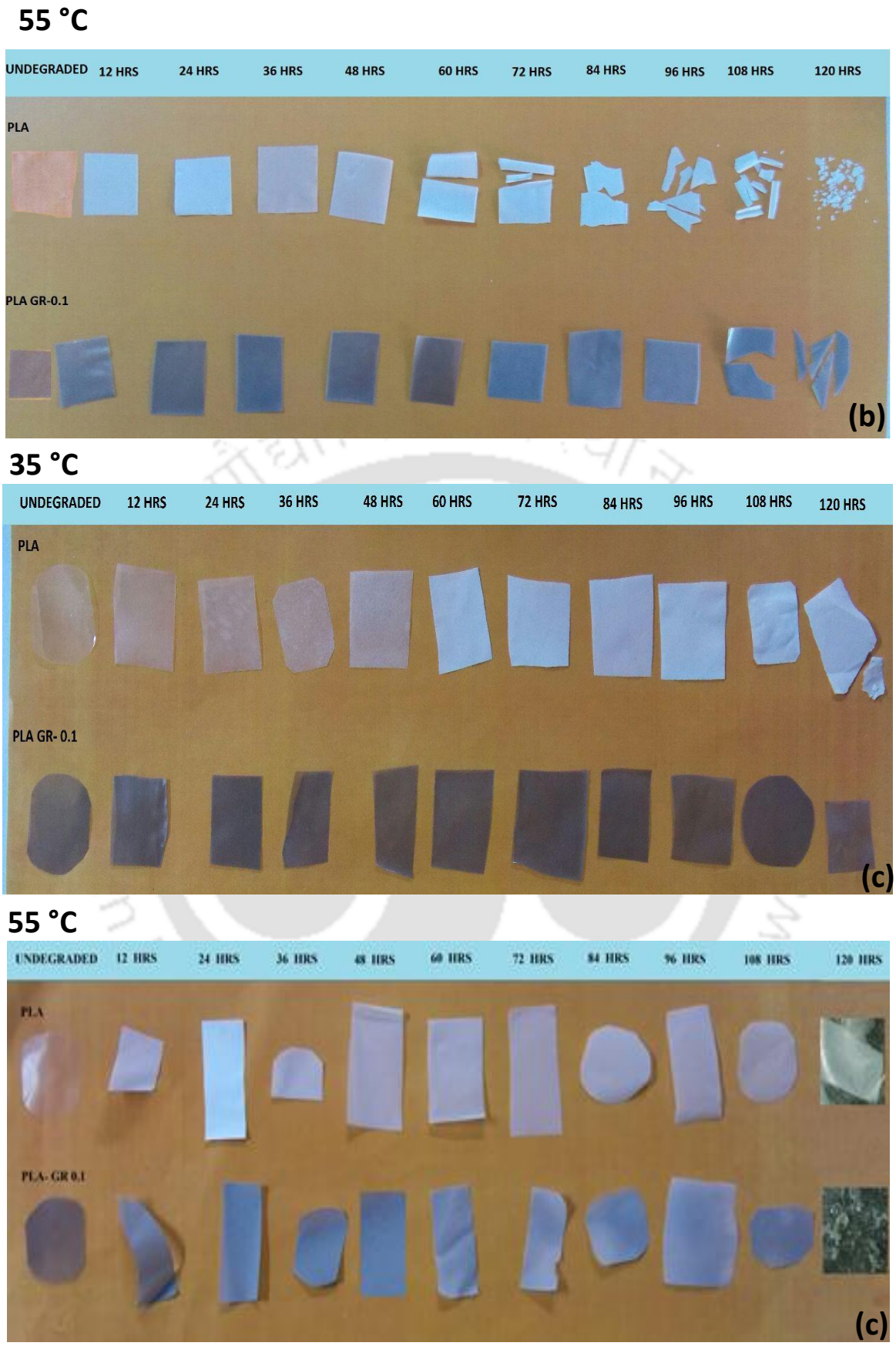

Figure 6.14. Optical images of PLA and PLA-GR-0.1 nanocomposite at (a) acidic (35 and 55 °C) (b) neutral (35 and 55 °C) (c) basic (35 and 55 °C) pH conditions

Table 6.5. Transmittance (%) for PLA and PLA-GR-0.1 nanocomposite at different pH and temperature conditions

Sample name	Transmittance (%)	Sample name	Transmittance (%)
PLA	72	PLA-GR-0.1	69
PLA-A-35-108	21	PLA-GR-0.1-A-35-108	19
PLA-A-55-108	4	PLA-GR-0.1-A-55-108	0.5
PLA-B-35-108	0.5	PLA-GR-0.1-B-35-108	0.7
PLA-B-55-108	0.5	PLA-GR-0.1-B-55-108	0.2
PLA-N-35-108	54	PLA-GR-0.1-N-35-108	40
PLA-N-55-108	14	PLA-GR-0.1-N-55-108	6

The transparency results obtained for PLA-GR-0.1 nanocomposite samples after degradation is presented in Table 6.5. It can be noticed that the nanocomposite sample (PLA-GR-0.1) displays the transmittance of 19, 40 and 0.7% under acidic, neutral and basic pH conditions at 35 °C for 108 h of degradation time. These results are indicative of increased crystallinity of the samples and the degradation is directly reflected in terms of opacity. The color change noticed in the samples also signifies that an increase in crystallinity hinders the transmission of light through the samples (Figure 6.14(a-c)).

6.4.2.7. GPC Analysis

The number average molecular weight (Mn), weight average molecular weight (Mw) and the polydispersive index (PDI) of PLA and PLA-GR-0.1 nanocomposite samples after degradation process are illustrated in Figures 6.7(a-c) and 6.15(a-c), respectively. Prior to degradation, the nanocomposite sample shows a Mn, Mw and PDI of ~131000, 220000 and 1.6. After the degradation in the base solution for 108 h, the decrement in the Mw values of ~27% at 35 °C and ~35% at 55 °C is noticed. In comparision with PLA and PLA-SP-5, PLA-GR-0.1 displays slower degradation rate due to the hydrophobic nature of graphene.

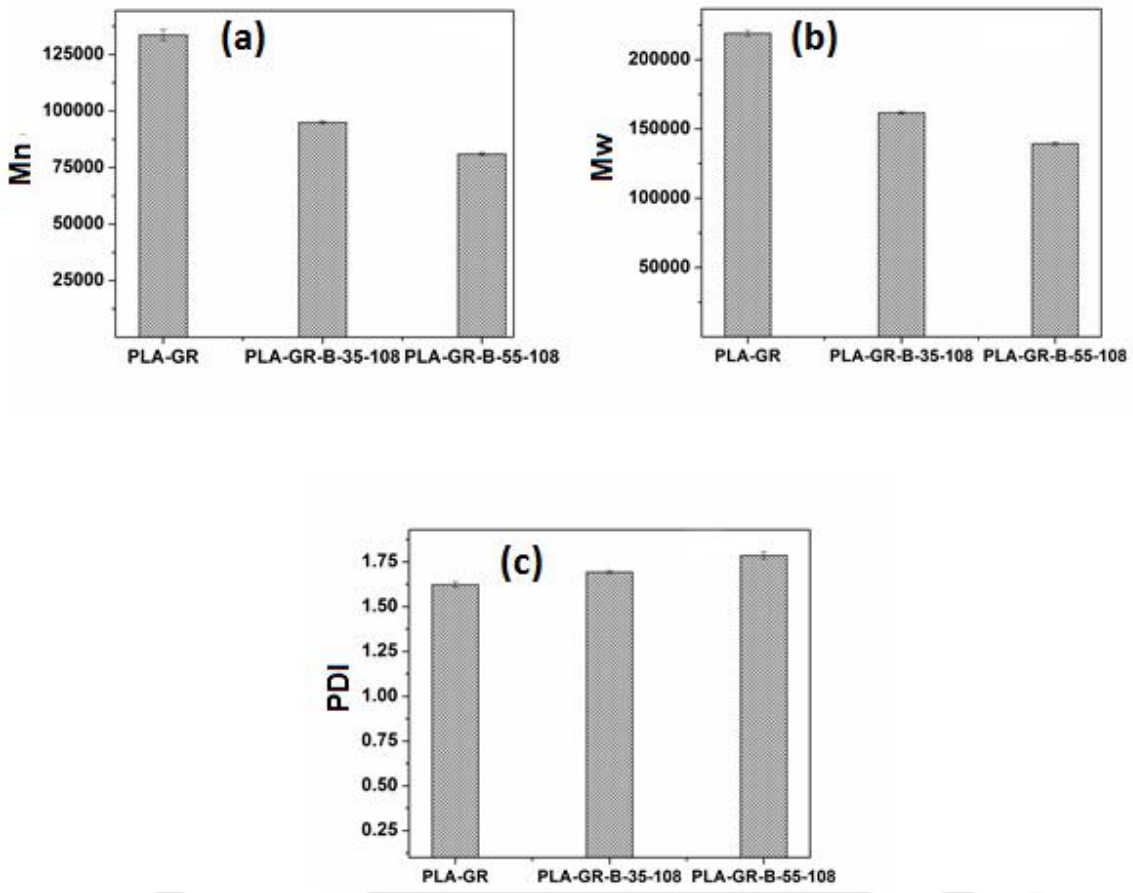

Figure 6.15. (a) Mn (b) Mw and (c) PDI for PLA-GR-0.1 samples (before and after degradation)

6.5. Conclusions

The study elucidates that basic pH conditions and the elevated temperature highly favor the hydrolytic degradation process for PLA, PLA-SP-5 and PLA-GR-0.1 nanocomposite samples. The higher percentage of residual weight loss observed for PLA-SP-5 nanocomposite indicates the faster rate of degradation as compared to PLA and PLA-GR-0.1 nanocomposite. DSC and XRD analysis reveal the improvement in crystallinity for all the samples with due course of the degradation period. The presence of cavities verified by SEM analysis signifies the leaching of the amorphous region into the solvent phase. GPC analysis also confirms the degradation phenomenon by displaying the reduction in molecular weight. On the whole, the presence of SP in the PLA matrix greatly influences the hydrolytic degradation of PLA.

CHAPTER 7

CONCLUSIONS AND FUTURE DIRECTIONS

This chapter presents the major inferences drawn from the doctoral work and an outlook for future studies.

7.1. Conclusions

The major conclusions drawn on the overall observation and main findings of the research work are as follows.

- The optimum temperature for thermal exfoliation of expandable graphite (EG) is achieved at 750 °C. The formation of monolayer GR from exfoliated graphite (EXG) is confirmed by the TEM image as well as SAED pattern obtained after sonication process. The XRD patterns of PLA-GR nanocomposites reveal the absence of graphitic peak at 2θ = 26.7°, which is indicative of exfoliation of GR in the PLA matrix.
- The maximum improvement in the thermal stability of ~31 °C is exhibited by PLA-GR-0.5 nanocomposite than that of neat PLA, when 10% weight loss is considered as a point of comparison. DSC analysis discloses the nucleating ability of GR nanofiller by showing improvement in the cold crystallization process of PLA. Addition of GR in the PLA matrix demonstrates ~4 °C enhancement in the melting temperature. The presence of GR in the PLA matrix shows considerable reduction in the transparency (53%) of PLA films as compared to neat PLA, in the UV-B region. The improvement in the tensile strength and elongation-at-break (%) of ~15% and 53%, respectively, is obtained for PLA-GR-0.1 nanocomposite as compared to neat PLA. In addition to this, the incorporation of 0.1 wt% GR in the PLA matrix guides to ~22% reduction in the oxygen barrier effects as compared to neat PLA.

- A significant improvement in terms of mechanical and oxygen barrier properties of PLA is experienced after the reinforcement of SP in the PLA matrix. DSC analysis authenticates the shift in cold crystallization temperature of PLA-SP composites to higher side with respect to SP loadings. This specifies that the incorporation of SP leads to suppress the diffusion rate of the PLA chains to the nucleus surface. The uniform dispersion of SP in the PLA matrix is verified through FE-SEM and TEM analysis. The maximum improvement in the tensile strength and elongation at break (%) by ~17% and ~56%, respectively is obtained for PLA-SP-5 nanocomposite as compared to neat PLA. The most significant improvement in terms of oxygen barrier effects is evidenced after the incorporation of SP in the PLA matrix. For 30 wt% loadings of SP, the reduction in oxygen permeability of 69% is noticed in comparison with neat PLA.
- The crystallization rate parameter values of PLA-GR and PLA-SP nanocomposites obtained by both Avrami and Tobin models exhibit increasing trend with respect to neat PLA, irrespective of the loadings, indicating the nucleation effect of fillers (GR and SP). The addition of both GR and SP displays the reduction in the nucleation induction period, which is confirmed by POM studies.
- The activation energy is found to vary with respect to conversion for PLA, PLA-GR and PLA-SP nanocomposites, which suggests that the thermal degradation of both PLA and its composites occurrs via complex mechanism. After the addition of GR in the PLA matrix, thermal stability of PLA is enhanced that is also confirmed by the enhancement of activation energy obtained by Coats-Redfern, Kissinger and Flynn-Wall-Ozawa methods. In case of PLA-SP composites, the reverse trend in terms of activation energy is observed, demonstrating the decrement in the thermal stability with addition of SP in the PLA matrix.
- The elevated temperature and basic pH conditions greatly influence the hydrolytic degradation process of PLA, PLA-GR-0.1 and PLA-SP-5 nanocomposites. The faster

rate of degradation is confirmed for the PLA-SP-5 nanocomposite, which exhibits a greater percentage of residual weight loss as compared to PLA and PLA-GR-0.1 nanocomposite. DSC and XRD analysis signify the enhancement in crystallinity of PLA, PLA-GR-0.1 and PLA-SP-5 nanocomposites with an increase in the degradation time. The leaching of amorphous region during the degradation is evidenced by the presence of cavities in the SEM images. This leads to decrement in the molecular weight, which is confirmed by GPC analysis. The presence of SP in the PLA matrix highly favors the hydrolytic degradation of PLA as compared to GR nanofiller.

7.2. Scope for future work

Based on the outcome of this work, some recommendations for future research are presented as follows:

- In order to enhance the barrier properties of PLA-GR composites, the dispersion of GR in the PLA matrix needs to be improved. This can be achieved by in-situ polymerization of lactic acid on GR followed by solution casting or melt blending of the resultant product in the PLA matrix.
- In order to avoid the earlier degradation of PLA-SP composites, the hydroxyl groups present in the SP can be modified and incorporated in the PLA matrix. The structural, morphological, thermal, mechanical and barrier properties of PLA/modified SP composites can be further investigated.
- In view of food packaging applications, migration studies for SP and GR from the PLA matrix into food material can be carried out to investigate the toxicity behaviour of the reinforcements. Further, anti-microbial properties of PLA-SP and PLA-GR composites can also be examined.

REFERENCES

Aboyade, A.O.; Carrier, M.; Meyer, E.L.; Knoetze, J.H.; and Gorgens, J.F. Model Fitting Kinetic Analysis and Characterization of the Devolatilization of Coal Blends with Corn and Sugarcane Residues, *Thermochim. Acta.* **2012**, 530, 95-106.

Afanasov, I.M.; Shornikova, O.N.; Kirilenko, D.A.; Vlasov, I.I.; Zhang, L.; Verbeeck, J.; Avdeev, V.V.; and Tendeloo, V.G. Graphite Structural Transformations during Intercalation by HNO_3 and Exfoliation, *Carbon.* **2010**, 48, 1862-1865.

Alexandre, M.; and Dubois, P. Polymer-Layered Silicate Nanocomposites: Preparation, Properties and Uses of New Class of Materials, *Mater. Sci. Eng.* **2000,** 28, 1-63.

Ali, S.S.; Tang, X.; Alavi, S.; and Faubion, J. Structure and Physical Properties of Starch/Poly Vinyl Alcohol/Sodium Montmorillonite Nanocomposite Films, *J. Agric. Food Chem.* **2011**, 59, 12384-12395.

Amano, M. PET Bottle System in Sweden and Japan: An Integrated Analysis from a Life-cycle Perspective, *Master of Science.* **2004,** LUND.

Amentano, I.; Bitinis, N.; Fortunati, E.; Mattioli, S.; Resciganano, N.; Verdejo, R.; Lopez-Manchado, M.A.; and Kenny, J.M. Multifunctional Nanostructured PLA Materials for Packaging and Tissue Engineering, *Prog. Polym. Sci*. **2013**, 38, 1720-1747.

Anderson, J.M.; and Shive M.S. Biodegradation and Biocompatibility of PLA and PLGA microspheres, *Adv. Drug. Deliv. Rev*. **1997**, 28, 5-24.

Andersson, S.R.; Hakkarainen, M.; and Albertsson, A.C. Stereocomplexation Between PLA-Like Substituted Oligomers and the Influence on the Hydrolytic Degradation, *Polymer*. **2013**, 54, 4105-4111.

Ang, P.K.; Jaiswal, M.; Lim, C.H.; Wang, Y.; Sankaran, J.; Li, A.; Lim, C.T.; Wohland, T.; Barbaros, O.; and Loh, K.P. A Bioelectronics Platform using a Graphene-lipid Bilayer Interface, *ACS Nano.* **2010**, 4, 7387-7394.

Antheunis, H.; Meer, J.C.; Geus, M.D.; Kingma, W.; and Koning, C.E. Improved Mathematical Model for the Hydrolytic Degradation of Aliphatic Polyesters, *Macromolecules.* **2009,** 42, 2462-2471.

Antheunis, H.; Meer, J.C.V.D.; Geus, M.D.; Heise, A.; and Koning, C.E. Autocatalytic Equation Describing the Change in Molecular Weight during Hydrolytic Degradation of Aliphatic Polyesters, *Biomacromolecules.* **2010**, 11, 1118-1124.

Arias, A.; Heuzey, M.C.; Huneault, M.A.; Ausias, G.; and Bendahou, A. Enhanced Dispersion of Cellulose Nanocrystals in Melt-processed Polylactide Based Nanocomposites, *Cellulose*. DOI 10.1007/s10570-014-0476-z.

Armentano, I.; Dottori, M.; Puglia, D.; and Kenny, J.M. Effects of Carbon Nanotubes (CNTs) on the Processing and In-vitro Degradation of Poly(DL-lactide-co-glycolide)/CNT Films, *J. Mater. Sci: Mater. Med.* **2008**, 19, 2377-2387.

Armentano, I.; Bitinis, N.; Fortunati, E.; Mattioli, S.; Rescignano, N.; Verdejo, R.; Lopez-Manchado, M.A.; and Kenny, J.M. Multifunctional Nanostructured PLA Materials for Packaging and Tissue Engineering, *Prog. Polym.Sci*. **2013**, 38, 1720-1747.

Arrieta, M.P.; Fortunati, E.; Dominici, F.; Rayon, E.; Lopez, J.; and Kenny, J.M. Multifunctional PLA-PHB/Cellulose Nanocrystal Films: Processing, Structural and Thermal Properties, *Carbohydr. Polym.* **2014**, 107, 16-24.

Asaithambi, B.; Ganesan, G.; and Kumar, S.A. Bio-Composites: Development and Mechanical Characterization of Banana/Sisal Fiber Reinforced Poly Lactic Acid (PLA) Hybrid Composites, *Fiber. Polym.* **2015,** 15, 847-854.

Auras, R.; Harte, B.; and Selke, S. An Overview of Polylactides as Packaging Materials, *Macromol. Biosci.* **2004**, 4, 835-864.

Ayana, B.; Suin, S.; and Khatua, B.B. Highly Exfoliated Eco-friendly Thermoplastic Starch (TPS)/Poly(lactic acid) (PLA)/Clay Nanocomposites Using Unmodified Nanoclay, *Carbohydr. Polym.* **2014**, 110, 430-439.

Azwar, E.; Vuorinen, E.; and Hakkarainen, M. Pyrolysis-GC-MS reveals Important Differences in Hydrolytic Degradation Process of Wood Flour and Rice Bran Filled Polylactide Composites, *Polym. Degrad. Stab*. **2012**, 97, 281-287.

Bagg, J. The Interpretation of Apparent Activation Energies Derived by the Least Squares Treatment of Kinetic Data, *J. Catal*. **1969**, 13, 271-282.

Baghaei, B.; Skrifvars, M.; and Berglin, L.; Manufacture and Characterization of Thermoplastic Composites made from PLA/Hemp Co-wrapped Hybrid Yarn Prepregs, *Composites: Part A*. **2013**, 50, 93-101.

Baheti, V.; Mishra, R.; Militky, J.; and Behera, B.K. Influence of Noncellulosic Content on Nano Scale Refinement of Waste Jute Fibers for Reinforcement in Poly(lactic acid) Films, *Fiber. Polym*. **2014**, 15, 1500-1506.

Bao, R.Y.; Yang, W.; Jiang, W.R.; Liu, Z.Y.; Xie, B.H.; and Yang, M.B. Polymorphism of Racemic Poly(l-lactide)/Poly(d-lactide) Blend: Effect of Melt and Cold Crystallization, *J. Phys. Chem. B.* **2013**, 117, 3667-3674.

Bao, Q.; Zhang, H.; Yang, J.; Wang, S.; Tang, D.Y.; Jose, R.; Ramakrishna, S.; Lim, C. T.; and Loh, K.P. Graphene-Polymer Nanofiber Membrane for Ultrafast Photonics, *Adv. Funct. Mater.* **2009**, 20, 782-791.

Barrau, S.; Vanmansart, C.; Moreau, M.; Addad, A.; Stoclet, G.; Lefebvre, J.M.; and Seguela, R. Crystallization Behavior of Carbon Nanotube-Polylactide Nanocomposites, *Macromolecules.* **2011**, 44, 6496-6502.

Bax, B.; and Mussig, J. Impact and Tensile Properties of PLA/Cordenka and PLA/Flax Composites, *Compos. Sci. Technol.* **2008**, 68, 1601-1607.

Beneyto, M.J.; Ortuno, N.; Devis, A.; Aucejo, S.; Puerto, M.; Praena, D.G.; Houtman, J.; Pichardo, S; Maisanaba, S.; and Jos, A. Use of Nanoclay Platelets in Food Packaging Materials: Technical and Cytotoxicity Approach, *Food Addit. Contam.* **2014**, 31, 354-363.

Bharadwaj, R.; Mohanty, A.K.; Drzal, L.T.; Pourboghrat, F.; and Misra, M. Renewable Resource-Based Green Composites from Recycled Cellulose Fiber and Poly(3-hydroxybutyrate-co-3-hydroxyvalerate) Bioplastic, *Biomacromolecules.* **2006**, 7, 2044-2051.

Bhatia, A.; Gupta, R.K.; Bhattacharya, S.N.; and Choi, H.J. Analysis of Gas Permeability Characteristics of Poly(Lactic Acid)/Poly(Butylene Succinate) Nanocomposites, *Journal of Nanomaterials*. **2012**, doi:10.1155/2012/249094.

Bie, P.; Liu, P.; Yu, L.; Li, X.; Chen, L.; and Xie, F. The Properties of Antimicrobial Films Derived From Poly(lactic acid)/Starch/Chitosan Blended Matrix, *Carbohydr. Polym.* **2013**, 98, 959-966.

Bonilla, J.; Fortunati, E.; Vargas, M.; Chiralt, A.; and Kenny, J.M. Effects of Chitosan on the Physiochemical and Antimicrobial Properties of PLA Films, *J. Food Eng.* **2013**, 119, 236-243.

Brizzolara, D.; Cantow, H.J.; Diederichs, K.; Keller, E.; and Domb, A.J. Mechanism of the Stereocomplex Formation between Enantiomeric Poly(lactide)s, *Macromolecules.* **1996**, 29, 191-197.

Burkersroda, F.; Schedl, L.; and Pferich, A. Why Degradable Polymers Undergo Surface Erosion or Bulk Erosion, *Biomaterials.* **2002**, 23, 4221-4231.

Byun, Y.; Kim, Y.T.; and Whiteside, S. Characterization of an Antioxidant Polylactic acid (PLA) Film Prepared with α-tocopherol, BHT and Polyethylene glycol using Film Cast Extruder, *Journal of Food Engineering*. **2010**, 100, 239-244.

Cao, Y.W.; Feng, J.C.; and Wu, P.Y. Alkyl-functionalized Graphene Nanosheets with Improved Lipophilicity, *Carbon*. **2010**, 48, 1683-1685.

Cao, Y.; Feng, J.; and Wu, P. Preparation of Organically Dispersible Graphene Nanosheet Powders through a Lyophilization Method and their Poly(lactic acid) Composites, *Carbon*. **2010**, 48, 3834-3839.

Carr, K.E. Intercalation and Oxidation Effects on Graphite of a Mixture of Sulphuric and Nitric Acids, *Carbon.* **1970**, 8, 155-158.

Cele, H.M.; Ojijo, V.; Chen, H.; Kumar, S.; Land, K.; Joubert, T.; Villiers, M.F.R.; and Ray, S.S. Effect of Nanoclay on Optical Properties of PLA/Clay Composite Films, *Polym. Test.* **2014**, 36, 24-31.

Chang, J.H.; An, Y.U.; Cho, D.; and Giannelis, E.P. Poly(lactic acid) Nanocomposites: Comparison of their Properties with Montmorillonite and Synthetic Mica (II), *Polymer.* **2003**, 44, 3715-3720.

Chen, G.; Wu, D.; Weng, W.; and Wu, C. Exfoliation of Graphite Flake and its Nanocomposites, *Carbon*. **2003**, 41, 619-621.

Chen, E.C.; and Wu, T.M. Isothermal Crystallization Kinetics and Thermal Behavior of Poly(ε-caprolactone)/Multi-Walled Carbon Nanotube Composites, *Polym. Degrad. Stab*. **2007**, 9, 1009-1015.

Chen, H.; Chen, J.; Chen, J.; Yang, J.; Huang, T.; Zhang, N.; and Wang, Y. Effect of Montmorillonite on Cold Crystallization and Hydrolytic Degradation of Poly(L-lactide), *Polym. Degrad. Stab*. **2012**, 97, 2273-2283.

Chen, H.; Zhang, W.; Du, X.; Yang, J.; Zhang, N.; Huang, T.; and Wang Y. Crystallization Kinetics and Melting Behaviors of Poly(l-lactide)/Graphene oxide Composites, *Thermochim Acta* **2013**, 566, 57-70.

Chen, H.M.; Feng, C.X.; Zhang, W.B.; Yang, J.H.; Huang, T.; Zhang, N.; and Wang, Y. Hydrolytic Degradation Behavior of Poly(L-lactide)/Carbon Nanotubes Nanocomposites*, Polym. Degrad. Stab.* **2013**, 98, 198-208.

Chen, H.M.; Wang, Y.P.; Chen, J.; Yang, J.H.; Zhang, N.; Huang, T.; and Wang, Y. Hydrolytic Degradation Behaviour of Poly(L-lactide)/SiO_2 Composites, *Polym. Degrad. Stab*. **2013**, 98, 2672-2679.

Cheng, S.; Lau, K.; Liu, T.; Zhao, Y.; Lam, P.; and Yin, Y. Mechanical and Thermal Properties of Chicken Feather Fiber/PLA Green Composites, *Composites: Part* B. **2009**, 40*,* 650-654.

Chou, P.M.; Mariatti, M.; Zulkifli, A.; and Sreekantan, S. Evaluation of the Flexural Properties and Bioactivity of Bioresorbable PLLA/PBSL/CNT and PLLA/PBSL/TiO_2 Nanocomposites, *Composites: Part B*. **2012**, 43, 1374‑1381.

Chrissafis, K. Detail Kinetic Analysis of the Thermal Decomposition of PLA with Oxidized Multiwalled Carbon nanotubes, *Thermochim. Acta.* **2010**, 511, 163-167.

Compton, O.C.; and Nguyen, S.T. Graphene oxide, Highly Reduced Graphene oxide and Graphene: Versatile Building Blocks for Carbon-based Materials, *Small*. **2010**, 6, 711-723.

Corma, A.; Iborra, S.; and Velty, A. Chemical Routes for the Transformation of Biomass into Chemicals, *Chem. Rev*. **2007**, 107, 2411-2502.

Criado, J.M.; Malek, J.; and Ortega, A. Applicability of the Master Plots in Kinetic Analysis of Non-isothermal Data, *Thermochim. Acta.* **1989**, 147, 377-385.

Cui, P.; Lee, J.; Hwang, E.; and Lee, H. One-pot Reduction of Graphene oxide at Subzero Temperatures, *Chem. Commun.* **2011**, 47, 12370-12372.

Dallyn, H.; and Shorten, D. Hygiene Aspects of Packaging in the Food Industry, *Int. Biodeterior.* **1988**, 24, 387-392.

Defeng, W.; Wu, L.; Wu, L.; Xu, B.; Zhang, Y.; and Zhang, M. Nonisothermal Cold Crystallization Behavior and Kinetics of Polylactide/Clay Nanocomposites, *J. Polym. Sci: Part B: Polym Phys*. **2007**, 45, 1100-1113.

Desantis, P.; and Kovacs, A.J. Molecular Conformation of Poly(S-lactic acid), *Biopolymers.* **1968**, 6, 299-.306.

Dias, J.C.; Ribeiro, C.; Sencadas, V.; Botelho, G.; Ribelles, J. L.G.; and Mendez, S.L. Influence of Fiber Diameter and Crystallinity on the Stability of Electrospun Poly(L-lactic acid) Membranes to Hydrolytic Degradation, *Polym. Degrad. Stab*. **2012**, 31, 770-776.

Dong, Y.; Ghataura, A.; Takagi, H.; Haroosh, H.J.; Nakagaito, A.N.; and Lau, K.T. Polylactic acid (PLA) Biocomposites Reinforced with Coir Fibers: Evaluation of Mechanical Performance and Multifunctional Properties, *Compos. Part A-Appl. S.* **2014**, 36, 76-84.

Fan, Y.; Nishida, H.; Shirai, Y.; and Endo T. Thermal Stability of Poly (L-lactide): Influence of End Protection by Acetyl Group, *Polym. Degrad. Stab*. **2004**, 84, 143-149.

Fan, Y.; Nishida, H.; Shirai, Y.; Tokiwa, Y.; and Endo, T. Thermal Degradation Behaviour of Poly(lactic acid) Stereocomplex, *Polym. Degrad. Stab.* **2004**, 86, 197-208.

Fang, G.; Li, H.; Chen, Z.; and Liu, X. Preparation and Properties of Palmitic acid/SiO_2 Composites with Flame Retardant as Thermal Energy Storage Materials, *Sol. Energ. Mat. Sol. C.* **2011**, 95, 1875-1881.

Fernandez, J.; Larranaga, A.; Etxeberria, A.; and Sarasua, J.R. Effect of Chain Microstructures and Derived Crystallization Capability on Hydrolytic Degradation of Poly(L-lactide/Ɛ-Caprolactone) Copolymers, *Polym. Degrad. Stab*. **2013**, 98, 481-489.

Flynn, J.H.; and Wall, L.A. A Quick Direct Method for the Determination of Activation Energy from the Thermogravimetric Data, *J. Polym. Sci*. **1966**, 4, 323-328.

Fortunati, E.; Peltzer, M.; Armentano, I.; Torre, L.; Jimenez, A.; and Kenny, J.M. Effects of Modified Cellulose Nanocrystals on the Barrier and Migration Properties of PLA Nanobiocomposites, *Carbohydr. Polym.* **2012**, 90, 948-956.

Fortunati, E.; Armentano, I.; Zhou, Q.; Puglia, D.; Terenzi, A.; Berglund, L.A.; and Kenny, J.M. Microstructure and Nonisothermal Cold Crystallization of PLA Composites based on Silver Nanoparticles and Nanocrystalline Cellulose, *Polym. Degrad. Stab.* **2012**, 97, 2027-2036.

Fortunati, E.; Luzi, F.; Puglia, D.; Dominici, F.; Santulli, C.; Kenny, J.M.; and Torre, L. Investigation of Thermo-mechanical, Chemical and Degradative Properties of PLA-limonene Films Reinforced with Cellulose Nanocrystals Extracted from Phormium tenax Leaves, *Eur. Polym. J.* **2014**, 56, 77-91.

Fukushima, K.; Abbate, C.; Tabuani, D.; Gennari, M.; and Camino, G. Biodegradation of Poly(lactic acid) and its Nanocomposites, *Polym. Degrad. Stab.* **2009**, 94, 1646-1655.

Fukushima, K.; Murariu, M.; Camino, G.; and Dubois, P. Effect of Expanded Graphite/Layered-Silicate Clay on Thermal, Mechanical and Fire Retardant Properties of Poly(lactic acid), *Polm. Degrad. Stab.* **2010**, 95, 1063-1076.

Fukushima, K.; Tabuani, D.; Dottori, M.; Armentano, I.; Kenny, J.M.; and Camino, G. Effect of Temeprature and Nanopartyicle Type on Hydrolytic Degradation of Poly(lactic acid) Nanocomposites, *Polym. Degrad. Stab*. **2011**, 96, 2120-2129.

Gaona, L.A.; Ribelles, J.L.G.; Perilla, J.E.; and Lebourg, M. Hydrolytic degradation of PLLA/PCL Microporous Membranes Prepared By Freeze Extraction, *Polym. Degrad. Stab*. **2012,** 97, 1621-1632.

Garlotta, D. A Literature Review of Poly(lactic acid), *J. Polymer. Environ*. **2001**, 9, 63-84.

George, K.A.; Chirila, T.V.; and Byrne, E.W. Effect of Crosslink Density on Hydrolytic Degradation of Poly(L-lactide)-Based Networks, *Polym. Degrad. Stab*. **2012**, 97 964-971.

Goffin, A.L.; Raquez, J.M.; Duquesne, E.; Siqueria, G.; Habibi, Y.; and Dufresne, A. From Interfacial Ring-Opening Polymerization to Melt Processing of Cellulose Nanowhisker-Filled Polylactide-Based Nanocomposites, *Biomacromolecules.* **2011**, 12, 2456-2465.

Gong, X.; Pan, L.; Tang, C.Y.; Chen. L.; Hao, Z.; Law, W.C.; Wang, X.; Tsui, C.P.; and Wu, C. Preparation, Optical and Thermal Properties of CdSe-ZnS/Poly(lactic acid) (PLA) Nanocomposites, *Compos. Part B: Eng.* **2014**, 66, 494-499.

Goriparthi, B.K.; Suman, K.N.S.; and Rao, N.M. Effect of Fiber Surface Treatments on Mechanical and Abrasive Wear Performance of Polylactide/jute Composites, *Composites. Part A.* **2012**, 43, 1800-1808.

Gorrasi, G.; and Pantani, R. Effect of PLA Grades and Morphologies on Hydrolytic Degradation at Composting Temperature: Assessment of Structural Modification and Kinetic Parameters, *Polym. Degrad. Stab.* **2013,** 98, 1006-1014.

Gotor, F.J.; Criado, J.M.; Malek, J.; and Koga. K. Kinetic Analysis of Solid State Reactions: The University of Master Plots for Analyzing Isothermal and Nonisothermal Experiments, *J. Phys. Chem. A*. **2000**, 104, 10777-10782.

Grapnuer, N. Application of Lignin as Natural Adhesion Promoter in Cotton Fibre-Reinforced Poly(lactic acid) (PLA) Composites, *J. Mater. Sci*. **2008**, 43, 5222-5229.

Grizzi, I.; Garreau, H.; Li, S.; and Vert, M. Hydrolytic Degradation of Devices Based on Poly (DL-Lactic Acid) Size Dependence, *Biomaterials.* **1995,** 16, 305-311.

Han, H.S.; You, J.; Jeong, H.; and Jeon, S. Synthesis of Graphene oxide Grafted Poly(lactic acid) with Palladium Nanoparticles and its Application to Serotonin Sensing, *Appl. Surf. Sci.* **2013**, 284, 438-445.

Han, Q.; Wang, Y.; Shao, C.; Zheng, G.; Li, Q.; and Shen, C. Nonisothermal Crystallization Kinetics of Biodegradable Poly(lactic acid)/Zinc Phenylphosphonate Composites, *J. Comp. Mater.* **2013**, doi: 10.1177/0021998313502064.

Hernandez, J.J.; Garcia-Gutierrez, M.C.; Nogales, A.; Rueda, D.R.; Kwiatkowska, M.; Szymczyk, A.; Roslaneic, Z.; Concheso, A.; Guinea, I.; and Ezquerra, T.A. Influence of Preparation Procedure on the Conductivity and Transparency of SWCNT-Polymer Nanocomposites, *Compos. Sci. Technol*. **2009**, 69, 1867-1872.

Hoogsteen, W.; Postema, A.R.; Pennings, A.J.; and Brinke, G.T. Crystal Structure, Conformation and Morphology of Solution-spun Poly(L-lactide) Fibers, *Macromolecules*. **1990**, 23, 634-642.

Hosseini, S.G.; Pourmortazavi, S.M.; and Hajimirsadeghi, S.S. Thermal Decomposition of Pyrotechnic Mixtures Containing Sucrose with either Potassium Chlorate or Potassium Perchlorate, *Comb. Flame.* **2005**, 141, 322-326.

Huang, K.J.; Niu, D.J.; Sun, J.Y.; Han, C.H.; Wu, Z.W.; Li, Y.L.; and Xiong, X.Q. Novel Electrochemical Sensor Based on Functionalized Graphene for Simultaneous Determination of Adenine and Guanine in DNA, *Colloids. Surf. B.* **2010**, 82, 543-549.

Huang, Y.; Zhang, C.; Pan, Y.; Zhou, Y.; Jiang, L.; and Dan, Y. Effect of NR on the Hydrolytic Degradation of PLA, *Polym. Degrad. Stab.* **2012,** 98, 943-950.

Huda, M.S.; Drzal, L.T.; Mohanty, A.K.; and Misra, M. Effect of Chemical Modifications of the Pineapple Leaf Fiber Surfaces on the Interfacial and Mechanical Properties of Laminated Biocomposites, *Compos. Interface*. **2008**, 15, 169-191.

Hung, C.Y.; Huang, D.K.; Wang, C.C.; and Chen, C.Y. Preparation, Crystallization Behavior, and Morphology of Poly(lactic acid) Clay Hybrids via Wet Kneading Masterbatch Process, *J. Inorg. Organomet. Polym.* **2013**, 23, 1389-1396.

Hussain, F.; Hojjati, M.; Okamoto, M.; and Gorga, R.E. Polymer-Matrix Nanocomposites, Processing, Manufacturing and Application: An Overview, *J. Compos. Mater*. **2006**, 40, 1511-1575.

Iovino, R.; Zullo, R.; Rao, M.A.; Cassar, L.; and Gianfreda, L. Biodegradation of Poly(lactic acid)/Starch/Coir Biocomposites Under Controlled Composting Conditions, *Polym. Degrad. Stab.* **2007**, 93, 147-157.

Jamshidian, M.; Tehrany, E.A.; Imran, M.; Akhtar, M.J.; Cleymand, F.; and Desobry, S. Structural, Mechanical and Barrier Properties of Active PLA-Antioxidant Films, *J. Food. Eng.* **2012**, 110, 380-389.

Jang, J.Y.; Jeong, T.K.; Oh, H.J.; Youn J.R.; and Song, Y.S. Thermal Stability and Flammability of Coconut Fiber Reinforced Poly(lactic acid) Composites, *Compos. Part B:Eng.* **2012,** 43, 2434-2438.

Jankovic, B.; Adnadevic, B.; and Jovanovic, J. Application of Model-Fitting and Model-Free Kinetics to the Study of Nonisothermal Dehydration of Equilibrium Swollen Poly(acrylic acid) Hydrogel, Thermo Gravimetric Analysis, *Thermochim. Act*a. **2007**, 452, 106-115.

Jankovic, B. Kinetic Analysis of the Nonisothermal Decomposition of Potassium Matabisulfite Using the Model-Fitting and Isoconversional (model free) Methods, *Chem. Eng. J*. **2008**, 139, 128-135.

Janorkar, A.V.; Metters, A.T.; and Hirt, D.E. Modification of Poly(lactic acid) Films: Enhanced Wettability from Surface-Confined Photografting and Increased Degradation Rate due to an Artifact of the Photografting Process, *Macromolecules.* **2004**, 37, 9151-9159.

Ji, S.G.; Hwang, J.H.; Cho, D.; and Kim, H.J. Influence of Electron beam Treatment of Jute on the Thermal Properties of Random and Two-Directional Jute/Poly(lactic acid) Green Composites, *J. Adhes. Sci. Technol.* **2013**, 27, 12, 1359-1373.

Jiang, L.; Zhang, J.; and Wolcott, M.P. Comparison of Polylactide/Nano-sized Calcium carbonate and Polylactide/Montmorillonite Composites: Reinforcing Effects and Toughening Mechanisms, *Polymer.* **2007**, 48, 7632-7644.

Jong, S.J.; Arias, E.R.; Rijkers, D.T.S.; Nostrum, C.F.; Bosch, J.J.; and Hennink, W.E. New Insights into the Hydrolytic Degradation of Poly(Lactic Acid): Participation of the Alcohol Terminus, *Polymer.* **2001,** 42, 2795-2802.

Kaewpirom, S.; and Worrarat, C. Preparation and Properties of Pineapple Leaf Fiber Reinforced Poly(lactic acid) Green Composites, *Fibers and Polymers.* **2014**, 15, 1469-1477.

Kalaitzidou, K.; Fukushima, H.; and Drzal, L.T. A New Compounding Method for Exfoliated Graphite-Polypropylene Nanocomposites with Enhanced Flexural Properties and Lower Percolation Threshold, *Compos. Sci. Technol.* **2007**, 67, 2045-2051.

Katiyar, V.; Gerds, N.; Koch, C.B.; Risbo, J.; Hansen, H.C.B.; and Plackett, D. Poly l-lactide-layered Double Hydroxide Nanocomposites via In-situ Polymerization of l-lactide, *Polym. Degrad. Stab.* **2010**, 95, 2563-2573.

Katiyar, V.; Gerds, N.; Koch, C.B.; Risbo, J.; Hansen, H.S.B.; and Plackett, D. Melt Processing of Poly(L-lactic acid) in the Presence of Organomodified Anionic or Cationic Clays, *J. Appl. Polym. Sci.* **2011**, 122, 112-125.

Kelly, F.H.C.; and Brown, D.W. Thermal Decomposition and Colour Formation in Aqueous Sucrose Solutions, *Sugar. Technol. Rev.* **1978**, 6, 1-48.

Khawan, A.; and Flanagan, D.R. Solid State Kinetic Models: Basics and Mathematical Fundamentals, *J. Phys. Chem. B*. **2006**, 110, 17315-17328.

Kissinger, H.E. Reaction Kinetics in Differential Thermal Analysis, *Anal. Chem*. **1957**, 29, 1702-1706.

Kong, Y.; and Hay, J.N. Multiple Melting Behaviour of Poly(ethylene terephthalate), *Polymer.* **2003**, 44, 623-633.

Koutsomitopoulou, A.F.; Benezet, J.C.; Bergeret, A.; and Papanicolaou, G.C. Preparation and Characterization of Olive Pit Powder as a Filler to PLA-matrix Biocomposites, *Powder Technol.* **2014**, 255, 10-16.

Krikorian, V.; and Pochan, D.J. Poly (L-Lactic Acid)/Layered Silicate Nanocomposite: Fabrication, Characterization, and Properties, *Chem. Mater.* **2003**, 15, 4317-4324.

Krishna, S.V.; and Pugazhenthi, G. Properties and Thermal Degradation Kinetics of Polystyrene/Organoclay Nanocomposites Synthesized by Solvent Blending Method:

Effect of Processing Conditions and Organoclay Loading, *J. Appl. Polym.Sci.* **2011**, 120, 1322-1336.

Kuan, C.F.; Chen, C.H.; Kuan, H.C.; Lin, K.C.; Chiang, C.L.; and Peng, H.C. Multi-Walled Carbon Nanotube Reinforced Poly(L-lactic acid) Nanocomposites Enhanced by Water-Crosslinking Reaction, *J. Phys. Chem. Solids.* **2008**, 69, 1399-1402.

Kumar, R.; Yakubu, M.K.; and Anandjiwala, R.D. Biodegradation of Flax Fiber Reinforced Poly(lactic acid), *Express Polym. Letters.* **2010**, 4, 423-430.

Langlois, V.; Rehel, K.V.; Peron, J.J.; Borgne, A.l.; Walls, M.; and Gurein, P. Synthesis and Hydrolytic Degradation of Graft Copolymers Containing Poly(lactic acid) Side Chains: In Vitro Release Studies of Bioactive Molecules, *Polym. Degrad. Stab.* **2002**, 76, 411-417.

Lee, B.H.; Kin, H.S.; Lee, S.; Kim, H.Y.; and Dorgan, J.R. Bio-composites of Kenaf Fibers in Polylactide: Role of Improved Interfacial Adhesion in the Carding Process, *Compos. Sci. Technol.* **2009,** 69, 2573-2579.

Lee, T.W.; and Jeong, Y.G. Enhanced Electrical Conductivity, Mechanical Modulus, and Thermal Stability of Immiscible Polylactide/Polypropylene Blends by the Selective Localization of Multi-Walled Carbon Nanotubes, *Compos. Sci. Technol.* **2014**, 103, 78-84.

Li, B.; Dong, F.X.; Wang, X.L.; Yang, J.; Wang, D.Y.; and Wang, Y.Z. Organically Modified Rectorite Toughened Poly(lactic acid):Nanostructures, Crystallization and Mechanical Properties, *Eur. Polym. J.* **2009**, 45, 2996-3003.

Li, J.; Zheng, W.; Lia, L.; Zheng, Y.; and Lou, X. Thermal Degradation Kinetics of g-HA/PLA Composite, *Thermochim. Acta*. **2009**, 493, 90-95.

Li, Y.; Wang, S.; Yang, X.; and Zhang, X. Preparation and Characterization of Silver Palmitate, *Int. J. Nanosci.* **2009**, 8, 97-102.

Li, Q.H.; Zhou, Q.H.; Deng, D.; Yu, Q.Z.; Gu, L.; Gong, K.D.; and Xu, K.H. Enhanced Thermal and Electrical Properties of Poly (*D*,*L*-lactide)/Multi-Walled Carbon Nanotubes Composites by In-situ Polymerization, *Trans. Nonferrous Met. Soc. China.* **2013**, 23, 1421-1427.

Liao, R.; Yang, B.; Yu, W.; and Zhou, C. Isothermal Cold Crystallization Kinetics of Polylactide/Nucleating Agents, *J. Appl. Polym. Sci.* **2007**, 104, 310-317.

Liu, X.; Zou, Y.; Li, W.; Cao, G.; and Chen, W. Kinetics of Thermo-oxidative and Thermal Degradation of Poly(D,.L-lactide) (PDLLA) at Processing Temperature, *Polym. Degrad. Stab.* **2006,** 91, 3259-3265.

Liu, L.; Jin, T.Z.; Coffin, D.R.; and Hicks, K.B. Preparation of Antimicrobial Membranes: Coextrusion of Poly(lactic acid) and Nisaplin in the Presence of Plasticizers, *J. Agric. Food Chem.* **2009**, 57, 8392-8398.

Liu, D.Y.; Yuan, X.W.; Bhattacharyya, D.; and Easteal, A.J. Characterization of Solution Cast Cellulose Nanofibre-reinforced Poly(lactic acid), *Express Polym. Lett.* **2010**, 4, 26-31.

Liu, Y.; Wang, L.; He, Y.; Fan, Z.; and Lia, S. Non-isothermal Crystallization Kinetics of Poly(L-lactide), *Polym. Int.* **2010**, 59, 1616-1621.

Loo, S.C.J.; Ooi, C.P.; and Boey, Y.C.F. Influence of Electron-Beam Radiation on the Hydrolytic Degradation Behaviour of Poly(lactide-co-glycolide) (PLGA), *Biomaterials*, **2004**, 26, 3809-3817.

Lu, D.R.; Xiao, C.M.; and Xu, S.J. Starch-based Completely Biodegradable Polymer Materials, *Express Polym. Lett.* **2009**, 3, 366-375.

Lu, T.; Liu, S.; Jiang, M.; Xu, X.; Wang, Y.; Wang, Z.; Gou, J.; Hui, D.; and Zhou, Z. Effects of Modifications of Bamboo Cellulose Fibers on the Improved Mechanical Properties of Cellulose Reinforced Poly(lactic acid), *Composites: Part B.* **2014**, 62, 191‑197.

Luo, Y.B.; Wang, X.L.; and Wang, Y.Z. Effect of TiO_2 Nanoparticles on the Long-term Hydrolytic Degradation Behavior of PLA, *Polym. Degrad. Stab.* **2012,** 97, 721-728.

Mai, T.T.T.; Nguyen, T.T.T.; Le, Q.D.; Nguyen, T.N.; Ba, T.C.; Nguyen, H.B.; Phan, T.B.H.; Tran, D.L.; Nguyen, X.P.; and Park, J.S. A Novel Nanofiber Cur-loaded Polylactic acid Constructed by Electrospinning, *Adv. Nat. Sci. Nanosci. Nanotechnol.* **2012**, 3, 25014-25019.

Mai, T.T.T.; Nguyen, T.T.T.; Le, Q.D.; and Park, J.S. Chitosan and O-carboxymethyl Chitosan Modified Fe_3O_4 for Hyperthermic Treatment, *Adv. Nat. Sci.: Nanosci. Nanotechnol.* **2012**, 3, 25014-25019.

Maiti, P.; Yamada, K.; Okamoto, M.; Ueda, K.; and Okamoto, K. New Polylactide/Layered Silicate Nanocomposites: Role of Organoclays, *Chem. Mater.* **2002,** 14, 4654-4661.

Maiti, S.N.; and Hemalatha. Nonisothermal Crystallization Kinetics of PA6 and PA6/SEBS-g-MA Blends, *J. Polym. Res.* **2012**, 19, 9926-9942.

Marsh, K.; and Bugusu, B. Food Packaging Roles, Materials, and Environmental Issues, *J. Food. Sci.* **2007**, 72, 1750-3841.

Mauch, W. The Chemical Properties of Sucrose, *Sugar. Technol. Rev.* **1971,** 1, 239-290.

Meng, Q.K.; Hetzer, M.; and Kee, D.D. PLA/Clay/Wood Nanocomposites: Nanoclay Effects on Mechanical and Thermal properties, *J. Compos. Mater.* **2011**, 45, 1145-1158.

Michel, J.; Mcallister.; Li, J.L.; Admson, D.H.; Schniepp, H.C.; Abdala, A.A.; Liu, J.; Alonso, M.H.; Milius, D.L.; Reoberto, C.; Prudhomme, R.K.; and Aksay, I.A. Single Sheet Functionalized Graphene by Oxidation and Thermal Expansion of Graphite, *Chem. Mater.* **2007**, 19, 4396-4404.

Mittal, V. Polymer Layered Silicate Nanocomposites: A Review, *Materials*. **2009**, 2, 992-1057.

Mubarak, Y.; Harkin-Jones, E.M.A.; Martin, P.J.; and Ahmad, M. Modeling of Non-isothermal Crystallization Kinetics of Isotactic Polypropylene, *Polymer.* **2001**, 42, 3171-3182.

Murariu, M.; Dechief, A.L.; Bonnaud, L.; Paint, Y.; Gallos, A.; Fontaine, G.; Bourbigot, S.; and Dubois, P. The Production and Properties of Polylactide Composites filled with Expanded Graphite, *Poly. Degrad. Stab.* **2010**, 95, 889-900.

Najafi, N.; Heuzey, M.C.; and Carreau, P.J. Poly(lactic acid)-Clay Nanocomposites Prepared by Melt Compounding in the Presence of Chain Extender, *Compos. Sci. Technol.* **2012**, 72, 608- 615.

Nam, T.H.; Ogihara, S.; and Kobayashi, S. Interfacial, Mechanical and Thermal properties of Coir Fiber-Reinforced Poly(Lactic acid) Biodegradable Composites, *Adv. Compos Mater.* **2012**, 21, 103-122.

Narimissa, E.; Gupta, R.; Bhaskaran, M.; and Sriram S. Influence of Nano-graphite Platelet Concentration on Onset of Crystalline Degradation in Polylactide Composites, *Polym. Degrad. Stab.* **2012**, 97, 829-832.

Ndazi, B.S.; and Karlsson, S. Characterization of Hydrolytic Degradation of Polylactic Acid/Rice Hulls Composites in Water at Different Temperatures, *Express Polym. Lett*. **2011**, 5, 119-131.

Niyogi, S.; Bekyarova, E.; Itkis, M.E.; McWilliams, J.L.; Hamon, M.A.; and Haddon, R.C. Solution Properties of Graphite and Graphene, *J. Am. Chem. Soc.* **2006**, 128, 7720-7721.

Nofar, M.; Zhu, W.; Park, C.B.; and Randall, J. Crystallization Kinetics of Linear and Long-Chain-Branched Polylactide, *Ind. Eng. Chem. Res.* **2011**, 50, 13789-13798.

Nostrum, C.F.; Veldhuis, T.F.J.; Bos, G.W.; and Hennink, W.E. Hydrolytic Degradation of Oligo(Lactic Acid): A Kinetics and Mechanistic Study, *Polymer.* **2004**, 45, 6779-6787.

Olewnik, E.; Czerwinski, W.; and Nowaczyk, J. Hydrolytic Degradation of Copolymers Based on L-Lactic Acid and Bis-2-Hydroxyethyl Terephthalate, *Polym. Degrad. Stab*. **2007**, 92, 24-31.

Oyama, H.T.; Tanaka, Y.; and Kadosaka, A. Rapid Controlled Hydrolytic Degradation of Poly(L-lactic acid) by Blending with Poly(asparitic acid-co-L-lactide), *Polym. Degrad. Stab*. **2009**, 94, 1419-1426.

Oza, S.; Ning, H.; Ferguson, I.; and Lu, N.; Effect of Surface Treatment on Thermal Stability of the Hemp-PLA Composites: Correlation of Activation Energy with Thermal Degradation, *Composites: Part B.* **2014**, 67, 227–232.

Pamula, E.; Blazewicz, M.; Paluszkiewicz, C.; and Dobrzynski, P.J. FTIR Study of Degradation Products of Aliphatic Polyesters-Carbon Fibres Composites, *J. Mol. Struct*. **2001**, 596, 69-75.

Pan, Y.X.; Yu, Z.Z.; Ou, Y.C.; and Hu, G.H. A New Process of Fabricating Electrically Conducting Nylon 6/Graphite Nanocomposites via Intercalation Polymerization, *J. Polym. Sci. Part B: Polym. Phys*. **2000**, 38, 1626-1633.

Pan, P.; Yang, J.; Shan, G.; Bao, Y.; Weng, Z.; Cao, A.; Yazawa, K.; and Inoue, Y. Temperature-Variable FTIR and Solid-State ^{13}C NMR Investigations on Crystalline Structure and Molecular Dynamics of Polymorphic Poly(l-lactide) and Poly(l-lactide)/Poly(d-lactide) Stereocomplex, *Macromolecules.* **2012**, 45, 189-197.

Park, S.H.; Lee, S.G.; and Kim, S.H. Isothermal Crystallization Behavior and Mechanical Properties of Polylactide/Carbon Nanotube Nanocomposites, *Composites: Part A*. **2013**, 46, 11-18.

Patel, R.M.; Jain, P.; Story, B.; and Chum, S. Polyethylene - An Account of Scientific Discovery and Industrial Innovations, *Innovations in Industrial and Engineering Chemistry*. **2008,** 74 -102.

Paul, M.A.; Delcourt, C.; Alexandre, M.; Degee, P.; Monteverde, F.; and Dubois, P. Polylactide/Montmorillonite Nanocomposites: Study of the Hydrolytic Degradation, *Polym. Degrad. Stab*. **2005**, 87, 535-542.

Paula, E.L.D.; Mano, V.; and Pereira, F.V. Influence of Cellulose Nanowhiskers on the Hydrolytic Degradation Behaviour of Poly(D,lactide), *Polym. Degrad. Stab*. **2011**, 96, 1631-1638.

Pei, A.; Zhou, Q.; and Berglund, L.A. Functionalized Cellulose Nanocrystals as Biobased Nucleation Agents in Poly(L-lactide) (PLLA) - Crystallization and Mechanical Property Effects, *Compos. Sci. Technol.* **2010**, 70, 815-821.

Peng, F.; Shaw, M.T.; Olson, J.R.; and Wei, M. Hydroxyapatite Needle-Shaped Particles/Poly(l-lactic acid) Electrospun Scaffolds with Perfect Particle-along-Nanofiber Orientation and Significantly Enhanced Mechanical Properties, *J. Phys. Chem. C.* **2011**, 115, 15743-15751.

Perinovic, S.; Andricic, B.; and Erceg, M. Thermal Properties of Poly(L-lactide)/Olive Stone Flour Composites, *Thermochim. Acta*. **2010**, 510, 97-102.

Pistner, H.; Bendix, D.R.; Muhling, J.; and Reuther, J.F. Poly(L-lactide): A Long-Term Degradation Study In Vivo: Part III. Analytical Characterization, *Biomaterials.* **1993,** 14, 291-298.

Poletto, M.; Zattera, A.J.; and Santana R.M.C. Thermal Decomposition of Wood: Kinetics and Degradation Mechanisms, *Biores.Technol.* **2012**, 126, 7-12.

Pracella, M.; Haque, M.; and Puglia, D. Morphology and Properties Tuning of PLA/Cellulose Nanocrystals Bionanocomposites by Means of Reactive Functionalization and Blending with PVAc, *Polymer.* **2014**, 55, 3720-3728.

Predoi, D. Physico-chemical Studies of Sucrose Thin Films, *J. Nanomater. Bios.* **2010**, 5, 373-377.

Proikkakis, C.S.; Mamouzelos, N.J.; Tarantili, P.A.; and Andreopoulos, A.G. Swelling and Hydrolytic Degradation of Poly(D,L-lactic caid) in Aqueous Solutions*, Polym. Degrad. Stab*. **2006**, 91, 614-619.

Qiu, Z.; and Li, Z. Effect of Orotic Acid on the Crystallization Kinetics and Morphology of Biodegradable Poly(l-lactide) as an Efficient Nucleating Agent, *Ind. Eng. Chem. Res.* **2011**, 50, 12299-12303.

Rahim, J.W.; Hong, S.L.; and Ha, C.S. Tensile, Water Vapor Barrier and Antimicrobial Properties of PLA/Clay Composites Films, *Food Sci. Technol.* **2009**, 42, 612-617.

Raja, M.; Ryu, S.H.; and Shanmugharaj, A.M. Thermal, Mechanical and Electroactive Shape Memory Properties of Polyurethane (PU)/poly (lactic acid) (PLA)/CNT Nanocomposites, *Eur. Polym. J.* **2013**, 49, 3492-3500.

Ramzy, A.; Beermann, D.; Steuernagel, L.; Meiners, D.; and Ziegmann, G. Developing a new Generation of Sisal Composite Fibers for Use in Industrial Applications, *Compos. Part B: Eng.* **2014,** 66, 287-298.

Raquez, J.M.; Habibi, Y.; Murariu, M.; and Dubois, P. Polylactide (PLA)-based Nanocomposites, *Prog. Polym. Sci*. **2013**, 38, 1504-1542.

Ravi, V.; Pugazhenthi, G.; and Katiyar, V. Thermal Degradation Kinetics of Sucrose Palmitate Reinforced Poly(lactic acid) Biocomposites, *Int.J.Bio.Macromol*. **2014**, 65, 275-283.

Ravari, F.; Mashak, A.; Nekoomanesh, M.; and Mobedi, H. Non-Isothermal Cold Crystallization Behavior and Kinetics of Poly(L-lactide): Effect of L-lactide Dimer, *Polym. Bull.* **2013**, 70, 2569-2586.

Ray, S.S.; and Bousmina, M. Biodegradable Polymers and Their Layered Silicate Nanocomposites: In Greening the 21st Century Materials World, *Prog. Mater. Sci*. **2005**, 50, 962-1079.

Ray, S.S; Maiti, P.; Okamoto, M.; Yamada, K.; and Ueda, K. New Polylactide/Layered Silicate Nanocomposites. 1. Preparation, Characterization, and Properties, *Macromolecules*. **2002**, 35, 3104-3110.

Ray, S.S.; Yamada, K.; Okamoto, M.; and Ueda, K. New Polylactide-Layered Silicate Nanocomposites. 2. Concurrent Improvements of Material Properties, Biodegradability and Melt Rheology, *Polymer*. **2003**, 44, 857-866.

Richards, G.N; and Shafizadeh, F. Mechanism of Thermal Degradation of Sucrose - A Preliminary Study, *J. Chem.* **1978**, 31, 1825-1832.

Richards, G.N. Initial Steps in Thermal Degradation of Sucrose, *Int. Sug. J*. **1986**, 88, 145-148.

Rudeekit, Y.; Numnoi, J.; Tajan, M.; Chaiwutthinan, P.; and Leejarkpai, T. Determining Biodegradability of Poly(lactic acid) Under Different Environments, *J. Mate. Mat. Min.* **2008**, 18, 83-87.

Ryoo, S.R.; Kim, Y.K.; Kim, M.H.; and Min, D.H. Behaviors of NIH-3T3 Fibroblasts on Graphene/Carbon Nanotubes: Proliferation, Focal Adhesion, and Gene Transfection Studies, *ACS Nano.* **2010**, 4, 6587-6598.

Saha, S.K.; and Tsuji, H. Effect of Molecular Weight and Small Amounts of D-lactide Units on Hydrolytic Degradation of Poly(L-lactic acid)s, *Polym. Degrad. Stab*. **2006**, 91, 1665-1673.

Sanchez-Garcia, M.D.; Gimenez, E.; and Lagaron, J.M. Morphology and Barrier Properties of Solvent Cast Composites of Thermoplastic Biopolymers and Purified Cellulose Fibers, *Carbohydr. Polym.* **2008**, 71, 235-244.

Sawai, D.; Takahashi, K.; Sasashige, A.; Kanamoto, T.; and Hyon, S.H. Preparation of Oriented β-form Poly(L-lactic acid) by Solid-state Co-extrusion: Effect of Extrusion Variables, *Macromolecules.* **2003**, 36, 3601-3605.

Shan, X.; Song, L.; Xing, W.; Hu, Y.; and Lo, S. Effect of Nickel-Containing Layered Double Hydroxides and Cyclophosphazene Compound on the Thermal Stability and Flame Retardancy of Poly(lactic acid), *Ind. Eng. Chem. Res.* **2012**, 51, 13037-13045.

Shih, Y.F.; Huang, R.H.; and Yu, Y.H. Preparation and Characterization of Sol-gel Modified Pineapple Leaf Fiber/Polylactic acid Composites, *J. Sol-Gel Sci. Technol*. **2014**, 70, 491-499.

Shih, Y.F.; Chang, W.C.; Liu, W.C.; Lee, C.C.; Kuan, C.S.; and Yu, Y.H. Pineapple Leaf/Recycled Disposal Chopstick Hybrid Fiber-Reinforced Biodegradable Composites, *J. Taiwan. Inst. Chem. E*. **2014,** 45, 2039-2046.

Siengchin, S. Reinforced Flax Mat/Modified Polylactide (PLA) Composites: Impact, Thermal and Mechanical Properties, *Mechanics of Composite Materials.* **2014**, 50, 257-266.

Simkovic, I; Surina, I.; and Vrican, M. Primary Reactions of Sucrose Thermal Degradation, *J. Anal. Appl. Pyrolysis.* **2003,** 70: 493-504.

Simoneit, B.R.T.; Medeiros, P.M.; and Didyk, B.M. Combustion Products of Plastics as Indicators for Refuse Burning in the Atmosphere, *Environ. Sci. Technol.* **2005**, *39*, 6961-6970.

Singh, K.S.W.; Everett, D.H.; Haul, R.A.W.; Moscou, L.; Pierotti, R.A.; Rouquerol, J.; and Siemieniewska, T. Reporting Physisorption Data for Gas/Solid Systems with Special Reference to the Determination of Surface Area and Porosity, *Pure & Appl. Chem*. **1985**, 57, 603-619.

Siracusa, V.; Rocculi, P.; Romani, S.; and Rosa, D.M. Biodegradable Polymers for Food Packaging: A Review, *Trends. Food. Sci. Tech.* **2008**, 19, 634-643.

Song, W.; Zheng, Z.; Tang, W.; and Wang, X. A Facile Approach to Covalently Functionalized Carbon Nanotubes with Biocompatible Polymer, *Polymer*. **2007**, 48, 3658-3663.

Song, L.; Xuan, S.; Wang, X; and Hu, Y. Flame Retardancy and Thermal Degradation Behaviors of Phosphate in Combination with POSS in Polylactide Composites, *Thermochim. Acta*. **2012**, 527, 1-7.

Song, Y.; Liu, J.; Chen, S.; Zheng, Y.; Ruan, S.; and Bin, Y. Mechanical Properties of Poly (Lactic Acid)/Hemp Fiber Composites Prepared with a Novel Method, *J. Polym. Environ.* **2013**, 21, 1117-1127.

Sorrentino, A.; Gorrasi, G.; and Vittoria, V. Potential Perspective of Bionanocomposites for Food Packaging Applications, *Trends. Food. Sci. Tech.* **2007**, 18, 84-95.

Stankovich, S.; Dikin, D.A.; Piiner, R.D.; Kohlhass, K.A.; Kleinhammes, A.; Jai, Y.; Wu, Y.; Naguyen, S.T.; and Rouf, R.S. Synthesis of Graphene-based Nanosheets via Chemical Reduction of Exfoliated Graphite Oxide, *Carbon.* **2007**, 45, 1558-1565.

Stankovich, S.; Dikin, D.A.; Dommett, G.H.B.; Kohlhaas, K.M.; Zimney, E.J.; Stach, E.A.; Piner, D.; Nguyen, S.T.; and Ruoff, R.S. Graphene-based Composite Materials, *Nature.* **2006**, 442, 282-286.

Sun, Y.; and He, C. Synthesis and Stereocomplex Crystallization of Poly(lactide)-Graphene Oxide Nanocomposites, *ACS Macro. Lett*. **2012**, 1, 709-713.

Surin, P.; Rakkwamsuk, P.; Wimolmala, E.; and Sombatsompop, N. Effect of Coir Fiber and Maleic Anhydride Modification on the Thermoplastic Starch/PLA Composite Laminates, *J. Nat. Fibers*. **2015,** 12, 108-120.

Tanase, C.; and Spiridon, I. PLA/Chitosan/Keratin Composites for Biomedical Applications, *Materials Science and Engineering C*. **2014**, 40, 242-247.

Taubner, V.; and Shishoo, R. Influence of Processing Parameters on the Degradation of Poly(L-lactide) During Extrusion, *J. Appl. Polym. Sci*. **2001**, 79, 2128-2135.

Tawakkal, I.S.M.A.; Cran, M.J.; and Bigger, S.W. Effect of Kenaf Fiber Loading and Thymol Concentration on the Mechanical and Thermal properties of PLA/Kenaf/Thymol Composites*, Ind. Crop. Prod.* **2014**, 61, 74-83.

Teramoto, N.; Urata, K.; Ozawa, K.; and Shibata, M. Biodegradation of Aliphatic Polyester Composites Reinforced by Abaca Fiber, *Polym. Degrad. Stab*. **2004**, 86, 401-409.

Tsai, P.; Chiu, W.M.; Lin, C.; and Wu, J. Fabrication and Characterization of PLA/SiO_2/Al_2O_3 Composites Prepared by Sol-gel Process, *Polymer-Plastics Technology and Engineering.* **2013**, 52, 1488-1495.

Tsuji, H.; Sawada, M.; and Bouapao, L. Biodegradable Polyesters as Crystallization-Accelerating Agents of Poly(l-lactide), *ACS Appl. Mater. Inter.* **2009**, 1, 1719-1730.

Tsuji, H.; and Tsuruno, T. Accelerated Hydrolytic Degradation of Poly(L-lactide)/Poly(D-lactide) Stereocomplex up to Late Stage, *Polym. Degrad. Stab*. **2010**, 95, 477-484.

Tudorachi, N.; Lipsa, R.; and Mustata, F.R. Thermal Degradation of Carboxymethyl Starch-g-Poly(lactic acid) Copolymer by TG-FTIR-MS Analysis, *Ind. Eng. Chem. Res.* **2012**, 51, 15537-15545.

Urbanczyk, L.; Ngoundjo, F.; Alexandre, M.; Jerome, C.; Detrembleur, C.; and Calberg, C. Synthesis of Polylactide/Clay Nanocomposites by In-situ Intercalative Polymerization in Supercritical Carbon dioxide, *Eur. Polym. J.* **2009**, 45, 643-648.

Vasanthan, N.; Ly, H.; and Ghosh, S. Impact of Nanoclay on Isothermal Cold Crystallization Kinetics and Polymorphism of Poly(l-Lactic Acid) Nanocomposites, *J. Phys. Chem. B.* **2011**, 115, 9556-9563.

Viculis, L.S.; Mack, J.J.; Mayer, O.M.; Hahn, H.T.; and Kaner, R.B. Intercalation and Exfoliation Routes to Graphite Nanoplatelets, *J. Mater. Chem.* **2005**, 15, 974-978.

Vert M.; Mauduit, J.; and Li, S. Biodegradation of PLA/GA Polymers: Increasing Complexity, *Biomaterials.* **1999,** 15, 1209-1213.

Wang, Y.; and Mano, J.F. Influence of Melting Conditions on the Thermal Behaviour of Poly(L-lactic acid), *Eur. Polym. J.* **2005**, 41, 2335-2342.

Wang, Y.; Steinhoff, B.; Brinkmann, C.; and Alig, I. In-line Monitoring of the Thermal Degradation of Poly(L-lactic acid) during Melt Extrusion by UV-Vis Spectroscopy, *Polymer*. **2008**, 49, 1257-1265.

Wang, X.; Xing, W.; Zhang, P.; Song, L.; Yang, H.; and Hu, Y. Covalent Functionalization of Graphene with Organosilane and its Use as a Reinforcement in Epoxy Composites, *Compos. Sci. Technol*. **2012**, 72, 737-743.

Wang, D.Y.; Gohs, U.; Kang, N.J.; Leuteritz, A.; Boldt, R.; Wagenknecht, U.; and Heinrich, G. Method for Simultaneously Improving the Thermal Stability and Mechanical Properties of Poly(lactic acid): Effect of High-Energy Electrons on the Morphological, Mechanical, and Thermal Properties of PLA/MMT Nanocomposites, *Langmuir.* **2012**, 28, 12601-12608.

Wang, L.; Jing, X.; Cheng, H.; Hu, X.; Yang, L.; and Huang, Y. Blends of Linear and Long-Chain Branched Poly(l-lactide)s with High Melt Strength and Fast Crystallization Rate, *Ind. Eng. Chem. Res.* **2012**, 51, 10088-10099.

Wang, Y.; Xu, Y.; He, D.; Yao, W.; Liu, C.; and Shen, C. “Nucleation Density Reduction” Effect of Biodegradable Cellulose Acetate Butyrate on the Crystallization of Poly(lactic acid), *Mater. Lett.* **2014**, 128, 85-88.

Wu, D.F.; Wu, L.; Wu, L.F.; and Zhang, M. Rheology and Thermal Stability of Polylactide/Clay Nanocomposites, *Polym. Degrad. Stab*. **2006**, 91, 3149-3155.

Wu, D.; Wu, L.; Xu, B.; Zhang, Y.; and Zhang, M. Nonisothermal Cold Crystallization Behavior and Kinetics of Polylactide/Clay Nanocomposites, *J. Polym. Sci., Part B: Polym. Phys.* **2007**, 45, 1100-1113.

Wu, D.F.; Wu, L.; Zhang, M.; and Zhao, Y.L. Viscoelasticity and Thermal Stability of Polylactide Composites with Various Functionalized Carbon Nanotubes, *Polym. Degrad. Stab*. **2008**, 93, 1577-1584.

Wu, J.H.; Yen, M.S.; Kuo, M.C.; and Chen. B.H. Physical Properties and Crystallization Behavior of Silica Particulates Reinforced Poly(lactic acid) Composites, *Mater. Chem. Phys.* **2013**, 142, 726-733.

Xiang, H.; Zhang, K.; Ji, G.; Lee, J.Y.; Zou, C.; Chen, X.; and Wu, J. Graphene/Nanosized Silicon Composites for Lithium Battery Anodes with Improved Cyclic Stability, *Carbon.* **2011**, 49, 1787-1796.

Xu, Z.; Niu, Y.; Wang, Z.; Li, H.; Yang, L.; Qiu, J.; and Wang, H. Enhanced Nucleation Rate of Polylactide in Composites Assisted by Surface Acid Oxidized Carbon Nanotubes of Different Aspect Ratios, *ACS Appl. Mater. Interfaces*. **2011**, 3, 3744-3753.

Xu, L.; Crawford, K.; and Gorman, C.B. Effect of Temperature and pH on the Degradation of Poly(lactic acid) Brushes, *Macromolecules.* **2011**, 44, 4777-4782.

Yang, D.J.; Zhang, Q.; Chen, G.; Yoon, S.F.; Ahn, J.; Wang, S.G.; Zhou, Q.; Wang, Q.; and Li, J.Q. Thermal Conductivity of Multiwalled Carbon Nanotubes, *Phys. Rev B.* **2002**, 66, 165440-165446.

Yang, T.C.K.; Lin, S.S.Y.; and Chuang, T.H. Kinetic Analysis of the Thermal Oxidation of Metallocene Cyclic Olefin Copolymer (mCOC)/TiO_2 Composites by FTIR Microscopy and Thermogravimetry, *Polym. Degrad. Stab*. **2002**, 78, 525-532.

Yang, K.K.; Wang, X.L.; and Wang, Y.Z. Progress in Nanocomposite of Biodegradable Polymer*, J. Ind. Eng. Chem.* **2007**, 13, 485-500.

Yasmin, A.; Luo, J.J.; and Daniel, I.M. Processing of Expanded Graphite Reinforced Polymer Nanocomposites, *Compos. Sci. Technol.* **2006**, 66, 1179-1189.

Yasuniwa, M.; Sakamo, K.; Ono, Y.; and Kawahara, W. Melting behavior of Poly(l-lactic acid): X-ray and DSC Analyses of the Melting Process, *Polymer.* **2008**, 49, 1943-1951.

Yi, L.; and Han, C. Isothermal and Nonisothermal Cold Crystallization Behaviors of Asymmetric Poly(l-lactide)/Poly(d-lactide) Blends, *Ind. Eng. Chem. Res.* **2012**, 51, 15927-15935.

Yoon, J.T.; Lee, S.C.; and Jeong, Y.G. Effects of Grafted Chain Length on Mechanical and Electrical Properties of Nanocomposites Containing Polylactide-Grafted Carbon Nanotubes, *Compos. Sci. Technol.* **2010**, 70, 776-782.

Yu, H.; Huang, N.; Wang, C.; and Tang, Z. Modeling of Poly(L-lactide) Thermal Degradation: Theoretical Prediction of Molecular Weight and Polydispersity Index, *J. Appl. Polym. Sci.* **2003**, 88, 2557-2562.

Yu, T.; Jiang, N.; and Li, Y. Functionalized Multi-walled Carbon Nanotube for improving the Flame Retardancy of Ramie/Poly(lactic acid) Composite, *Compos. Sci. Technol.* **2014**, 104, 26-33.

Yu, T.; Jiang, N.; and Li, Y. Study on Short Ramie Fiber/Poly(lactic acid) Composites Compatabilized by Maleic Anhydride, *Composites: Part A.* **2014**, 64, 139-146.

Yuzay, I.E.; Auras, R.; Valdez, H.S.; and Selke, S. Effects of Synthetic and Natural Zeolites on Morphology and Thermal Degradation of Poly(lactic acid) Composites, *Polym. Degrad. Stab.* **2010**, 95, 1769-1777.

Zakaria, Z.; Islam, S.; Hassan, A.; Haafiz, M.M.K. Arjmandi, R.; Inuwa, I.M.; and Hasan, M. Mechanical Properties and Morphological Characterization of PLA/Chitosan/Epoxidized Natural Rubber Composites, *Advances in Materials Science and Engineering.* **2013**, dx.doi.org/10.1155/2013/629092.

Zeng, J.B.; Li, Y.D.; He, Y.S.; and Wang, Y.Z. Improving Flexibility of Poly(l-lactide) by Blending with Poly(l-lactic acid) Based Poly(ester-urethane): Morphology, Mechanical Properties, and Crystallization Behaviors, *Ind. Eng. Chem. Res.* **2011**, 50, 6124-6131.

Zhang, R.; Zheng, H.; Lou, X.; and Ma, D. Crystallization Characteristics of Polypropylene and Low Ethylene Content Polypropylene Copolymer with and without Nucleating Agents, *J. Appl. Polym. Sci.* **1994**, 51, 51-56.

Zhang, K.; Mohanty, A.K.; and Misra, M. Fully Biodegradable and Biorenewable Ternary Blends from Polylactide, Poly(3-hydroxybutyrate-co-hydroxyvalerate) and Poly(butylene succinate) with Balanced Properties, *ACS Appl. Mater. Interfaces.* **2012**, 4, 3091-3101.

Zhang, B.; and Wang, Q. Development of Highly Ordered Nanofillers in Zein Nanocomposites for Improved Tensile and Barrier Properties, *J. Agric. Food Chem.* **2012**, 60, 4162-4169.

Zhang, C.; Lu, W.; Xie, X.; Tang, D.; Liu, C.; and Yang, Q.H. Towards Low Temperature Thermal Exfoliation of Graphite Oxide for Graphene Production, *Carbon.* **2013**, 62, 11-24.

Zhou, Q.; and Xanthos, M. Nanoclay and Crystallinity Effect on the Hydrolytic Degradation of Polylactides, *Polym. Degrad. Stab*. **2008**, 93, 1450-1459.

Zhou, Q.; and Xanthos, M. Nanosize and Microsize Clay Effects on the Kinetics of the Thermal Degradation of Polylactides, *Polym. Degrad. Stab.* **2009,** 94, 327-338.

Zhu, Y.; Murali, S.; Cai, W.; Li, X.; Suk, J.W.; Potts, J.R.; and Ruoff, R.S. Graphene and Graphene oxide: Synthesis, Properties and Applications, *Adv. Mater.* **2010**, 22, 3906-3924.

Zhu, R.; Liu, H.; and Zhang, J. Compatibilizing Effects of Maleated Poly(lactic acid) (PLA) on Properties of PLA/Soy Protein Composites, *Ind. Eng. Chem. Res.* **2012**, 51, 7786-7792.

RESEARCH PUBLICATIONS

Journals

- **Ravibabu Valapa**, G. Pugazhenthi, and Vimal Katiyar, Synthesis and Characterization of Sucrose Palmitate Reinforced Poly(lactic acid) Bionanocomposites. *Journal of Applied Polymer Science*, **2015**, 132, pp 41320-41330.
- **Ravibabu Valapa**, G. Pugazhenthi, and Vimal Katiyar, Thermal Degradation Kinetics of Sucrose Palmitate Reinforced Poly(lactic acid) Bionanocomposites, *International Journal of Biological Macromolecules*, **2014**, 65, pp 275-283.
- **Ravibabu Valapa**, G. Pugazhenthi, and Vimal Katiyar, Non Isothermal Crystallization Kinetic Studies for Sucrose Palmitate Reinforced Poly (lactic acid) Bionanocomposites, *Polymer Bulletin,* **2015***,* DOI 10.1007/s00289-015-1468-3.
- **Ravibabu Valapa**, G. Pugazhenthi, and Vimal Katiyar, Effect of Graphene Content on the Properties of Poly(lactic acid)/Graphene Composites for Packaging Application, *RSC Advances*, **2015**, 5, 28410-28423.
- **Ravibabu Valapa**, G. Pugazhenthi, and Vimal Katiyar, Influence of Graphene on Thermal Degradation and Crystallization Kinetics Behaviour of Poly(lactic acid), *Journal of Polymer Research*, **2015**, 175,1-14.
- **Ravibabu Valapa**, G. Pugazhenthi, and Vimal Katiyar, Hydrolytic Degradation Behaviour of Sucrose Palmitate Reinforced Poly(lactic acid) Bionanocomposites (*To be submitted*).
- **Ravibabu Valapa**, G. Pugazhenthi, and Vimal Katiyar, Hydrolytic Degradation Behaviour of Graphene Reinforced Poly(lactic acid) Bionanocomposites (*To be submitted*).

Conference Proceedings

- **Ravibabu Valapa,** G. Pugazhenthi, and Vimal Katiyar, Non-Isothermal Degradation Studies of Poly (lactic acid)/Sucrose Ester Nanocomposites, American Institute of Chemical Engineers Annual meeting (AIChE-2013), 16-21 November 2013, San Francisco (USA).
- **Ravibabu Valapa,** G. Pugazhenthi, and Vimal Katiyar, Fabrication and Thermal Degradation Studies of Exfoliated Graphene Reinforced Poly (lactic acid) Nanocomposite, American Institute of Chemical Engineers Annual meeting (AIChE-2013), 16-21 November 2013, San Francisco (USA).
- **Ravibabu Valapa,** G. Pugazhenthi, and Vimal Katiyar, Sucrose Ester/ Poly(lactic acid) Nanocomposites for Food Packaging Application: Fabrication and Characterization, American Institute of Chemical Engineers Annual meeting (AIChE-2013), 16-21 November 2013, San Francisco (USA).
- **Ravibabu Valapa,** G. Pugazhenthi, and Vimal Katiyar, Non Isothermal Cold Crystallization Kinetics for Sucrose Palmitate Reinforced Poly (lactic acid) Bionanocomposites, Polymer Processing Society Asia/Australia conference (PPS-2013), 04-07 December 2013, Mumbai, India.
- **Ravibabu Valapa,** G. Pugazhenthi, and Vimal Katiyar, Non Isothermal Crystallization Kinetics for Graphene Reinforced Poly (lactic acid) Nanocomposites, National School on Sustainable Polymers & First Symposium on Advances in Sustainable Polymers (ASP-14), 06-11January 2014, Indian Institute of Technology Guwahati, India.